2016

Microfluidic devices for high-throughput plant phenotyping and bioenergy harvesting from microbes and living plants

Huawei Jiang
Iowa State University

Microfluidic devices for high-throughput plant phenotyping and bioenergy harvesting from microbes and living plants

by

Huawei Jiang

A dissertation submitted to the graduate faculty

in partial fulfillment of the requirements for the degree of

DOCTOR OF PHILOSOPHY

Major: Electrical Engineering

Program of Study Committee:
Liang Dong, Major Professor
Sumit Chaudhary
Santosh Pandey
Jiming Song
Cindy Long Yu

Iowa State University

Ames, Iowa

2016

TABLE OF CONTENTS

NOMENCLATURE

FEA	Finite Element Analysis
PDMS	Polydimethylsiloxane
MS	Murashige and Skoog
WT	Wild-type
GFP	Green Fluorescent Protein
DI	Deionized
im	*immutans*
CLSM	Confocal Laser Scanning Microscopy
GUS	β-glucoronidase
ENMs	Electrospun Nanofibrous Membranes
SGC	Seed Growth Chips
PEO	Polyethylene Oxide
PDLC	Polymer Dispersed Liquid Crystal
MFC	Microbial Fuel Cell
µMFCs	Miniaturized MFCs
PEDOT	Poly(3,4-ethylenedioxythiophene)
CNTs	Carbon Nanotubes
PANI	Polyaniline
GO	Graphene Oxide
PSS	Poly(4-styrenesulfonate)
PVP	Poly(vinyl-pyrrolidone)

IBA	Isobornyl Acrylate
PEM	Proton Exchange Membrane
SEM	Scanning Electron Microscopy
TEM	Transmission Electron Microscopy
GF	Graphene Foam
FT	Flow-Through
CV	Cyclic Voltammetry
EIS	Electrochemical Impedance Spectroscopy
R_{ct}	Charge Transfer Resistance
k_o	Electron Transfer Rate Constant
PMFCs	Plant Microbial Fuel Cells
µPMFC	Miniature PMFC
PMMA	Poly(methyl methacrylate)
GC-MS	Gas Chromatography-Mass Spectroscopy

ACKNOWLEDGMENTS

This dissertation summarizes the research work during my Ph.D program in Iowa State University. I have to thank many people who guided and supported me during this period.

First, I would like to thank my committee chair and major professor, Dr. Liang Dong. Thanks for his support and patient guidance. I also want to thank my committee members, Dr. Sumit Chaudhary, Dr. Santosh Pandey, Dr. Jiming Song and Dr. Cindy Long Yu, for their guidance and instruction throughout the whole process of this research.

Second, I want to express my gratitude for Dr. Larry Halverson, Dr. Maneesha R. Aluru, Dr. Bing Yang, and Dr. Chiliang Chen for the collaboration on the plant phenotyping and microbial fuel cell projects and providing helpful discussions. I want to offer my appreciation and thanks to my colleagues in Laboratory for MEMS & Lab-Chips: Depeng Mao, Zhen Xu, Xinran Wang, Qiugu Wang, Yifei Wang, Yuncong Chen, Jikang Qu, Peng Liu, Xuan Qiao, Seval Yavas, Shawana Tabassum, and Yueyi Jiao.

The research presented in the thesis was supported in part by the U.S. National Science Foundation under Grant #DBI-1331390, the Iowa Corn Promotion Board, and the Iowa State University's Plant Sciences Institute Faculty Scholar Program.

In addition, I want to express my gratitude for my parents who always great support to me no matter what kind of difficulties I come across.

ABSTRACT

Microfluidics and micro/nanofabrication techniques provide powerful technological platforms to develop miniature bioassay devices for studying cellular and multicellular organisms. Microfluidic devices have many advantages over traditional counterparts, including good throughput due to parallel experiments, low infrastructural cost, fast reaction, reduced consumption of agent and reagent, and avoidance of contamination. This thesis is focused on the development of a microfluidic toolkit with several miniature devices to tackle important problems that the fields of plant phenotyping and bioenergy harvesting are facing. The ultimate goal of this research is to realize high-throughput screening methods for studying environment-genomics of plants through phenomics, and understanding microbial and plant metabolisms that contribute to harvesting bioenergy from microbes and living plants in different environments.

First, we develop vertical microfluidic plant chips and miniature greenhouses for high throughput phenotyping of *Arabidopsis* plants. The vertical design allows for gravitropic growth of multiple plants and continuous monitoring of seed germination and plant development at both the whole-plant and cellular levels. An automatic seed trapping method is developed to facilitate seed loading process. Also, electrospun nanofibrous membranes are incorporated with a seed germination chip to obtain a set of incubation temperatures on the device. Furthermore, miniature greenhouses are designed to house the plant and seed chips and to flexibly change temperature and light conditions for high-throughput plant phenotyping on a multi-scale level.

Second, to screen bacteria and mutants for elucidating mechanisms of electricity generation, we develop two types of miniature microbial fuel cells (μMFCs) using conductive poly(3,4-ethylenedioxythiophene) nanofibers and porous graphene foam (GF) as three-

dimensional (3D) anode materials. It is demonstrated that in the nanofiber-based μMFC, the nanofibers are suitable for rapid electron transfer and *Shewanella oneidensis* can fully colonize the interior region of the nanofibers. The GF-based μMFC is featured with a porous anolyte chamber formed by embedding a GF anode inside a microchannel. The interconnected pores of the GF provide 3D scaffolds favorable for cell attachment, inoculation and colonization, and more importantly, allow flowing nutritional and bacterial media throughout the anode with minimal waste. Therefore, the nutrients in bio-convertible substrates can be efficiently used by microbes for sustainable production of electrons.

Last, we develop a first miniature plant-MFC or μPMFC device as a technological interface to study bioenergy harvesting from microbes and living plants. A pilot research is conducted to create the μPMFC device by sandwiching a hydrophilic semi-permeable membrane between a μMFC and a plant growth chamber. Mass transport of carbon-containing organic exudates from the plant roots to the μMFC is quantified. This work represents an important step towards screening plants, microbes, and their mutants to maximize energy generation of PMFCs.

CHAPTER 1. INTRODUCTION

1.1 Introduction to plant phenotyping

Plant phenotyping as the set of methodologies and protocols is used to assess plant complex traits (shown in Figure 1.1), such as plant growth, development, tolerance, resistance, architecture, physiology, ecology, yield, and composition with a certain accuracy and precision at different scales of organization, from organs to canopies [1]. In particular, the measurement parameters include growth situations of seed (i.e., size and number), stem (i.e., diameter and height), and leaf (i.e., area, colour, angle, rolling, and elongation) in each growth stage and characteristic moments (i.e., flowering time, germination time). In addition, other phenotypic parameters include chlorophyll fluorescence, compactness, stress pigment concentration, etc. [1, 2]. Plant phenomics is regarded as a bridge linking genomics, plant function and agricultural traits. Accordingly, obtaining a phenotypic database is vital to link gene sequence to plant structure, development, composition, and performance [2].

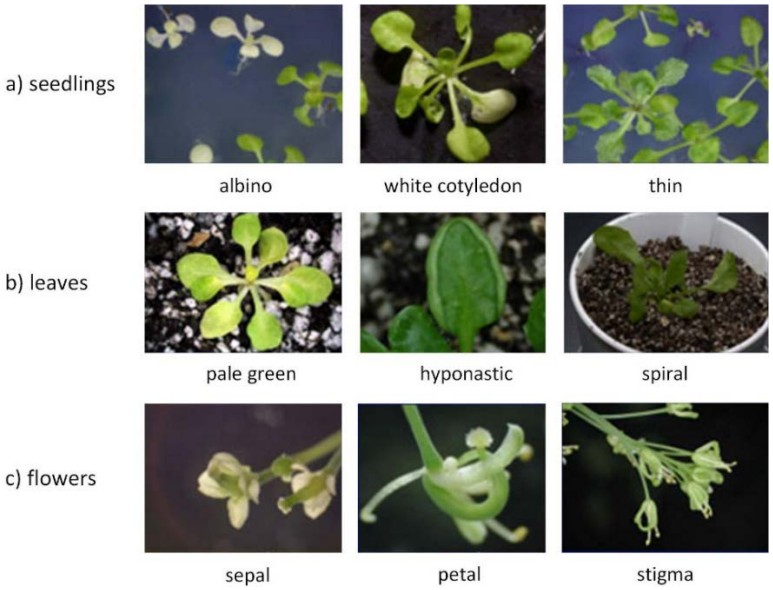

Figure 1.1 *Plant phenotyping of Arabidopsis thaliana [3].*

1.1.1 Importance of plant genotyping and phenotyping

Plant science is an area that has huge social and economic impact. Plant genotyping enables to discover the molecular markers in both model and crop plants by producing vast amounts of DNA sequence data [4]. Plant phenotyping allows presuming relevant gene function and illuminating the close relationship between the genotypes and the phenotype of a plant (shown in Figure 1.2 [5]).

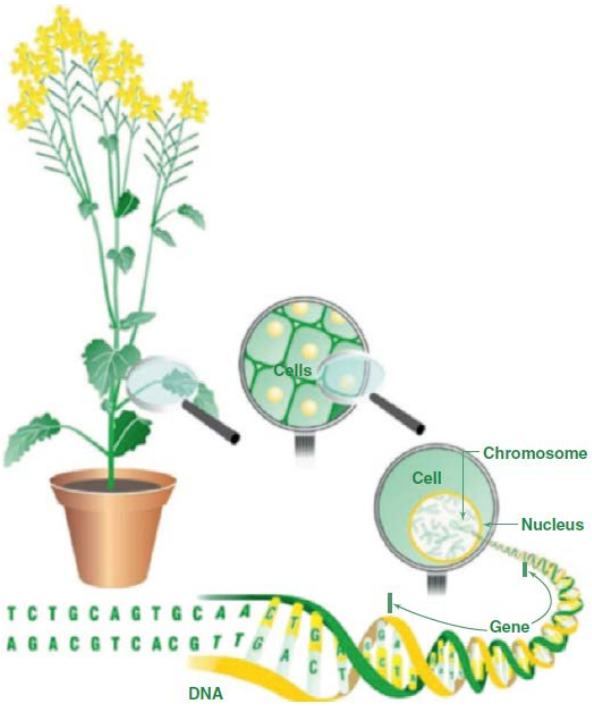

Figure 1.2 *Plant phenomics is the study of plant, growth, performance and composition [5].*

Advances in high-throughput biotechnologies have acquired much information about the genotype(s) [6, 7]. Post completion of genome sequencing projects has been directed to deciphering the function of individual genes, especially for model organisms such as the plant *Arabidopsis thaliana* [8-12]. Plentiful data from genomics studies using existing devices and instruments is available from several public databases [11, 13-18]. But, information about the complete phenome (e.g., the observable traits and characteristics of an organism) has a large challenge to study. The field of plant phenomics deals with large-scale quantitative studies of plant

phenotypes, and with linking these complex phenotypic traits to individual genes or a collection of genes. In particular, smaller genomes contain tens of thousands of gens, such as *Arabidopsis thaliana* [19-22].

In the past, plant phenotyping was mainly based on experience and intuition. In recent year, plant phenotyping has been improved by many non-invasive imaging and analysis technologies. These new techniques have enabled access to the level of analyzing dynamic and spatially distinct parameters [2, 5].

1.1.2 Inference of environment-genomics through phenomics

Environment-genomics is an interactional research for predicting how organisms will respond to changes in their external environment [23]. It is a synthetic subject that has the integrative ability of a team in all relative subjects (e.g., molecular biology, physiology, toxicology, ecology, systems biology, epidemiology, and population genetics). Environment-genomics can help researchers to assess the risk of developing disease, and identify and understand basic pathogenic mechanisms. Since the genomes are diverse in different environments, accurate classification and prognostication for disease process is critical. However, the application of genomics to resolve problems in specific environments still has numerous challenges [1, 23].

Phenotype represents a critical interface between the genotype and the environment. Therefore, genotypic variation plays a significant role in how to reveal the potential loci of phenotypic variation under selection by the environment. In reverse, how to infer the plant genotyping through phenotyping in appropriate environments? Figure 1.3 shows the interaction of the genotype, the phenotype, and the environment in a complex and dynamic manner. Therefore, high-throughput phenotyping is necessary for building a comprehensive tree of life [24].

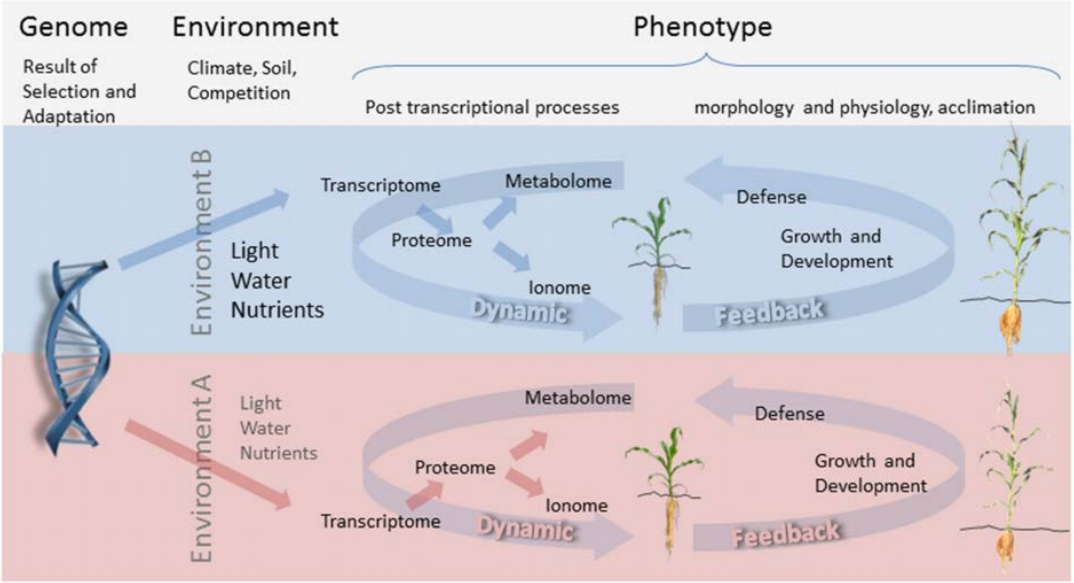

Figure 1.3 Relation between genotype and phenotype [25].

Plant phenotypic characteristics (i.e., shoot and root growth) are influenced by different environmental factors. Based on these phenotypic results, scientists are able to interpret some phenomena. For example, phenotypes respond to the environments but can, in turn, shape their living environments [26], which further infers the causation relationships through given gene(s) and its associated phenotype [27]. The most of existing instrumentation and software have been developed for identifying and analyzing genome sequencing, such as RNA's, proteins and metabolites [28-31]. Compared to the rapid advances in instrumentation for genomic studies, high-throughput plant phenotyping tools for systematic characterization of plant phenotypes is still at the earlier stage.

1.2 State-of-art plant phenotyping technologies

Traditional phenotypic analysis of plant relies on culturing seeds in pots and/or Petri dishes placed in tissue culture facility, subsequently mounting them for imaging [32-38]. Figure 1.4 and 1.5 show the phenotyping of the whole plant, such as cotyledon, hypocotyl, and rood. Scientists have made tremendous effort to build a standard and adequate database for the phenotypic

characters in model species, such as *Arabidopsis*. The well-established method basically relies on imaging plants over a long period of time, and then, extracting useful information, such as growth dynamics and morphological characters, through imaging analysis and mathematical treatment.

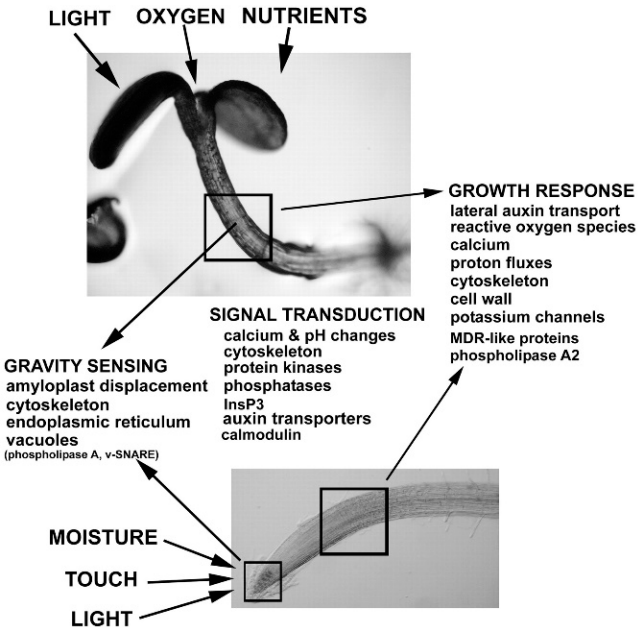

Figure 1.4 *Model of root and shoot gravitropism summarizing the identity of molecules, organelles, and processes functioning in all phases of the pathway and illustrating the environmental factors that influence the process [33].*

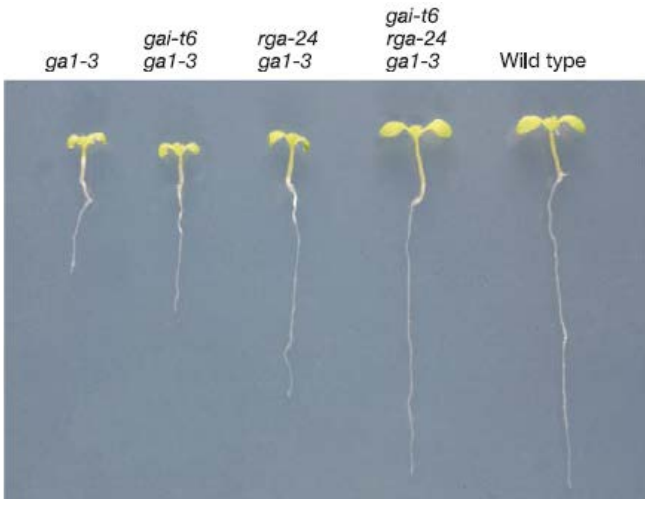

Figure 1.5 *Representative 5-day-old primary seedling roots of selected gentypes. Mean lengths were determined (±s.e., n = 30): ga1-3, 1.0 ± 0.1 cm; gai-t6 ga1-3, 1.3 ± 0.2 cm; rga-24 ga1-3, 2.0 ± 0.1 cm; gai-t6 rga-24 ga1-3, 3.6 ± 0.2 cm; wild type, 3.7 ± 0.2 cm [38].*

Recently, many applications using the growth-imaging technique have been implemented [5]. For example, researchers have used a high-throughput imaging method to screen drought tolerance [39], examined photosynthetic responses to drought stress [40], and identified plant development [41]. Also, they have used mathematical tools and analysis software to predit plant development with a series of generative rules for different plant organs [42]. This technique has provided insight into the model plant development. Building a database of phenomics information still needs a comprehensive metadata description and agreed ontologies.

1.2.1 In-field phenotyping methods

In-field phenotyping is increasingly recognized as a reliable method to deliver the requisite throughput in real-world cropping systems based on numbers of plants and description of relevant traits. Existing methods of phenotyping field crops depend on visual assessment and manual use of portable measurement devices [43, 44]. In order to acquire punctual sampling in large areas, it is necessary to develop a precise screening method to quantify in-field phenotyping, such as yield, plant development/physiology parameters, ecological biotic growth factors, and stress response under realistic conditions.

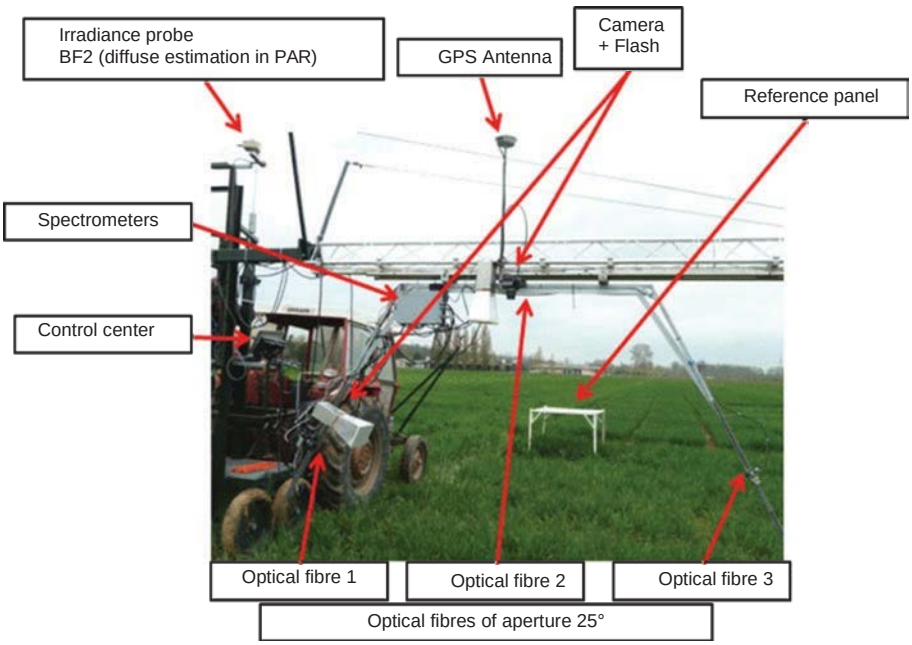

Figure 1.6 *The system used to sample the micro-plots [45].*

Figure 1.7 *The system of Scanalyzer^{Field} [46].*

Figure 1.6 shows a semi-automatic system developed to monitor small plots of wheat cultivars for in-field phenotyping. The system is based on a hyperspectral radiometer and 2 RGB cameras measuring 100 micro-plots per hour from multiple angles and direction, and then automatically collects and registers data. This system can well describe the dynamics of each micro-plot along the growth cycle [45]. LemnaTec (shown in Figure 1.7) built a rail-bound crane systems called Scanalyzer^{Field} to transport a measurement platform over field crops for in-field

phenotyping (i.e., growth, morphology and physiology). This platform is equipped with visible light, near infrared, infrared cameras and 3D scanners and moves precisely and reproducible to capture images information. Scanalyzer^{Field} can carry on a sequence of work from imaging collection to data analysis, and also compete high-throughput in-field plant phenotyping measurement from remote sensing to individual plant [46]. In addition, WPS provided another effective field phenotyping platform, which combines real time automated image analysis and associated environmental data [47]. In short, in-field phenotyping, using low cost and easy-to-use method, is an essential part of the breeding pipeline.

1.2.2 In-laboratory large scale phenotyping methods

In-field phenotyping is regarded as the most reliable approach to obtain important traits of crops. But, the study of the holistic characterization of plant phenotyping, such as the initial characterization of single plant traits in controlled environment, is necessary to be processed with in-laboratory facility. Thus, numerous greenhouses, growth chambers, automated tools and facilities have emerged for comparing hundreds plants in given condition [43].

The phenotyping facility (shown in Figure 1.8) contains a fully climate controlled growth house (or greenhouse) integrated with multiple imaging systems, allowing for repeated image capture and analysis at multiple time points and growth stages [48, 49]. Qubit Phenomics developed innovative plant phenotyping instruments (e.g., modular instruments, chlorophyll fluorescence imaging system, digital image acquisition and processing) for high-throughput plant phenotyping [50].

Figure 1.8 *The in-laboratory large scale facility [49].*

PlantScreen™ [51] (shown in Figure 1.9) is a high-throughput plant screening system that can monitor different species and many aspects of plant growth under controlled environmental conditions. The system design is flexible as new features based on customers' needs can be added, including RGB and morphometric analysis, chlorophyll fluorescence imaging, hyperspectral imaging, thermal imaging, etc. KeyGene [52] (shown in Figure 1.10) developed a digital phenotyping facility called PhenoFab, which can analyze, measure, and characterize plant growth and traits with high-throughput digital plant imaging technology. This facility offers the highest analysis rate of over 400 plants/hrs and the integration of phenotypic data with DNA profiles.

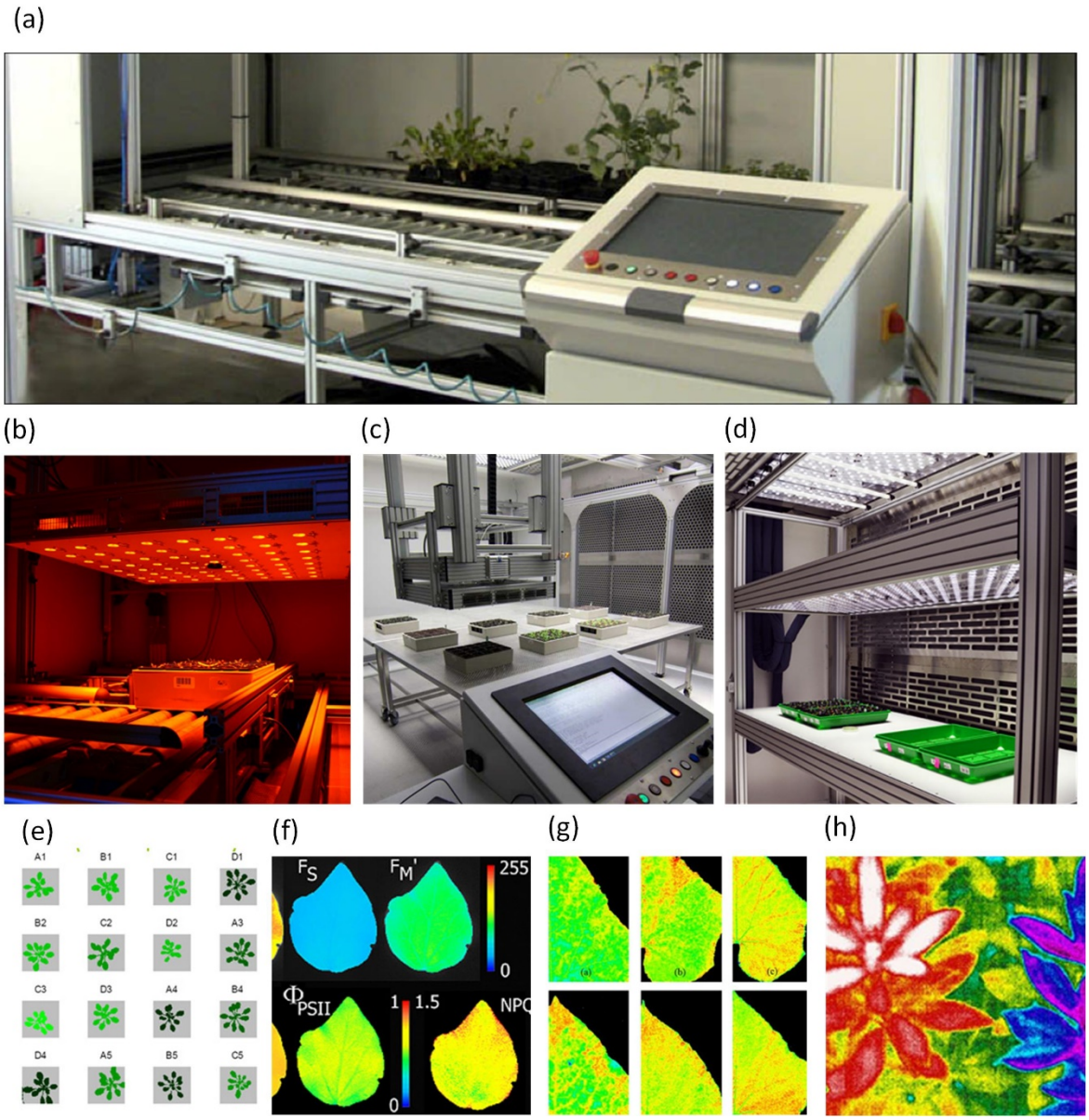

Figure 1.9 *(a) The panorama of PlantScreen™ System, (b) the Conveyor System, (c) Robotic XYZ System, (d) Controlled Environments, (e) RGB and Morphometric Imaging, (f) Chlorophyll Fluorescence Imaging, (g) Hyperspectral Imaging, and (f) Thermal Imaging [51].*

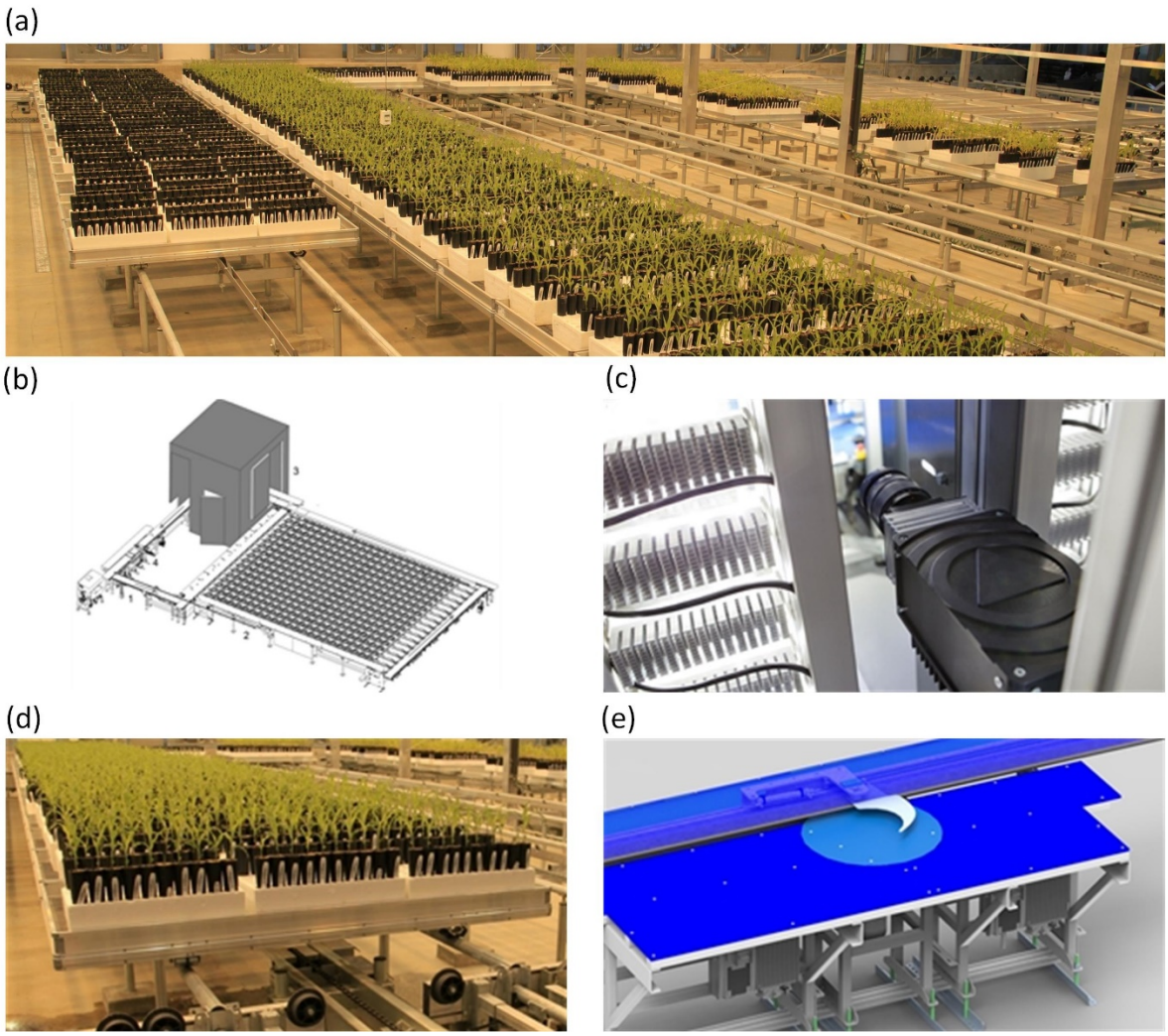

Figure 1.10 *(a) The panorama of PhenoFab System, (b) the Automated Phenotyping, (c) the RGB Imaging Sensor, (d) the Bench-based Phenotyping, (e) the Imaging Station Turntable [52].*

The in-laboratory large scale facilities, however, may suffer from high cost of instruments, chemical and biological agents and regents because of large amounts of experiments, and relatively low accuracy for imaging the plant roots in the soil and plant cells at the microscopic scale. And also, sometimes destructive dissection is needed to observe microscopic plant tissues and cells. Last but not the least, the traditional plant phenotyping approaches exist hidden troubles in low spatial morphological resolution at the millimeter scale and low throughput of obtaining phenotype information [53-55].

1.2.3 On-chip phenotyping technique

Recently, microfluidics, as an emerging technology, has been widely used for biological studies. Microfluidics-based bioassays have advantages over traditional methods in terms of throughput due to parallel experiments, morphological accuracy due to the use of transparent device materials, reduced cost due to batch fabrication, and shorter operating time due to the small length scale where molecular diffusion takes a shorter time. Therefore, it has a great potential to realize combinatorial screening of phenotypes and genotypes for different organisms. For example, microfluidics has provided powerful platforms to interrogate whole multicellular organisms such as *Drosophila melanogaster* and *Caenorhabditis elegans* [6, 7, 56, 57]. Many microfluidic devices have been developed for observation of behavioral and physiological phenotypes of various organisms in a real-time manner [8-13, 58]. These technologies have facilitated high-throughput studies at both the organismal and cellular levels with significantly reduced costs and experimental times, while concomitantly increasing the accuracy of experiments.

Recently, several applications of microfluidic devices for plant studies have been reported [59-65]. A root chip (shown in Figure 1.11) has been realized for characterizing phenotypic changes of multiple growing roots in different chemical environments [60]. *Arabidopsis thaliana* seeds first germinated and grew in conventional agar-filled pipettes in the first five days, and then planted into the root chip for further growth. When the root of the plant reached the bottom under gravity effect, it changed its growth direction to horizontal microfluidic channels. A RootArray shown in Figure 1.12 was developed to monitor real-time screening of gene expression, where 64 *Arabidopsis thaliana* seedlings grew in the chip and their roots automatically imaged by confocal laser scanning microscopy over several days [62]. This system reconstructed three-dimensional shape with high resolution and allowed multiple roots on different conditions to be tracked

simultaneously. To manipulate multiple growing plant cells under efficient and high-throughput control, a TipChip (shown in Figure 1.13) was developed using microfluidic technology [63]. The tip in a pollen tube germinated from a pollen grain, and then, grew along within a microchannel in horizontal direction to get exposed to a specified environment. This method allowed phenotyping serially arranged growing tip cells under repeatable and controllable conditions. A plant-in-chip platform (shown in Figure 1.14) was also fabricated for *Arabidopsis* plant, where the root development and root-pathogen interactions were imaged by a stereozoom microscope at a cellular resolution [65]. The roots were grown in parallel microchannels, immersed in different culture medium, and inoculated with plant pathogens for observing their phenotypic parameters.

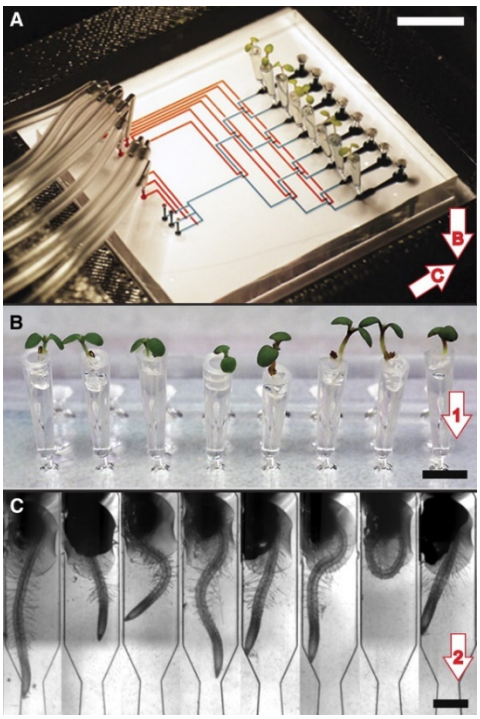

Figure 1.11 *The RootChip. (A) Image of a PDMS chip with eight mounted live plants. Control and flow channels of the chip are filled for illustration with red and blue food coloring, respectively. Bar = 1 cm. (B) Top view of the eight plants in conical cylinders filled with agar and mounted onto the chip. Arrow indicates the growth direction of the root. Bar = 0.5 cm (C) Bottom view of the microchannels containing roots of seedlings 7 d after germination (cf. Supplemental Movies online). Arrows indicate the perspective for (B) and (C). Bar = 0.5 mm [60].*

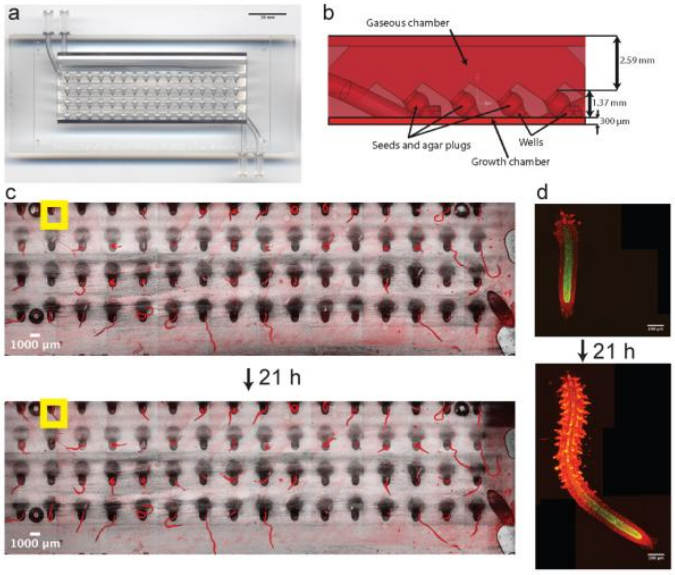

Figure 1.12 *The RootArray. (a) Image shows the RootArray with 64 wells (b) Cross-section with dimensions of the design features. The wells connect both chambers allowing the roots to grow into the liquid chamber and the shoots to emerge into the gaseous chamber. The upper and lower limits indicate the coverslips that are used to seal the array. The growing roots can be imaged over many hours (c,d). An example is given of an overview image at low resolution (c) and the stitched high-resolution images of individual roots (d)[62].*

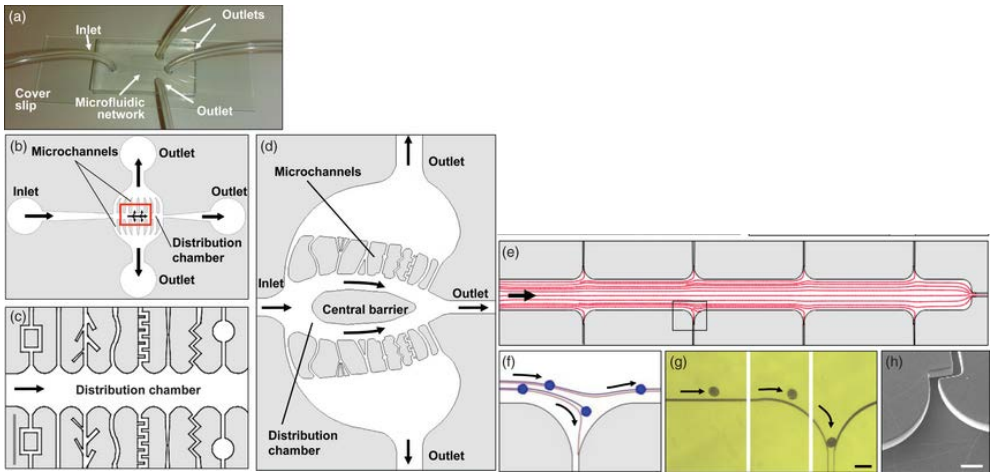

Figure 1.13 *Overall design of the TipChip. (a) Image of the TipChip showing the PDMS layer attached to a cover slip and the attached inlet and outlets. (b) General design principle of the microfluidic network in the TipChip. The pollen suspension is injected through the inlet, and the pollen grains move through the distribution chamber and either become trapped at the entrances of the microchannels or are evacuated through the distribution chamber outlet. (c) Modular portion of the TipChip with a rectangular distribution chamber as shown in (b), illustrating various types of microchannel geometries. Scale bar = 500 µm (dark gray in lower left corner). (d) Alternative design for the distribution chamber with a central barrier. (e) Fluid flow simulation showing the streamlines within the distribution chamber. (f) Detail of the simulated streamlines (red) and experimentally observed pollen grain movement (blue) through the distribution chamber. (g) Micrographs of a pollen grain driven by fluid flow and trapped at the entrance of a microchannel. The images show the same pollen grain at three different times. Scale bar = 100 µm. (h) Scanning electron micrograph of a trap entrance. Scale bar = 100 µm [63].*

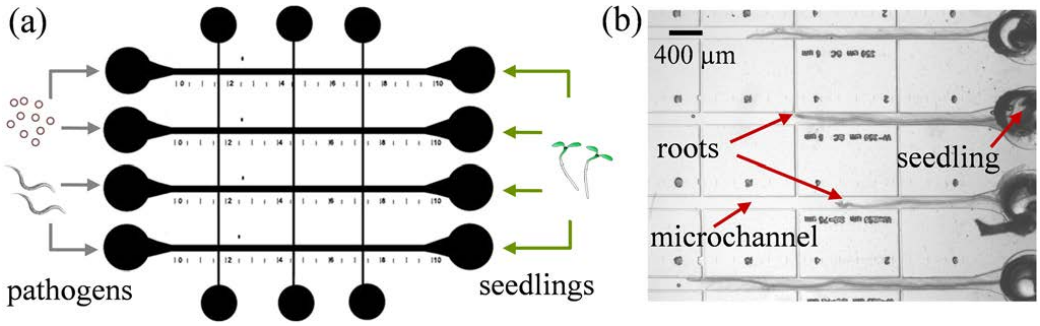

Figure 1.14 *(Color online) (a) Mask layout of the microfluidic device showing the parallel microchannels with ports for housing seedlings and inoculation of pathogens, (b) snapshot of multiple Arabidopsis roots growing in the microchannels filled with DI water. The image is taken after 60 h of planting the seedlings in the input ports [65].*

1.3 Introduction to microbial fuel cell

As one of the efforts to harvest electricity from renewable resources without carbon dioxide emission, microbial fuel cells (MFC) technology has been demonstrated as a promising method to convert bio-convertible substrates to electricity through the catalytic reactions by microorganisms [66]. This environment-friendly, inexpensive, and versatile technology allows for extended use of organic sources from industrial, agricultural, and residential wastes to generate electricity by using bacteria to biodegrade organic matters in the wastes [67-70]. While the electricity generation through microbial catabolism was first reported a century ago, extensive research and development in the area of MFCs have only been boosted in the past decade. The outcomes of the recent efforts have greatly impacted on multiple disciplines, such as microbial electrochemistry, materials science, and engineering.

1.3.1 Theory and basic structure

Figure 1.15 shows a schematic of a typical double-chamber MFC for electricity production. The anodic and cathodic chambers were separated by a proton exchange membrane (PEM) [70-72]. Microorganisms in the anodic chamber oxidize the substrates (organic matter) and generate electrons, protons, and carbon dioxide. Then, electrons flow from the anode to the cathode through an external electrical circuit which usually connects a resistive load. Protons pass through the PEM

and arrive at the cathode chamber to form water with oxygen. While the carbon dioxide is emitted from this process, it will be used in the photosynthesis process of plants. Take acetate as an example, the chemical reactions are listed below.

Anodic reaction: $CH_3COO^- + 2H_2O \xrightarrow{Microbes} 2CO_2 + 7H^+ + 8e^-$ (1)

Cathodic reaction: $O_2 + 4e^- + 4H^+ \rightarrow 2H_2O$ (2)

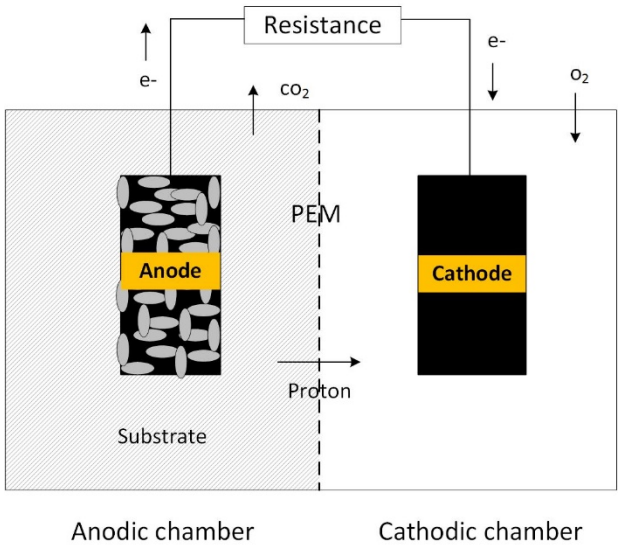

Figure 1.15 *Schematic of a typical duoble-chamber MFC [70].*

As shown in Figure 1.15, the components of typical double-chamber MFC contain an anodic chamber and a cathodic chamber separated by a PEM, as well as anode and cathode in corresponding chambers. Table 1.1 summarized the components of MFC and materials [70].

Table 1.1 *Basic components of microbial fuel cells [70].*

Items	Materials	Remarks
Anode	Graphite, graphite felt, carbon paper, carbon-cloth, Pt, Pt black, reticulated vitreous carbon (RVC)	Necessary
Cathode	Graphite, graphite felt, carbon paper, carbon-cloth, Pt, Pt black, RVC	Necessary
Anodic chamber	Glass, polycarbonate, Plexiglas	Necessary
Cathodic chamber	Glass, polycarbonate, Plexiglas	Optional
Proton exchange system	Proton exchange membrane: Nafion,Ultrex, polyethylene.poly (styrene-co-divinylbenzene); salt bridge, porcelain septum, or solely electrolyte	Necessary
Electrode catalyst	Pt, Pt black, MnO_2, $Fe^{3+,}$ polyaniline, electron mediator immobilized on anode	Optional

1.3.1.1 Microbes and substrates of MFCs

Microbes play a catalyst role on the surface or pores of the anode to accelerate the metabolism during the electrochemical reaction. Reversely, the oxidation of the substrate can gain the energy and carbon sources for self-growth of microbes [70, 73, 74]. Many microorganisms have been reported to generate electricity from complete oxidation of organic substrates, including *Geothrix fermentans*, *Rhodoferax ferrireducens*, *Shewanella species*, and *Geobacter species*, etc [75-79]. The details of microbes are listed in Table 1.2.

Bio-convertible substrates are another important factor for electricity production, ranging from pure compounds to mixtures of organic matter in wastewater. Acetate is a common substrate for generating electricity in MFCs [70, 80, 81]. Another commonly used substrate is glucose. But, glucose is a fermentable substrate, which means the consumption by diverse competing metabolisms (i.e., fermentation and methanogenesis) does not lead to sufficient electricity generation [82]. Synthetic or chemical wastewater can be easily controlled in terms of loading strength, pH, and conductivity. Besides, lignocellulosic biomass, brewery wastewater, starch

processing wastewater, and dye wastewater, etc. have been popular substrates for MFCs. Table 1.2 lists a partial substrates that have been used in MFC studies [80].

Table 1.2 *Microbes used in MFCs [70].*

Microbes	Substrate	Applications
Actinobacillus succinogenes	Glucose	Neutral red or thionin as electron mediator
Aeromonas hydrophila	Acetate	Mediator-less MFC
Alcaligenes faecalis, Enterococcus gallinarum, Pseudomonas aeruginosa G	Glucose	Self-mediate consortia isolated from MFC with a maximal level of 4.31 W m^{-2}
Clostridium beijerinckii	Starch, glucose, lactate, molasses	Fermentative bacterium
Clostridium butyricum	Starch, glucose, lactate, molasses	Fermentative bacterium
Desulfovibrio desulfuricans	Sucrose	Sulphate/sulphide as mediator
Erwinia dissolven	Glucose	Ferric chelate complex as mediators
Escherichia coli	Glucose sucrose	Mediators such as methylene blue needed
Geobacter metallireducens	Acetate	Mediator-less MFC
Geobacter sulfurreducens	Acetate	Mediator-less MFC
Gluconobacter oxydans	Glucose	Mediator (HNQ, resazurin or thionine) needed
Klebsiella pneumoniae	Glucose	HNQ as mediator biomineralized manganese as electron acceptor
Lactobacillus plantarum	Glucose	Ferric chelate complex as mediators
Proteus mirabilis	Glucose	Thionin as mediator
Pseudomonas aeruginosa	Glucose	Pyocyanin and phenazine-1-carboxamide as mediator
Rhodoferax ferrireducens	Glucose, xylose sucrose, maltose	Mediator-less MFC
Shewanella oneidensis	Lactate	Anthraquinone-2,6-disulfonate (AQDS) as mediator
Shewanella putrefaciens	Lactate, pyruvate, acetate, glucose	Mediator-less MFC, but incorporating an electron mediator like Mn (IV) or NR into the anode enhanced the electricity production
Streptococcus lactis	Glucose	Ferric chelate complex as mediators

1.3.1.2 Anode of MFCs

Many efforts have been made to improve each component of MFCs over the past decade years. Anodic materials must be conductive, biocompatible, and chemically stable in the anolyte. Metals [83], graphite (e.g., plates, rods, or granules), carbon materials (e.g., carbon cloth, paper, and fiber veil) [84-86], and modified carbon materials (e.g., polymer-coated carbon and ammonia-treated carbon cloth) [87, 88] are widely used as anode materials of MFCs (shown in Table 1.1). It is required that anode materials should be inexpensive and have a high surface-area-to-volume (SAV) ratio [89-91]. Substantially, many porous micro/nanomaterials, such as polyaniline-platinium composites, meet the SAV ratio requirement [92, 93] to improve the current generation of MFCs through assisting the direct oxidation of microorganisms [94-96]. In addition, 3D conductive nanomaterials and structures, such as carbon-nanotubes, graphite fiber brush, and graphene foam, have been reported to provide a large surface area for bacterial attachment and rapid electron transfer.

1.3.1.3 Structure of MFCs

MFCs are generally divided into two variants, i.e., double-chamber MFCs and single-chamber MFCs (SCMFCs). The double-chamber MFC uses two bottles connected by a glass tube imbedding a cation/proton exchange membrane (CEM/PEM) or a salt bridge [70, 89]. The schematic and phototype of double-chamber MFCs are shown in Figure 1.16 [70, 97-99]. But, SCMFC do not use a cathodic chamber because air can indirectly contact with the cathode. No any liquid catholyte is thus needed. The schematic and phototype of a typical SCMFCs are shown in Figure 1.17 [100, 101].

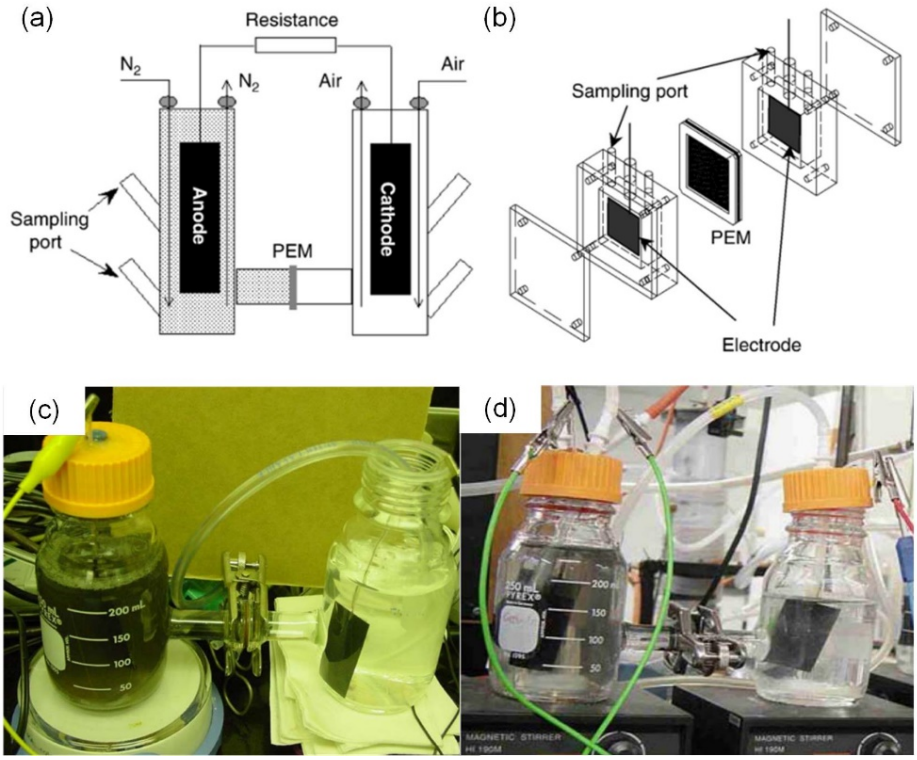

Figure 1.16 *Schematics of a double-chamber MFCs in (a) cylindrical shape [79] (drawn to illustrate a photo [106]), (b) rectangular shape [107]. The phototype of double-chamber MFCs (c) (d) [97, 99].*

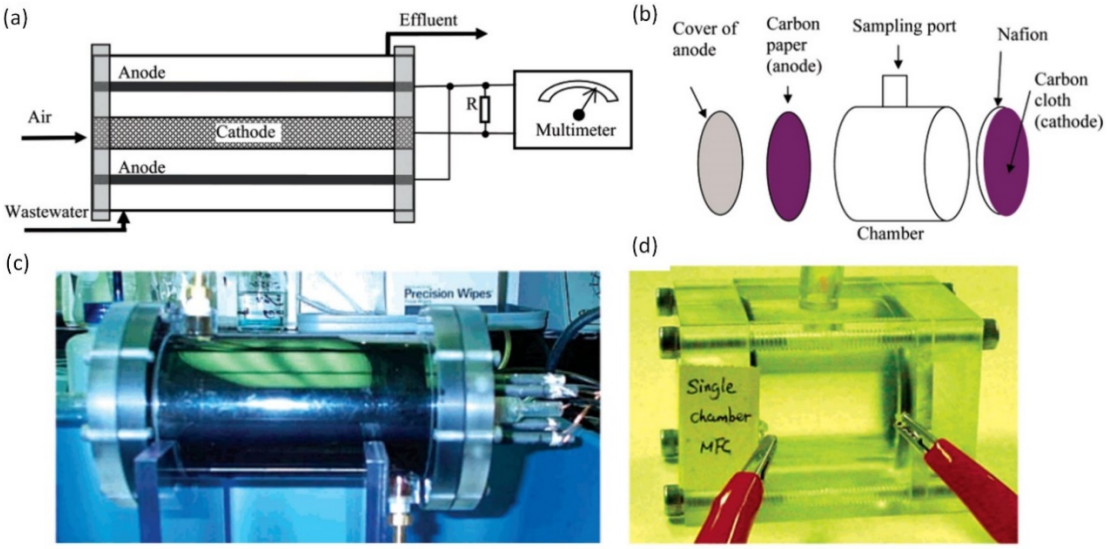

Figure 1.17 *Schematics and phototype of single-chamber MFCs [100, 101].*

1.3.2 MFC applications

Many applications of MFCs have been exploited in the area of industrial analysis and control, such as monitoring and controlling biological oxygen demand (BOD) of wastewater for pollutant analysis. Also, the detection of toxic compounds in water can be accomplished by using MFCs. The MFC systems shown in Figure 1.18 were used as BOD sensors for real-time wastewater monitoring. Figure 1.18a, b show a mediator-less double-chamber MFC [102] where graphite felt was used as an electrode in each chamber. A steady-state current was reached within 60 min and the measured BOD value was up to 100 mg/l after the MFC was fed with sample solution. Figure 1.18c, d show a SCMFC for treating organic matter present in wastewater [103], where polyacrylonitrile (PAN)-carbon/graphite felt and carbon cloth were used as the anode and cathode materials, respectively. Because of using the porous material, the cathode of SCMFCs was exposed directly to the air and there is no need of aeration in a cathode chamber.

Electricity generation was regarded as one of the most important applications for MFCs, during which the devices convert energy stored in chemicals to electricity with the help of microorganisms as mentioned earlier [79, 104]. To enhance voltage or current output, MFCs have been connected in parallel or linked together in series to enhance voltage or current output (the structure shown in Figure 1.18e)[105].

In addition, the recent studies in MFCs have been focused on large scale degradating environmental pollutants. To some extent, this application may be more valuable than electricity generation [73]. *Geobacter* species provide an ability to anaerobically degrade petroleum components and landfill leachate contaminants in ground water [106-109]. Pure cultures of *Geobacter metallireducens* are able to oxidize benzoate [75], and toluene [110].

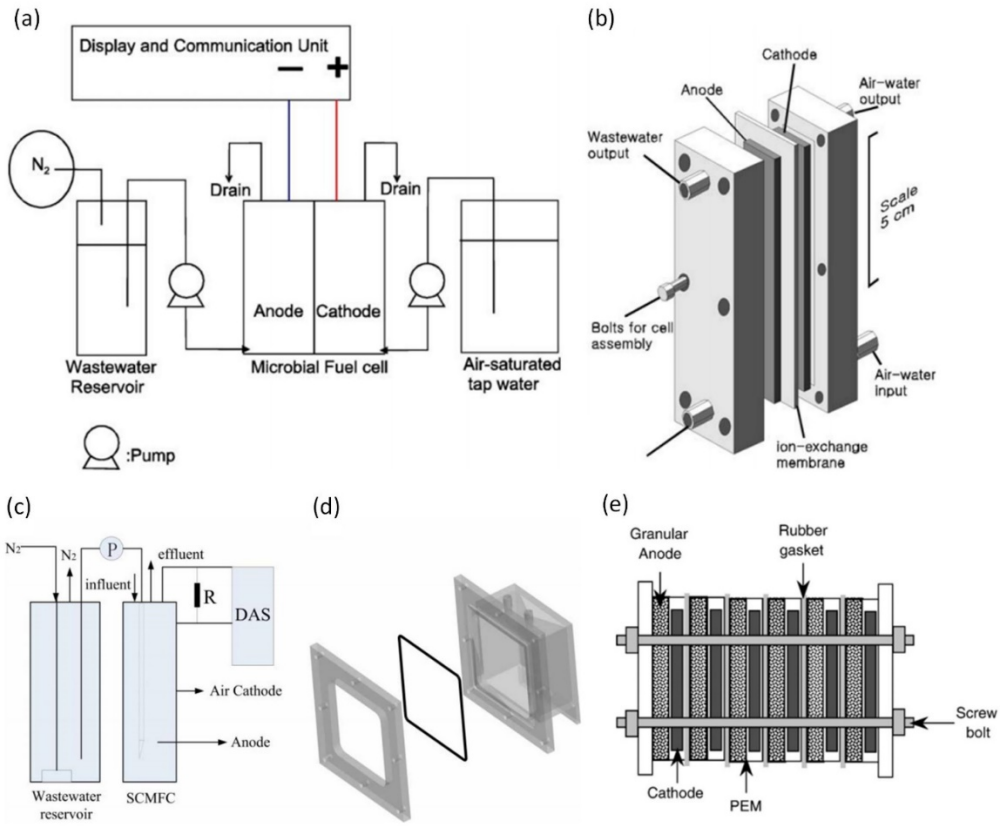

Figure 1.18 *Schematic diagram of (a) double-chamber biosensor system and (b) microbial fuel cell [102], Schematic diagram of (c) SCMFC biosensor and (d) SCMFC [103], and (e) Stacked MFCs consisting of six individual units with granular graphite anode. (Figure drawn to illustrate a photo in [105]).*

1.3.3 Introduction to miniature MFC devices

Recently, miniaturized MFCs have attracted considerable interest for portable green power sources and high throughput microbial assays. The microbes propagate in small chambers with proper supplements of their culture medium to enable long-term and self-sustained power output. Compared to conventional assay methods based on using a large double-chamber MFCs, the miniature MFCs features large SAV ratios, short electrode distance and startup time, small material consumption, and high throughput. Many miniature MFCs have been developed for on-chip powering and rapid screening of optimal operation conditions [111, 112].

As a potential micro-power source, the miniature MFCs consume a relatively small amount of materials, but produce a large power density. Choi et al. reported a MFC featured with a 4.5 µL

anode/cathode chamber that produces a power density of 2300 mW/cm^3 (4.7 mW/cm^2) using a *Geobacter*-enriched mixed bacterial culture (Figure 1.19a) [113]. Qian et al. developed a 1.5 µL MFC using *Shewanella oneidensis* strain MR-1 in a chip [114]. A maximum power density of 15 W/m^3 was achieved and a biofilm was observed to grow on the gold anode (Figure 1.19d). Siu et al. developed a polydimethylsiloxane (PDMS) MFC with embedded micropillar electrodes to increase anode surface area [115] (Figure 1.20a). Mink et al. reported a SCMFC using CMOS-compatible processes and employed multiwalled carbon nanotubes (MWCNTs) as anode. The device showed a promise to produce stable power for ultra-low-power electronics (Figure 1.20b) [116]. Fraiwan et al. compared six micro/nanostructured anodes in MFCs with volume of 47 µL, including carbon nanotubes, carbon nanofibers, gold/poly (ε-caprolactone) microfiber, gold/poly(ε-caprolactone) nanofibers, planar gold, and conventional carbon paper [117]. The performance of MFCs using 3D anodes excelled those using 2D anodes (Figure 1.20c).

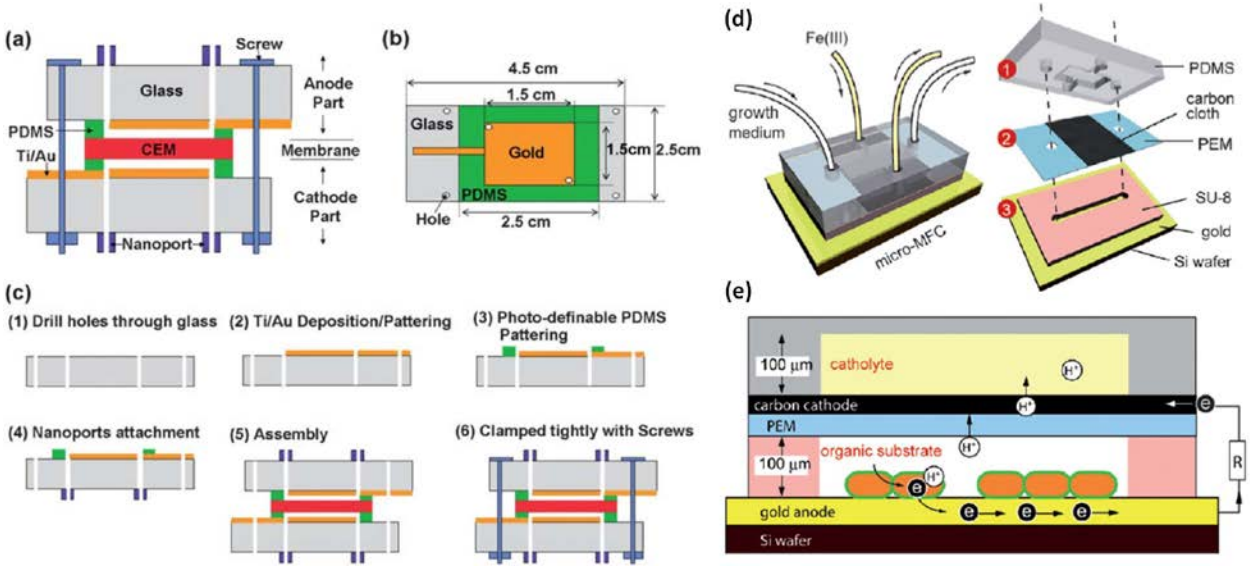

Figure 1.19 *Left: schematic of MEMS MFCs; (a) across section, (b) top view, and (c) fabrication process of the MEME MFCs [113]. Right: Micro-MFCs design and assembly. (d) Schematic representation of the MFCs components. (e) Operating principles of a MFC [114].*

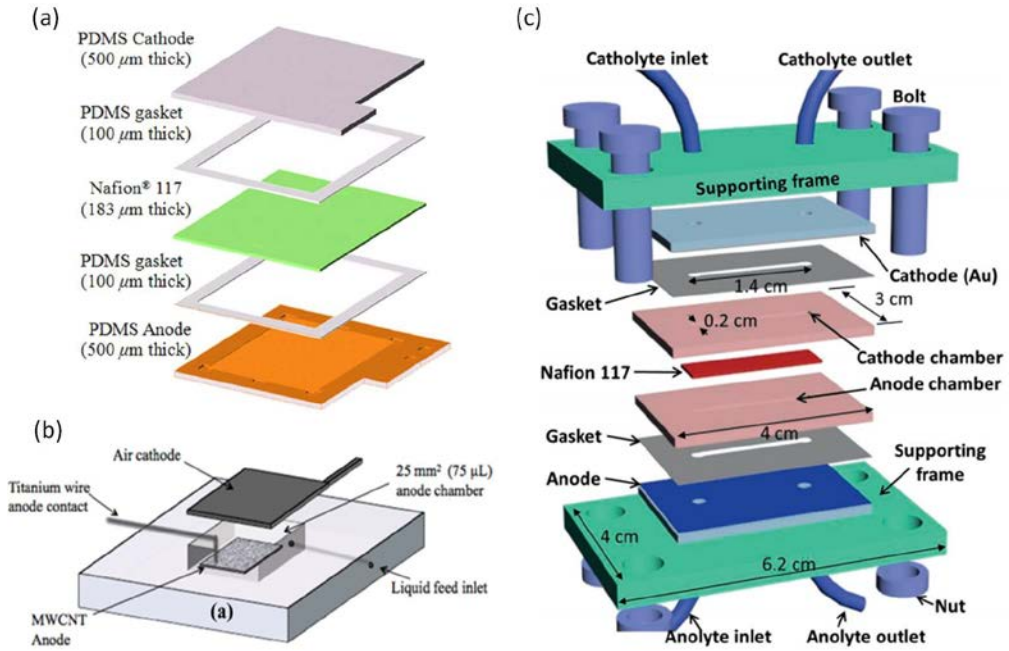

Figure 1.20 *Exploded view of the micro-size microbial fuel cell structure (a) PDMS MFCs [115], (b) single-chambered [116], and (c) dual-chambered [117].*

To increase power density, new design strategies for miniature MFCs have been reported. The parallel MFC array has been developed that connected multiple units together [111]. Hou et al. developed a MFC array that consists of 24 independent testing units capable of achieving fast and high-throughput screening for electrochemically active microbes (Figure 1.21a) [118]. Chen et al. fabricated a 25 µL single-chamber miniature MFC array with eight units [119]. This air-cathode MFC array has better performance in terms of current and power density (2148 mA/m^2, 29 mW/m^2, respectively) (Figure 1.21b). Mukherjee et al. presented a six-well MFC array with anodic/cathodic volume of 15 µL, resulting in smaller deviation (1.4%) than that of mL-scale MFCs (>25%) and other MFC arrays (>8%) (Figure 1.21c) [120]. Fraiwan et al. designed a paper-based bacteria-powered battery array, which showed a short startup time of 50 min, compared to conventional MFCs and other miniature MFCs [121] (Figure 1.21d).

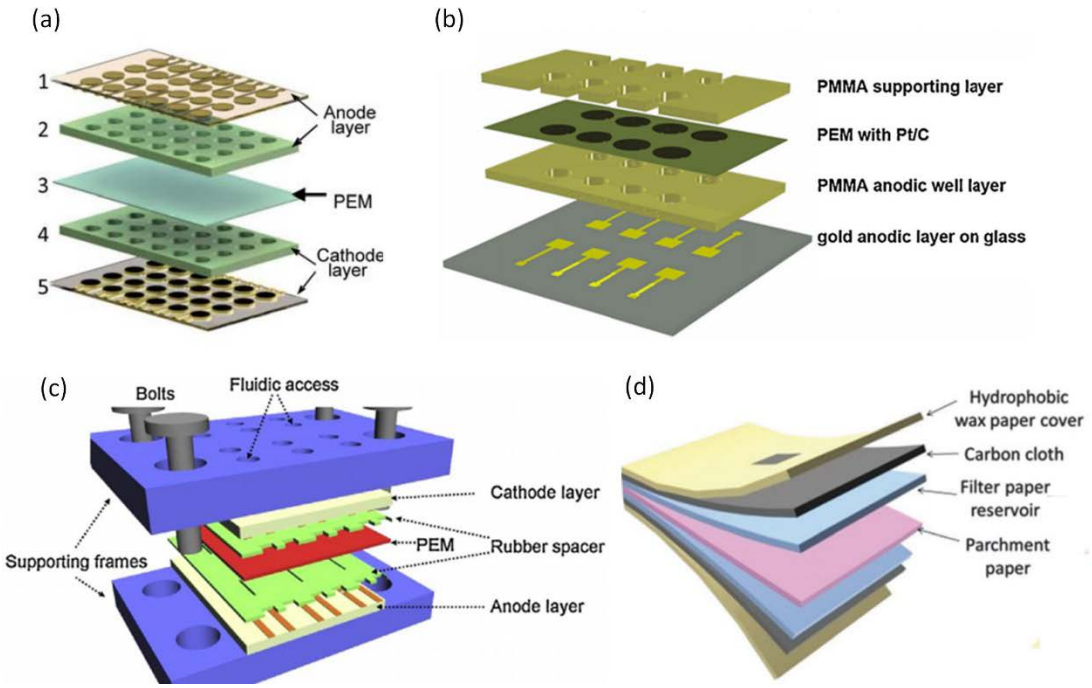

Figure 1.21 *Exploded view of the micro-scale MFC arrays, (a) 24-well [118], (b) air-cathode 8-well [119], (c) 6-well [120], and (d) paper-based 6-well MFC arrays [121].*

In addition, photosynthetic miniature MFCs have been reported [122-125], which could produce bioelectric power by using biocatalytic reaction of photosynthetic microorganisms (e.g., cyanobacteria or algae) to convert light energy into electrical power. As shown in Figure 1.22 [122], two processes are involved in photosynthetic MFCs. First, the microorganisms capture light energy to convert carbon dioxide and water into oxygen and carbohydrates during photosynthesis [122]. Second, the converted oxygen and carbohydrates are used to regenerate carbon dioxide and water during respiratory reaction. Thus, photosynthetic MFCs can continuously produce electricity from solar energy without requiring additional organic matter at both day and night [122]. Overall, the photosynthetic MFCs mimic the natural ecosystem, in which living organisms and nonliving components of their environment depend correlatively on each other in order to achieve a self-sustainable and self-maintainable system [122].

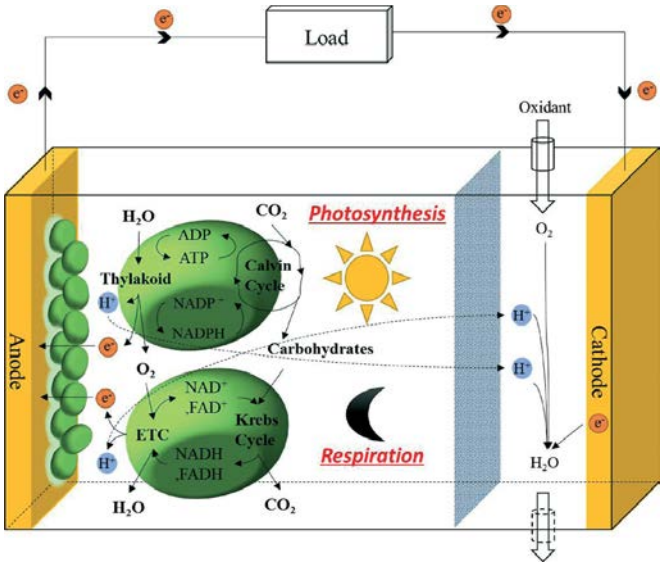

Figure 1.22 *Principle of operation in a bio-solar cell. Schematic representation of the photosynthetic and respiratory electron transport pathways in cyanobacteria [122].*

1.4 Plant microbial fuel cells

The current climate and living environment are under the threatening of greenhouse gas emissions from the combustion of fossil fuels. In the past two decades, plant materials have been used as an energy source through biomass fermentation. In 2008 researchers at Wageningen University in the Netherlands proposed to use the organic matter exudated from the roots of living plants as carbon source to sustain microbes used in MFCs [126]. Plant MFCs or PMFCs are thus considered as a clean and renewable energy technology. Unlike other biomass-to-energy conversion techniques (e.g., torrefaction and gasification) that are produced by the anaerobic digestion of biomass, there is no emission from the PMFCs [127].

1.4.1 Theory and basic structure

The PMFCs involves in transforming solar energy into electricity in a clean and efficient manner by integrating the plant roots in the anodic chamber of a MFC. Specifically, the living plants capture carbon dioxide through photosynthesis and store carbon in their leaves. In spite of plants varied with species, age and environmental conditions, only part of the organic matter

(exudates including sugars, glucose, acetate, butyrate, and propionate; and secretions including polymeric carbohydrates and enzymes [128]) exuded via photosynthesis is used for plant growth, while a large portion of them (up to 70%) are excreted into the soil through the roots. And then microorganisms around the roots break down the organic compounds to generate electricity from the living plants [129,130]. More specifically, the PMFC operation relies on rhizodeposition of organic compounds by plant roots and electricity produced by organic matter (shown in Figure 1.23). The plant roots as a "carbon donor" that are often integrated in the anode section of a MFC. The electrochemically active bacteria with substrate through rhizodeposition are present in the anode of the MFCs, and then convert the substrate into carbon dioxide, protons and cast-off electrons that can be harvested by electricity through MFCs. This technology is based on natural ecological process as plants continue to grow while electricity is generated [129-131].

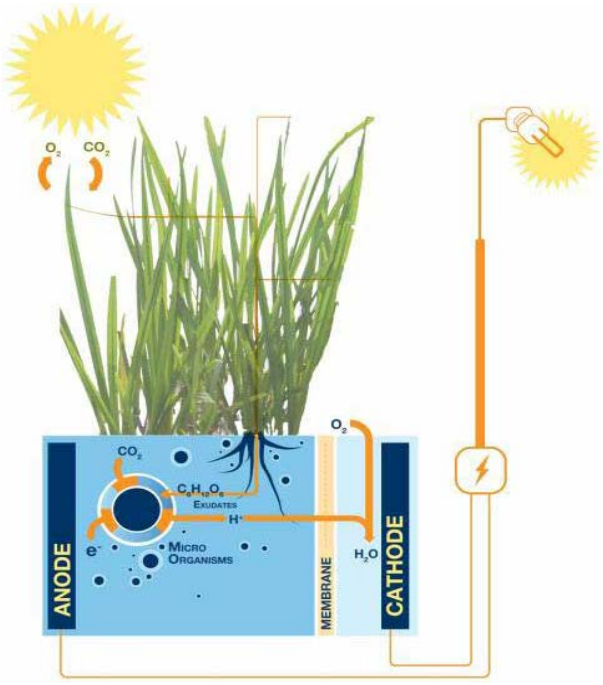

Figure 1.23 *A model of a plant microbial fuel cell [128].*

Since a suitable plant species contributes to electricity generation, aquatic plants are constantly being chosen in PMFCs due to sensitivity for solution conductivity. Up to now, common aquatic plants include reed manna grass (*Glyceria maxima*), rice plant, *S. anglica*, *Anisogramma anomala*, and *Arundo donax* [128, 132-134]. Meanwhile, the usage of aquatic plants in PMFCs will can lower the installation costs and elongate electricity generation [135].

1.4.2 State-of-art in PMFC research

Many experiments have been developed to prove that plants can serve as a source of green and renewable energy [124, 135-137, 139-141]. Researchers at Wageningen University developed PMFCs that produce electrons remained in the soil around living plants' roots [136]. Plant-e, a technology company spun off from Wageningen University, is planning to scale up the PMFCs for a wide variety of potential application. They believe that their technology could be used to supply electricity to flat roofs, even households within a few years. Right now, it only can produce 0.4 w/m^2, which is the same order of magnitude to that of old-fashioned wood-burning (about 0.7 w/m^2). But their system should be able to generate as much as 3.2 w/m^2 in further. The team hoped to approach a maximum power density by altering the size and shape of the PMFCs for the purpose of decreasing their internal resistance [130].

Researchers in Belgium studied the power output generated from rhizodeposition of living rice plants [137]. This process exploited the potential of plant-driven power generation, which is up to 330 W/ha (0.33 W/m^2). In order to increase current and power density, Helder et al. designed a flat-plate PMFC by means of minimizing internal resistances as opposed to previously tubular design [138]. Bombeli et al. compared two different species (i.e., *O. sativa* and *E. glabrescens*) of vascular plant grown in PMFCs with same soil and glasshouse condition, as well as avoiding

additional energy input [139]. The result shows the average power output generated by *O. sativa* was obviously up to 10 times higher than that by *E. glabrescens* (shown in Figure 1.24).

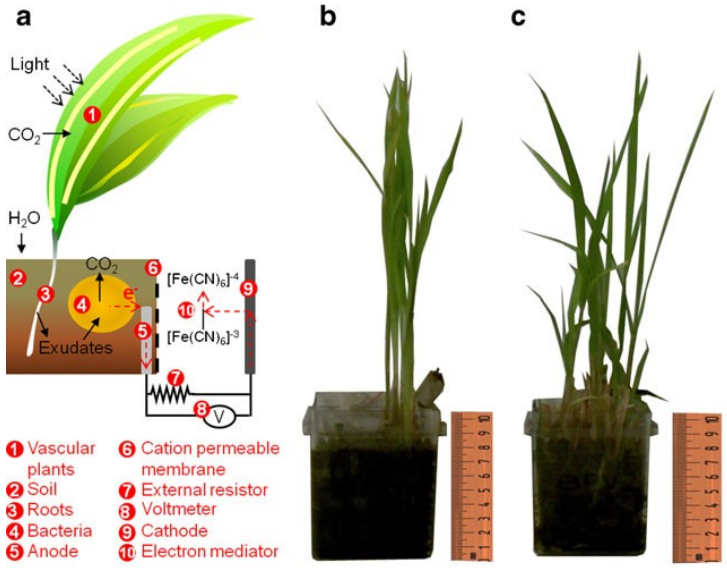

Figure 1.24 *(a) Schematic illustration showing positions of the anode and cathode relative to established plants of O. sativa and E. glabrescens; (b) image of O. sativa Vascular plant bio-photovoltaics (VP-BPV) system; (c) image of E. glabrescens VP-BPV system. The scale of the rulers is in centimetres [139].*

To maximize power output, Wetser et al. [140] tried to substitute a biological oxygen reducing cathode with a chemical ferricyanide cathode, because oxygen has minimal resistance and high redox potential. After operating for 151 days, the maximum and average power density are 679 mW/m^2 and 240 mW/m^2 (shown in Figure 1.25). Goto et al. [141] investigated the power generation of soil MFCs and PMFCs through the addition of graphene oxide (GO). The optimal concentration of GO (1.0 g/kg) that was tested by generating the highest power in soil MFCs, was then applied to PMFCs. The result shows that greater power generation (49 mW/m^2) was obtained compared to PMFCs with no added GO (shown in Figure 1.26).

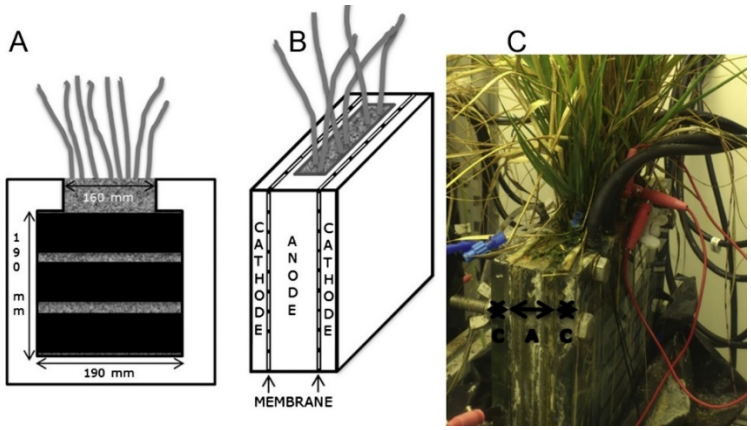

Figure 1.25 *Schematic overview of a cross section of the anode (A), the position of the electrodes in the PMFC (B) and a picture of PMFC (C)[140].*

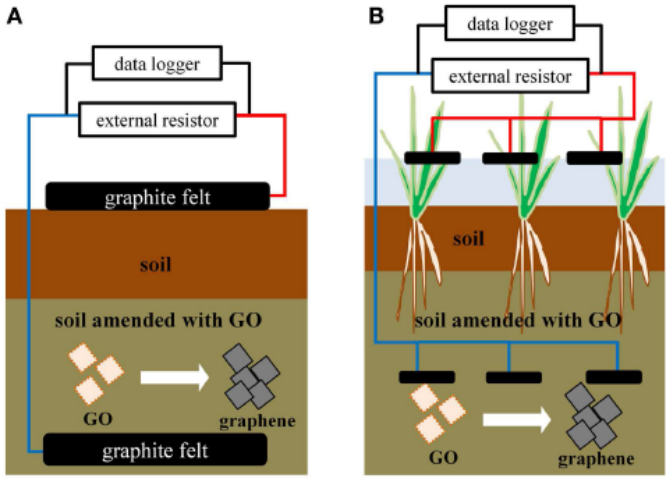

Figure 1.26 *Structures of SMFC (A), and PMFC (B), with the addition of GO [141].*

1.5 Problems, Objective, Goal and Approach

1.5.1 Problems to be solved

While in-field plant phenotyping approaches have generated important phenotypic database able to partially link gene sequence to plant structure, development, and growth, there are many challenges related to large-scale phenotypic analyses, such as high cost for infrastructure facility, intensive labor and time spent, and large material and energy consumption. Existing in-laboratory phenotyping methods grow plants in pots with non-transparent soil or in plates with agar which is not fully clear. The spatial resolution of the obtained phenotypes is low. Real-time

phenotyping plant roots is challenging, due to the use of opaque soil and semi-transparent agar in laboratory. Studying plant phenotypes at the tissue and cellular levels use the destructive process. Existing microfluidic plant phenotyping devices mainly focus on plant root, but no such practical experience in studying the complete plant phenome (e.g., seed germination, hypocotyl, cotyledon, leaf growth). Furthermore, seed germination and plant development and growth are sensitive to environmental conditions (e.g., temperature, light intensity, moisture, and drought) that result in inferring the plant genotyping through the displayed phenotyping in controlled environments. Current practice to change environments relies on using large greenhouses and expensive growth chambers. It's inconvenient to flexibly change a large number of environmental conditions to study the inference of environment-genomics through phenomics. Also, the general development of instrumentation for large and multi-scale phenotypic profiling lags behind the rapid advances in instrumentation for genomic studies. Therefore, there is an urgent need for developing innovative and transformative high-throughput plant phenotyping instrumentation.

Compared to conventional large size MFCs, miniature MFCs are featured with short startup time and small material consumption. The miniature MFC technology has a great potential to not only provide a micro-power source, but also screen bacteria and mutant strains to elucidate mechanisms of electricity generation with high throughput. However, the small device size becomes a major barrier to obtain high electric current, due to insufficient formation of bacterial biofilms on the surface of anode materials. Therefore, to obtain high-performance miniature MFCs, it is imperative to seek for a suitable anode that is capable of high conductivity, large surface area, preferable bacterial attachment, and biofilm formation. Also, with continuing efforts in miniaturizing MFCs, the volume of bio-convertible substrate solutions present in the device dramatically decreases. It is desirable to build an increased ability to efficiently use the nutrients

in the substrates for sustainable production of energy from the substrates in a space-limited MFC device. There is an urgent need to develop a strategy to improve electrochemical reactions between the bio-convertible substrates and bacteria in the small device.

As a natural technological interface between living plants and microbial fuel cells, PMFCs are regarded as a clean and renewable energy harvester. Initial research efforts have recently demonstrated a possibility of generating electricity from living plants on large scale. But, the power and current densities obtained by this truly infancy stage approach are too low to support adequate levels of practical electricity needs. To move this technology forward, we believed that there would be a great need to develop a high-sensitivity, high-throughput tool for screening suitable microbes and plant species for use in PMFCs. Unfortunately, no efforts have been initiated in this regard. We also realized that there would be some major issues associated with building a device for the purpose of screening both plants and microbes and their mutants. First, the microbes used in the MFC should not enter the plant growth chamber as they may contaminate the roots and other parts of the plant. In the current large scale PMFC research efforts, from the device structure perspective, no any mechanisms have been reported to prevent this occurrence of this vital issue. Second, the exudates and secretions from the plant roots need to rapidly transport to the MFC chamber to sustain the life of the colonized microbes on the surface of anode. Third, the nutrients in the growth medium for the microbes may also diffuse to the plant growth chamber, which may further complex the design. Overall, it is important to find approach for regulating both microbes and plant to achieve the state of the coexistence for each other, with an aim at generating high power density from PMFCs.

1.5.2 Objectives and basic approaches of this thesis

The first objective of the thesis is to develop high-throughput plant phenotyping device and miniature greenhouses. The target goals for this objective are listed below:

- To design a microfluidic vertical plant device for high-throughput phenotyping of *Arabidopsis* plants. This device not only allows for gravitropic growth of multiple plants, but also conveniently and continuously monitor plant phenotyping at both the whole organismal level and cellular level. Meanwhile, seeds are loaded into seed holding sites by automatically hydrodynamic trapping method.
- To develop a microfluidic seed growth chips (SGCs) by incorporating electrospun nanofiber membrane (ENMs) to create desired temperature conditions for seed growth. By adjusting spinning time of electrospinning deposition to control pore size distributions of ENMs and then changing amount of thermal energy to achieve the effect of controlling temperature in SGCs.
- To create high-throughput miniature greenhouses for the vertical microfluidic plant chips and other possible plants. The miniature greenhouses provides environmental controls for studying plant phenotyping on a multi-scale level via adjusting a set of environmental parameters, such as temperature and light intensity.

The second objective is to develop high performance miniature MFCs with 3D porous biofilms and flow-through graphene foam (GF). The specific goals for this objective are listed below:

- To study the performance of miniature MFCs with 3D nanofibers-based porous anode. The PEDOT nanofibers are fabricated by electrospinning poly(vinyl-pyrrolidone) oxidant nanofibers and subsequent vapor-phase polymerization of 3,4-ethylenedioxythiophene

(EDOT) monomer with high conductivity, allowing for electron transfer and bacterial attachment on a large interfacial contact area.

- To develop miniature MFC using a microfluidic flow-through mechanism to improve electrochemical reactions between the bio-convertible substrates and bacteria in the device. A porous anolyte chamber is formed by embedding 3D porous GF anode in a microfluidic channel. The interconnected pore network of the GF not only provides 3D scaffolds for cell attachment, inoculation and colonization, but more importantly, allows flowing nutritional and bacterial media throughout the anode with minimal waste substrates.

The third objective is to conduct a pilot research on the development of miniature PMFC devices by integrating MFCs and plant growth chambers. This serves an initial and exploratory step towards screening plants, microbes, and their mutants in the future to maximize energy generation of large scale PMFCs. The goals for this objective are listed below:

- To design and build a miniature PMFC where rice plants are placed in the top chamber and a miniature MFC locate at the bottom. A semi-permeable membrane is used between the two units to block bacteria in the MFC from entering the plant growth chamber.
- To quantify mass transport of the exudates from the plant roots to the MFC device, and mass transport of important nutrients from the MFC to the plant.

References

1. http://www.lemnatec.com/applications/high-throughput-screening/

2. F. Fiorani and U. Schurr, *Annu. Rev. Plant Biol.*, 2013, **64**, 267-291.

3. http://www.rikenresearch.riken.jp/eng/research/4582/

4. http://plato.stanford.edu/entries/genotype-phenotype/

5. R. T. Furbank and M. Tester, *Trends Plant Sci.*, 2011, **16**, 635-644.

6. P. B. Allen, A. E. Sgro, D. L. Chao, B. E. Doepker, J. S. Edgar, K. Shen and D. T. Chiu, *J. Neurosci. Methods*, 2008, **173**, 20-26.

7. S. Preibisch, S. Saalfeld and P. Tomancak, *Bioinformatics*, 2009, **25**, 1463-1465.

8. S. E. Hulme, S. S. Shevkoplyas, A. P. McGuigan, J. Apfeld, W. Fontana and G. M. Whitesides, *Lab Chip*, 2010, **10**, 589-597.

9. M. A. Unger, H. P. Chou, T. Thorsen, A. Scherer and S. R. Quake, *Science*, 2000, **288**, 113-116.

10. G. M. Whitesides, *Nature*, 2006, **442**, 368-373.

11. M. Meier, E. M. Lucchetta and R. F. Ismagilov, *Lab Chip*, 2010, **10**, 2147-2153.

12. H. M. Zhang and B. G. Forde, *Science*, 1998, **279**, 407-409.

13. S. Svistoonoff, A. Creff, M. Reymond, C. Sigoillot-Claude, L. Ricaud, A. Blanchet, L. Nussaume and T. Desnos, *Nat. Genet.*, 2007, **39**, 792-796.

14. I. Casimiro, T. Beeckman, N. Graham, R. Bhalerao, H. M. Zhang, P. Casero, G. Sandberg and M. J. Bennett, *Trends Plant Sci.*, 2003, **8**, 165-171.

15. C. Bermejo, J. C. Ewald, V. Lanquar, A. M. Jones and W. B. Frommer, *Biochem. J.*, 2011, **438**, 1-10.

16. J. E. Malamy, *Plant Cell Environ.*, 2005, **28**, 67-77.

17. A. Walter, W. K. Silk and U. Schurr, *Annu. Rev. Plant Biol.*, 2009, **60**, 279-304.

18. S. Okumoto, *Curr. Opin. Biotechnol.*, 2010, **21**, 45-54.

19. S. Takayama, J. C. McDonald, E. Ostuni, M. N. Liang, P. J. A. Kenis, R. F. Ismagilov and G. M. Whitesides, *Proc. Natl. Acad. Sci. U. S. A.*, 1999, **96**, 5545-5548.

20. F. Migliaccio, A. Fortunati and P. Tassone, *Plant Signal. Behav.*, 2009, **4**, 183-190.

21. S. de Dorlodot, B. Forster, L. Pages, A. Price, R. Tuberosa and X. Draye, *Trends Plant Sci.*, 2007, **12**, 474-481.

22. K. S. Osmont, R. Sibout and C. S. Hardtke, *Annu. Rev. Plant Biol.*, 2007, **58**, 93-113.

23. D. A. Schwartz, J. H. Freedman and E. A. Linney, *Hum. Mol. Gen.*, 2004, **13**, R217-R224.

24. J. G. Burleigh, K. Alphonse, A. J. Alverson, H. M. Bik, C. Blank, A. L. Cirranello, H. Cui, M. Daly, T. G. Dietterich, G. Gasparich, J. Irvine, M. Julius, S. Kaufman, E. Law, J. Liu, L. Moore, M. A. O'Leary, M. Passarotti, S. Ranade, N. B. Simmons, D. W. Stevenson, R. W. Thacker, E. C. Theriot, S. Todorovic, P. M. Velazco, R. L. Walls, J. M. Wolfe and M. Yu, *PLoS Curr.*, 2013, **5**, 1-9.

25. A. Walter, F. Liebisch and A. Hund, *Plant Methods*, 2015, **11**, 1-11.

26. D. Houle, D. R. Govindaraju and S. Omholt, *Nat. Rev. Genet.*, 2010, **11**, 855-866.

27. J. M. Kaplan and M. Pigliucci, *Biol. Philos.*, 2001, **16**, 189-213.

28. V. Zabrouskov, L. Giacomelli, K. J. van Wijk and F. W. McLafferty, *Mol. Cell. Proteomics*, 2003, **2**, 1253-1260.

29. J. K. C. Rose, S. Bashir, J. J. Giovannoni, M. M. Jahn and R. S. Saravanan, *Plant J.*, 2004, **39**, 715-733.

30. L. W. Sumner, P. Mendes and R. A. Dixon, *Phytochemistry*, 2003, **62**, 817-836.

31. P. Zimmermann, M. Hirsch-Hoffmann, L. Hennig and W. Gruissem, *Plant Physiol.*, 2004, **136**, 2621-2632.

32. N. D. Miller, B. M. Parks and E. P. Spalding, *Plant J.*, 2007, **52**, 374-381.

33. E. B. Blancaflor and P. H. Masson, *Plant Physiol.*, 2003, **133**, 1677-1690.

34. E. B. Blancaflor, J. M. Fasano and S. Gilroy, *Plant Physiol.*, 1998, **116**, 213-222.

35. C. S. Buer and G. K. Muday, *Plant Cell*, 2004, **16**, 1191-1205.

36. G. T. S. Beemster and T. I. Baskin, *Plant Physiol.*, 1998, **116**, 1515-1526.

37. G. T. S. Beemster and T. I. Baskin, *Plant Physiol.*, 2000, **124**, 1718-1727.

38. X. D. Fu and N. P. Harberd, *Nature*, 2003, **421**, 740-743.

39. C. Granier, L. Aguirrezabal, K. Chenu, S. J. Cookson, M. Dauzat, P. Hamard, J. J. Thioux, G. Rolland, S. Bouchier-Combaud, A. Lebaudy, B. Muller, T. Simonneau and F. Tardieu, *New Phytol.*, 2006, **169**, 623-635.

40. M. Jansen, F. Gilmer, B. Biskup, K. A. Nagel, U. Rascher, A. Fischbach, S. Briem, G. Dreissen, S. Tittmann, S. Braun, I. De Jaeger, M. Metzlaff, U. Schurr, H. Scharr and A. Walter, *Funct. Plant Biol.*, 2009, **36**, 902-914.

41. L. d. F. Costa and R. M. Cesar, Jr., *Shape Classification and Analysis: Theory and Practice, Second Edition*, 2009.

42. P. Prusinkiewicz, L. Mundermann, R. Karwowski, B. Lane and A. C. M. Acm, *Siggraph 2001 Conference Proceedings*, 2001, 289-300.

43. http://www.lemnatec.com/applications/field-phenotyping/

44. J. Luis Araus and J. E. Cairns, *Trends Plant Sci.*, 2014, **19**, 52-61.

45. A. Comar, P. Burger, B. de Solan, F. Baret, F. Daumard and J.-F. Hanocq, *Funct. Plant Biol.*, 2012, **39**, 914-924.

46. http://www.lemnatec.com/products/hardware-solutions/scanalyzer-field/

47. http://www.wps.eu/en/plant-phenotyping/applications/field-phenotyping

48. https://www.danforthcenter.org/scientists-research/core-technologies/phenotyping

49. http://www.lemnatec.com/PAG-2011/Development-of-High-Throughput-Plant-Phenotyping-Facilities-at-Aberystwyth.pdf

50. http://qubitphenomics.com/

51. http://qubitphenomics.com/plantscreen-conveyor/

52. http://www.wps.eu/en/plant-phenotyping/overview-products-plant-phenotyping

53. K. Chung, Y. Kim, J. S. Kanodia, E. Gong, S. Y. Shvartsman and H. Lu, *Nat. Methods*, 2011, **8**, 171-U103.

54. R. T. Clark, R. B. MacCurdy, J. K. Jung, J. E. Shaff, S. R. McCouch, D. J. Aneshansley and L. V. Kochian, *Plant Physiol.*, 2011, **156**, 455-465.

55. C. Samara, C. B. Rohde, C. L. Gilleland, S. Norton, S. J. Haggarty and M. F. Yanik, *Proc. Natl. Acad. Sci. U. S. A.*, 2010, **107**, 18342-18347.

56. C. L. Gilleland, C. B. Rohde, F. Zeng and M. F. Yanik, *Nat. Protoc.*, 2010, **5**, 1888-1902.

57. E. M. Lucchetta, J. H. Lee, L. A. Fu, N. H. Patel and R. F. Ismagilov, *Nature*, 2005, **434**, 1134-1138.

58. A. S. Nezhad, *Lab Chip*, 2014, **14**, 3262-3274.

59. M. Horade, N. Yanagisawa, Y. Mizuta, T. Higashiyama and H. Arata, *Microelectron. Eng.*, 2014, **118**, 25-28.

60. G. Grossmann, W.-J. Guo, D. W. Ehrhardt, W. B. Frommer, R. V. Sit, S. R. Quake and M. Meier, *Plant Cell*, 2011, **23**, 4234-4240.

61. A. M. Jones, G. Grossmann, J. A. H. Danielson, D. Sosso, L.-Q. Chen, C.-H. Ho and W. B. Frommer, *Curr. Opin. Plant Biol.*, 2013, **16**, 389-395.

62. W. Busch, B. T. Moore, B. Martsberger, D. L. Mace, R. W. Twigg, J. Jung, I. Pruteanu-Malinici, S. J. Kennedy, G. K. Fricke, R. L. Clark, U. Ohler and P. N. Benfey, *Nat. Methods*, 2012, **9**, 1101-1106.

63. C. G. Agudelo, A. S. Nezhad, M. Ghanbari, M. Naghavi, M. Packirisamy and A. Geitmann, *Plant J.*, 2013, **73**, 1057-1068.

64. A. S. Nezhad, M. Ghanbari, C. G. Agudelo, M. Naghavi, M. Packirisamy, R. B. Bhat and A. Geitmann, *Biomed. Microdevices*, 2014, **16**, 23-33.

65. A. Parashar and S. Pandey, *Appl. Phys. Lett.*, 2011, **98**, 263703.

66. D. R. Lovley, *Curr. Opin. Biotech.*, 2006, **17**, 327-332.

67. R. M. Allen and H. P. Bennetto, *Appl. Biochem. Biotech.*, 1993, **39**, 27-40.

68. H. Moon, I. S. Chang and B. H. Kim, *Bioresource Technol.*, 2006, **97**, 621-627.

69. D. H. Park and J. G. Zeikus, *Appl. Environ. Microb.*, 2000, **66**, 1292-1297.

70. Z. Du, H. Li and T. Gu, *Biotechnol. Adv.*, 2007, **25**, 464-482.

71. B. H. Kim, I. S. Chang, G. C. Gil, H. S. Park and H. J. Kim, *Biotechnol. Lett.*, 2003, **25**, 541-545.

72. K. Rabaey and W. Verstraete, *Trends Biotechnol.*, 2005, **23**, 291-298.

73. A. E. Franks and K. P. Nevin, *Energies*, 2010, **3**, 899-919.

74. D. R. Lovley, *Nat. Rev. Microbiol.*, 2006, **4**, 497-508.

75. D. R. Bond, D. E. Holmes, L. M. Tender and D. R. Lovley, *Science*, 2002, **295**, 483-485.

76. D. R. Bond and D. R. Lovley, *Appl. Environ. Microb.*, 2003, **69**, 1548-1555.

77. K. P. Nevin, H. Richter, S. F. Covalla, J. P. Johnson, T. L. Woodard, A. L. Orloff, H. Jia, M. Zhang and D. R. Lovley, *Environ. Microbiol.*, 2008, **10**, 2505-2514.

78. D. R. Bond and D. R. Lovley, *Appl. Environ. Microb.*, 2005, **71**, 2186-2189.

79. S. K. Chaudhuri and D. R. Lovley, *Nat. Biotechnol.*, 2003, **21**, 1229-1232.

80. D. Pant, G. Van Bogaert, L. Diels and K. Vanbroekhoven, *Bioresource Technol.*, 2010, **101**, 1533-1543.

81. Z. Liu, J. Liu, S. Zhang and Z. Su, *Biochem. Eng. J.*, 2009, **45**, 185-191.

82. K.-J. Chae, M.-J. Choi, J.-W. Lee, K.-Y. Kim and I. S. Kim, *Bioresource Technol.*, 2009, **100**, 3518-3525.

83. C. Dumas, A. Mollica, D. Feron, R. Basseguy, L. Etcheverry and A. Bergel, *Electrochim. Acta*, 2007, **53**, 468-473.

84. S. Cheng, H. Liu and B. E. Logan, *Environ. Sci. Technol.*, 2006, **40**, 2426-2432.

85. B. Min and B. E. Logan, *Environ. Sci. Technol.*, 2004, **38**, 5809-5814.

86. F. Zhao, N. Rahunen, J. R. Varcoe, A. Chandra, C. Avignone-Rossa, A. E. Thumser and R. C. T. Slade, *Environ. Sci. Technol.*, 2008, **42**, 4971-4976.

87. X. Wang, S. Cheng, Y. Feng, M. D. Merrill, T. Saito and B. E. Logan, *Environ. Sci. Technol.*, 2009, **43**, 6870-6874.

88. S. Cheng and B. E. Logan, *Electrochem. Commun.*, 2007, **9**, 492-496.

89. B. E. Logan, B. Hamelers, R. A. Rozendal, U. Schrorder, J. Keller, S. Freguia, P. Aelterman, W. Verstraete and K. Rabaey, *Environ. Sci. Technol.*, 2006, **40**, 5181-5192.

90. D. H. Park and J. G. Zeikus, *J. Bacteriol.*, 1999, **181**, 2403-2410.

91. G. C. Gil, I. S. Chang, B. H. Kim, M. Kim, J. K. Jang, H. S. Park and H. J. Kim, *Biosens. Bioelectron.*, 2003, **18**, 327-334.

92. Z. He, S. D. Minteer and L. T. Angenent, *Environ. Sci. Technol.*, 2005, **39**, 5262-5267.

93. N. Kim, Y. Choi, S. Jung and S. Kim, *B. Kor. Chem. Soc.*, 2000, **21**, 44-48.

94. D. A. Lowy, L. M. Tender, J. G. Zeikus, D. H. Park and D. R. Lovley, *Biosens. Bioelectron.*, 2006, **21**, 2058-2063.

95. J. Niessen, U. Schroder, M. Rosenbaum and F. Scholz, *Electrochem. Commun.*, 2004, **6**, 571-575.

96. U. Schroder, J. Niessen and F. Scholz, *Angew. Chem. Int. Edit.*, 2003, **42**, 2880-2883.

97. B. K. Min, S. A. Cheng and B. E. Logan, *Water Res.*, 2005, **39**, 1675-1686.

98. G. M. Delaney, H. P. Bennetto, J. R. Mason, S. D. Roller, J. L. Stirling and C. F. Thurston, *J. Chem. Tech. Biot. B.*, 1984, **34**, 13-27.

99. B. E. Logan, C. Murano, K. Scott, N. D. Gray and I. M. Head, *Water Res.*, 2005, **39**, 942-952.

100. H. Liu, R. Ramnarayanan and B. E. Logan, *Environ. Sci. Technol.*, 2004, **38**, 2281-2285.

101. H. Liu and B. E. Logan, *Environ. Sci. Technol.*, 2004, **38**, 4040-4046.

102. I. S. Chang, J. K. Jang, G. C. Gil, M. Kim, H. J. Kim, B. W. Cho and B. H. Kim, *Biosens. Bioelectron.*, 2004, **19**, 607-613.

103. G.-X. Yang, Y.-M. Sun, X.-Y. Kong, F. Zhen, Y. Li, L.-H. Li, T.-Z. Lei, Z.-H. Yuan and G.-Y. Chen, *Water Sci. Technol.*, 2013, **68**, 1914-1919.

104. K. Rabaey, G. Lissens, S. D. Siciliano and W. Verstraete, *Biotechnol. Lett.*, 2003, **25**, 1531-1535.

105. P. Aelterman, K. Rabaey, H. T. Pham, N. Boon and W. Verstraete, *Environ. Sci. Technol.*, 2006, **40**, 3388-3394.

106. B. Lin, M. Braster, B. M. van Breukelen, H. W. van Verseveld, H. V. Westerhoff and W. F. M. Roling, *Appl. Environ. Microb.*, 2005, **71**, 5983-5991.

107. J. N. Rooney-Varga, R. T. Anderson, J. L. Fraga, D. Ringelberg and D. R. Lovley, *Appl. Environ. Microb.*, 1999, **65**, 3056-3063.

108. D. R. Lovley, M. J. Baedecker, D. J. Lonergan, I. M. Cozzarelli, E. J. P. Phillips and D. I. Siegel, *Nature*, 1989, **339**, 297-300.

109. R. T. Anderson, J. N. Rooney-Varga, C. V. Gaw and D. R. Lovley, *Environ. Sci. Technol.*, 1998, **32**, 1222-1229.

110. T. Zhang, S. M. Gannon, K. P. Nevin, A. E. Franks and D. R. Lovley, *Environ. Microbiol.*, 2010, **12**, 1011-1020.

111. S. Choi, *Biosens. Bioelectron.*, 2015, **69**, 8-25.

112. H.-Y. Wang, A. Bernarda, C.-Y. Huang, D.-J. Lee and J.-S. Chang, *Bioresource Technol.*, 2011, **102**, 235-243.

113. S. Choi, H.-S. Lee, Y. Yang, P. Parameswaran, C. I. Torres, B. E. Rittmann and J. Chae, *Lab Chip*, 2011, **11**, 1110-1117.

114. F. Qian, M. Baum, Q. Gu and D. E. Morse, *Lab Chip*, 2009, **9**, 3076-3081.

115. C.-P.-B. Siu and M. Chiao, *J. Microelectromech. S.*, 2008, **17**, 1329-1341.

116. J. E. Mink and M. M. Hussain, *Acs Nano*, 2013, **7**, 6921-6927.

117. A. Fraiwan, S. P. Adusumilli, D. Han, A. J. Steckl, D. F. Call, C. R. Westgate and S. Choi, *Fuel Cells*, 2014, **14**, 801-809.

118. H. Hou, L. Li, Y. Cho, P. de Figueiredo and A. Han, *Plos One*, 2009, **4**, e6570.

119. Y.-P. Chen, Y. Zhao, K.-Q. Qiu, J. Chu, R. Lu, M. Sun, X.-W. Liu, G.-P. Sheng, H.-Q. Yu, J. Chen, W.-J. Li, G. Liu, Y.-C. Tian and Y. Xiong, *Biosens. Bioelectron.*, 2011, **26**, 2841-2846.

120. S. Mukherjee, S. Su, W. Panmanee, R. T. Irvin, D. J. Hassett and S. Choi, *Sensors Actuat. A-Phys.*, 2013, **201**, 532-537.

121. A. Fraiwan and S. Choi, *Phys. Chem. Chem. Phys.*, 2014, **16**, 26288-26293.

122. H. Lee and S. Choi, *Lab Chip*, 2015, **15**, 391-398.

123. J. M. Pisciotta, Y. Zou and I. V. Baskakov, *Plos One*, 2010, **5**, e10821.

124. M. Rosenbaum, Z. He and L. T. Angenent, *Curr. Opin. Biotech.*, 2010, **21**, 259-264.

125. Y. Zou, J. Pisciotta, R. B. Billmyre and I. V. Baskakov, *Biotechnol. Bioeng.*, 2009, **104**, 939-946.

126. https://www.wageningenur.nl/en/show/Plants-create-energy.htm

127. http://www.gizmag.com/plant-microbial-fuel-cell/25163/

128. D. P. B. T. B. Strik, H. V. M. Hamelers, J. F. H. Snel and C. J. N. Buisman, *Int. J. Energ. Res.*, 2008, **32**, 870-876.

129. S. K. Chirag and B. N. Yagnik, *Res. J. Biotechnol.*, 2013, **8**, 84-90.

130. http://spectrum.ieee.org/energy/environment/plugging-in-to-plant-roots

131. http://plant-e.com/technology.html

132. M. Helder, D. P. B. T. B. Strik, H. V. M. Hamelers, A. J. Kuhn, C. Blok and C. J. N. Buisman, *Bioresource Technol.*, 2010, **101**, 3541-3547.

133. K. Takanezawa, K. Nishio, S. Kato, K. Hashimoto and K. Watanabe, *Biosci. Biotech. Bioch.*, 2010, **74**, 1271-1273.

134. R. A. Timmers, D. P. B. T. B. Strik, H. V. M. Hamelers and C. J. N. Buisman, *Appl. Microbiol. Biot.*, 2010, **86**, 973-981.

135. H. Deng, Z. Chen and F. Zhao, *Chemsuschem*, 2012, **5**, 1006-1011.

136. http://www.treehugger.com/clean-technology/plant-microbial-fuel-cell-produces-power-plants.html

137. L. de Schamphelaire, L. van den Bossche, H. S. Dang, M. Hofte, N. Boon, K. Rabaey and W. Verstraete, *Environ. Sci. Technol.*, 2008, **42**, 3053-3058.

138. M. Helder, D. P. B. T. B. Strik, H. V. M. Hamelers and C. J. N. Buisman, *Biotechnol. Biofuels*, 2012, **5**, 70.

139. P. Bombelli, D. M. R. Iyer, S. Covshoff, A. J. McCormick, K. Yunus, J. M. Hibberd, A. C. Fisher and C. J. Howe, *Appl. Microbiol. Biot.*, 2013, **97**, 429-438.

140. K. Wetser, E. Sudirjo, C. J. N. Buisman and D. P. B. T. B. Strik, *Appl. Energ.*, 2015, **137**, 151-157.

141. Y. Goto, N. Yoshida, Y. Umeyama, T. Yamada, R. Tero and A. Hiraishi, *Front. Bioeng. Biotechnol.*, 2015, **3**, 42.

CHAPTER 2. PLANT-CHIP FOR HIGH-THROUGHPUT PHENOTYPING OF *ARABIDOPSIS*

A paper published in *Lab on a chip*

Huawei Jiang, Zhen Xu, Maneesha R Aluru, and Liang Dong

Abstract

We report on the development of a vertical and transparent microfluidic chip for high-throughput phenotyping of *Arabidopsis* thaliana plants. Multiple *Arabidopsis* seeds can be germinated and grown hydroponically over more than two weeks in the chip, thus enabling large-scale and quantitative monitoring of plant phenotypes. The novel vertical arrangement of this microfluidic device not only allows for normal gravitropic growth of the plants, but also, more importantly, makes it convenient to continuously monitor phenotypic changes in plants at the whole organismal level, including seed germination and root and shoot growth (hypocotyls, cotyledons, and leaves), as well as at the cellular level. We also developed a hydrodynamic trapping method to automatically place single seeds into seed holding sites of the device, and to avoid potential damage to seeds that might occur during manual loading. We demonstrated general utility of this microfluidic device by showing clear visible phenotypes of the *immutans* mutant of *Arabidopsis*, and also with changes occurring during plant-pathogen interactions at different developmental stages. *Arabidopsis* plants grown in the device maintained normal morphological and physiological behaviour, and distinct phenotypic variations consistent with apriori data were observed via high-resolution images taken in real-time. Moreover, the timeline for different developmental stages for plants grown in this device was highly comparable to growth on conventional agar plate method. This prototype plant-chip technology is expected to lead to the

establishment of a powerful experimental and cost-effective framework for high-throughput and precise plant phenotyping.

2.1 Introduction

The recent completion of the genome sequencing projects, along with advances in high-throughput technologies (e.g., microarrays, next generation sequencing) have made it possible for a high-throughput "systems approach", to acquire a great wealth of information about the genotype, i.e., the genetic makeup of an organism [1-7]. Much of the existing instrumentation and software have also been built with the key goal of identifying and analysing various biomolecules (e.g., DNA, RNA, metabolites). But, information about the genotype is only useful in so far as it allows us to make predictions about the phenotype, i.e., the observable traits and characteristics of an organism. Phenomics is an emerging area of science that links observations from genotypes with the phenotypes [8, 9]. However, characterization of the complete plant phenome poses a difficult challenge, as even plants with smaller genomes such as *Arabidopsis* thaliana contain tens of thousands of genes [10-12].

Previous plant phenotype analyses relied on culturing seeds and growing plants in soil pots and agarose plates using culture facilities (e.g., greenhouse, growth chamber) under controlled environments, and on using imaging technology to measure plant characteristics and phenotypic changes [13-19]. Multi-well plates have also been utilized for chemical screening of a large number of seedling roots [20-21]. However, there are several concerns worth noting. First, screening of plant phenotypes using traditional greenhouses and growth chambers is costly and the number of experiments is limited. Flexibility and accuracy of changing plant growth environments are also relatively low. Second, due to the use of soil pots and agarose plates, a relatively large amount of chemicals and biological species is needed. Third, spatial resolution of

morphological measurements for seed, root, and shoot phenotypes is often on the millimetre scale as soil pots and agarose plates are not optically transparent. Real-time observation of cellular behaviours (e.g., cell division, elongation, host-pathogen interactions) is also not easy. As a result, low temporal resolution may lead to missing information about progressive and subtle changes in phenotypes during plant growth. Therefore, while progress has been made in this area, the traditional plant phenotyping approaches suffer from expense, labour, and time involved in large-scale phenotypic analyses (especially under varying environmental conditions), low spatial and temporal resolution, low throughput for obtaining phenotype information, and frequent manual intervention during growth and imaging [22-24].

Microfluidic technology provides a powerful and flexible platform to interrogate cellular and multicellular organisms. General advantages of microfluidics-based bioassays include high throughput and improved data statistic due to parallel processing, reduction of agent consumption, fast reaction, and avoidance of contamination. Prior developments in microfluidic devices have greatly advanced high-throughput analyses of model organisms, such as Drosophila melanogaster and Caenorhabditis elegans [25-30]. But, microfluidic technology is still relatively underdeveloped and underutilized for applications in plant sciences, an area with huge social and economic impact.

Recently, *Arabidopsis* root development and Camellia pollen tube growth have been studied using microfluidic devices [31-36]. A RootChip was developed for high-throughput plant gene expression analysis [32], where *Arabidopsis* seeds germinated and grew initially in conventional pipettes for several days, and then, transferred into the chip for root gene expression studies. More recently, a RootArray was reported, where multiple *Arabidopsis thaliana* seedlings grew in the chip and their roots were imaged by confocal laser scanning microscopy over several

days [35]. Our group also developed a microfluidic device for in-chip seed germination and seedling growth at different growth temperatures over several days, thus expanding the utility of microfluidic technology for manipulating plant environmental conditions [33]. Although these approaches have advanced the use of microfluidics in plant sciences, phenotypic measurements with these devices were restricted only to plant roots [32-36], and quantitative measurements of other organ phenotypes (e.g., seed germination, hypocotyl, cotyledon, leaf growth) was not feasible. Therefore, the existing microfluidic devices are of limited use for characterization of the complete plant phenome.

Here, we report on the development of a novel microfluidic device for high-throughput phenotyping of *Arabidopsis* plants. Unlike the previous microfluidic devices where the plant roots were grown horizontally in microchannels, specimen transfer was sometimes required after a certain period of growth, and phenotypic measurement was allowed only for root systems over a relatively short growth time, the present device consists of a transparent and vertical microfluidic chip where multiple *Arabidopsis* seeds can be germinated and grown vertically in the chip, not only allowing for normal gravitropic growth of the plants, but also, more importantly, making it convenient for continuous and non-invasive monitoring of phenotypic changes of different plant organs, including both root and shoot systems, over various plant developmental stages. Also, in the present device, *Arabidopsis* plants can grow over a longer growth period than the existing devices (i.e., more than two weeks vs. several days).

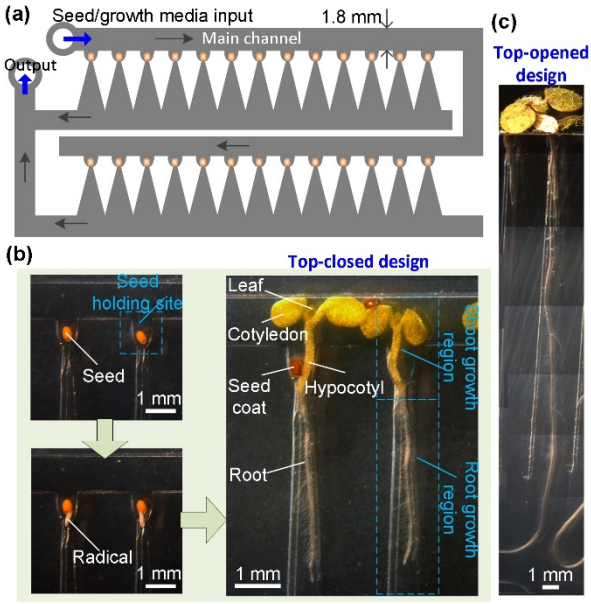

Figure 2.1 *(a) Schematic of the plant-chip for high-throughput plant phenotyping. (b) In-chip seed germination and plant growth. Major plant organs and device structures are labelled and highlighted. In this top-closed design, the main channel is closed during the growth of the plants. (c) A top-opened design for plant phenotyping over a longer growth period. The top part of the main channel is cut off. The shoot system of the plants is grown outside of the top-opened device.*

2.2 Methods and experimental section

2.2.1 Overall design of device

Figure 2.1a shows the schematic of the present microfluidic plant chip. The device allows multiple plants to simultaneously grow in vertical direction in multiple growth regions. Each growth region includes a funnel-shaped seed holding site on the top and a tapered expanding microchannel on the bottom. The seeds are germinated inside the seed holding sites. The plant roots grow downward into the tapered channel. The main channel above the seed holding sites allows sufficient space for the plant shoots to grow upward (Figure 2.1a). To accommodate phenotyping of different plant species growing to different stages of interest, the number of the seed holding sites and the structure and geometry of the root and shoot growth regions can be flexibly changed during device design and fabrication. In the device presented here, 26 *Arabidopsis* plants are distributed on two connecting floors. To hold *Arabidopsis* seeds and

provide enough room for seed germination, the lower and upper openings of the funnel is designed to be 350 µm and 725 µm wide, respectively. The root and shoot growth region is designed to be 10 mm and 1.8 mm tall, respectively. All the channels of the device are 400 µm deep. In the case that the main channel is closed (Figure 2.1b), the plants can grow within the device for about eleven days, during which seed germination, and emergence and growth of plant root, hypocotyl, cotyledon, and first two true leaves can be clearly imaged. By opening up the main channel of the device, the plants can grow over more than two weeks and the plant phenotypes through later growth stages can be observed and recorded (Figure 2.1c). This transparent device, in conjunction with a conventional microscopic imaging system, can facilitate easy and high-quality observation of plant phenotypes at the whole organismal as well as at the cellular level.

3.2.2 Design for hydrodynamic trapping of seeds

Generally, individual *Arabidopsis* seeds are handled by sterilized tools such as toothpicks or forceps. Due to their small size, it would be difficult to manually pick and load seeds individually into multiple devices for large-scale analyses. The seeds may get contaminated or even destroyed during manual handling. To overcome this issue, we developed a hydrodynamic microfluidic trapping method to automatically load seeds into individual seed holding sites of the chip. Each trapping site was patterned like a funnel. The top opening of the funnel was large enough to allow a seed to come in, while the bottom opening was relatively smaller to prevent the seed from falling out of the funnel. Multiple seeds were infused into the main channel by flowing liquid medium through the inlet of the device (Figure 2.1a). A sucking pressure was applied at the outlet by withdrawing the fluid out of the device, forcing the seeds to flow against the lower wall of the main channel. As the seeds flowed by a funnel, the fluid streamlines would carry the seed

entering the funnel. Since each funnel is designed to allow hosting only one seed, other seeds have to flow over this funnel to successive ones, allowing for a single seed to be trapped.

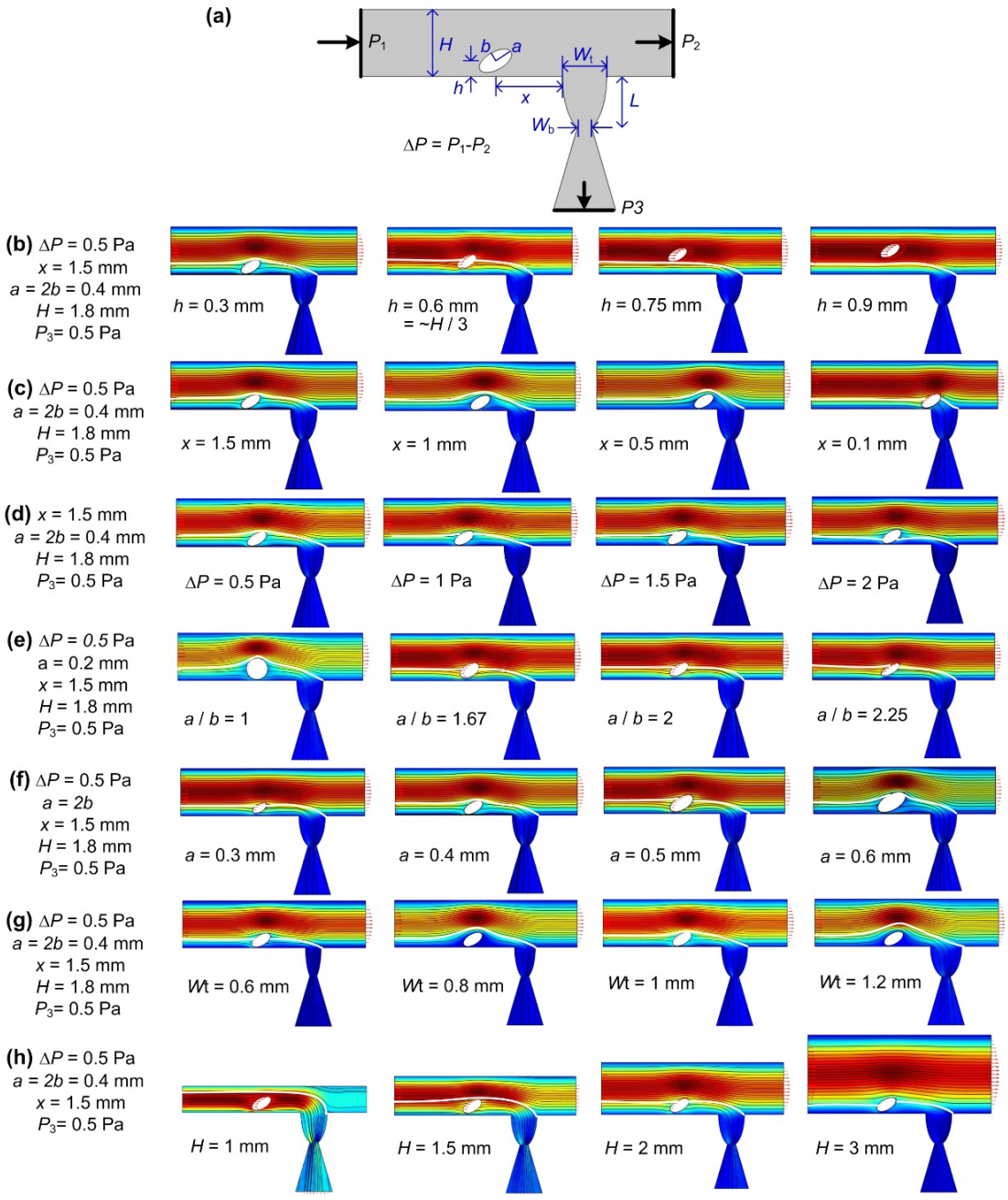

Figure 2.2 *(a) A FEA model for simulating fluid dynamics during hydrodynamic trapping of a seed into a funnel-like trapping site. (b) Distributions of fluid velocity when the seed is flowing at different distances from the lower sidewall of the main channel in the vertical direction. From left to right, h = 0.3, 0.6, 0.75, and 0.9 mm, respectively. (c) Distributions of fluid velocity when the seed is located at different distances from the upper left corner of the funnel in the longitudinal or horizontal direction. From left to right, x = 1.5, 1, 0.5, and 0.1 mm, respectively. (d) Distributions of fluid velocity under different pressure drops along the main channel over a single trapping site in the longitudinal direction. From left to right, ΔP = 0.5, 1, 1.5, and 2 Pa, respectively. (e) Influence of the shape of a*

seed on the distribution of fluid velocity. From left to right, a/b = 1, 1.67, 2, and 2.25, respectively, while a is fixed at 0.2 mm. (f) Influence of the size of a seed on the distribution of fluid velocity. From left to right, a = 0.3, 0.4, 0.5, and 0.6 mm, respectively, while a/b is fixed at 2. (g) Influence of the width of the top opening of the funnel on the distribution of fluid velocity. From left to right, W_t = 0.6, 0.8, 1 and 1.2 mm, respectively, while W_b is fixed at 0.3 mm. (h) Influence of the height or width of the main channel on the distribution of fluid velocity. From left to right, H = 1, 1.5, 2, and 3 mm, respectively. In (a)-(h), the colour scale represents the fluid velocity, where red indicates high and blue indicates low. The white lines added to the distribution profiles of fluid velocity represent the critical streamlines.

To better understand the seed trapping mechanism and to study the influences of the seed and device geometries, and the infusion and withdrawal flow rates on the seed trapping, we conducted fluid dynamic simulations for the device by using finite element analysis (FEA) software COMSOL. A model was thus built for the simulation (Figure 2.2a). The key structural and geometrical parameters include the widths of the top and bottom openings (W_t and W_b, respectively) and the depth of the funnel (L), the height or width of the main channel (H), the lengths of the semi-major and semi-minor axes of the seed (a and b, respectively), and the ratio of a to b or a/b. Because the present device was designed for phenotyping of *Arabidopsis* plants, based on possible sizes and shapes of different types of *Arabidopsis* seeds, we set reasonable dimension ranges for the aforementioned parameters as follows: $1 \leq a/b \leq 2.25$, 0.3 mm $\leq a \leq 0.6$ mm, $1 \leq H \leq 3$ mm, $2a < W_t < 4a$, $W_b < 2b$, and $2a < L < 4a$.

All the FEA simulations were conducted under a rotational equilibrium condition that a seed was assumed to move axially without rotation while moving in the main channel. Through extensive simulational trials, the rotational equilibrium of the seeds was achieved at an angle of about 30 degrees between the seed's semi-major axis and the longitudinal direction of the main channel. The criteria for successful seed trapping was that the volumetric centre of the seed should be located above a critical streamline (highlighted by the white lines in Figure 2.2b-h) that starts at the input of the main channel and ends at the upper-right corner of the funnel.

We first studied how the pressure drop ΔP over a trapping site along the main channel impacted the seed trapping. Figure 2.2b shows that when the volumetric centre of the seed was located above one-third the height or width of the main channel from the lower horizontal sidewall of the main channel, the seed would pass by rather than flowing into the funnel under a low ΔP = 0.5 Pa. To simplify, all the seeds in the following simulations were set to flow against the lower sidewall of the main channel. Figure 2.2c indicates that regardless of the lateral distance x between the seed and the funnel, the seed could be trapped into the funnel as long as the seed was flowing against the sidewall under ΔP = 0.5 Pa. But, as ΔP gradually increased to 2 Pa (Figure 2.2d), the critical streamline moved closer to the sidewall and overlapped the volumetric centre of the seed (see the first panel from right in Figure 2.2d). This indicates that by applying a higher ΔP, the seed would pass by the funnel.

Subsequently, the influence of the shape and size of a seed on the seed trapping was studied. The simulated results show that as the value of a/b increased from 1 to 2.25 while keeping a = 400 µm (Figure 2.2e) or as the seed scaled up in all dimensions while keeping a/b = 2 (Figure 2.2f), the seed would be trapped under a low ΔP = 0.5 Pa as long as the volumetric centre of the seed was located below the corresponding critical streamline.

In addition, the influence of the structure of the main channel and the funnel on the seed trapping was investigated. The simulated result shows that increasing the width of the top opening of the funnel caused the critical streamline to elevate, which, in turn, would make it easier to trap the seed (Figure 2.2g). On the other hand, as the width of the main channel increased from 1 to 3 mm, the seed flowing along against the lower sidewall of the main channel would still be trapped (Figure 2.2h).

It is worthwhile to point out that since dimensional variations among different types of *Arabidopsis* seeds are actually minor (at the size scale of several hundreds of micrometres), it should be relatively easy to tune the key structural parameters of the device to adapt to different seeds, without the need of establishing a new model for simulations.

Experimentally, in order for the seed to flow in the lower part of the main channel, a pulling pressure was applied at the outlet of the device (Figures 2.1a and 2.2a). Thus, two syringe pumps were simultaneously used during seed trapping, one for infusion and the other for withdrawal of fluid. We experimentally studied how the infusion/withdrawal flow rates affected the trapping rate of *Arabidopsis* seeds. Here, the trapping rate refers to the success rate of trapping *one or two* seeds in a funnel. It is noted that trapping two seeds in a single funnel was possible as the sizes and shapes of the seeds (of even the same type) were not uniform. Figure 2.3a demonstrates that (i) as the withdrawal flow rate increased from 0 to 20 μL/s, the trapping rate increased from 4.6 ± 2.9% to 97 ± 2.2%; (ii) the lower the infusion flow rate, the easier the seed trapping, and thus, the higher the trapping rate, which followed the trend seen in Figure 2.2h; and (iii) the trapping rate decreased gradually and then relatively abruptly with increasing the infusion flow rate from 5 to 75 μL/s. Figure 2.3b shows the experimental result of how the width of the main channel affected the trapping rate. As W_t increased from 1.4 to 3 mm, the seeds flowing in the lower part of the main channel relatively reduced in quantity, and thus, the trapping rate was observed to decrease from 97 ± 2.2% to 16 ± 6.5% at the infusion flow rate of 20 μL/s and the withdrawal flow rate of 20 μL/s. It should be noted that by increasing the withdrawal flow rate, the trapping rate of the device having a wider channel could be increased to be nearly 100% as demonstrated in Figure 2.3b.

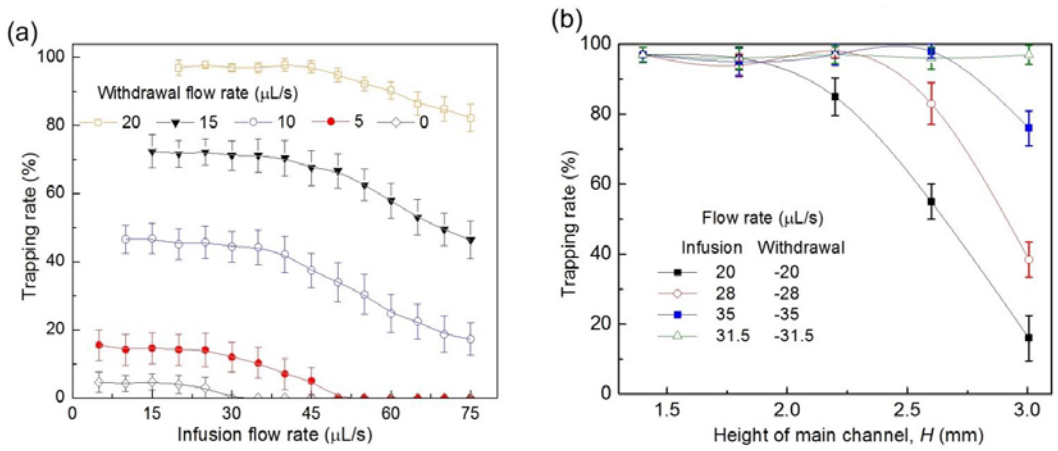

Figure 2.3 *(a) Experimental result of the seed trapping rate as a function of infusion flow rate for different withdrawal flow rates. Arabidopsis seeds used here has a/b = 1.88 ± 0.2. (b) Experimental result of the trapping rate as a function of the width of the main channel at different infusion and withdrawal flow rates. The trapping sites used here are shown in Figure 2.2b. Each measurement is the mean ± standard deviation obtained from 10 measurements.*

2.2.3 Device fabrication

The microfluidic devices were fabricated using a conventional soft lithography technique [37]. Briefly, to master a mould for the microchannels, a silicon wafer was first patterned with SU-8 photoresist (Microchem, MA, USA). Then, a high-resolution transparency film (10,160 dpi, Fineline Imaging, CO, USA) was used as a photomask in photolithography. A prepolymer mixture of polydimethylsiloxane or PDMS (Sylgard 184, Dow Corning, MI, USA) and its curing agent with a weight ratio of 10:1 was poured onto the master mould and then thermally cured on a hotplate at 90 ^{o}C for 1 hour. Subsequently, the hardened PDMS polymer was pealed from the mould and bonded to a microscope glass slide (75 mm × 50 mm × 0.9 mm) by using oxygen plasma treatment. Lastly, the inlet and outlet ports of the device were manually punched with a mechanical puncher.

It should be pointed out that the formation of the PDMS-based structures on a glass slide is not expected to modify *Arabidopsis* growth patterns. PDMS-glass microfluidic devices have been widely used in characterization of both cellular and multicellular organisms [28, 38, 39].

Moreover, *Arabidopsis* plants are routinely grown in glass flasks containing hydroponic growth media for biochemical and physiological studies. As discussed later in Table 2.1, our result shows that the growth stages for *Arabidopsis* plants grown in the fabricated devices were comparable to those grown in conventional petri dish. This further demonstrates that materials used for the fabrication of the devices had little or even no influence on the growth patterns of *Arabidopsis* plants.

2.2.4 Culture Media

Three different liquid culture media were prepared and used, including tap water, Murashige and Skoog (MS) medium, and standard medium [40]. All the chemicals used were of analytical reagent grade. Deionized water was used throughout to prepare the three nutrient media. MS salts were purchased from Sigma-Aldrich, MO, USA. Culture media were sterilized in an autoclave at 15 psi at 121 ºC for 30 mins and stored at 4 ºC in a refrigerator. They were loaded into the device using a 3 mL syringe (Beckton Dickinson, NJ, USA) with a microbore tubing (Cole-Parmer, IL, USA) before the seeds were transferred into the device.

2.2.5 Preparation of *Arabidopsis* seeds

Wild-type (WT) *Arabidopsis thaliana* ecotype Columbia, the *immutans* mutant of *Arabidopsis*, and transgenic *Arabidopsis* seeds containing the *IM* promoter: green fluorescent protein (GFP) reporter fusion construct were used in this study. GFP activity assays were performed using confocal laser scanning microscopy with seeds and seedlings grown within the device. Seeds were surface-sterilized by soaking in 70% ethanol (v/v) for 1 min, followed by 50% (v/v) Clorox and 0.02% (v/v) Triton for 15 min. They were then washed three times with autoclaved deionized (DI) water.

To trap and hold *Arabidopsis* seeds in the vertical device, the lower opening size of the seed holding site must be less than the small diameter of the oval shaped seed. But, if the lower opening was made too small, the root growth of the seeds would be influenced due to the limited space. Therefore, *Arabidopsis* seeds were soaked in a petri dish containing autoclaved DI water for 3-5 hrs and allowed to expand in size slightly prior to loading.

2.2.6 Trapping of *Arabidopsis* seeds

Before seed trapping, all channels in the device were filled with one particular culture medium of interest by using a syringe via a tubing connection. Care was taken to avoid introducing air bubbles into the channels. Subsequently, the soaked seeds were sucked from the soaking petri dish up into a 500-µm-inner diameter microbore tubing manually by a syringe. The tubing was then connected to the inlet port of the device. After that, a syringe pump (KDS200, KD Scientific, MA, USA) was used to inject the seeds directly from the tubing into the device through the inlet port at an infusion flow rate of 20 µL/s. The other syringe pump (same model) applied a sucking pressure through the outlet of the device at a withdrawal flow rate of -20 µL/s, forcing the seeds to flow along the lower sidewall of the channel. It took 3−4 s to complete the seed trapping process.

2.2.7 *Arabidopsis* plant growth conditions

After the seeds were trapped in the seed holding sites, the device was stored at 4 ºC in a refrigerator for 40−48 hrs to stratify seeds. Subsequently, the device was placed vertically under a plant growth light source (fluorescent daylight). The light intensity was set to ~100 µE/m^2s, and plants were grown at room temperature (21−22 ºC). The environmental relative humidity was ~40 %. For the top-closed device (Figures 2.1a and b), growth media was changed in the device on a daily basis using a syringe pump. In the case that the main channel was opened, the fluid level in the device was controlled by slowly flowing growth media (2−3 µL/hr) into the device using a

syringe pump through the port where sucking force was applied during the seed trapping process (see Figure 2.1b). The seeds germinated and the plants grew in the device, and their growth was monitored after exposure to light (or starting from the completion of stratification).

A microscope (MZ 205FA, Leica, Germany) with a video camera (QICAM, QImaging, Canada) was used to image plants growing in the device. The system was used to collect phenotypic data of interest, including seed phenotype (e.g., germination), root phenotype (e.g., length, diameter), shoot phenotype (e.g., hypocotyl, cotyledon and leaf emergence and dimensions), and cell phenotype (e.g., cell division and elongation). All data points reflect the average from five replicates performed on five chips, with each chip having 20−26 plants on a device. Error bars are standard deviations.

2.3 Results and discussion

2.3.1 Hydrodynamic seed trapping

Figure 2.4 shows results of the hydrodynamic seed trapping method (also see video clip in ESI). Almost all of the seed holding sites in the device held seeds. 70−80% of these sites had a *single* seed while the rest of the sites trapped more than one seed. This is because the *Arabidopsis* seeds were not uniform in size and multiple smaller seeds could be trapped into one holding site. We observed that after a seed fell into a trapping site other seeds were not trapped. The percentage of the trapped seeds with respect to the total input seeds was 30−40%. The untapped seeds were flowed out of the device.

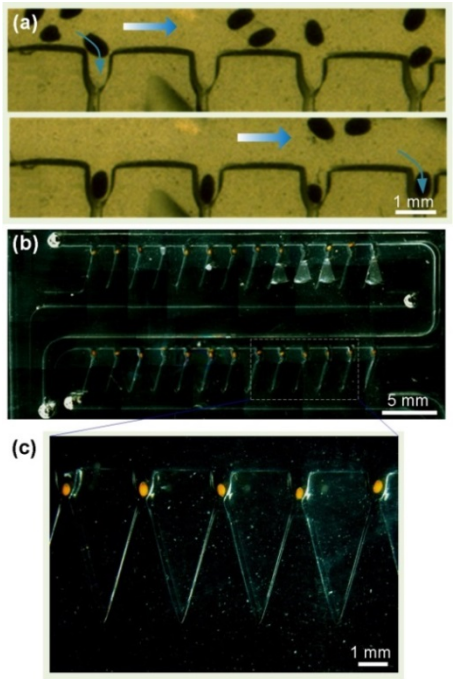

Figure 2.4 *(a) Hydrodynamic trapping of Arabidopsis seeds. (b) Microfluidic plant chip after seed trapping process. (c) Magnified image showing individual seeds trapped in seed holding sites.*

2.3.2 Seed germination and plant growth

As a first step to optimize *Arabidopsis* growth within the device, we tested three different hydroponic media (tap water, MS medium and standard medium) previously used in conventional tissue culture methods. Figure 2.5 shows time-lapse images for the development of *Arabidopsis* plants inside the devices containing the three different growth media. Plant growth and development, including root and shoot systems, were continuously monitored up to 11 days, and images were taken at regular intervals while the plants were growing inside the device. Plants grown in all three media appeared to maintain all of the morphological and physiological traits of plants grown in potting soil and on petri plate.

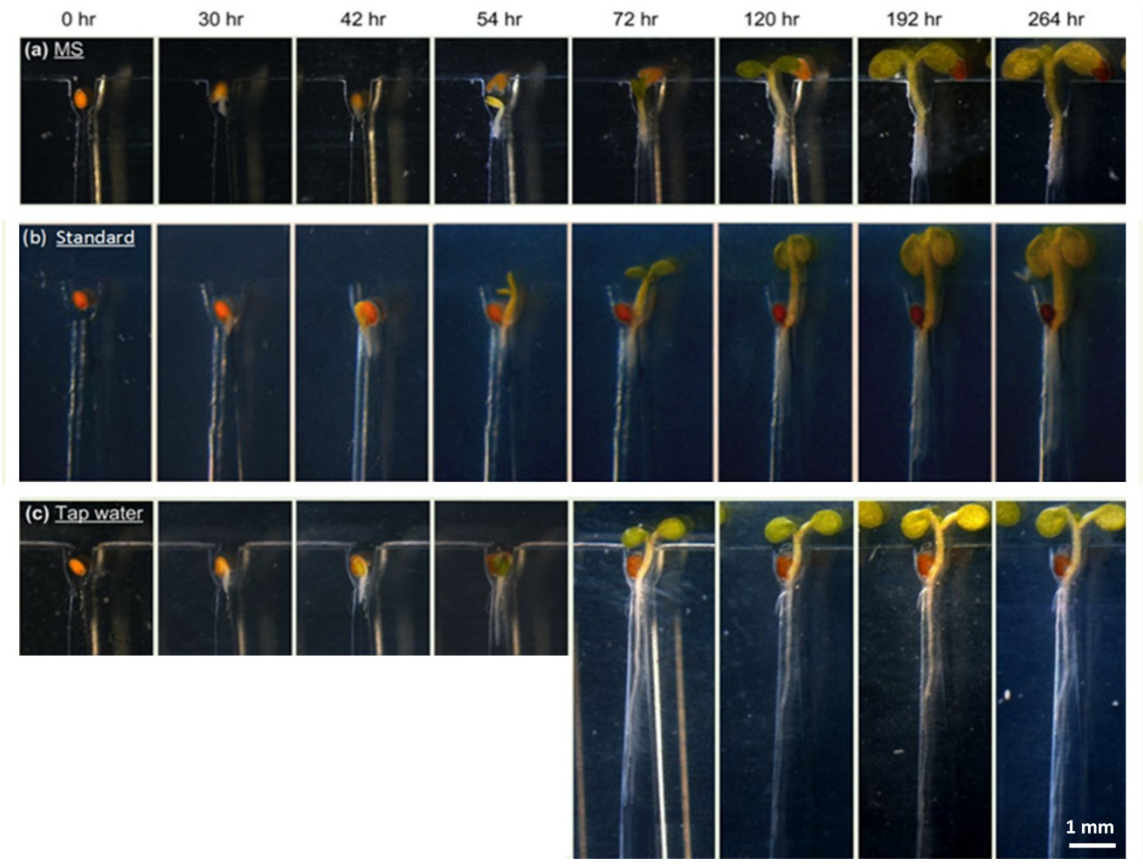

Figure 2.5 *Seed germination and growth of WT Arabidopsis thaliana plants in the vertical microfluidic device with (a) MS medium, (b) standard medium, and (c) tap water.*

Arabidopsis seeds generally follow a two-step germination process with rupture of the seed coat in 20−24 hrs and the emergence of the white radical following endosperm rupture in 30−33 hrs [41]. As shown in Figure 2.5, in-chip germination of *Arabidopsis* seeds was similarly comparable to the previously reported results with observation of radical around 30 hrs in light in all growth media. It should be noted that due to different orientation of the seeds in the holding sites, the radicals of many seeds were not oriented initially downward. But, as the roots grew longer, they tended to grow along a sidewall of the holding sites, and then, entered downward into the tapered growth region towards the bottom of the device. Quantitative analysis of root length as a function of growth time (Figure 2.6a), where root length was measured as the distance from the root tip to the base of the hypocotyl, shows that the roots grew rapidly up to 5 days, but slowly

thereafter. Furthermore, in agreement with previously reported literature [41-45], the roots growing in tap water were observed to be longer and thinner with sparser root hairs while those growing in MS media and standard media were shorter and wider with more number of root hairs. As expected, the green cotyledons were observed to grow up towards the light and in opposite direction of the roots (Figure 2.5). The emergence and growth of the hypocotyl and cotyledon of *Arabidopsis* plants growing within the device could be conveniently imaged and quantitatively analysed over 11 days without manual intervention. The growth of hypocotyl was similar for all plants in different growth media (Figure 2.6b). However, the growth and size of the cotyledons was significantly influenced, with MS medium showing the greatest increase in the surface area (Figure 2.6c). The time-frame for emergence of cotyledons was similar in all media with the two cotyledons emerging approximately 52−54 hrs after exposure to light, following which they grew rapidly for 11 days of plant growth.

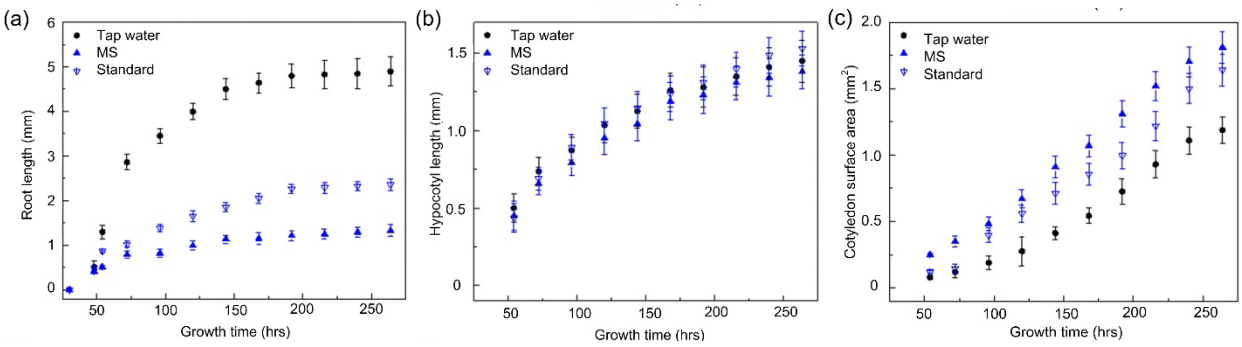

Figure 2.6 *Major phenotypic parameters of WT Arabidopsis thaliana plants as a function of growth time, including (a) root length, (b) hypocotyl length, and (c) cotyledon surface area. The data were obtained by using Matlab based on the images taken at different time points.*

To assess whether WT *Arabidopsis* growth and development within the microfluidic device was similar to *a priori* data, we compared our results with the plants germinated and grown on conventional tissue culture plates [46]. Table 2.1 shows that the timeline for many of the plant growth stages was highly comparable between the conventional plate method and the newly

developed device. However, slight variations between these two methods were also observed. For example, the appearance of 2 rosette leaves is somewhat delayed (in hrs) when compared to the petri plate method. It should be noted that petri plate-based method generally uses gelling *agar* to prevent seeds from rolling, while plants in our device grew in hydroponic media and the seeds were held by microstructures. Thus, these discrepancies may be caused by differences in geometric structure of growth chambers (channels vs. plates) or the surrounding physical environment of seeds (liquid vs. agar gel). These discrepancies are negligibly small, and would not interfere with high-throughput plant phenotyping as long as phenotypic comparisons between different genotypes and plant organs can be simultaneously observed.

***Table 2.1**: Comparison of growth stages for WT Arabidopsis plants growing in microfluidic device and petri dish.*

Growth Stage	*Microfluidic device (days)*			*Plate (days)*
	Tap water	MS	Standard	Agar + MS[45]
Seed coat breakage	0.8±0.2	1.2±0.2	1.0±0.2	ND
Radicle emergence	1.2±0.2	1.7±0.3	1.2±0.2	1.3±0.4
Length of primary root (0.6 mm)	2.2±0.2	2.0±0.2	2.2±0.3	ND
Cotyledon &hypocotyl emergence	2.5±0.2	2.2±0.1	2.0±0.2	2.5±0.6
Cotyledons fully opened	3.0±0.2	3.0±0.1	3.0±0.2	3.0±0.5
2 rosette leaves	9.0±0.3	8.0±0.2	8.0±0.3	7.3±0.5

Note: All data exclude days of stratification.

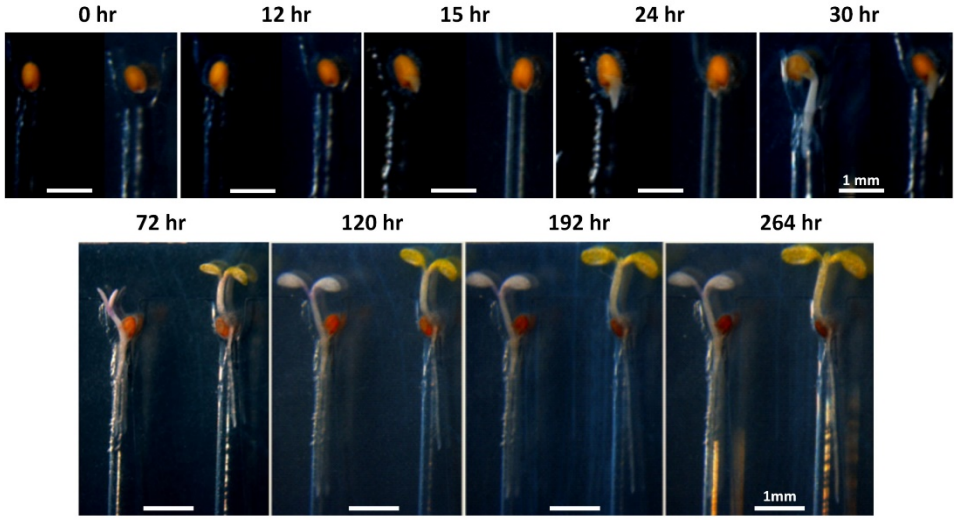

Figure 2.7 *Time course study of growth and development of WT Arabidopsis and immutans plants growing in standard medium in the vertical microfluidic device.*

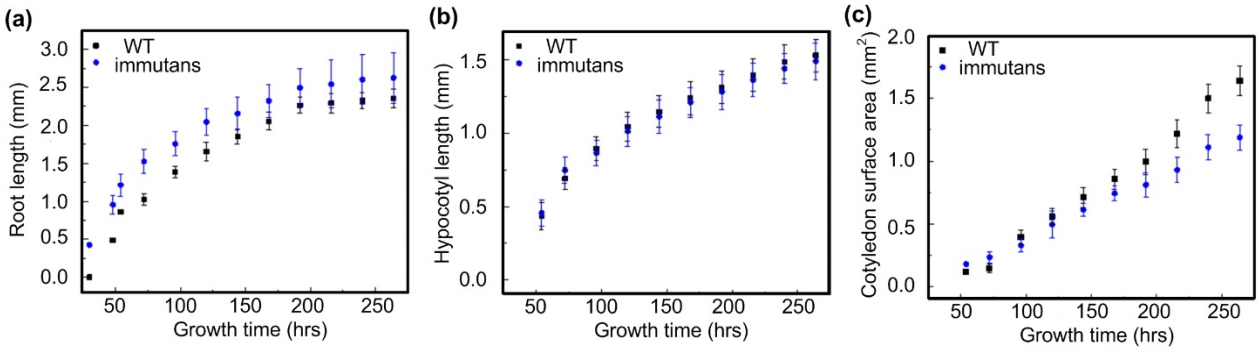

Figure 2.8 *Major phenotypic parameters of WT Arabidopsis and immutans mutant as a function of growth time, including (a) root length, (b) hypocotyl length, and (c) cotyledon surface area.*

2.3.3 Phenotyping of *Arabidopsis* mutants

We used a well-characterized carotenoid-deficient mutant, the *immutans* (*im*) mutant of *Arabidopsis* [47, 48] as an example to demonstrate general utility of the present device for phenotyping *Arabidopsis* plants, at the whole organismal as well as at the cellular level. The *immutans* mutant of *Arabidopsis* has green-white leaves due to a mutation in the nuclear recessive gene, *IMMUTANS* (*IM*). The *im* seeds have been previously shown to germinate similar to WT *Arabidopsis* under various light conditions. Our results show that *im* seeds germinate and growth under normal light conditions also within the device (Figure 2.7). However, we further show that

seed germination and radical protrusion occurs much earlier (~12 hrs) in *im* when compared to WT *Arabidopsis* (~20 hrs). Although the exact reason for this phenomenon is not known, it is clear that the new device enables more in-depth exploration and quantitation of the seed germination process in a real-time manner.

Depending on the light intensity, germinated seedlings of *im* give rise to green, green-white and/or white cotyledons, and leaves. An increase in light intensity increases white sector formation whereas low light conditions result in all-green plants. Consistent with previous reports, the cotyledons of *im* growing in-chip under normal light conditions are white and/or green with the green being somewhat lighter than WT. Seedlings with white cotyledons do not give rise to true leaves and are not viable after 11 days of growth in the hydroponic medium, whereas green coloured seedlings grow true leaves after ~194 hrs of growth (Figure 2.7). Under our growth conditions, *immutans* root and hypocotyl lengths are somewhat similar to WT (Figures 2.8a and b). But, the growth of the cotyledons slows down significantly after ~8 days of growth (Figure 2.8c). This is in agreement with the slower growth phenotype of *im* plants versus WT *Arabidopsis*.

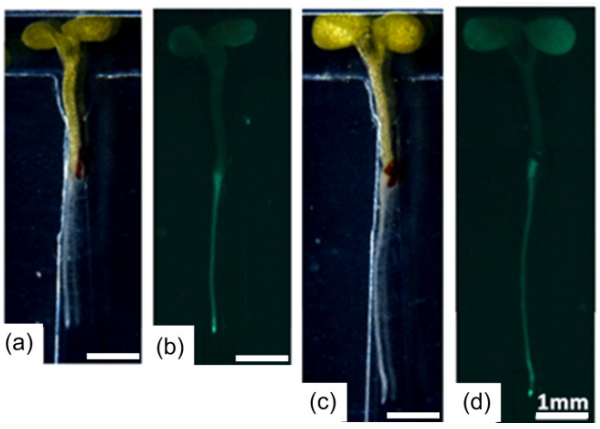

Figure 2.9 *Growth of IM: GFP plants in the vertical microfluidic device. Optical images (a, c) and fluorescence images (b, d) of 5-day and 7-day old seedlings, respectively.*

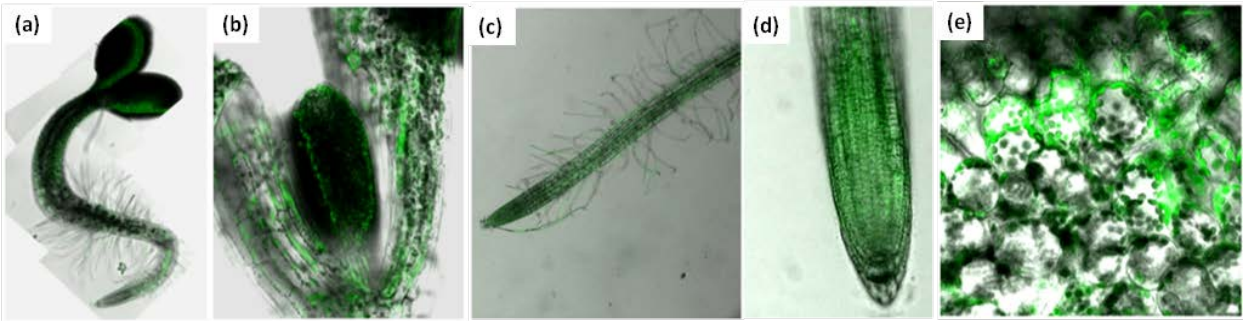

Figure 2.10 *Confocal laser scanning microscopy images for IM: GFP seedlings growing in the device. (a) 1-day old seedlings at a magnification of 10x. (b) 5-day old leaves at 20x. (c) 5-day old root at 10x. (d) 5-day old root tip at 40x. (e) 5-day old cotyledons at 80x.*

To obtain a more detailed cellular description of the *Arabidopsis im* phenotype, we applied confocal laser scanning microscopy (CLSM) and fluorescence stereomicroscopy (Leica M205FA), and performed *in vivo im* gene expression analyses using transgenic *IM*-GFP seeds/plants. *IM* promoter: β-glucoronidase (GUS) activity assays have previously shown that *IM* is expressed in all shoot and root tissues throughout development in *Arabidopsis* plants [48]. Similarly, in this study, we show *IM* promoter-GFP activity in 1 day, 5 day and 7 day old seedlings, with green fluorescence observed in all tissues including root, hypocotyl, and cotyledons (Figures 2.9 and 2.10). The 5 and 7 day old low resolution images were obtained with the fluorescence stereomicroscope equipped with a GFP filter set to image whole seedlings. This expression pattern was also maintained in developing leaves and roots, with increased expression observed in the root tips, as seen in the images in Figure 2.10. Moreover, *im* expression was found to be restricted to the chloroplasts within individual cells in green tissues (Figure 2.10e), which is consistent with the function of *IM* in plants. However, our results suggest that *im* is also expressed very early in the seed germination process. This is illustrated by the presence of green fluorescence first in regions around the embryo, even prior to seed coat breakage and radicle protrusion. Subsequently, the GFP fluorescence extends into the embryo and then into the protruding radicle as the seed germinates (Figures 2.11a-c). These results could not be observed previously with GUS activity assays,

perhaps due to the fact that the GFP reporter, unlike GUS reporter, allows nondestructive monitoring of cellular and sub-cellular activities without the need for sample preparation or the uptake of exogenous substrate. No GFP fluorescence was observed in non-transgenic WT control seeds and seedlings (data not shown).

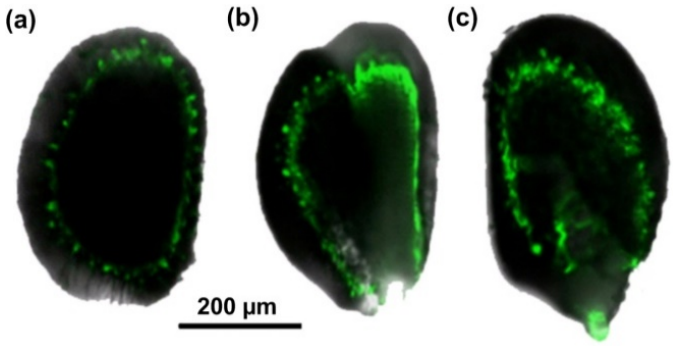

Figure 2.11 *Time course study of the seed germination process of IM: GFP seeds growing in the vertical device. (a) 0 hr , (b) 12 hrs , and (c) 18 hrs, after 2 day stratification.*

2.3.4 Plant-pathogen interactions

As another example of the utility of the present device for plant phenotyping, we show results from study of plant-pathogen interactions. Specifically, we demonstrate early interactions of *Phytophthora sojae* zoospores with wild-type *Arabidopsis* plants on the vertical microfluidic device. Fungal and oomycete pathogens such as *P. sojae* cause many destructive diseases of plants and genetic approaches pose difficulty for observing early phenotypic interactions between pathogens and plant roots and shoots [49, 50]. *P. sojae* zoospores were flowed into the vertical device with tap water at 24 hrs after the *Arabidopsis* seeds were trapped into the seed holding sites. The motile zoospores swam randomly until the root radicals emerged. High resolution images show that the zoospores accumulated down at the root tip and root hairs 5-10 hrs after their adhesion to the device (Figure 2.12a), and then, started invading the root and the shoot systems. At ~50 hrs, multiple dark brown spots were observed on the root, which are the symptoms of

apoptosis and cell death (Figure 2.12b). Several dark brown spots were also observed on the emerging cotyledons and hypocotyl at later stages of infection.

These spots were observed all the way toward the cotyledon, particularly at the intersection between the hypocotyl and root, indicating severe invasion and growth of zoospores inside these organs (Figures 2.12c and 2.12d).

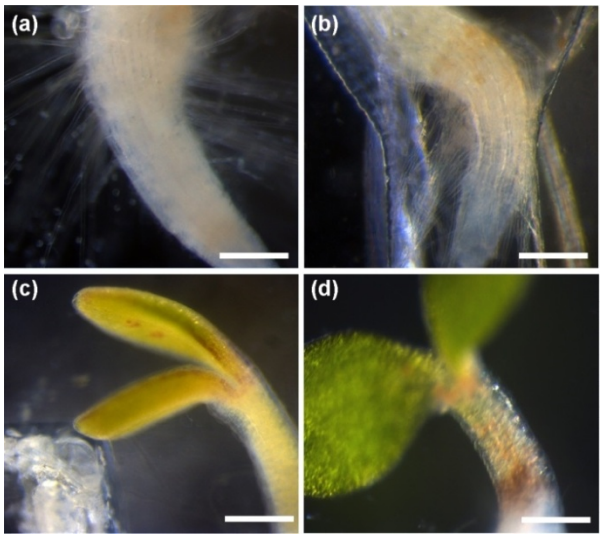

Figure 2.12 *(a) Formation of clusters of P. sojae zoospores on the root and root hairs of Arabidopsis plant, observed at 31 hrs. Dark brown spots on the root (b), cotyledon (c), and hypocotyl (d), observed at 50 hrs, 124 hrs, and 192 hrs respectively. Scale bars are 100 µm.*

2.3.5 Top-opened device for phenotyping *Arabidopsis* plants over a longer period of growth

In general, growth and development of WT *Arabidopsis* did not appear to be affected during its 11-day growth in the microfluidic device however, the device presented above used a closed-top design, which in turn limited the space of the channels above the seed holding site for shoot growth. Hence, the shoot phenotype could be monitored only through the stage of emergence of two rosette leaves on the plants. To accommodate developmental stages beyond the 2-leaf stage, we further created a top-open device in which the main channel above the seed holding site is open to air. This allowed for observing and recording cotyledon and leaf phenotypes over a longer period

of growth. Specifically, after *Arabidopsis* seeds were trapped, the top part of the channel above the seed holding sites was manually cut off by a razor blade. The level of growth medium in the device was adjusted by slowly flowing growth medium into the device as described earlier. Figure 2.13 shows *Arabidopsis* plants grown for a longer period of 15 days in the top-opened device in standard medium. The standard medium allowed similar and measurable growth of both shoot and root regions when compared to the other two media. Similar to observations made with the closed device, we observed radical emergence at ~32 hrs, and the hypocotyl and cotyledon emergence at ~54 hrs. The two early rosette leaves were observed at ~192 hrs, and then, more leaves emerged in the following days. The leaves were growing upward outside the channel while the roots were still elongating inside the channel. At the end of 15 days, we observed 5 rosette leaves. This is consistent with previous reports of plants growing on MS agar plates where 5 rosette leaves developed at 14.7±1.8 days (excluding 3 days of stratification) [46]. Thus, by simply opening up the main channel above the seed holding sites, the issue of limited growth space inside the device could be largely eliminated, which would make it possible to observe and record plant phenotypes through later growth stages, thus further expanding the utility of the device for plant phenotyping.

Figure 2.13 *Growth of a WT Arabidopsis thaliana plant over 15 days in the top-open vertical microfluidic device. The inset in the bottom-left corner shows cotyledons and leaves growing out of the vertical device.*

2.4 Conclusions

Systematic characterization of plant phenotypes remains a major challenge due to their large genome sizes, and tens of thousands of genes which respond differentially to various external and internal stimuli. Because of this inherent complexity, analyzing plant phenotypes on a large and multi-scale level with sufficient throughput, resolution and precision has been difficult and expensive. Previous work has addressed this challenge to some extent, but these studies were mainly focused on phenotyping of roots [32-36]. In this paper, we demonstrate the development of a new microfluidic device that is easy and cost-effective to use, and also enables seamless monitoring of both root and shoot phenotypes. We have provided a few examples and applications of the prototype device in this study. However, the device design can be flexibly changed to further enhance its application in the plant phenomics area. For example, with a top-open device (Figure

2.13), plants can be grown over longer periods of time, allowing for different and multiple types of *Arabidopsis* genotypes to be simultaneously characterized at the physiological, biochemical and molecular level, and at various stages of growth. In fact, the vertical device was able to sustain plant growth for over 4 weeks (data not shown).

Further research and development remain to be done to realize an ultimate screening platform for high-throughput plant phenotyping. Other microfluidic and microsystem techniques can be developed and integrated into this present microfluidic device. Through microfluidic tuning, flexible control over chemical concentration and composition in each growth channel can provide a large number of different nutrimental, chemical and biological environments for the plants growing in the microfluidic device. Different means of generating concentration gradients have been demonstrated [51-54], such as using universal concentration generator and on-chip dilution approach. Also, to control plant growth temperature, a simple thin-film resistive heater and temperature sensor can be integrated on the plant chip. These types of modifications will further expand the utility of the present device as multiple plants can be analysed under different environmental conditions in a single experiment. Furthermore, by employing an automated robotic imaging system, it is possible to take a large number of images for different plant growth regions in the devices. Therefore, we believe that the present vertical microfluidic plant chip technology can contribute towards establishing a powerful experimental framework for high-throughput and precise plant phenotyping, and will create a paradigm-shift in the plant phenomics area.

References

1. T. Thorsen, S. J. Maerkl and S. R. Quake, *Science*, 2002, **298**, 580-584.
2. J. Melin and S. R. Quake, *Annu. Rev. Biophys. Biomol. Struct.*, 2007, **36**, 213-231.
3. S. R. Quake and A. Scherer, *Science*, 2000, **290**, 1536-1540.
4. M. A. Unger, H. P. Chou, T. Thorsen, A. Scherer and S. R. Quake, *Science*, 2000, **288**, 113-116.

5. C. Bolle, A. Schneider and D. Leister, *Curr. Genomics*, 2011, **12**, 1-14.

6. T. Kuromori, T. Wada, A. Kamiya, M. Yuguchi, T. Yokouchi, Y. Imura, H. Takabe, T. Sakurai, K. Akiyama, T. Hirayama, K. Okada and K. Shinozaki, *Plant J.*, 2006, **47**, 640-651.

7. T. Kuromori, S. Takahashi, Y. Kondou, K. Shonozaki and M. Matsui, *Plant Cell Physiol.*, 2009, **50**, 1215-1231.

8. D. Houle, D. R. Govindaraju and S. Omholt, *Nat. Rev. Genet.*, 2010, **11**, 855-866.

9. R.T. Furbank and M. Tester, *Trends Plant Sci.*, 2011, **16**, 635-644.

10. P.K. Gupta, S. Rustgi and R.R. Mir, *Heredity*, 2008, **101**, 5-18.

11. J.D. Hoheise, *Nat. Rev. Genet.*, 2006, **7**, 200-210.

12. P. Liu, N. Koizuka, T. M. Homrichhausen, J. R. Hewitt, R. C. Martin, and H. Nonogaki, *Plant J.*, 2005, **41**, 936-944.

13. D. C. Boyes, A. M. Zayed, R. Ascenzi, A. J. MacCaskill, N. E. Hoffman, K. R. Davis and J. Gorlach, *Plant Cell*, 2001, **13**, 1499-1510.

14. A. Sessions, E. Burke, G. Presting, G. Aux, J. McElver, D. Patton, B. Dietrich, P. Ho, J. Bacwaden, C. Ko, J. D. Clarke, D. Cotton, D. Bullis, J. Snell, T. Miguel, D. Hutchison, B. Kimmerly, T. Mitzel, F. Katagiri, J. Glazebrook, M. Law and S. A. Goff, *Plant Cell*, 2002, **14**, 2985-2994.

15. M. R. Ponc1, P. Robles and J. L. Micol, *Mol. Gen. Genet.*, 1999, **261**, 408-415.

16. J. M. Alonso, A. N. Stepanova, T. J. Leisse, C. J. Kim, H. M. Chen, P. Shinn, D. K. Stevenson, J. Zimmerman, P. Barajas, R. Cheuk, C. Gadrinab, C. Heller, A. Jeske, E. Koesema, C. C. Meyers, H. Parker, L. Prednis, Y. Ansari, N. Choy, H. Deen, M. Geralt, N. Hazari, E. Hom, M. Karnes, C. Mulholland, R. Ndubaku, I. Schmidt, P. Guzman, L. Aguilar-Henonin, M. Schmid, D. Weigel, D. E. Carter, T. Marchand, E. Risseeuw, D. Brogden, A. Zeko, W. L. Crosby, C. C. Berry and J. R. Ecker, *Science*, 2003, **301**, 653-657.

17. Q. Dong, S. D. Schlueter and V. Brendel, *Nucleic Acids Res.*, 2004, **32** (suppl. 1), D354-D359.

18. R. Subramanian, E. P. Spalding and N. J. Ferrier, *Mach Vision Appl.*, 2013, **24**, 619-636.

19. P. Zimmermann, M. Hirsch-Hoffmann, L. Hennig and W. Gruissem, *Plant Physiol.*, 2004, **136**, 2621-2632.

20. J. K. C. Rose, S. Bashir, J. J. Giovannoni, M. M. Jahn and R. S. Saravanan, *Plant J.*, 2004, **39**, 715-733.

21. M. M. Bushey and J. W. Jorgenson, *Anal. Chem.*, 1990, **62**, 161-167.

22. V. Zabrouskov, L. Giacomelli, K. J. van Wijk and F. W. McLafferty, *Mol. Cell Proteomics*, 2003, **2**, 1253-1260.

23. L. W. Sumner, P. Mendes and R. A. Dixon, *Phytochemistry*, 2003, **62**, 817-836.

24. A. S. Iyer-Pascuzzi, O. Symonova, Y. Mileyko, Y. Hao, H. Belcher, J. Harer, J. S. Weitz and P. N. Benfey, *Plant Physiol.*, 2010, **152**, 1148-1157.

25. E. M. Lucchetta, J. H. Lee, L. A. Fu, N. H. Patel and R. F. Ismagilov, *Nature*, 2005, **434**, 1134-1138.

26. George M. Whitesides, *Nature*, 2006, **442**, 368-373.

27. N. Chronis, M. Zimmer and C. I. Bargmann, *Nat. Methods*, 2007, **4**, 727- 731.

28. K. Chung, M. M. Crane and H. Lu, *Nat. Methods*, 2008, **5**, 637-643.

29. P. Liu, R. J. Martin and L. Dong, *Lab Chip*, 2013, **13**, 650-661.

30. P. Liu, D. Mao, R. J. Martin and L. Dong, *Lab Chip*, 2012, **12**, 3458-3466.

31. C. G. Agudelo, A. S. Nezhad, M. Ghanbari, M. Naghavi, M. Packirisamy and A. Geitmann, *Plant J.*, 2013, **73**, 1057-1068.

32. G. Grossmann, W. Guo, D. W. Ehrhardt, W. B. Frommer, R. V. Sit, S. R. Quake and M. Meier, *Plant Cell*, 2011, **23**, 4234-4240.

33. H. Jiang, Y. Jiao, M. R. Maneesha and L. Dong, *J. Nanosci. Nanotechnol.*, 2012, **12**, 6333-6339.

34. M. Meier, E. M. Lucchetta and R. F. Ismagilov, *Lab Chip*, 2010, **10**, 2147-2153.

35. W. Busch, T. M. Brad, M. Bradley, D. L. Mace, R. W. Twigg, J. Jung, I. Pruteanu-Malinici, S. J. Kennedy, G. K. Fricke, R. L. Clark, U. Ohler and P. N. Benfey, *Nat. Methods*, 2012, **9**, 1101-1106.

36. A. Parashar and S. Pandey, *Appl. Phys .Lett*., 2011, **98**, 263703.

37. D. B. Weibel, W. R. DiLuzio and G. M. Whitesides, *Nat. Rev.Microbiol*., 2007, **5**, 209-218.

38. A. S. Reyhani, J. Kaplinsky, E. Burgin, M. Novakova, A. J. deMello, R. H. Templer, P. Parker, M. A. Neil, O. Ces, P. French, K. R. Willison and D. Klug, *Lab Chip* , 2011, **11**, 1256-1261.

39. D. D. Carlo, L. Y. Wu and L. P. Lee, *Lab Chip*, 2006, **6**, 1445-1449.

40. P. Berthomieu, G. Conéjéro, A. Nublat, W. J. Brackenbury, C. Lambert, C. Savio, N. Uozumi, S. Oiki, K. Yamada, F. Cellier, F. Gosti, T. Simonneau, P. A. Essah, M. Tester, A. A. Véry, H. Sentenac and F. Casse, *EMBO J.*, 2003, **22**, 2004-2014.

41. P. P. Liu, N. Koizuka, T. M. Homrichhausen, J. R. Hewitt, R. C. Martin and H. Nonogaki, *Plant J.*, 2005, **41**, 936-944.

42. T. Ingestad and G. I. Agren, *Ecol.l Appl.*, 1991, **1**, 168-174.

43. H. Zhang, A. J. Jennings and B. G. Forde, *J. Exp. Bot.*, 2000, **51**, 51-59.

44. H. Zhang and B. G. Forde, *Science*, 1998, **279**, 407-409.

45. H. Zhang, A. Jennings, P. W. Barlow and B. G. Forde, *Proc. Natl. Acad. Sci. U.S.A.*, 1999, **96**, 6529-6534.

46. D. C. Boyes, A. M. Zayed and R. Ascenzi, *Plant Cell*, 2001, **13**, 1499-1510.

47. C. M. Wetzel, C. Z. Jiang, L. J. Meehan, D. F. Voytas and S. R. Rodermel, *Plant J.*, 1994, **6**, 161-175.

48. M. Aluru, H. Bae, D. Wu and S. Rodermel, *Plant Physiol.*, 2001, **127**, 67-77.

49. W. Grunewald, G. van Noorden, G. van Isterdael, T. Beeckman, G. Gheysen and U. Mathesius, *Plant Cell*, 2009, **21**, 2553-2562.

50. N. Wuyts, G. Lognay, R. Swennen and D. De Waele, *J. Exp. Biol.*, 2006, **57**, 2825-2835.

51. C. Hao and M. J. Christian, *Appl. Phys. Lett.*, 2004, **84**, 2193-2195.

52. N. L. Jeon, S. K. W. Dertinger, D. T. Chiu, I. S. Choi, A. D. Stroock and G. M. Whitesides, *Langmuir*, 2000, **16**, 8311-8316.

53. X. Jiang, Q. Xu, S. K. W Dertinger, A. D. Stroock, T. M. Fu and G. M. Whitesides, *Anal. Chem.*, 2005, **77**, 2338-2347.

54. D. Irimia D, D. A. Geba and M. Toner, *Anal. Chem.*, 2006, **78**, 3472-3477.

CHAPTER 3. ELECTROSPUN NANOFIBROUS MEMBRANSE FOR TEMPERATURE REGULATION OF MICROFLUIDIC SEED GROWTH CHIPS

A paper published in *Journal of Nanoscience and Nanotechnology*

Huawei Jiang, Yueyi Jiao, Maneesha R Aluru, and Liang Dong

Abstract

This paper reports a simple and effective approach to control statistical pore size distributions within electrospun nanofibrous membranes (ENMs), by choosing appropriate spinning times of electrospinning deposition. Mean pore diameter of ENMs decreases exponentially with increasing spinning time. This pore-size control method is demonstrated to regulate amount of heat energy reaching microfluidic seed growth chips (SGC) and thus growth temperature of seeds on the chips, without using sophisticated semiconductor manufacturing techniques or additional on-chip electronic circuits. Decreasing mean pore diameter of ENMs causes to decrease the on-chip temperature, following a second-order polynomial trend. Phenotypic study based on real-time observation of root architecture is conducted on multiple SGCs under various temperature conditions obtained by using ENMs with different pore size distributions.

3.1 Introduction

Electrospinning provides a simple, inexpensive and high throughput means to produce nanofibers and fibrous membranes from polymers or polymer blends [1]. This electrostatic processing method utilizes a high strength electric field to draw a charged polymer solution into a liquid jet. The jet experiences thinning, bending and stretching effects, during which volatile solvent is evaporated from the jet. Solid nanofibers are collected on a collector [2]. Electrospun nanofibrous membranes (ENMs) have remarkable features of large surface-area-to-volume ratio

due to small fiber diameter [3, 4]. Porous structure of ENMs has been harnessed to find many applications such as in filtration [5], tissue engineering [6], and energy harvesting [7]. For example, electrospun filtration membranes capture particles and permit gas transport, depending largely on pore size of membranes [5]. In tissue engineering, electrospun scaffold constructs provide porous network of interconnected pores to enable rapid tissue growth through pores for tissue regeneration [6]. High porosity also allows enhancing penetration of viscous gel and polymer electrolytes, making ENMs an excellent candidate for potential supercapacitor material [7]. Research in the field of electrospun fibers is still rapidly expanding.

Seed development is the first critical process in life cycle of plants. Root growth, particularly during seed germination and seedling development, is influenced by a variety of environmental stimuli such as chemicals and climate conditions. Genetic analysis of roots is often employed to identify genes that are sensitive to different stimuli [8], while phenotypic analysis of roots provides their morphological changes under these stimuli [9]. Conventional phenotypic analysis relies on culturing seeds in soil pots and measuring root dimensions [10], which may suffer from two limitations. First, spatial resolution of root morphology is low on the millimeter scale [11]. Second, flexible creation of environmental conditions is difficult since it involves using relatively bulky seed culture facility or even greenhouse [12-14]. Recently, transparent microfluidic channels have been used to study seed root development in different growth media with the help of a high resolution microscope [11]. Despite this, the microchannel approach has rarely been used to study influence of climate conditions such as temperature on seed development. Generally, temperature regulation on microfluidic chips (e.g., polymerase chain reaction chips) is realized by electric current through thin film resistors. These on-chip resistors are fabricated by sophisticated semiconductor manufacturing techniques such as evaporation, photolithography,

etching, and wire bonding [15, 16]. Additional electronic circuits are also needed to control heat generations of the resistors [15].

In this paper, we develop a simple and cost-effective approach to create desired temperature conditions for microfluidic seed growth chips (SGCs) by incorporating ENMs with the SGCs (Figure 3.1a). We hypothesize that by means of adjusting spinning time of electrospinning deposition, it is possible to control statistically pore size distributions of ENMs, changing amount of thermal energy (from an external source) reaching the SGC and thus temperature conditions of seeds growing in the SGC. Figures 3.1c-d display a schematic for the SGC. The SGC consists of multiple channels with total twenty seed sites. Each seed site contains a single seed. The channels are 1000 μm wide and 250 μm deep. Seed growth medium is loaded into the channels at an inlet of the device. Electrospinning is used to deposit an ENM on a glass slide with a specific spinning time. The ENM is placed underneath the SGC above a thermal radiation source. Seed roots develop laterally into the channel (Figure 3.1b). Microscopic monitoring of multiple seeds in parallel at a single seed level provides a reliable data set and thus an improved statistic.

3.2 Experimental details

Different ENMs of polyethylene oxide (PEO, MW = 10,000, Sigma) are electrospun on glass slides, to study influences of spinning time on temperature at the seed sites of the SGC and internal structure of ENMs. A PEO precursor is prepared by dissolving PEO powder in 70% (V/V) ethanol (diluted with deionized water) with the weight ratio of 0.3:0.7. The mixed solution is magnetically stirred for 6 h at room temperature and then filtered using a 200-nm-diameter sterile syringe filter (Corning) to remove particulate materials. The precursor solution is loaded into a 3 mL syringe (BD Bioscience). The syringe is attached to a syringe pump (KDS210, Kd Scientific).

A stainless steel needle (18 gauge; Howard Electronic Instruments) is screwed onto the syringe and connected to a high DC voltage power supply (Gamma High Voltage Research). To attract nanofibers onto the glass slide, an aluminum foil is electrically grounded and placed right below the slide. The distance between the tip of the needle and the slide is 8 cm. The voltage of 10 kV is applied to the needle. The precursor solution is driven by the pump under the flow rate of 1 mL/h. The spinning time is varied from 1 to 35 minutes. The diameter of the PEO nanofibers obtained is 563 ± 114 nm (Figure 3.1a).

The SGCs used here are made of polydimethylsiloxane (PDMS) by soft-lithography technique [17]. A silicon (Si) wafer is patterned with SU-8 photoresist (Microchem) to create a master mold for microfluidic channels. A pre-polymer mixture of polydimethylsiloxane or PDMS (Sylgard 184, Dow Corning) and its curing agent with a weight ratio of 10:1 is poured onto the master mold and was thermally cured. Then, the hardened PDMS polymer is pealed from the master mold. To allow flowing growth media into and out of the device, inlet and outlet ports of the device are manually punched with a mechanical puncher. Seed sites are formed by punching 2-mm diameter holes in the PDMS until the channels are reached. Subsequently, the PDMS slab is bonded to a glass slide through oxygen plasma treatment. Lastly, the glass slide coated with electrospun nanofibrous membrane is placed beneath the PDMS slab. Thus, the microfluidic SGC is formed. A replicate molding process allowed fabricating multiple SGCs.

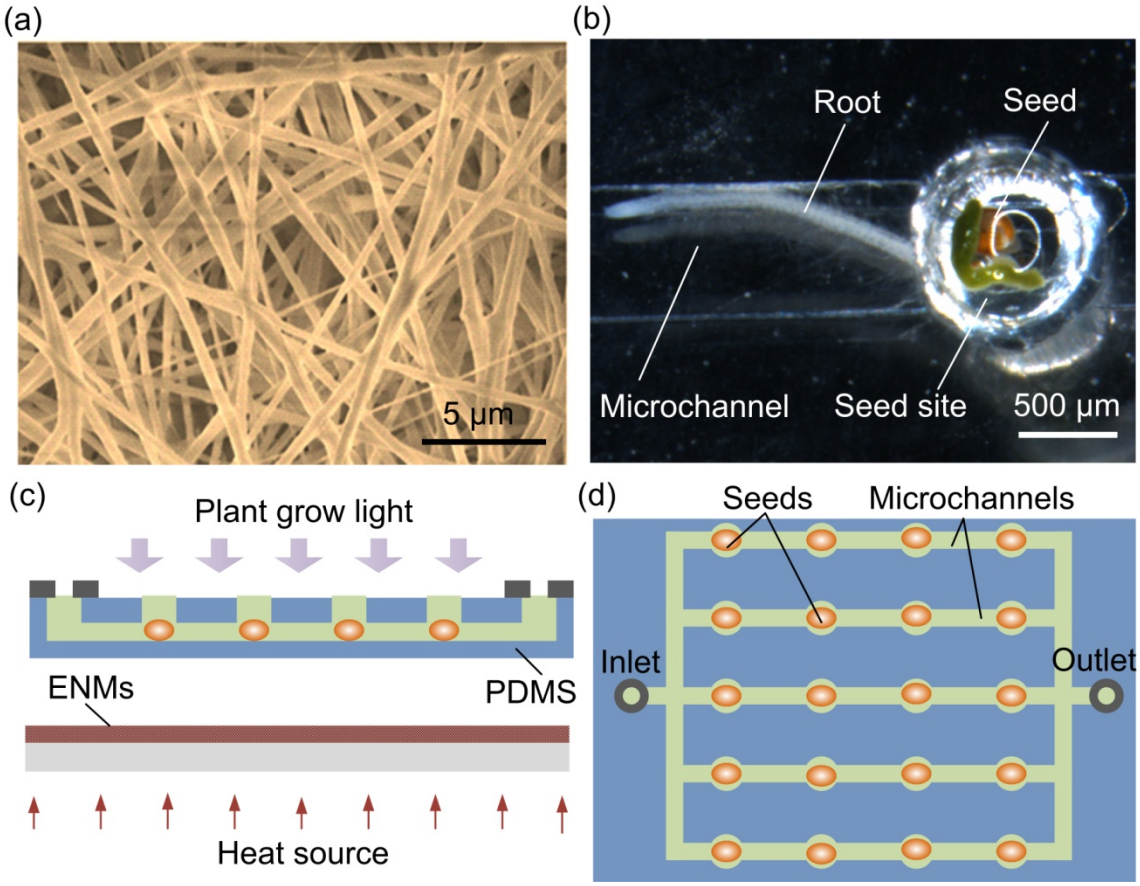

Figure 3.1 *(a) A PEO ENM fabricated on a glass slide by electrospinning. The pore size distribution of the ENM is controlled by spinning time. (b) Optical image for root development of an Arabidopsis seed growing in the SGC. (c) Cross-sectional view of the SGC. The ENM with a specific pore size distribution is placed below the SGC above a thermal radiation source. Plant grow light illumination comes from the top. (d) Top view of the SGC.*

Arabidopsis is popular as a model organism in plant biology and genetics. We use a var2-5 mutant of *Arabidopsis* as model seeds to grow in the fabricated SGCs. The seeds are sterilized by treating in a 5% sodium hypochlorite solution, followed by washing three times with deionized water. The seeds are then put at 4 ºC for 48 hours to germinate at the same time. After that, they are manually loaded into individual seed sites in the channels filled up with water. A standard cooled plant grow light source is placed 20 cm above the SGC, with the light intensity of 95 $\mu E/m^2s$. A standard low-light infrared heater (emitting power 50 W) is placed 30 cm below the SGC. The glass slide coated with the ENM is located 15 cm above the infrared heater. A

stereomicroscope (M205 FA, Leica) with a camera (QIC-F-CLR-12-C, QImaging) captures images of seed roots once a day over a period of 7 days.

3.3 Results and discussion

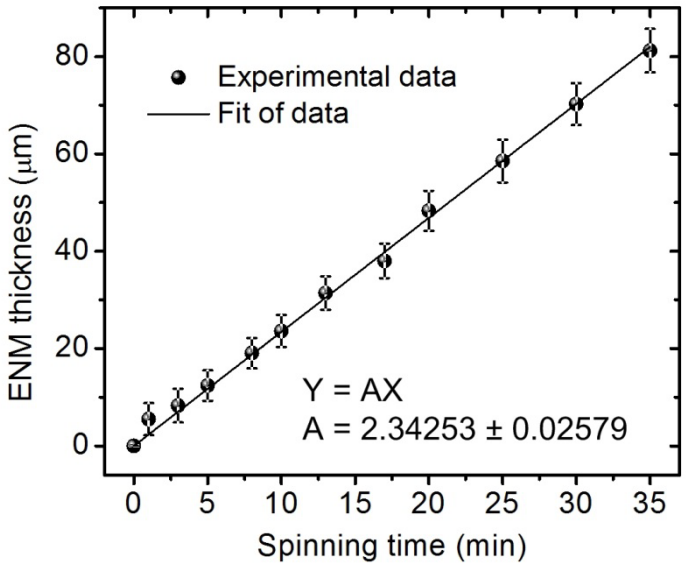

Figure 3.2 *Thickness of the ENM as a function of spinning time*

Figure 3.2 shows a linear relationship between the ENM thickness and spinning time. By fitting the experimental data to a linear function, the deposition rate for the ENM is found to be approximately 2.34 μm per minute. We then examine temperature uniformity at the seed sites of the SGC that incorporates the prefabricated different PEO ENMs. Type-K thermocouples are inserted to six seed sites selected (four at the corners and two near the center of the SGC). Temperature values are read by using temperature monitors (HH501DK, Omega). It is found that these seed sites experience the same time-temperature profiles and the relative temperature variation is as small as less than 3%. Figure 3.3a displays temperature rise profiles at the seed site located near the center of the SGC incorporating different ENMs. In each curve, the temperature increases rapidly before reaching an equilibrium temperature point, while increasing rate decreases gradually. As the spinning time increases from 1 to 35 minutes, the final steady state temperature

T_s is decreased from 37.2 to 25.3 ºC. The thermal response time of the SGC (defined as time to reach 63% of final steady state temperature [18]) is about 12.5 minutes, which seems little dependent on the spinning time and thus the thickness of the ENM (Figure 3.3b).

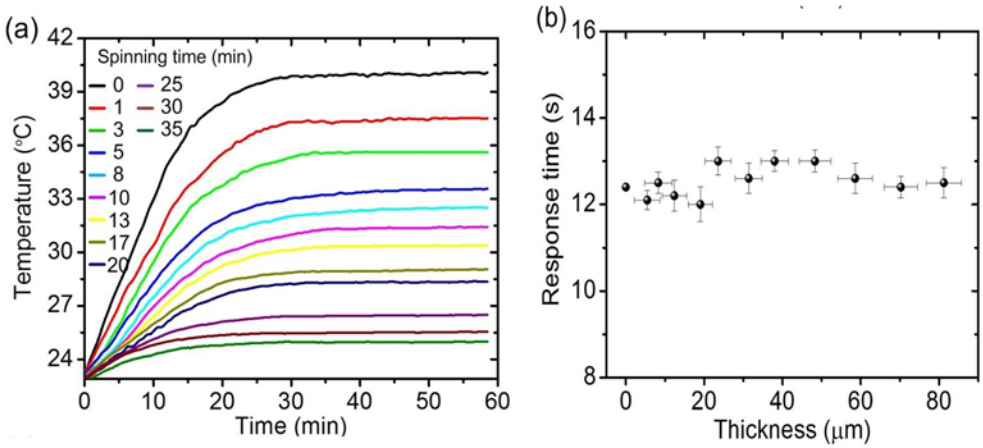

Figure 3.3 *(a) Temperature rise profiles measured at the seed sites of the SGC incorporating different ENMs. These membranes are distinguished by spinning time. (b) Thermal response time of the SGC as a function of thickness of the ENM.*

Figure 3.4a shows the tendency of decreasing temperature measured at the SGC as a function of the thickness of the ENM (black dotted plot). Here, each temperature data is obtained by averaging the results measured with five ENMs having the same spinning time. An important observation is that the relative deviation of temperature is as low as about 3.4%, indicating a considerably high temperature reproducibility of the ENM approach. The possible explanation of the temperature regulation is as follows. Because the ENM is not in direct contact with the SGC, thermal radiation from the heat source to the device is the dominant heat transfer mechanism. We speculate that by stacking a different number of nanofiber layers, statistical pore diameter distributions of the ENMs can be changed with changing spinning time. The longer the spinning time, the thicker the ENM and the smaller the mean pore size, given that the fiber diameter in the different ENMs is the same. Probably, thermal radiation from the heat source experiences a more significant scattering and dispersion effect in a small mean pore size ENM than that it does in a

large mean pore size ENM. Thus, when a thick ENM is used, a less amount of thermal energy is received at the device surface and thus a lower temperature is found at the seed sites.

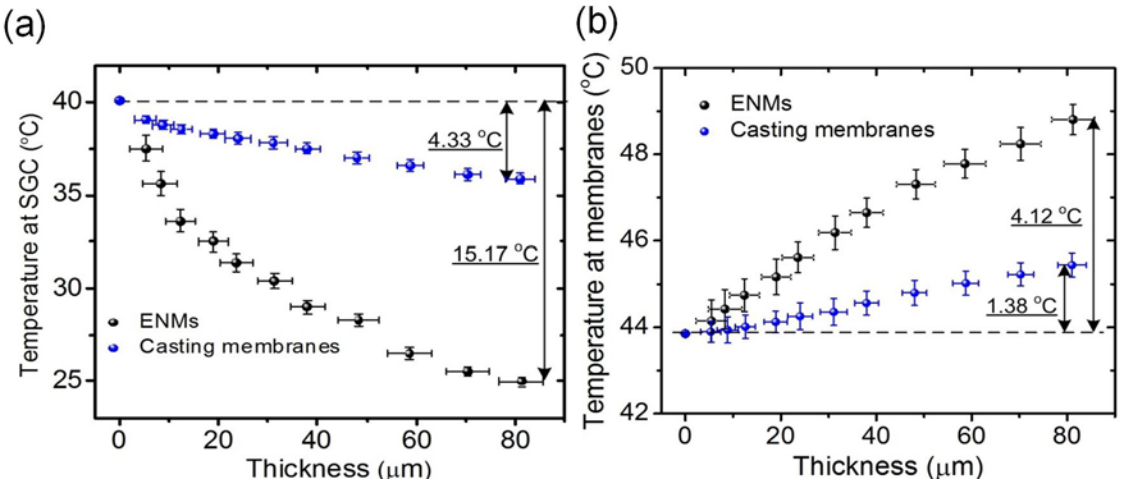

Figure 3.4 *(a) Temperature measured at the SGC as a function of thickness of the PEO ENM and casting membrane. (b) Temperature measured at the PEO ENM and casting membrane as a function of thickness of the PEO ENM and casting membrane.*

In fact, the thickness and pore size of the ENMs are two linked variables. As shown later, increasing the thickness of the ENM leads to decreasing its mean pore size. Thus, it is almost impossible to change membrane thickness while keeping membrane pore size unchanged, nor to change membrane pore size while keeping membrane thickness unchanged. This makes it difficult to directly determine the contributions from the thickness or the pore size of the ENM for regulating the temperature at the SGC. Nevertheless, we conduct an experiment with casting PEO membranes. The precursor solution for the casting PEO membranes has the same composition as that for the ENMs mentioned early. Thickness of different casting membranes is identical to that of the ENMs and controlled by height of a mold made of SU-8 photoresist. Here, our attempt is to obtain a temperature change at the SGC with the casting PEO membrane ($\Delta T'_{SGC}$), and then, subtract $\Delta T'_{SGC}$ from a temperature change at the SGC with the ENM (ΔT_{SGC}). Roughly, ΔT_{SGC} –

$\Delta T'_{SGC}$ can be used to represent a temperature change at the SGC attributed to the pore size of the ENM.

To this end, we measure the respective temperatures at the cast membrane ($T_{cast\text{-}m}$) and at the ENM (T_{ENM}). It is found in Figure 3.4b that increasing the thickness of the casting membranes up to 82 μm results in only a minor increase of 1.38 ºC in $T_{cast\text{-}m}$, but a large increase of 4.12 ºC in T_{ENM}. The result here provides supportive evidence for the fact that the porous structure of the ENM can contribute to regulate the amount of electromagnetic waves absorbed by and transmitted through the ENM. As discussed further later, the mean pore size of thick ENMs is smaller than that of thinner ENMs. Consequently, electromagnetic waves are scattered more strongly and reflected many more times, and thus, absorbed more efficiently when they interact with the large pore-size ENMs than they are when they interact with the small pore-size ones. Also, as seen in Figure 3.4a, the local temperature at the SGC (T_{SGC}) decreases very slightly ($\Delta T'_{SGC}$ = 4.33 ºC) with increasing thickness of the casting membrane, but significantly (ΔT_{SGC} = 15.17 ºC) with increasing thickness of the ENM. This further demonstrates the capability of the ENMs in regulating the amount of thermal radiation power from the source to the SGC. Therefore, the thickness variation-induced temperature change roughly counts 33.3% and 28.5% of the total temperature change at the ENM and at the SGC, respectively. The majority of the temperature change at the ENM and the SGC is attributed to the variation in the porous structure of the ENM.

To further verify the speculation of the relationship between the temperature regulation and the porous structure of the ENMs, we measure the mean pore diameter distributions of the ENMs by using a capillary flow porometer (CFP-1100 AEX, PMI). To obtain a reliable data set, each group has three ENMs (named A1 to 3, B1 to 3, and so forth) with the same spinning time. For the A1-3 group (spinning time: 1 min; Figure 3.5a), the measurement result reveals that although the

pore diameter ranges widely from 0.89 to 9.12 µm, about 35 % of pore diameter falls between 4 µm to 4.5 µm with the mean pore diameter of 4.37 µm. Interestingly, both the pore diameter range and the mean pore diameter are decreased with increasing spinning time. For the D1-3 group (spinning time: 35 mins; Figure 3.5d), the pore diameter distribution is concentrated in a narrower band between 0.05 to 0.5 µm and about 40% of pore diameter falls in the range of 0.2 to 0.25 µm with the mean pore diameter of 0.3 µm. The histograms for the three samples of each group confirm that they have a consistent distribution of pore diameters. It is revealed in Figure 3.5e that the mean pore diameter of the ENMs is decreased exponentially with the spinning time. Also, the standard deviation of pore diameter from the mean pore diameter is found to decrease with increasing spinning time. By combining the results shown in Figure 3.2, Figure 3.4a (black dotted plot), and Figure 3.5e, it is confirmed in Figure 3.5f that decreasing (increasing) mean pore diameter of the ENM causes to decrease (increase) the temperature at the seed sites and their relationship can be described by the second-order polynomial fit inserted in Figure 3.5f.

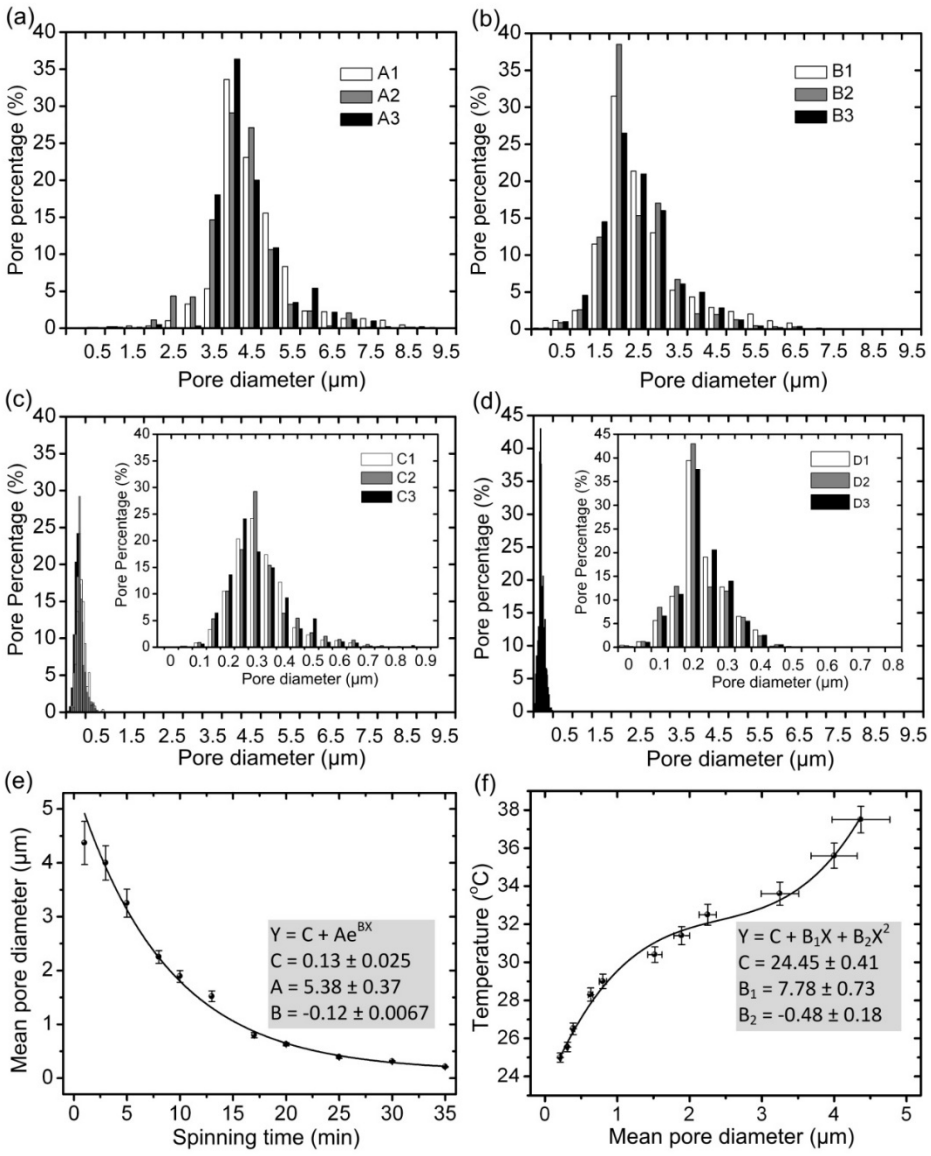

Figure 3.5 *Histograms of pore diameter distributions in the ENMs with different spinning times: t = 1 min (a), 8 mins (b), 25 mins (c), and 35 mins (d). (e) Mean pore diameter of ENMs as a function of spinning time. (f) Mean temperature values at the seed sites of the SGC as a function of mean pore diameter of the ENMs.*

Figure 3.6a presents a typical root development process of *Arabidopsis* seed growing in the SGC over a 7-day period. The growth temperature of 28.2 ºC is determined by the ENM with the spinning time of 20 minutes. The root grows rapidly in the first three days; afterwards the growing speed slows down. To demonstrate creating various temperature points simultaneously in multiple SGCs under a heat source, an array of six SGCs are fabricated to grow *Arabidopsis* seeds,

with each incorporating a different ENM. Figures 3.6b-c plot the root growth parameters (diameter and length) of *Arabidopsis* seeds growing at different temperatures. High temperatures cause to slow down root growth significantly. The final root length at the end of the observation period is shorter for the seeds under high temperature conditions than those under low temperature conditions. But the root diameter is decreased very little with the increase of the growth temperature. We point out that the root development of *Arabidopsis* seeds in the SGC follows exactly the same tendency as that in a petri plate (not shown in Figure 3.6). Thus, the SGCs incorporating the ENMs are suitable for phonemic study of seed development. Here, the temperature conditions of seeds are created without using any semiconductor manufacturing techniques or additional electronic circuits.

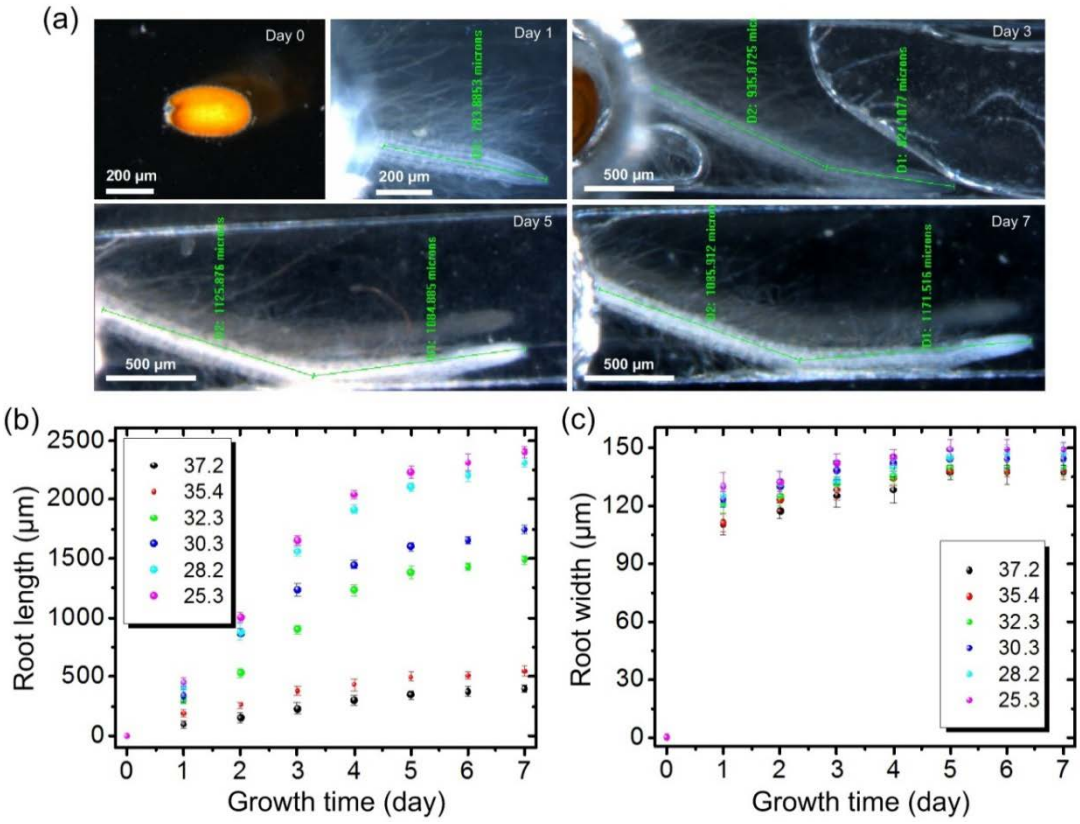

Figure 3.6 *(a) A typical root development procedure of an Arabidopsis seed growing in the SGC at 28.2 ºC obtained by using the PEO ENM with the spinning time of 20 minutes. (b, c) Root length and diameter of the seed as a function of growth time at different temperatures determined by the spinning time for depositing ENMs.*

While this work has demonstrated experimentally a simple and effective approach to control the pore size distributions of the PEO ENMs and its application to regulate the growth temperature of the SGCs, there is much work to be done in the future. For example, many factors and their interplays contribute to determine temperature conditions in the SGC, including scattering, reflection, and absorption effects of electromagnetic waves (from the heat source), thermal radiation from the ENM, and heat transfer from the heat source to the membrane to the device. Having a theoretical model for modeling uneven pore size distribution in an ENM will allow us to theoretically analyze and understand interactions between electromagnetic waves and ENMs and to elucidate how each factor can exert influence to determine a final temperature condition obtained in the SGC. Actually, there is no specific reason of choosing the PEO ENMs as the demonstration in this work. Many other polymers can be electrospun to form ENMs for regulating the temperature at the SGCs. Deposition rate and diameter of nanofiber products can be affected by many other factors such as material selection and process conditions (e.g., voltage, distance between spinneret and collector, temperature, humidity, etc.) of the electrospinning. However, the concept will remain the same: the temperature at the SGC can be regulated, simply by changing the spinning time (or the thickness of ENMs).

3.4 Conclusions

In conclusion, we have demonstrated that by changing the spinning time of electrospinning deposition, it is possible to control statistically the pore size distributions of ENMs. The mean pore diameter is decreased exponentially from several micrometers to a couple of hundred nanometers, with increasing spinning time. The decrease of the mean pore size may possibly cause to attenuate the amount of heat energy from a remote heat source. This pore-size regulation approach enables

us to create various temperature conditions on the microfluidic chips for phonemic analysis of seed growth.

References

1. D. Li and Y. N. Xia, *Adv. Mater.*, 2004, **16**, 1151-1170.

2. J. Miao, M. Miyauchi, T. J. Simmons, J. S. Dordick and R. J. Linhardt, *J. Nanosci. Nanotechnol.*, 2010, **10**, 5507-5519.

3. J. Doshi and D. H. Reneker, *J.Electrostat.*, 1995, **35**, 151-160.

4. Z. M. Huang, Y. Z. Zhang, M. Kotaki and S. Ramakrishna, *Compos. Sci. Technol.*, 2003, **63**, 2223-2253.

5. P. Gibson, H. Schreuder-Gibson and D. Rivin, *Colloid Surf. A*, 2001, **187**, 469-481.

6. W. J. Li, C. T. Laurencin, E. J. Caterson, R. S. Tuan and F. K. Ko, *J. Biomed. Mater. Res.*, 2002, **60**, 613-621.

7. D. S. Kim, H. B. Park, J. W. Rhim and Y. M. Lee, *J. Membrane Sci.*, 2004, **240**, 37-48.

8. P. Achard, H. Cheng, L. De Grauwe, J. Decat, H. Schoutteten, T. Moritz, D. Van der Straeten, J. R. Peng and N. P. Harberd, *Science*, 2006, **311**, 91-94.

9. D. C. Boyes, A. M. Zayed, R. Ascenzi, A. J. McCaskill, N. E. Hoffman, K. R. Davis and J. Gorlach, *Plant Cell*, 2001, **13**, 1499-1510.

10. C. S. Buer, J. Masle and G. O. Wasteneys, *Plant Cell Physiol.*, 2000, **41**, 1164-1170.

11. M. Meier, E. M. Lucchetta and R. F. Ismagilov, *Lab Chip*, 2010, **10**, 2147-2153.

12. L. M. Mortensen, *Sci. Hortic.*, 1986, **29**, 301-307.

13. J. M. Aaslyng, J. B. Lund, N. Ehler and E. Rosenqvist, *Environ. Model. Softw.*, 2003, **18**, 657-666.

14. G. D. Pasgianos, K. G. Arvanitis, P. Polycarpou and N. Sigrimis, *Comput. Electron. Agric.*, 2003, **40**, 153-177.

15. D. S. Yoon, Y. S. Lee, Y. Lee, H. J. Cho, S. W. Sung, K. W. Oh, J. Cha and G. Lim, *J. Micromech. Microeng,*, 2002, **12**, 813-823.

16. D. J. Sadler, R. Changrani, P. Roberts, C. F. Chou and F. Zenhausern, *IEEE Trans. Compon. Packag.*, 2003, **26**, 309-316.

17. Y. N. Xia and G. M. Whitesides, *Annu. Rev. Mater. Sci.*, 1998, **28**, 153-184.

18. R. W. Lewis, P. Nithiarasu, and K. N. Seetharamu, *John Wiley & Sons (West Sussex, England)*, 2004.

CHAPTER 4. PLANT MINIATURE GREENHOUSE

A paper to be submitted to *PLOS One*

Huawei Jiang, Xinran, Wang, Maneesha R Aluru, and Liang Dong

Abstract

We report on the development of a miniature greenhouse for phenotyping *Arabidopsis thaliana* plants. This greenhouse is able to flexibly create and adjust a set of environment conditions including temperature and light intensity through electronic circuits. The device uses light emitting diodes (LEDs) as a light source, combines a thermoelectric cooler and a heater to realize tuning internal growth temperature, and uses a liquid crystal shutter to allow automatic imaging from outside of the device when needed. This technology has a potential to extend to an array of miniature greenhouses for realizing plant phenotyping on a large and multi-scale level with sufficient throughput.

4.1 Introduction

Seed germination and seedling development are the critical processes in life cycle of plants. They are influenced by many environmental factors, such as light intensity, temperature, humidity, and soil microbes. For example, plants are able to select microorganisms parasitized in the rhizosphere, which influence the plant physiology. They also acquire nutrients from soil to complete their necessary growth process. In addition, plants need suitable temperature, light, and humidity conditions to produce and emit small chemicals that ensure their photosynthetic process to be completed successfully [1-9].

Most of the existing devices and instruments have been built for identifying and analyzing genome [10, 11]. Thus, plentiful data from genomics studies is available from several public databases [12-18]. As a foundation of biology, plant phenomics and genomics are two inseparable aspects [3, 19]. The field of plant phenomics in particular, deals with large-scale quantitative studies of plant phenotypes, and with linking these complex phenotypic traits to individual genes or a collection of genes. However, characterization of the complete phenome has been confronted with a difficult challenge, because of smaller genomes such as *Arabidopsis thaliana* contain tens of thousands of genes [20-23].

Conventional phenotypic analysis of plants may suffer from low spatial morphological resolution at the millimeter scale and low throughput of obtaining phenotype information [24-30]. The benefits of emerging microfluidic devices include high throughput and improved data statistic, reduction costs, and avoidance of contamination. Particularly, microfluidics has provided powerful platforms to interrogate whole multicellular organisms such as *Drosophila melanogaster* and *Caenorhabditis elegans* [10, 11, 31, 32]. Recently, several excellent root chips (e.g., RootChip, RootArray and TipChip) have been developed for characterizing phenotypic changes of multiple roots in different study environments [33-39]. In Chapter 2, we have developed transparent microfluidic devices capable of germinating and growing multiple *Arabidopsis thaliana* seeds at different growth conditions [40].

Although the aforementioned efforts have shown the potential of using microfluidics for plant phenomics analysis, phenotypic measurements on these devices are restricted to single environment only. To the best of our knowledge, measurements at different growth environments have not been achieved. Here in this Chapter, we report on the development of a miniature greenhouse, in conjunction with the plant chips described in Chapter 2, to facilitate phenotypic

assays of multiple plants at different light intensity and temperature to observe the whole organismal level, including seed germination, plant root growth, and shoot growth.

4.2 Design of miniature greenhouse

4.2.1 The initial design of miniature greenhouse

A miniature greenhouse is designed to control environmental conditions for plants growing on the plant chips. This device shown in Figure 4.1 consists of three main parts: a growth chamber, a temperature controller, a light intensity controller, and an imaging system. The following section will give an introduction about each component.

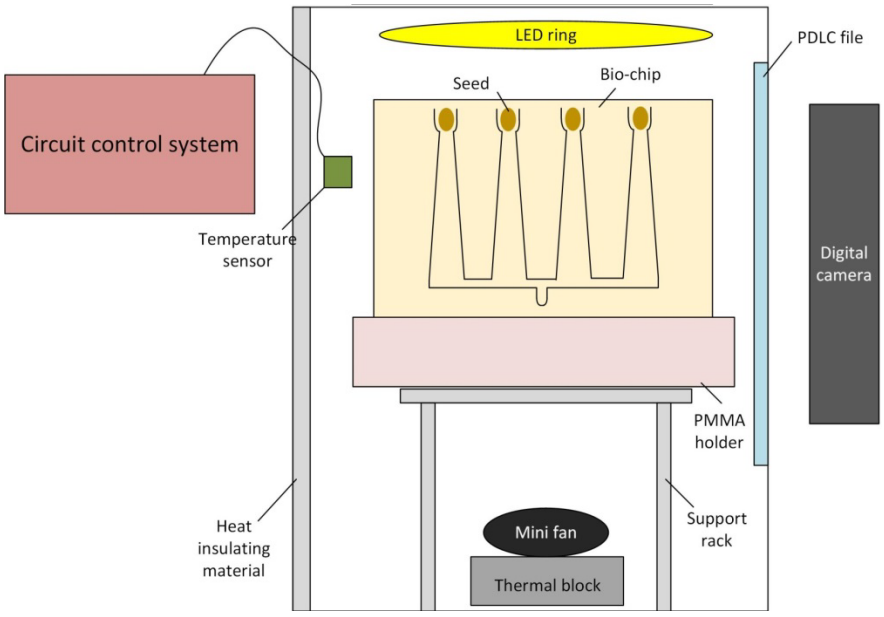

Figure 4.1 *Schematic of miniature greenhouse.*

4.2.1.1 Growth chamber

The growth chamber has the dimensions of 3.25"(width)×7.5"(height)×3.5"(depth). The front side of the chamber has a window covered by a polymer dispersed liquid crystal (PDLC) film (Smart Tint, Inc., USA). Because the PDLC film can be switched between a transparent and an opaque state by applying or removing a voltage, it allows us to take pictures for plants from outside

of the growth chamber, as shown in Figure 4.2. To obtain good thermal isolation and increase light intensity, the inner walls of the other three sides are covered with heat reflective insulating materials (Heatshield Products, Inc., Escondido, CA, USA).

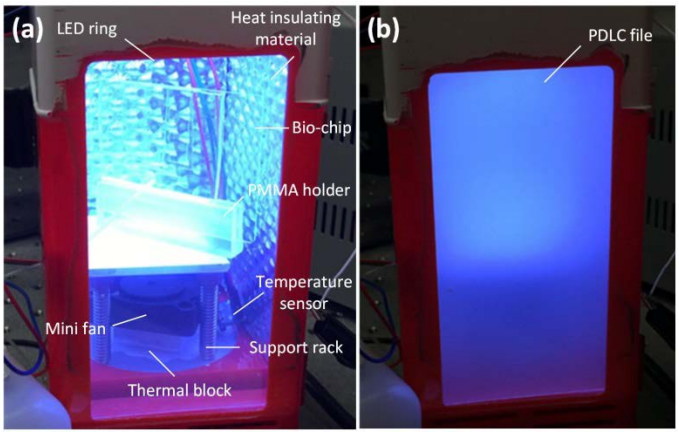

Figure 4.2 *Growth chamber (a) 110V voltage is applied, and (b) No voltage is applied.*

Inside the growth chamber, there are a mini fan, a support rack, a plastic holder, a LED ring, and a plant-chip. The mini fan is used to realize good air circulation for achieving fast cooling and heating within the chamber. The LED ring is used to provide light for the chamber. The light intensity can be easily controlled by adjusting voltage. The ring arrangement is suitable to provide a relatively uniform light intensity. A temperature sensor and a light intensity sensor are installed inside the growth chamber to track temperature and light conditions, which will be introduced in the circuit control section below.

4.2.1.2 Circuit control system

The flow chart of the circuit control system is shown in Figure 4.3. As mentioned before, there are two sensors in the growth chamber. The SHT11 temperature sensor (SENSIRION, Inc., Switzerland) is chosen due to its high accuracy, small size, and high speed. A photodiode PDB-C142 is selected as the light intensity sensor due to its low price, small size, and high accuracy. These two sensors act to detect the environment conditions and achieve data indicating the

temperature and light intensity within the growth chamber, and then feed these data to the central controller, i.e., Arduino UNO board (ARDUINO, Inc.). The Arduino UNO is a microcontroller board based on the ATmega328. It has 14 digital input/output pins (6 of which can be used as PWM outputs), 6 analog inputs, a 16 MHz ceramic resonator, and a USB connection. Besides, it is able to support SPI, I2C, and UART TTL serial communication and contains all necessary function needed to support the microcontroller. The Arduino UNO can connect to a computer with a USB cable or power up with an AC-to-DC adapter or battery. Serving as a central controller, it receives data coming from the sensors, and then analyzes data. On the other hand, according to the analyzing results, it also sends out commands to other specific control circuit boards, such as a current direction control board, to adjust the environment such as temperature and light intensity within the growth chamber.

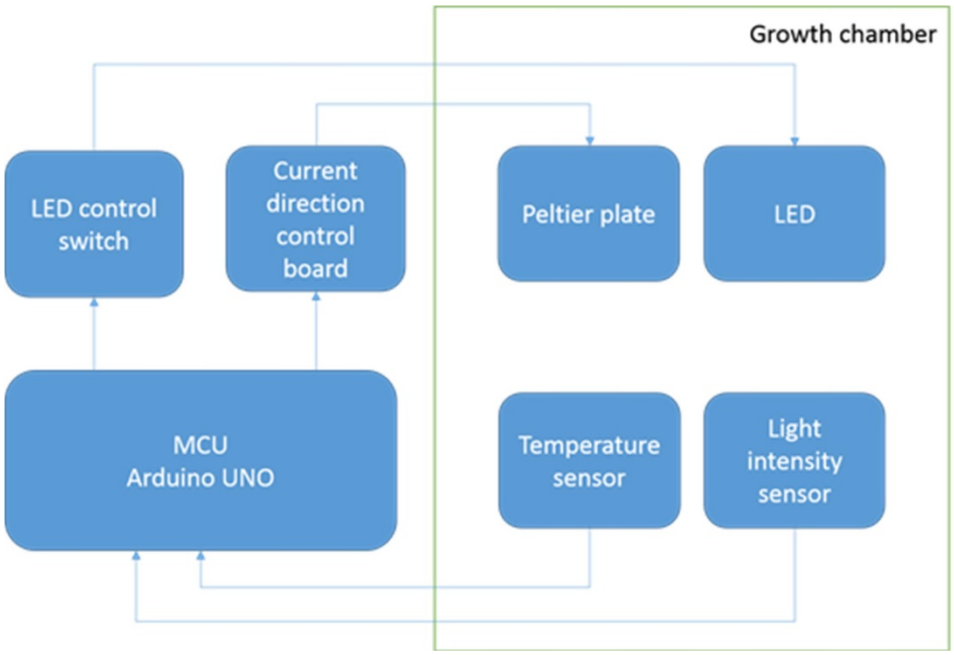

Figure 4.3 *Flow chart of circuit control system.*

For this design, a current direction control circuit is included in the system shown in Figure 4.4. The circuit provides an electric current for the thermoelectric or Peltier cooling plate attached

at the bottom of the chamber. The Peltier device is a plate-type element consisting of arrays of P-type and N-type semiconductors. If the direct current is supplied to the plate, one side surface generates heat and increases the local temperature, while the other side surface absorbs heat and decreases the local temperature. Therefore, changing the direction of the current supplied to the Peltier device allows for the heating and cooling operations. Therefore, an H-bridge circuit is used to control the current direction. Six MOSFETs are used, two of which are P channel (IRF5305PBF, a dual MOSFET) and others are N channel (IRL2703PBF, a dual MOSFET). These MOSFETs are positioned like in Figure 4.4a, so that full H-bridge control can be achieved with two I/O pins of the Arduino UNO board.

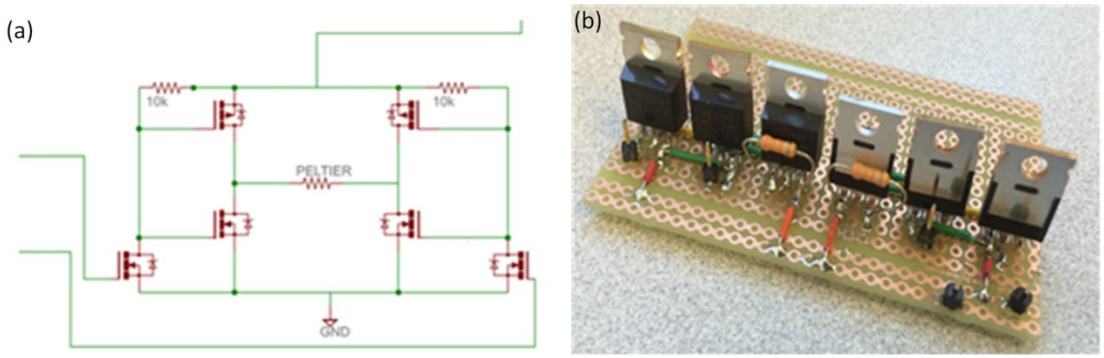

Figure 4.4 *Current direction control board (a) Schematic; (b) Physical board.*

By combining the microcontroller unit (MCU), the temperature sensor, and the Peltier plate, it is easy to get an accurate temperature control system. Its working process is described as follows. At the beginning, the temperature sensor gets the temperature data, and then the MCU compares this data with a pre-set value. If the current temperature within the chamber is higher than the pre-set value, then the MCU will write “1” and “0” to the two I/O pins connected to the two edge N channel MOSFETs. This indicates that one N MOSFET is opened, and the other one is closed. For example, if the left N MOSFET is opened and the right one is closed, then the current will flow through the Peltier plate from left to right. If the current is inversed, then the Pletier will

function as a cooler to decrease the temperature within the growth chamber. However, when the temperature within the chamber is lower than the pre-set value, the MCU will write “0” and “1” to the two I/O pins, thus, the working process is inversed.

The control method for light intensity is similar to the temperature control method mentioned above. The only difference is that instead of using H-bridge to change the current direction flowing through the Peltier plate, we use the switches to control turning the on/off states of the LEDs. As a matter of fact, in our control system, switches are just the name, since the I/O pins of the Arduino UNO board can play the roles. According to the datasheet of the Arduino UNO board, the high output voltage of its I/O port is 3.3 V, high enough to turn on LED. For high efficiency and saving I/O ports, 6 LEDs are connected to one I/O pin. As the LED ring used in our case contains 18 LEDs, three I/O pins are needed to control the light intensity. To get a uniform light intensity, the 18 LEDs are positioned like in Figure 4.5. The LEDs with the same uppercase letter are connected together. The working process is the same as the temperature controller, i.e., using the data obtained by the photodetector to decide the number of LEDs in the ON state. Of course, when a high light intensity is needed or the output voltage of the I/O pins is not high enough to turn on the LEDs, an external power can be added into this control system. In that case, the switches will be replaced by the indeed switches, such as relays, and also, the I/O pins on the Arduino UNO board will just provide a “turn-on” signal like in the temperature control system.

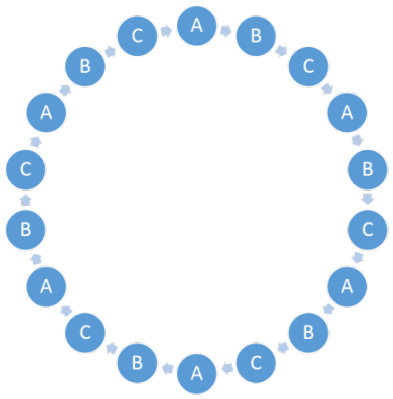

Figure 4.5 *Pattern of LEDs.*

4.2.1.3 Image system

For this miniature greenhouse, one digital camera is located in front of the growth chamber to shoot side views of the plant chip. Nissan S3200 digital camera is used due to its high resolution, cost efficiency, and low power consumption. In our system, Raspberry Pi 2 is used to control the camera through the USB port. Since the Raspberry Pi just has 4 USB ports, if more than 4 cameras are needed, a USB hub can be added into our system to expand the number of the USB ports with the help of an external power supply.

4.2.1.4 Characterization of miniature green house

Within the growth chamber, the obtained highest temperature is 86.4 ºC and the lowest temperature is 14.8 ºC. The highest light intensity is 581 µE m^{-2} s^{-1} (31.4×10^3 Lux) and the lowest light intensity is 10.7 µE m^{-2} s^{-1} (5.8×10^2 Lux). To measure the stability, the Arduino UNO board is connected to the computer through the USB cable, and then the data collected by the sensors can be saved through the Integrated Development Environment (IDE) based software developed to program the Arduino board. The testing result is shown in Figure 4.6a. The pre-set value is 25 ºC. From the plot, it is seen that after a few minutes, the temperature gets close to the pre-set value, and the variation is within $\pm$4 %. The response time is defined as the temperature changes, the time the system needs to reach a new stable state. In our testing, the temperature is changed from

23 ± 0.6 ºC to 29 ± 0.9 ºC. The result is shown in Figure 4.6b. According to the testing result shown in the inset curves of Figure 4.6b, the device needs less than 1 minute to increase or decrease 5 ºC, which is considered fast for the plant growth application.

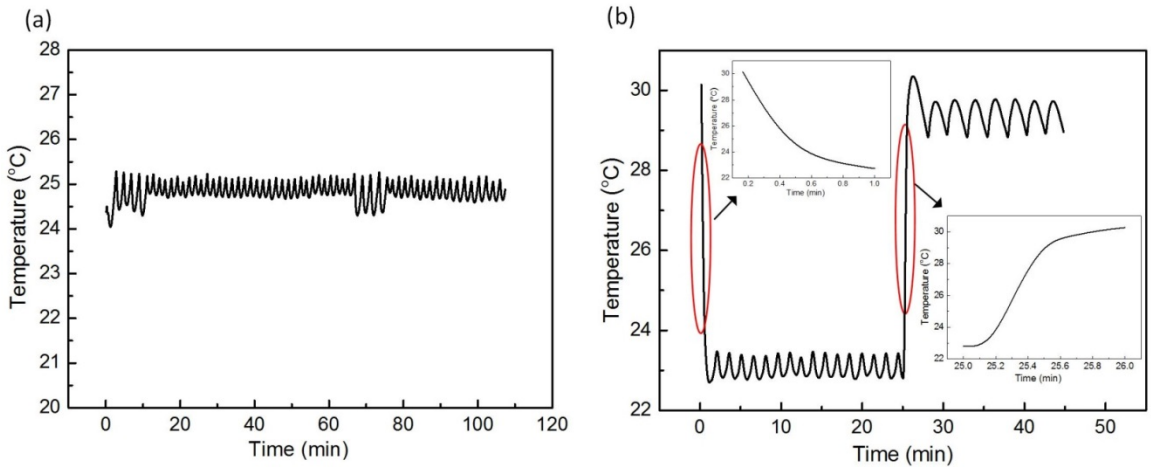

Figure 4.6 *(a) Stability of temperature measurement, and (b) Response time over the temperature changes.*

4.2.2 Improved miniature greenhouse system

An improved miniature greenhouse system is shown in Figure 4.7. It consists of six separate miniature chambers, a thermoelectric cooling system (200W, 24V thermoelectric cooler, Hoffman), a heating source (200W, 110V ceramic heater, My Heat), a fluorescence light bulb (500 W, GE), an electronic control circuit, and an image module. Each chamber has the outer dimensions of 8"(width)×8"(depth)×12"(height). Environment conditions to be controlled include light intensity and temperature.

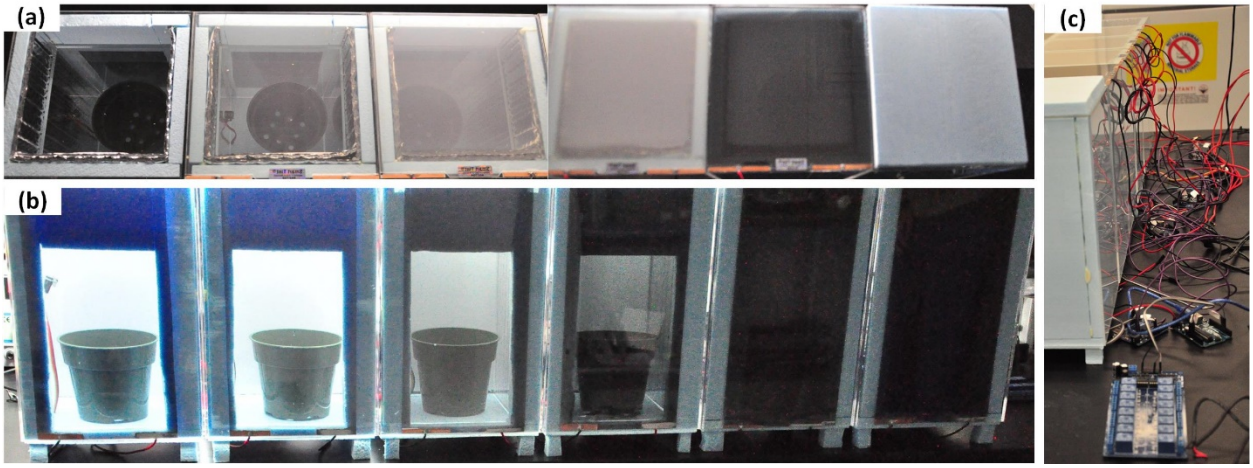

Figure 4.7 *Improved miniature greenhouses (a) the top view, (b) the front, and the circuits behind the greenhouses.*

4.2.2.1 Mechanical installation

Each growth chamber is made of two plexiglass boxes. The smaller one (6"(w) × 6"(d) × 9"(h)) is concentrically placed inside the bigger one (8"(w) × 8"(d) × 12"(h)). Their intestinal space (except for the top and front sides) is filled with insulating foam materials to prevent heat exchange between the internal space of the chamber and the outside environment. The top and front sides of need to be transparent so as to allow taking photos from outside of the chamber and adjusting light intensity. Moreover, aluminum foil is attached on the internal walls of the other sides of the inner plexiglass box. This can help to get uniform internal light intensity in the whole space of the chamber. Venting pipes for cold and hot air and electrical wires enter the chamber from the bottom through holes. Push-in straight connector fittings are used to connect pipes and the bottom plate (not shown in Figure). A pressure relief valve is also placed on the bottom to maintain normal air pressure in the growth chamber. A plant growth lamp (300W; 6500 K cool spectrum; Feliz) is installed above the chambers.

4.2.2.2 Light intensity control

A single plant growth lamp (300W; 6500 K cool spectrum; Feliz) is installed above all the chambers. Because of the PDLC (Smart Tint, Inc., USA) residing the top of each chamber, the

light intensity in each chamber can be individually adjusted by applying a specific voltage. The light transmittance through the PDLC cover is proportional to an applied voltage. At 110 V, the transmittance is 81%. With no voltage, the transmittance is 9%. In the experiment demonstrated later, six levels of light intensity (0, 10, 50, 100, 200, 500 μE m^{-2} s^{-1}) are realized by applying different voltages (from 0 to 110 V) to different PDLC covers.

4.2.2.3 Temperature control

Temperature adjustment is achieved by mixing cold air and hot air inside the chamber. Air pipes are controlled by a solenoid, an electromechanically operated valve (shown in Figure 4.7c). A temperature sensor (SHT11) is placed inside the chamber to get the instantaneous temperature value. The operating process is described below. For example, when the temperature value is below the set point 2 ºC, the hot air solenoid valve will be switched on. If the temperature value is above the set point, the cold air solenoid valve will be switched on. Otherwise, no air will be injected into the growth chamber. The tolerance value (here 2 ºC) is adjustable to meet different accuracy requirements.

4.2.2.4 Imaging

To take plant growth photos outside of the chambers, a transparent window is opened on the front face of each chamber and a PDLC is installed on this side. With this design, when no photos are taken, the window is nontransparent, thus not disturbing the plant growth light intensity. During imaging, 110V voltage is applied on the PDLC, such that the window becomes transparent again (shown in Figure 4.7b).

4.3 Preparation of plant chip

4.3.1 Plant growth chip

The plant growth chip is fabricated using a conventional soft lithography technique [41] to create a master mould for microfluidic channels. A mixture of polydimethylsiloxane (PDMS, Sylgard 184, Dow Corning, USA) and its curing agent with a weight ratio of 10:1 is poured onto the master mould and then cured on a hotplate at 90 ºC for 1 hour. Then, the hardened PDMS polymer is pealed from the master mould and bonded to a microscope glass slide (75 mm × 50 mm × 0.9 mm) through oxygen plasma treatment. The inlet and outlet ports of the device are manually punched with a mechanical puncher.

4.3.2 Culture media

Standard culture media are prepared and used. All the chemicals used are of analytical reagent grade. Deionized water is used throughout to prepare the media. The culture media are sterilized in an autoclave at 15 psi at 121 ºC for 30 min and stored at 4 ºC. They are loaded into the device using a 3 mL syringe (Beckton Dickinson, NJ, USA) with a microbore tubing (Cole-Parmer, IL, USA) before the seeds are transferred into the device.

4.3.3 Pre-treatment of *Arabidopsis* seeds

Wild-type (WT) *Arabidopsis thaliana* ecotype Columbia and *immutans* mutant of *Arabidopsis* are used in this experiment. All seeds are sterilized by treating in a solution containing 70% (V/V) ethanol for 1 min, 50% (V/V) Clorox and 0.02% (V/V) Trtion for 15 min. Then, the seeds are washed three times with autoclaved deionized (DI) water. Last, the seeds are soaked in a Petri dish containing autoclaved DI water for 5-6 hrs to expand by ~15% on the small diameter.

4.3.4 Plant growth conditions

After the seeds are trapped in the seed holding sites [40], the chips is stored at 4 ºC in a refrigerator for 48 hrs to stratify seeds. Subsequently, the chips is taken out of the refrigerator and vertically placed in the miniature greenhouse (shown in Figure 4.7b) under a specific plant growth light intensity at room temperature (~21 ºC). Six different light intensity are set, i.e., 0, 10, 50, 100, 200, and 500 µE m^{-2} s^{-1}. Another experiment is set under normal light source (50-100 µE m^{-2} s^{-1}) at different temperature, i.e., T ≤ 15 ºC, 23 ± 2 ºC, 30 ± 2 ºC and 42 ± 2 ºC. Also, we study the seeds grown at low light (10-15 µE m^{-2} s^{-1}) with different temperature (i.e., T = 10 ± 2 ºC, 23 ± 2 ºC and 30 ± 2 ºC). The environmental relative humidity is ~40 %. The growth medium of interest is replenished with new medium on a daily basis. The plants germinate and grow in the devices for 6-28 days. In the following section, the seed germination and plant growth (e.g., root, hypocotyl and cotyledon) of *Arabidopsis thaliana* are compared based on the acquired microscopic images.

A microscope (MZ205, Leica, Germany) with a video camera (QICamera) is used to image plant growth in the greenhouse. The system collect phenotypic data of seed germination, root length, hypocotyl, cotyledon and leaf emergence, all data points reflect the average of at least three replicates.

4.4 Results

To test light and temperature control of the newly designed miniature greenhouse for plant phenotyping studies, we monitored the growth phenotype of wild-type and *immutans* mutant of *Arabidopsis* [42, 43] for 4 weeks. Consistent with our previous report [40] Figures 4.8 and 4.9 show that under normal light conditions (100 µE m^{-2} s^{-1}), WT and *immutans* seeds germinate between 24-30 hrs. This timeline appears to be true also for seeds germinating under a range of light conditions (0 - 500 µE m^{-2} s^{-1}), except for *immutans* seeds germinating under very low light

conditions i.e., under dark or at 10 µE m^{-2} s^{-1} the germination is observed to be between 30 - 42 hrs. Similar to previous observations [44-48], maximum overall shoot and root growth of wild-type *Arabidopsis* plants was observed around normal light conditions ranging from 50 - 200 µE m^{-2} s^{-1}, whereas under dark/low light conditions and under higher than normal light conditions (500 µE m^{-2} s^{-1}), growth is either very slow or inhibited after ~7-9 days (Figures 4.8, 4.10c and f). Different growth light intensities had little influence on the growth of hypocotyl length except for those grown at 0 µE, which were longer as previously observed. However, the roots of plants growing at normal light intensity were longer with sparser root hairs than those growing at other light intensities. In addition, there was a significant difference in the number of leaves emerging under different light intensities. The first two leaves of WT emerged earlier than 180 hrs under 10, 50, 100 and 200 µE m^{-2} s^{-1}, while these for *immutans* only under 10 µE m^{-2} s^{-1}. As expected, the cotyledons and leaves are green in color for *immutans* plants grown under low light (10 - 50 µE m^{-2} s^{-1}) whereas cotyledons and leaves of plants grown under normal light (100 - 200 µE m^{-2} s^{-1}) have the typical white/green phenotype. Overall growth of *immutans* plants is similar to wild-type Arabidopsis under low light conditions (0 - 10 µE m^{-2} s^{-1}) and high light conditions (500 µE m^{-2} s^{-1}), but plants grow slowly under normal light conditions (50 - 200 µE m^{-2} s^{-1}) when compared to WT, and do not reach the reproductive stage even after 29 - 30 days (Figure 4.9). The growth of hypocotyl is similar to WT whereas the roots are shorter than WT (Figure 4.10a-d). This is in agreement with previous reports on slow growth of *immutans* plants versus WT. It should be noted that *immutans* seeds were allowed to germinate for 1-2 days under low light conditions before transferring the plant chips to different light intensities. This is because *immutans* does not germinate or germinates poorly under normal light conditions.

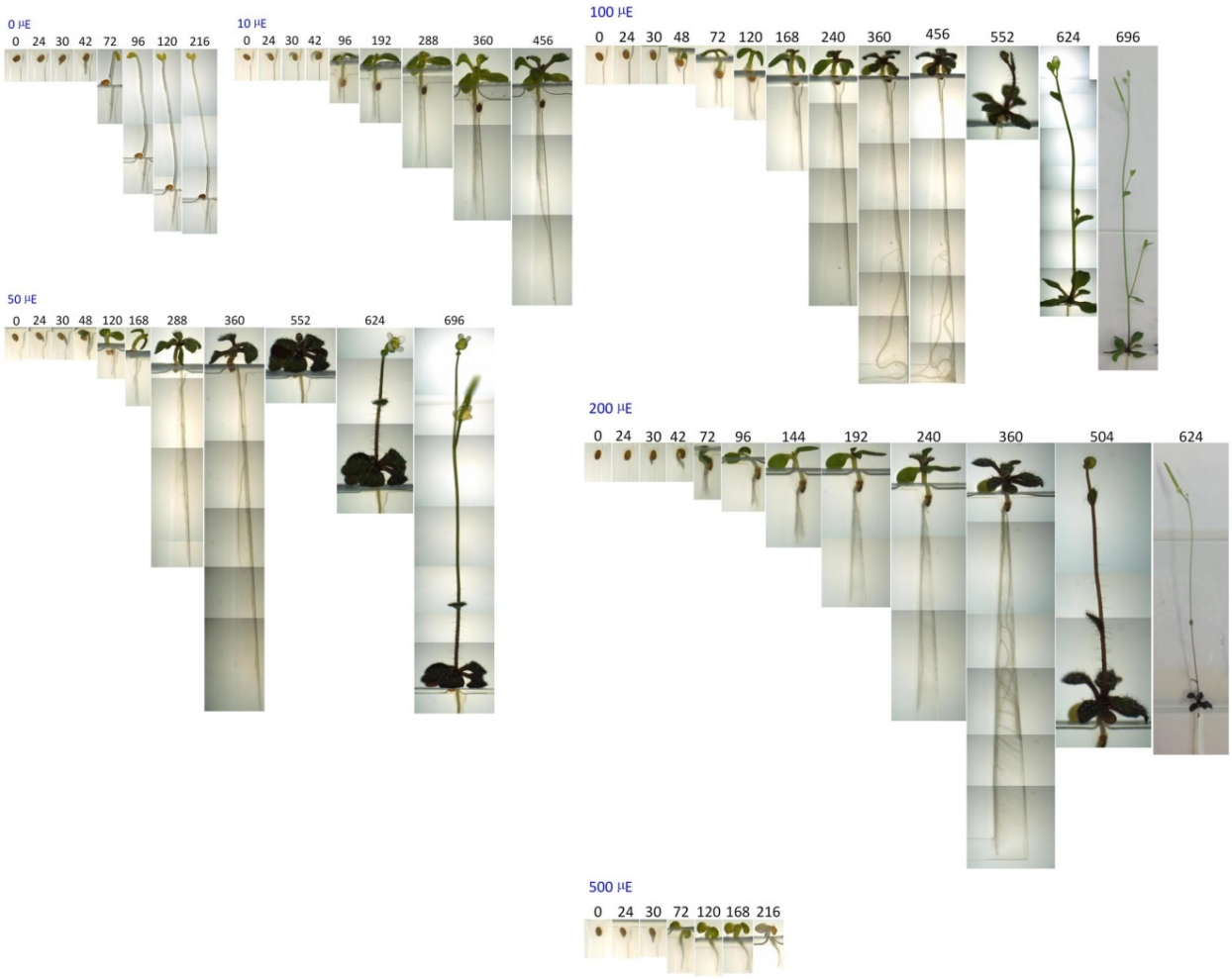

Figure 4.8 *Plant growth of WT at different light intensity (0, 10, 50, 100, 200, 500 µE m^{-2} s^{-1}).*

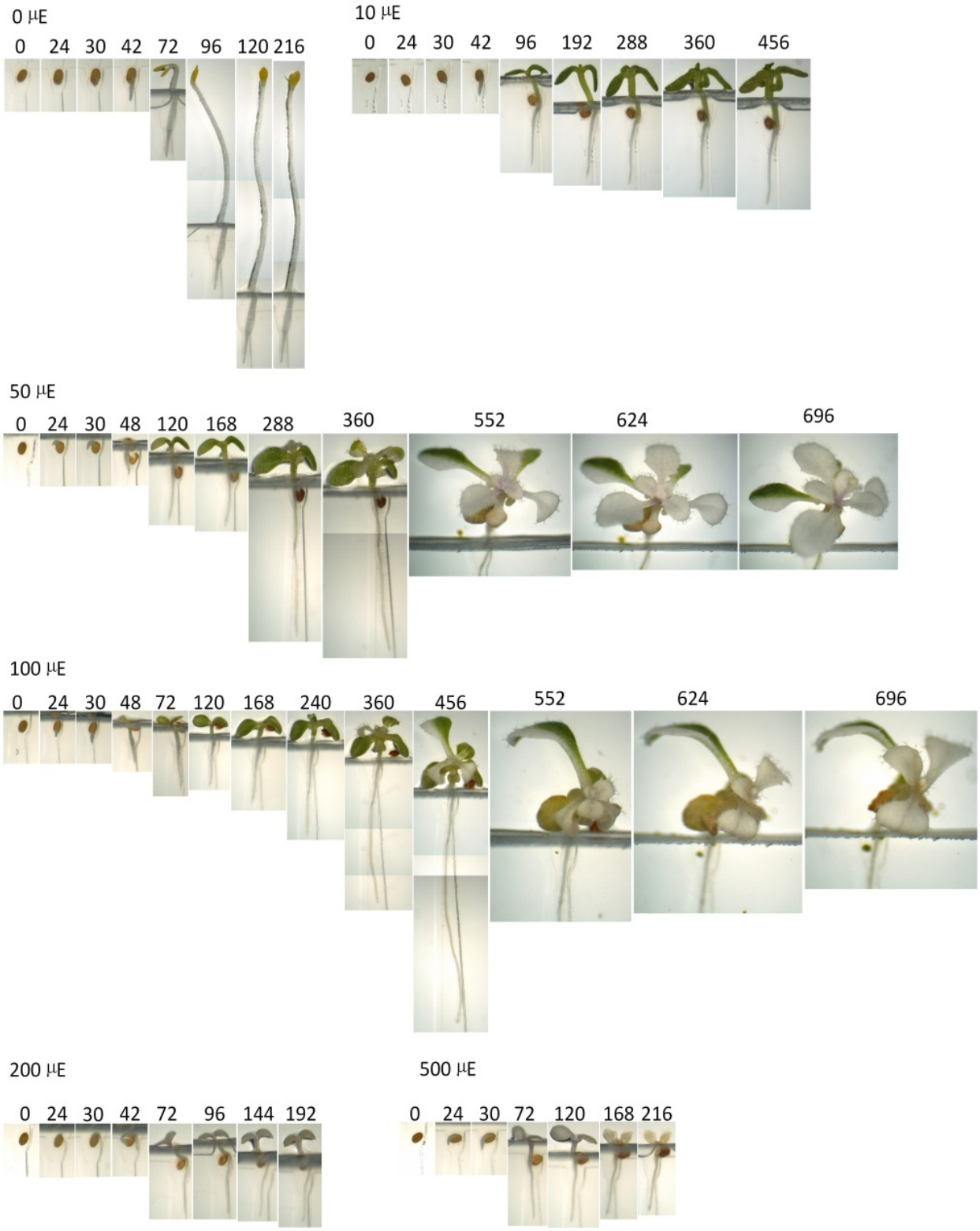

Figure 4.9 *Plant growth of Spotty at different light intensity (0, 10, 50, 100, 200, 500 µE m^{-2} s^{-1}).*

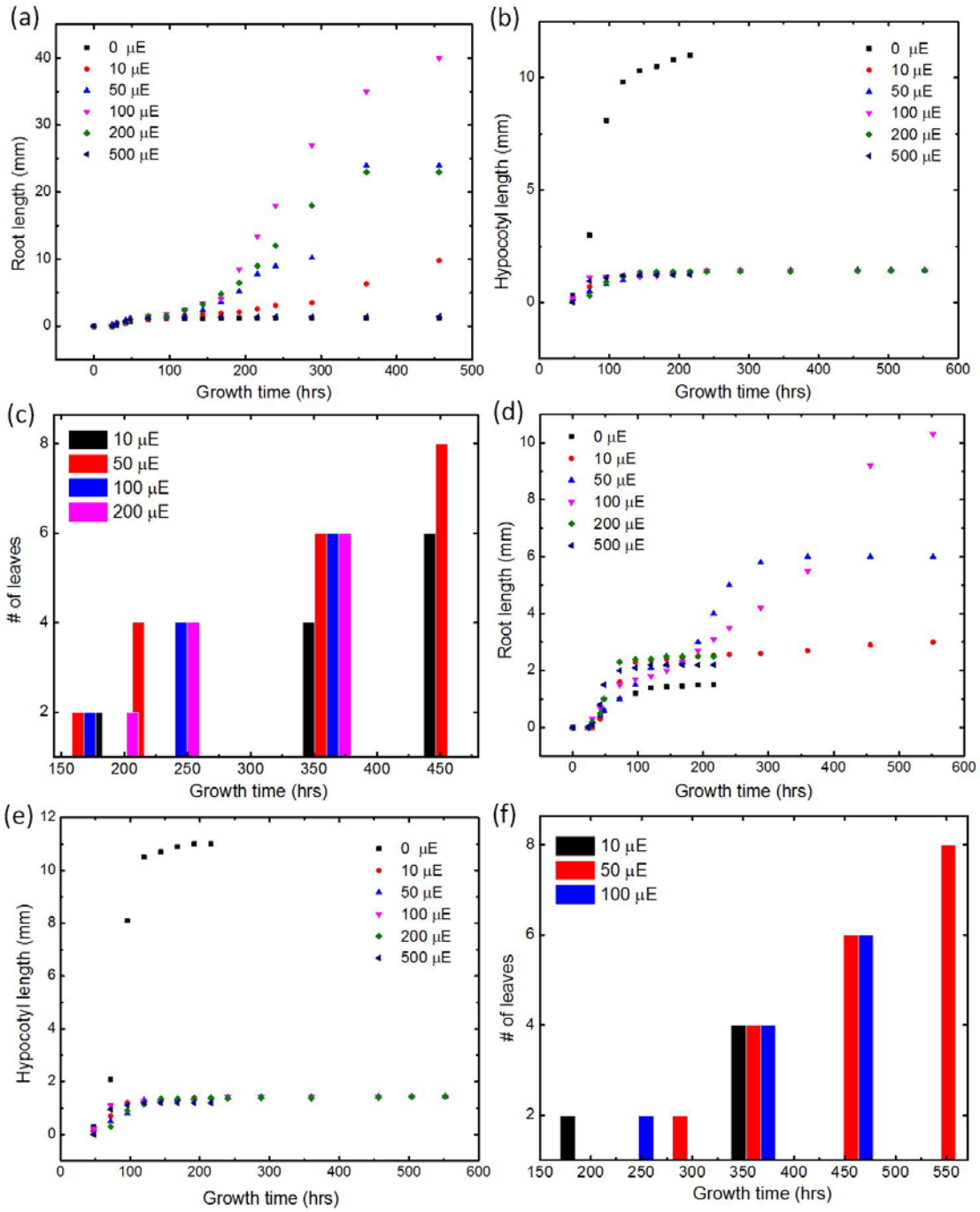

Figure 4.10 *Major phenotypic parameters of (a-c) WT and (d-f) Spotty at different light intensity, i.e., (a,d) root length, (b,e) hypocotyl length and (c,f) the number of leaves.*

We also determined the effect of a range of temperatures (~15 ºC-42 ºC) on the *Arabidopsis* growth phenotype (shown in Figure 4.11). At normal temperatures of 22-23 ºC, and at 30 ºC, both WT and *immutans* seeds germinate by 30 hrs. However, the germination was delayed at low

temperatures (15 ºC), and seeds did not germinate even after a week of incubation at 42 ºC. Similar to results obtained with different light conditions, root and hypocotyl growth are significantly influenced by temperature, with longer roots and hypocotyls for plants grown at normal temperature versus low temperature (Figure 4.12). Figure 4.12 also shows that roots of WT and *immutans* grew rapidly from 70 to 140 hrs, and had slower growth rates thereafter. As expected, WT cotyledons of plants grown under temperatures ranging from 15 ºC-30 ºC were all green in color, but cotyledons for *immutans* plants were always observed to be white under the same temperature conditions. One reason for this could be due to the light intensity under which these plants were grown. *Immutans* seedlings are known to give rise to white/albino cotyledons when germinated and grown under normal light conditions (100-200 µE m^{-2} s^{-1}). These albino plants do not grow further and eventually die without giving rise to leaves. Therefore, to better assess and compare growth phenotype(s) of WT and *immutans*, we germinated and grew both WT and the mutant under different growth temperatures while keeping the light intensity constant at 10-15 µE $m^{-2}s^{-1}$. Although green cotyledons were observed under these growth conditions, distinct phenotypic differences could be observed and monitored between WT and *immutans*. While the WT seeds germinated and grew as expected under low temperature and light conditions, there was significant delay in the germination of *immutans* seeds (Figure 4.13 at T=10 ºC), and cotyledon expansion, root length and overall growth of *immutans* plants (Figure 4.13 at T=30 ºC).

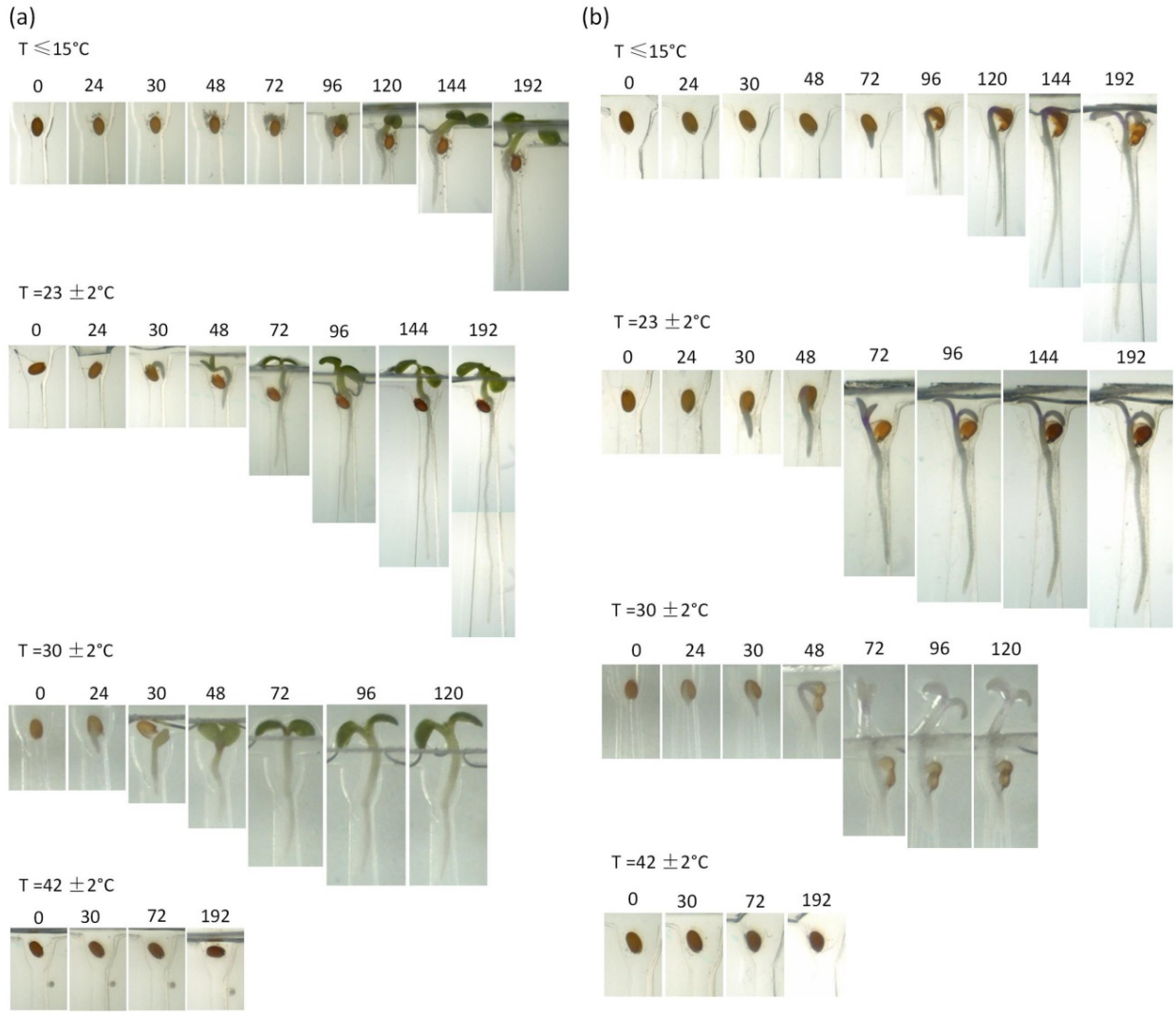

Figure 4.11 *Plant growth of (a) WT and (b) Plant growth of Spotty at different temperature (< 15, 23±2, 30 ±2, and 42 ±2 ºC).*

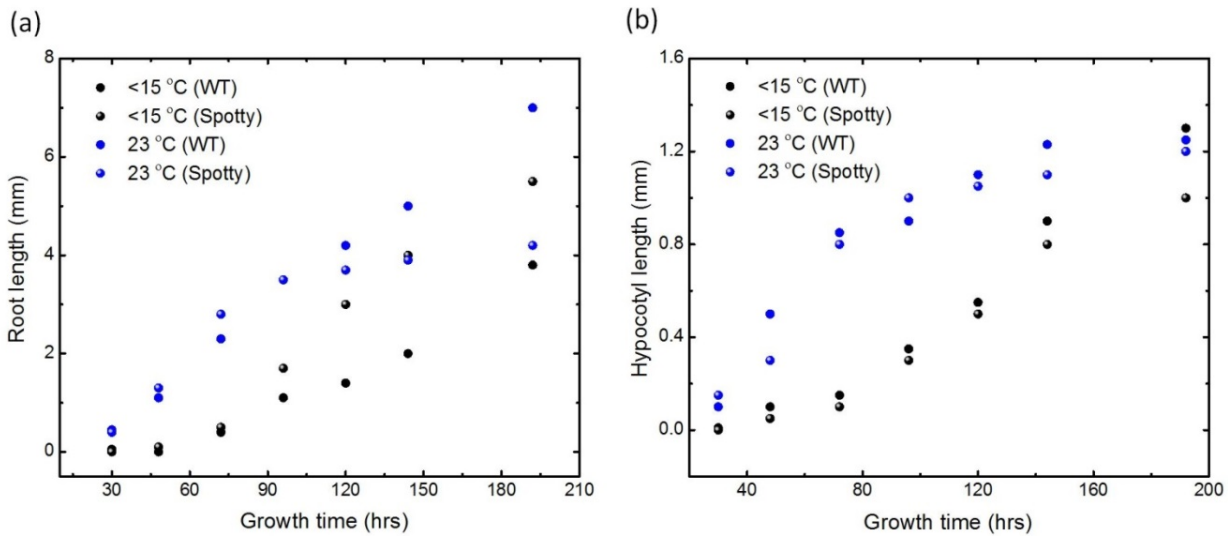

Figure 4.12 *Major phenotypic parameters of (a) WT and (b) Spotty at different temperature (root length, hypocotyl length and the number of leaves).*

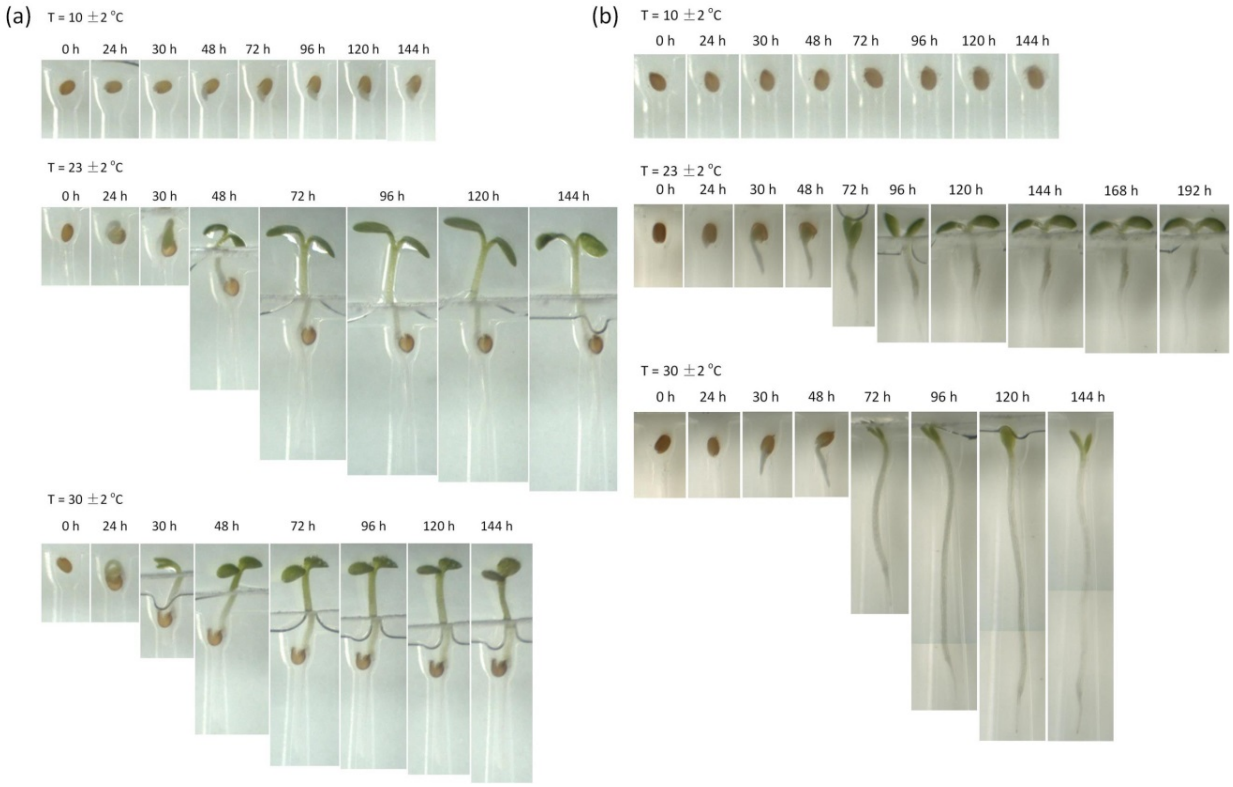

Figure 4.13 *(a) WT and (b) Spotty grown in low light at different temperature (10 ± 2, 23 ± 2, and 30 ± 2 ºC).*

Table 4.1 *Comparison of growth stages for WT and Spotty at different light intensity.*

Light intensity ($\mu E\ m^{-1}\ s^{-1}$)	*Plant type (WT/Spotty)*	*Growth stage (days)*					
		Seed coat breakage	*Radicle emergence*	*Length of primary root (0.6 mm)*	*Cotyledon & hypocotyl emergence*	*Cotyledonos fully opened*	*2 rosette leaves*
0	*WT*	1.0	1.2	2.2	2.0	3.0	ND
	Spotty	1.1	1.2	2.4	2.1	3.0	ND
10	*WT*	0.8	1.0	3.8	2.3	2.4	7.9
	Spotty	1.0	1.2	2.4	2.3	2.5	8.0
50	*WT*	0.8	0.9	2.0	1.5	1.8	7.0
	Spotty	0.8	0.9	2.4	1.8	2.0	7.0
100	*WT*	0.9	1.0	2.0	1.7	1.9	5.0
	Spotty	0.8	0.9	2.0	1.7	1.8	8.3
200	*WT*	1.1	1.2	2.0	1.9	2.6	6.0
	Spotty	1.0	1.1	2.1	1.9	2.2	ND
500	*WT*	0.9	1.0	2.8	2.4	2.6	ND
	Spotty	0.8	0.9	2.4	2.2	2.3	ND

Table 4.2 *Comparison of growth stages for WT and Spotty under normal light at different temperature.*

Temperature (°C)	*Plant type (WT/Spotty)*	*Growth stage*					
		Seed coat breakage	*Radicle emergence*	*Length of primary root (0.6 mm)*	*Cotyledon & hypocotyl emergence*	*Cotyledonos fully opened*	*2 rosette leaves*
<15	*WT*	2.0	2.2	4.1	3.8	4.0	ND
	Spotty	1.2	2.0	3.5	3.3	5.0	ND
23 ± 2	*WT*	1.0	1.2	2.0	1.7	1.9	8.0
	Spotty	1.0	1.1	2.1	1.9	2.0	ND
30 ± 2	*WT*	0.6	0.8	1.7	1.1	1.2	5.0
	Spotty	0.7	0.9	2.3	1.8	2.0	ND

4.5 Conclusions

This miniature greenhouse can flexibly change the environment condition to observe the phenotyping of *Arabidopsis thaliana* plants. Also, the usage of liquid crystal shutter enables easily accessing the inside of greenhouse without breaking growth condition. Through designed electronic circuits, it not only controls the plant growth environment for studying plant phenotypes on a multi-scale level with sufficient throughput, but commands multiple digital cameras to take images from outside of the device when needed.

References

1. M. Prathap and B. D. R. Kumari, *J. Plant Pathol. Microbiol.*, 2015, **6**, 266-266.

2. G. Krouk, S. Ruffel, R. A. Gutierrez, A. Gojon, N. M. Crawford, G. M. Coruzzil and B. Lacombe, *Trends Plant Sci.*, 2011, **16**, 178-182.

3. D. Houle, D. R. Govindaraju and S. Omholt, *Nat. Rev. Genet.*, 2010, **11**, 855-866.

4. J. K. Ward and J. K. Kelly, *Ecol. Lett.*, 2004, **7**, 427-440.

5. Y. H. Cheong, H. S. Chang, R. Gupta, X. Wang, T. Zhu and S. Luan, *Plant Physiol.*, 2002, **129**, 661-677.

6. M. N. Hemming, S. A. Walford, S. Fieg, E. S. Dennis and B. Trevaskis, *Plant Physiol.*, 2012, **158**, 1439-1450.

7. B. Berger, B. Parent and M. Tester, *J. Exp. Bot.*, 2010, **61**, 3519-3528.

8. M. Levin, N. Resnick, Y. Rosianskey, I. Kolotilin, S. Wininger, J. H. Lemcoff, S. Cohen, G. Galili, H. Koltai and Y. Kapulnik, *Plant Sci.*, 2009, **177**, 450-459.

9. C. Kami, S. Lorrain, P. Hornitschek and C. Fankhauser, *Plant Development*, 2010, **91**, 29-66.

10. P. B. Allen, A. E. Sgro, D. L. Chao, B. E. Doepker, J. S. Edgar, K. Shen and D. T. Chiu, *J. Neurosci. Methods*, 2008, **173**, 20-26.

11. S. Preibisch, S. Saalfeld and P. Tomancak, *Bioinformatics*, 2009, **25**, 1463-1465.

12. M. Meier, E. M. Lucchetta and R. F. Ismagilov, *Lab Chip*, 2010, **10**, 2147-2153.

13. S. Svistoonoff, A. Creff, M. Reymond, C. Sigoillot-Claude, L. Ricaud, A. Blanchet, L. Nussaume and T. Desnos, *Nat. Genet.*, 2007, **39**, 792-796.

14. I. Casimiro, T. Beeckman, N. Graham, R. Bhalerao, H. M. Zhang, P. Casero, G. Sandberg and M. J. Bennett, *Trends Plant Sci.*, 2003, **8**, 165-171.

15. C. Bermejo, J. C. Ewald, V. Lanquar, A. M. Jones and W. B. Frommer, *Biochem. J.*, 2011, **438**, 1-10.

16. J. E. Malamy, *Plant Cell Environ.*, 2005, **28**, 67-77.

17. A. Walter, W. K. Silk and U. Schurr, *Annu. Rev. Plant Biol.*, 2009, **60**, 279-304.

18. S. Okumoto, *Curr. Opin. Biotech.*, 2010, **21**, 45-54.

19. R.T. Furbank and M. Tester, *Trends Plant Sci.*, 2011, **16**, 635-644.

20. S. Takayama, J. C. McDonald, E. Ostuni, M. N. Liang, P. J. A. Kenis, R. F. Ismagilov and G. M. Whitesides, *P. Natl. Acad. Sci. USA*, 1999, **96**, 5545-5548.

21. F. Migliaccio, A. Fortunati and P. Tassone, *Plant Signal. Behav.*, 2009, **4**, 183-190.

22. S. de Dorlodot, B. Forster, L. Pages, A. Price, R. Tuberosa and X. Draye, *Trends Plant Sci.*, 2007, **12**, 474-481.

23. K. S. Osmont, R. Sibout and C. S. Hardtke, *Annu. Rev. Plant Biol.*, 2007, **58**, 93-113.

24. N. D. Miller, B. M. Parks and E. P. Spalding, *Plant J.*, 2007, **52**, 374-381.

25. E. B. Blancaflor and P. H. Masson, *Plant Physiol.*, 2003, **133**, 1677-1690.

26. E. B. Blancaflor, J. M. Fasano and S. Gilroy, *Plant Physiol.*, 1998, **116**, 213-222.

27. C. S. Buer and G. K. Muday, *Plant Cell*, 2004, **16**, 1191-1205.

28. G. T. S. Beemster and T. I. Baskin, *Plant Physiol.*, 1998, **116**, 1515-1526.

29. G. T. S. Beemster and T. I. Baskin, *Plant Physiol.*, 2000, **124**, 1718-1727.

30. X. D. Fu and N. P. Harberd, *Nature*, 2003, **421**, 740-743.

31. C. L. Gilleland, C. B. Rohde, F. Zeng and M. F. Yanik, *Nat. Protoc.*, 2010, **5**, 1888-1902.

32. E. M. Lucchetta, J. H. Lee, L. A. Fu, N. H. Patel and R. F. Ismagilov, *Nature*, 2005, **434**, 1134-1138.

33. M. Horade, N. Yanagisawa, Y. Mizuta, T. Higashiyama and H. Arata, *Microelectron. Eng.*, 2014, **118**, 25-28.

34. G. Grossmann, W.-J. Guo, D. W. Ehrhardt, W. B. Frommer, R. V. Sit, S. R. Quake and M. Meier, *Plant Cell*, 2011, **23**, 4234-4240.

35. A. M. Jones, G. Grossmann, J. A. H. Danielson, D. Sosso, L.-Q. Chen, C.-H. Ho and W. B. Frommer, *Curr. Opin. Plant Biol.*, 2013, **16**, 389-395.

36. W. Busch, B. T. Moore, B. Martsberger, D. L. Mace, R. W. Twigg, J. Jung, I. Pruteanu-Malinici, S. J. Kennedy, G. K. Fricke, R. L. Clark, U. Ohler and P. N. Benfey, *Nat. Methods*, 2012, **9**, 1101-1106.

37. C. G. Agudelo, A. S. Nezhad, M. Ghanbari, M. Naghavi, M. Packirisamy and A. Geitmann, *Plant J.*, 2013, **73**, 1057-1068.

38. A. S. Nezhad, M. Ghanbari, C. G. Agudelo, M. Naghavi, M. Packirisamy, R. B. Bhat and A. Geitmann, *Biomed. Microdevices*, 2014, **16**, 23-33.

39. A. Parashar and S. Pandey, *Appl. Phys. Lett.*, 2011, **98**.

40. H. Jiang, Z. Xu, M. R. Aluru and L. Dong, Lab Chip, 2014, 14, 1281-1293.

41. D. B. Weibel, W. R. DiLuzio and G. M. Whitesides, *Nat. Rev.Microbiol.*, 2007, **5**, 209-218.

42. C. M. Wetzel, C. Z. Jiang, L. J. Meehan, D. F. Voytas and S. R. Rodermel, *Plant J.*, 1994, **6**, 161-175.

43. M. Aluru, H. Bae, D. Wu and S. Rodermel, *Plant Physiol.*, 2001, **127**, 67-77.

44. P. P. Liu, N. Koizuka, T. M. Homrichhausen, J. R. Hewitt, R. C. Martin and H. Nonogaki, *Plant J.*, 2005, **41**, 936-944.

45. T. Ingestad and G. I. Agren, *Ecol.l Appl.*, 1991, **1**, 168-174.

46. H. Zhang, A. J. Jennings and B. G. Forde, *J. Exp. Bot.*, 2000, **51**, 51-59.

47. H. Zhang and B. G. Forde, *Science*, 1998, **279**, 407-409.

48. H. Zhang, A. Jennings, P. W. Barlow and B. G. Forde, *Proc. Natl. Acad. Sci. U.S.A.*, 1999, **96**, 6529-6534.

CHAPTER 5. A MINIATURE MICROBIAL FUEL CELL WITH CONDUCTING NANOFIBERS-BASED 3-DIMENSIONAL POROUS BIOFILM

A paper published in *Journal of Micromechanics and Microengineering*

Huawei Jiang, Larry J Halverson, Liang Dong

Abstract

Miniature microbial fuel cell (MFC) technology has received growing interest due to its potential applications in high-throughput screening of bacteria and mutants to elucidate mechanisms of electricity generation. This paper reports a novel miniature MFC with an improved output power density and short startup time, utilizing electrospun conducting poly(3,4-ethylenedioxythiophene) (PEDOT) nanofibers as a 3D porous anode within a 12 µL anolyte chamber. This device results in 423 µW/cm^3 power density based on the volume of the anolyte chamber, using *Shewanella oneidensis* MR-1 as a model biocatalyst without any optimization of bacterial culture. The device also excels in startup time of only 1hr. The high conductivity of the electrospun nanofibers makes them suitable for efficient electron transfer. The mean pore size of the conducting nanofibers is only several micrometers, which is favorable for bacterial penetration and colonization of surfaces of the nanofibers. We demonstrate that *S. oneidensis* can fully colonize the interior region of this nanofibers-based porous anode. This work represents a new attempt to explore the use of electrospun PEDOT nanofibers as a 3D anode material for MFCs. The presented miniature MFC potentially will provide a high-sensitivity, high-throughput tool to screen suitable bacterial species and mutant strains for use in large-size MFCs.

5.1 Introduction

Microbial fuel cells (MFCs) are a promising bioelectrochemical technology for the conversion of energy available in organic substrates into electricity. Inexpensive, self-sustaining,

and versatile microbial catalysts potentially allow for use of agricultural residues, municipal wastes, and industrial wastes as carbon and energy sources. However, MFC technology has not been much applied to practical waste material treatments due to its low efficiency to generate power. While many efforts have been made to improve MFC performance [1, 2], the common practice of screening different bacterial species and their mutant derivatives still relies on using larger two-chambered MFCs that often have high material requirements, long start-up times, and low throughput. Recently, miniature MFC technology has received growing interest due to its potential applications in high-throughput screening of bacteria and mutants to elucidate mechanisms of electricity generation [2-15]. Compared to conventional large two-chambered MFCs, miniature MFCs can offer shorter startup time, smaller material consumption, and higher throughput [2-15]. However, due to their small size and insufficient biofilm formation [2, 13-15], existing microfabricated MFCs can only produce a limited electric current that may not readily be measured with practical and economical electronic circuits required for robust screening of bacterial species and mutant strains.

Similar to large-size MFCs the anode features are considered a critical component for obtaining high-performance miniature MFCs. Our interest is to develop and integrate high-performance anode material into a miniature MFC to improve current/power generation while shortening startup time. Generally, enhancing power generation requires structural and material modifications to anode components to facilitate better bacterial adhesion and/or electron transfer to anodes [1]. Overall anode performance is based on parameters, such as conductivity, surface area, bacterial attachment, and biofilm formation [2]. Popular anode materials include metals [16], graphite, carbon materials (e.g., carbon cloth, paper, and fiber veil) [17-19], and modified carbon materials (e.g., polymer-coated carbon and ammonia-treated carbon cloth) [20, 21]. Among them,

metal electrodes are used as two-dimensional anodes due to their high electrical conductivity and resistance to corrosion. However, their flat and smooth surface provides only a small active surface area, limiting bacterial attachment. In contrast, carbon and modified carbon anodes can provide a large porous surface area for bacterial attachment. But, the small pore size of these materials may restrict access of bacteria and nutrients into the interior pores because these pores may be clogged by microbial growth.

Recently, many 3-dimensional (3D) meso/micro/nanostructured anode materials have been reported for MFCs. Futaba et al. developed densely packed and well aligned single-wall carbon-nanotubes (CNTs) by using the zipping effect of liquids to draw tubes together [22]. This material has features favorable to flexible electronics and supercapacitor electrodes, such as a large surface area, high flexibility, and good electrical conductivity. But, because they are densely packed, the small interstitial space between CNTs may be difficult for bacteria to enter the interstitial surfaces of the CNTs and may preclude bacterial colonization of surfaces and sufficient nutrient supply for robust bacterial growth. Logan and colleagues developed graphite fiber brush anodes with high surface area and high conductivity [23]. Qiao et al. reported a composite anode made of mesoporous titanium dioxide-polyaniline (TiO_2-PANI) capable of producing high power density [24]. Substrate transport, however, was limited by the partially opened porous structure of the anode. Xie et al. developed intertwined CNT-textile fibers containing large pores to increase the anolyte-biofilm-anode interfacial area [25]. Later, they modified the system by using a graphene-sponge anode with a stainless-steel current collector to reduce the cost of using textiles and sponge [26]. CNT-platinum modified graphite is another anode material developed by the Sharma group [27], in which the maximum power density of their MFCs was six times higher than that using bare graphite. Yong et al. used a graphene-PANI composite anode to obtain a power density much

higher than those using carbon cloth anodes [28]. Wang et al. also decorated the surface of graphene with poly(3,4-ethylenedioxythiophene) (PEDOT) through galvanostatic electropolymerization to fabricate a graphene-PEDOT hybrid anode [29]. Liu et al. formed nanoscale porous structure in the bulk of PEDOT via an in-situ electrochemical polymerization process to modify carbon cloth and carbon paper [30]. Numerous reports have described using PEDOT-based composites with other materials such as graphene, graphene oxide (GO), and CNTs, as electrodes in energy storage and optoelectronic devices [31-41]. For example, Xu et al. reported a hybrid material prepared from PEDOT and graphene that showed excellent transparency, electrical conductivity, and flexibility, as well as high thermal stability [40]. By in situ polymerization of PEDOT in the presence of reduced GO (rGO) and high molecular weight poly(4-styrenesulfonate) (PSS), a PEDOT:PSS/GO composite was developed for an organic thermoelectric device and dye-sensitized solar cell [33]. Ham et al. also improved electrical conductivity and flexibility of PEDOT:PSS/CNT composite via a layer-by-layer coating method [41].

Electrospinning is one of the most efficient techniques for manufacturing polymeric micro/nanofibers [42]. This method has been widely used to produce 3D extracellular matrix scaffolds in cell and tissue engineering, because electrospun fibers can provide not only a high surface area for cell attachment, but also a suitable pore size for cell infiltration, cell growth, and mass transport of nutrients, oxygen, growth factors, and waste [42]. Also, electrospinning has enabled the formation of electrically conductive nanofibers of various polymers and polymer-based blends, such as PANI [43], PANI-camphor sulfonic acid composite [44], and polypyrrole [45]. These nanofibers have well-defined morphology and physical stability, but often require adding a carrier polymer to improve the spinability of the intrinsically conductive polymer, thus

reducing the conductivity of the nanofiber products. To overcome this problem, various materials have been incorporated into the electrospinning process, including, for example, adding conductive polymer precursors that are converted into a conductive polymer via vapor-phase polymerization or by using core-shell coaxial electrospinning and then removing the non-conductive core [46-49].

In this paper, we present a high-performance miniature MFC incorporating a conductive PEDOT nanofiber-based porous anode within a 12 µL anolyte chamber (Figure 5.1a). The PEDOT nanofibers are formed by electrospinning poly(vinyl-pyrrolidone) (PVP) oxidant nanofibers and subsequent vapor-phase polymerization of 3,4-ethylenedioxythiophene (EDOT) monomer. The PEDOT nanofibers-based anode has a high conductivity of about 72 S/cm, allowing for good electron transfer, while its porous structure provides a large interfacial contact area between the anode and microbes (Figure 5.1b). PEDOT nanofibers have previously been reported [47], but their use as a 3D anode material for MFCs has yet not been explored. Our study shows the PEDOT nanofiber pore sizes are sufficient for bacterial penetration and transfer of substrates for attachment and growth of exoelectrogenic bacteria in the interior of the porous material (Figure 5.1c), thereby promoting electron transfer. Without any optimization of bacterial culture, the presented miniature MFC resulted in an improved volumetric power density (423 µW/cm^3 based on the total volume of anolyte chamber) and shorter start-up time (about one hour), using a pure *S. oneidensis* MR-1 culture as a model biocatalyst. With this improved performance, the miniature MFC potentially will provide a powerful tool to screen suitable bacterial species and mutant strains for large-size MFC-based bioenergy generation and for elucidating bacterial-mediated exoelectrogenic processes.

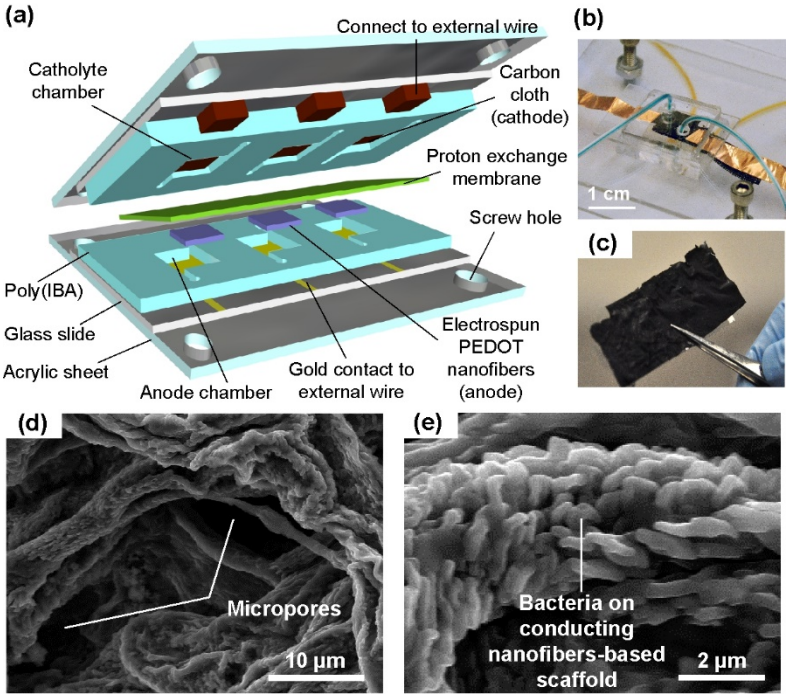

Figure 5.1 *(a) Schematic (not to the scale) of the miniature MFC. The parts of the device are separated to facilitate visualization of internal components. (b) An optical image of a single miniature MFC. (c) An optical image of the electrospun PEDOT nanofibers-based anode material. (d) Scanning electron microscopy (SEM) image of microscale pores formed within the PEDOT nanofibers-based porous anode. (e) SEM image of bacteria colonizing the PEDOT nanofiber surface.*

5.2 Experimental

5.2.1 Structure of miniature MFC

In this miniature MFC (Figure 5.1a), the anolyte and catholyte chambers are made of poly(isobornyl acrylate) or poly(IBA) on two respective glass slides and separated by a proton exchange membrane (PEM; thickness: 183 µm; Nafion 117; Fuel Cells Etc, College Station, TX). The anode is made of a conductive PEDOT nanofiber membrane electrospun onto a 100 nm thick gold electrode in the anolyte chamber (Figure 5.2h). The PEDOT nanofiber membrane is 100.6±13.5 µm (see details in Section 5.2.3). The anolyte chamber has an area of 10 mm×10 mm and a depth of 120 µm (Figure 5.2h). The total volume of the anolyte chamber is thus only 12 µL. Therefore, the space between the top surface of the PEDOT nanofiber membrane and the PEM is 19.3±13.5 µm high (Figure 5.2h). The catholyte chamber is 10 mm×10 mm in area and 375 µm in

height (Figure 5.2c). The cathode is made of fabric carbon cloth (thickness: 356 µm; model: 1071 HCB; Fuel Cell Store, College Station, TX). The cloth is trimmed to 14 mm × 40 mm, which is larger than the catholyte chamber (Figure 5.2c), and permits embedding and fixing 0.2 cm of one end of the carbon cloth strip inside the catholyte chamber structural material during the in situ polymerization process (Figure 5.2c, also described in Section 5.2.4). The other end of the carbon cloth strip is extended to the outside through the chamber structural material. Therefore, only a 10 mm×10 mm area of the carbon cloth is immersed in the catholyte (Figure 5.2c). This leaves a 19 µm separation between the carbon cloth cathode and the PEM. Independent supplies of the anolyte (culture medium) and catholyte are flowed into the corresponding chambers through the microfluidic tubing at the same flow rates. Multiple MFCs can be manufactured on a single substrate.

5.2.2 Electrospinning of PVP nanofibers

To electrospin PVP nanofibers, 0.3 g of PVP powder (1,300,000 g/mol; Sigma-Aldrich, St. Louis, MO) was dissolved in a mixture of 10 ml of Iron (III) p-toluene sulfonate (FeTos, Clevios CB40 V2; Heraeus, Santa Fe Springs, CA) and 10 µL of pyridine (0.5 mol mol^{-1} FeTos, Fisher Scientific, Fair Lawn, NJ) in a closed glass vial on a hotplate at 50 ˚C for 12 hours with a stirring rate of 200 rpm. The PVP precursor solution was delivered to a 10 mm diameter syringe with a stainless steel needle (18 gauge; Howard Electronic Instruments, El Dorado, KS). A syringe pump (KDS210; KD Scientific, Holliston, MA) was used to control the injection rate of the precursor solution. A high-voltage power supply (Gamma High Voltage Research, Ormond Beach, FL) was connected between the steel needle and an electrically grounded collector (a glass slide coated with a 100 nm thick gold electrode). The needle tip was 10 cm from the collector surface. The applied voltage was 15 kV. The flow rate of the polymer precursor solution was 0.65 mL/h. The

environmental relative humidity was controlled at 10% during electrospinning to avoid nanofiber liquidation. After 85 minutes of electrospinning, the thickness of the resulting PVP nanofiber membrane was about 93±12.2 μm (mean ± standard deviation of five independent measurements).

5.2.3 Vacuum vapour phase polymerization

Immediately after the PVP nanofibers were obtained, they were transferred to a vacuum chamber inside a chemical hood to minimize direct contact with the moist air. The liquid EDOT (Sigma-Aldrich, St. Louis, MO) was dripped into an opened vial placed on the bottom of the vacuum chamber and was vaporized to form monomer [47]. When the EDOT vapours came into contact with the PVP nanofibers, the nanofibers were progressively polymerized under vacuum. The polymerization process took 160 hours. After that, the nanofibers were kept inside the opened chamber for another 2 hours to ensure the evaporation process was completed. The resulting PEDOT nanofiber membrane (100.6±13.5 μm, mean ± standard deviation of five independent measurements) was slightly thicker than the original PVP nanofiber membrane (93.5±12.2 μm) mentioned above.

5.2.4 Miniature MFC fabrication

To fabricate the catholyte chamber, a 356 μm thick, 14 mm×40 mm carbon cloth (Nafion 117; Fuel Cell Store, College Station, TX) was placed on a glass slide (75mm×50mm×0.9mm; Corning, Tewksbury, MA) (Figure 5.2a). The inlet and outlet of the catholyte chamber was prepunched through the glass slide by a conventional milling machine with a 1 mm diameter diamond coated drill bit. Subsequently, the *in situ* liquid phase polymerization process was conducted to fabricate the catholyte chamber and to fix the carbon cloth cathode on the bottom of the chamber. In this step, 375 μm thick double sided tape (3M, St. Paul, MN) was used as spacers to create a 19 μm high cavity between the glass slide and a film photomask (Fineline Imaging,

Colorado Springs, CO) (Figure 5.2b). One end of the carbon cloth strip overlapped the film photomask by 0.2 cm. A photopatternable polymer solution was injected into the cavity using a plastic pipette (Figure 5.2b). The polymer solution was comprised of isobornyl acrylate (IBA), tetraethylene glycol dimethacrylate, and 2,2-dimethoxy-2-phenylacetophenone (all purchased from Sigma-Aldrich, St. Louis, MO) with a weight ratio of 32:1.7:1. The ultraviolet light intensity was set to 8.4 mW/cm^2 for a 20 second exposure, after which the catholyte chamber was formed by soaking the glass slide in 100% ethanol (Sigma-Aldrich, St. Louis, MO) for 2 minutes, followed by baking on a hotplate at 60 ºC for 1 hour (Figure 5.2c).

To form the analyte chamber, a 100 nm thick gold electrode was generated on another glass slide (75mm×50mm×0.9mm; Corning, Tewksbury, MA) by first depositing a 5 nm thick layer of titanium followed by a 100 nm thick gold layer using e-beam evaporation through an aluminium-based shadow mask (Figure 5.2d). Subsequently, the anode chamber was fabricated on the glass slide by the liquid phase polymerization process mentioned above. The materials and fabrication parameters used in making the anolyte chamber were the same as those used in making the catholyte chamber, except for using 120 µm thick double sided tape (3M, St. Paul, MN) as spacers (Figure 5.2e-f). The next step was to electrospin PVP nanofibers onto the gold electrode on the bottom of the anolyte chamber (Figure 5.2g). In this step, the gold electrode was electrically grounded. The process parameters were the same as those described in Section 5.2.2. The thickness of the electrospun PVP was about 93 µm (the same as that mentioned in Section 5.2.2). Because the PVP nanofibers were also deposited over the whole surface of the glass slide, the nanofibers outside of the anolyte chamber were carefully removed by a razor blade. Subsequently, a 100.6±13.5 µm thick PEDOT nanofiber-based membrane (the same as that mentioned in Section 5.2.2) was formed by using the aforementioned vacuum vapor phase polymerization process

(Figure 5.2h). Therefore, the gap between the PEDOT nanofiber-based membrane (formed on the 100 nm thick gold electrode) and the top surface of the anolyte chamber (120 µm thick) was 19.3±13.5 µm (Figure 5.2g).

The PEM (thickness: 183 µm; Nafion 117; Fuel Cells Etc, College Station, TX) was pretreated by sequentially boiling in hydrogen peroxide (30% v/v; Fisher Scientific, Fair Lawn, NJ) and deionized (DI) water, followed by soaking in 0.5 M sulfuric acid solution (Fisher Scientific, Fair Lawn, NJ) and then DI water, each for hour [5]. The activated PEM was stored in DI water before assembly.

Lastly, the MFC device was constructed by assembling all the components shown in Figure 5.1a. These components were clamped between two acrylic plates (100 mm×80 mm×3 mm; TAP Plastics, Oakland, CA) held together by cap screws (M4×0.7; Thorlabs, Newton, NJ) (Figure 5.2i). To build the electrical connections, copper tape (Sparkfun, Niwot, CO) was used to extend the anode and cathode (Figure 5.2j). The anolyte and catholyte chambers were accessed by polyethylene sterile tubing (Coleparmer, Vernon Hills, IL) through the inlet and outlet of the device.

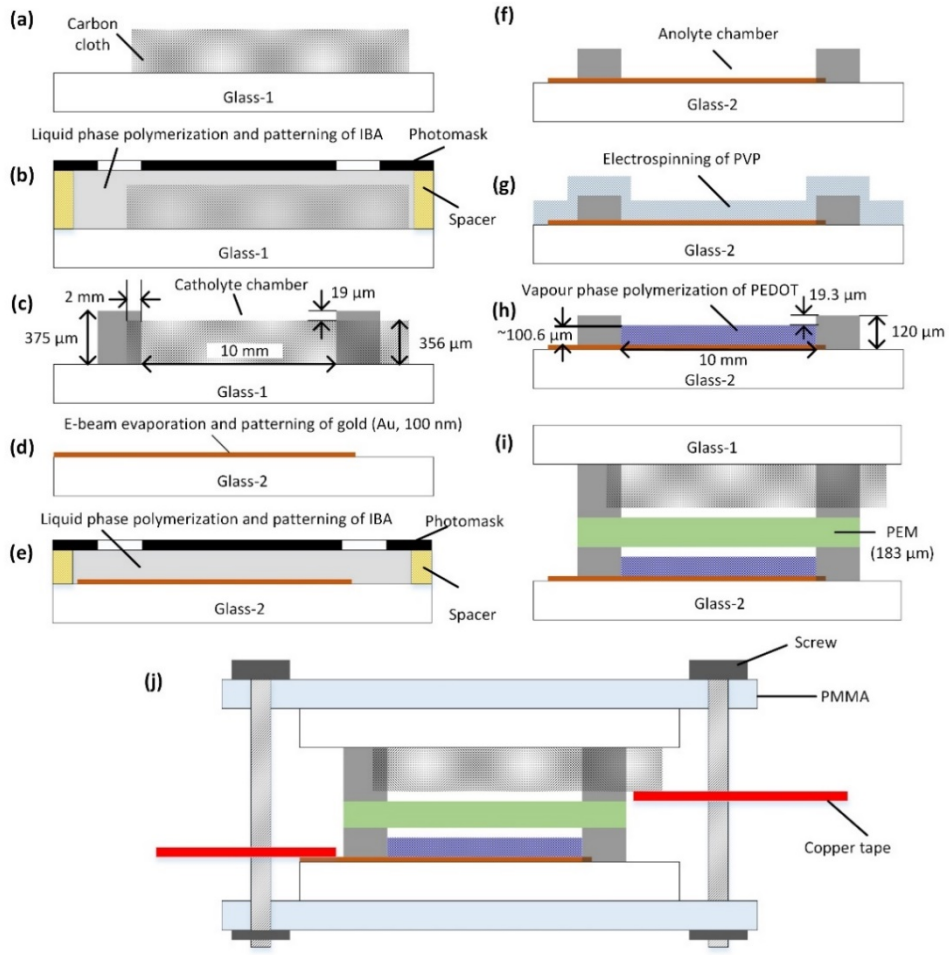

Figure 5.2 *Schematic (not to the scale) of the fabrication process flow for the miniature MFC device.*

5.2.5 Cell inoculation

The MFC device and tubing were sterilized by filling all of compartments with 70% ethanol and letting it sit for 20 minutes at room temperature. Subsequently, the device was flushed with 5 ml sterile water and then 5 ml culture medium (Tryptic soy broth, TSB; Sigma-Aldrich, St. Louis, MO). To operate the device, *Shewanella oneidensis* strain MR-1 was used as the model exoelectrogenic microbial biocatalyst. TSB was the nutrient source, which flowed into the anolyte chamber through the polyethylene tubing. To minimize possible oxygen contamination in the batch mode operation, the tubing was closed by steel clamps after the bacterial suspension was flowed

into the analyte chamber. The catholyte solution (potassium ferricyanide, $K_3[Fe(CN)_6]$; Fisher Scientific, Fair Lawn, NJ) was continuously supplied (10 µL/h) using a syringe pump.

5.2.6 Electrochemical measurements and calculations

Electrochemical properties of the PEDOT nanofibers were measured in phosphate buffer saline solution (pH = 7.0; Sigma-Aldrich, St. Louis, MO) containing 5 mM $[Fe(CN)_6]^{3-}$ as a redox species, by a potentiostat (DY2100B; Digi-Ivy, Austin, TX). A platinum wire was used as the counter electrode and a silver/silver chloride (Ag/AgCl) was used as the reference electrode. To measure the electricity generation capability of the MFC device, an external resistor was connected between the anode and cathode to form a closed circuit. The voltage potential U between the two electrodes was measured using a digital multimeter (Agilent 34401A; Santa Clara, CA) connected to a computer through an RS-232 port. Data was recorded every minute. The current I flowing through the resister was calculated via Ohm's law: $I=U/R$, where R is the resistance of the external resistor. The output power P was calculated as $P=U\times I$. The shunt current was measured to obtain the maximum output current. It's noted that each electrochemical/electrical measurement result given in this paper is representative of the typical result obtained over five independent experiments on five identical devices.

5.2.7 Bacterial fixation for SEM

For SEM images of the nanofibers-based biofilm, the MFC was disassembled, immersed in a glutaraldehyde solution (2%; Sigma-Aldrich, St. Louis, MO) to fix the adherent bacteria on the anode surface and incubated at 4 ºC for 12 hours. After rinsing with DI water, the anode was stained with 1% osmium tetroxide solution (Sigma-Aldrich, St. Louis, MO) for 2 hours, rinsed again, and then, dehydrated by pure ethanol. The treated sample was examined by a field-emission SEM (Quanta-250; FEI, Hillsboro, OR).

5.3 Results and discussion

Figure 5.3a-b display SEM of the electrospun PVP nanofibers and the PEDOT nanofibers synthesized using the vacuum vapor-phase polymerization. The PVP nanofibers had the diameter of 740±245 nm (mean ± standard deviation of five independent measurements), while after the polymerization with EDOT monomers the resulting PEDOT nanofibers had an increased diameter of 810±215 nm (mean ± standard deviation of five independent measurements). At the beginning of the polymerization process, the EDOT monomers were polymerized as a thin layer at the surface of the PVP nanofibers. As the reaction time went to 160 hours, the PEDOT nanofibers were formed. Figure 5.3c shows a transmission electron microscopy (TEM) image of the PEDOT nanofibers, indicating the original PVP nanofibers were almost all polymerized to form PEDOT nanofibers. Raman spectroscopy was used to characterize the PEDOT nanofibers (Figure 5.3d). The peaks at 996, 1139, and 1364 cm^{-1} are due to oxyethylene ring deformation, C-O stretching, and C-C stretching in plane modes, respectively. The dominant peaks at 1447 and 1505 cm^{-1} result from C=C stretching in plane modes (antisym.) and C=C stretching in plane modes (sym.), respectively. The peaks at 1594 and 1641 cm^{-1} are due to quinoid structure and thiophene ring vibration of the nanofibers, respectively. Also, by using a four-point probe system (FPP-100, Veeco Instruments, Plainview, NY), the electrical conductivity of the resulting PEDOT nanofiber membrane (~100.6 μm thick) was found to be as high as 72±5.2 S/cm (mean ± standard deviation of ten independent measurements).

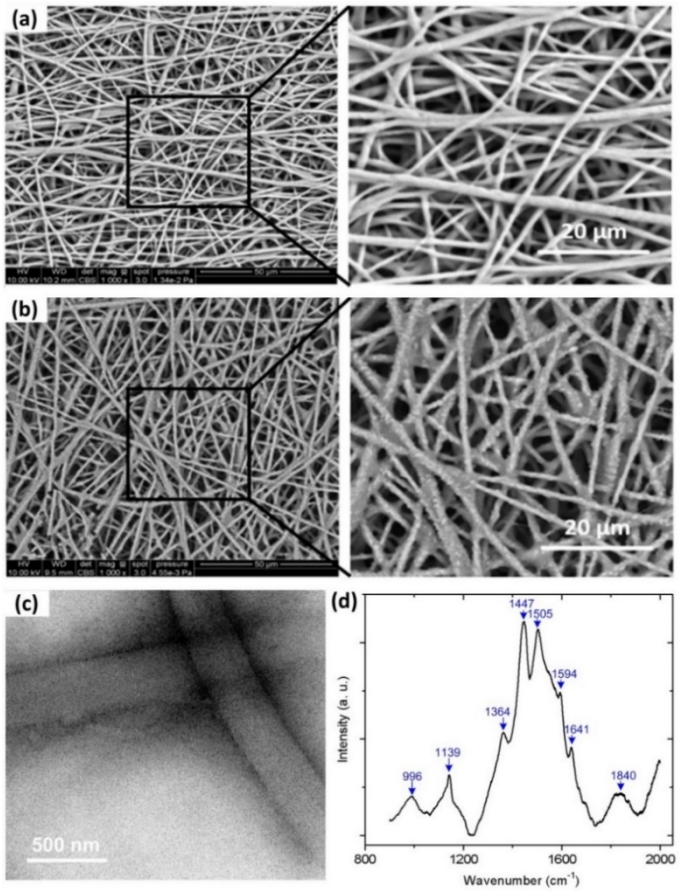

Figure 5.3 *(a) SEM image of typical electrospun PVP nanofibers. (b) SEM image of typical PEDOT nanofibers after the vacuum vapour-phase polymerization of EDOT monomers. (c) TEM image of the PEDOT nanofibers. (d) Raman spectrum of the PEDOT nanofibers.*

Figure 5.4a shows the cyclic voltammetry measurements of the PEDOT nanofibers. At the scan rate of 50 mV/s, an oxidation peak and a reduction peak was observed at 0.24 V and 0 V, respectively. These peaks were well-defined, confirming the good conductivity of the anode material. The measurement was also performed at different scan rates. It was found that the anodic peak current was linearly proportional to the scan rate ranging from 10 mV/s to 50 mV/s. This result indicates that the redox reaction was a diffusion-controlled process. Also, the current stability was tested over 10 cycles at the scan rate of 50 mV/s (Figure 5.4b), where a slight fluctuation was observed but the overall trend was almost flat.

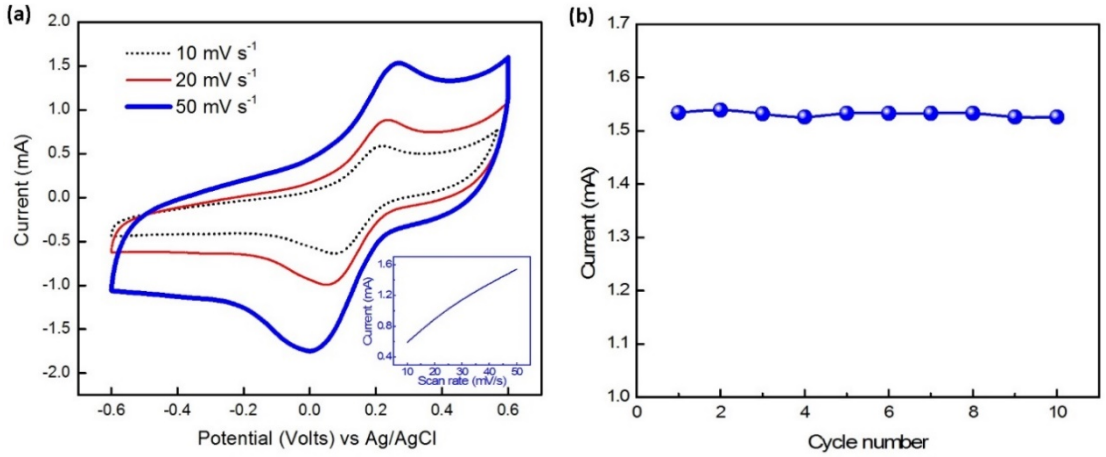

Figure 5.4 *(a) Cyclic voltammograms of the PEDOT nanofibers measured in PBS at a scan rate of 10, 20, and 50 mV/s. The inset shows the current vs. scan rate. (b) Current during cycling at 50 mV/s. The counter electrode was made of a platinum wire. The reference electrode was made of an Ag/AgCl wire.*

To evaluate the performance of the MFC in the batch mode operation, the device was cleaned by rinsing in 100% ethanol for 1 hour, followed by blow-drying in a stream of nitrogen gas for 5 minutes. Electrical generation was tested by using a closed circuit carrying an external resistive load of 10 kΩ. TSB medium was injected into the anolyte chamber through the inlet. The background current, without presence of *S. oneidensis* bacteria, was only 22±10 nA (mean ± standard deviation of five independent measurements). After 2 hours, TSB medium containing bacteria was injected into the anolyte chamber. After the chamber was filled, the flow was stopped, and then, two clips were used to pinch closed the microfluidic tubing. As shown in Figure 5.5, in the first batch of cell inoculation, the output current rapidly increased to 9.5 µA within 1 hour and then decreased over the next 7 hours. Once the current dropped to the baseline, fresh TSB medium was infused into the anolyte chamber. Within an hour after supplying fresh medium there was a dramatic increase in current output, which exceeded the output following the initial inoculation and was about 3-orders of magnitude greater than the background current. This pattern was observed repeatedly whenever fresh medium was supplied in a 14-hour cycle. It is worth noting that the response time for the current generation after inoculation was much shorter than for

conventional large size MFCs that often have a lag period of days in large-scale devices [50]. As mentioned earlier, the background current of the miniature MFC without inoculation was considerably lower than that after inoculation of *S. oneidensis* MR-1 culture in TSB medium. Also, the inoculum was not manipulated prior to delivering it to the anolyte chamber. Therefore, the fast current response of the miniature MFC is believed to benefit from using the PEDOT nanofibers-based anode. We presume that the porosity of the nanofibers permitted greater bacterial colonization of internal surfaces and diffusion of growth medium into the interior of the nanofiber membrane compared to other systems. Consequently, there are greater bacteria-anode interactions facilitating electron transfer.

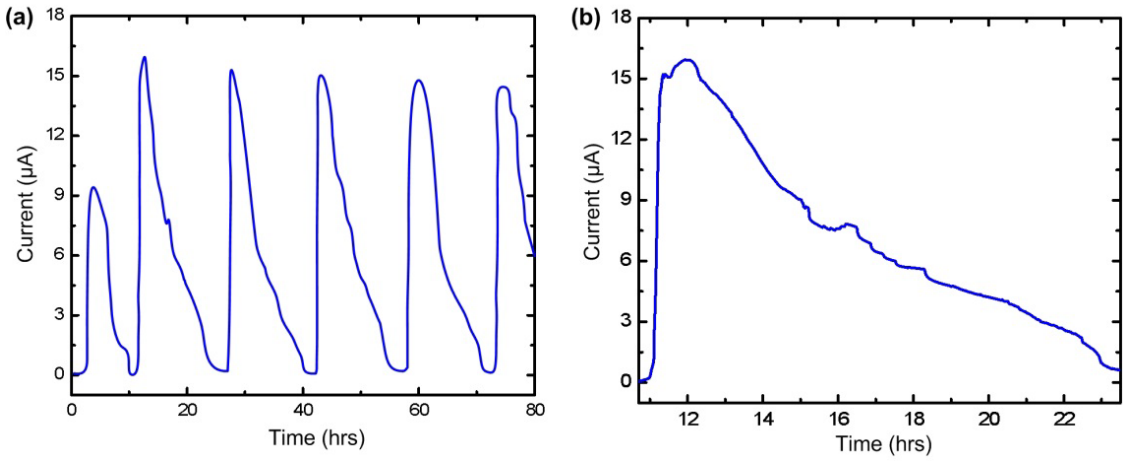

Figure 5.5 *(a) Current output of the MFC in the batch mode operation over 80 hours in response to inoculation with S. oneidensis MR-1 culture in TSB growth medium followed by repeated additions of fresh medium once current output returned to zero; (b) A close up of the current vs. time in the period of t = 10.5 to 23.5 hours.*

By measuring the output voltage and current of the device at different external resistive loads, we generated polarization and power density curves (Figure 5.6a). According to the literature [1], polarization curves can be divided into three regions reflecting activation loss (region 1), ohmic loss (region 2), and mass transfer loss (region 3). At the activation loss stage, the current increased from 0 (at the open circuit voltage of 380 mV) to 3.5 μA. Due to the need of activation

energy for oxidation reactions, the activation loss occurred at the surface of the anode during the electron transfer. As the external resistance decreased, the output voltage reduced. The output voltage decreased linearly with current when the current fell in the current range from 3.5 μA and 18 μA. The internal resistance of 7.5 kΩ was obtained through linear fitting of the curve in the ohmic region (see "region 2" in Figure 5.6a). Also, R^2 value (a common statistical measure of how close the data are to the fitted regression line) shows that 97.6% of the variability in voltage can be explained by the predicted value from a linear regression model using the output current as the explanatory variable (not shown). In addition, the output power density reached a maximum value of 2.25 μW/cm^2 in the ohmic region. In contrast, the output voltage decreased dramatically in the mass transfer loss region 3 where mass transport of organic materials was limited.

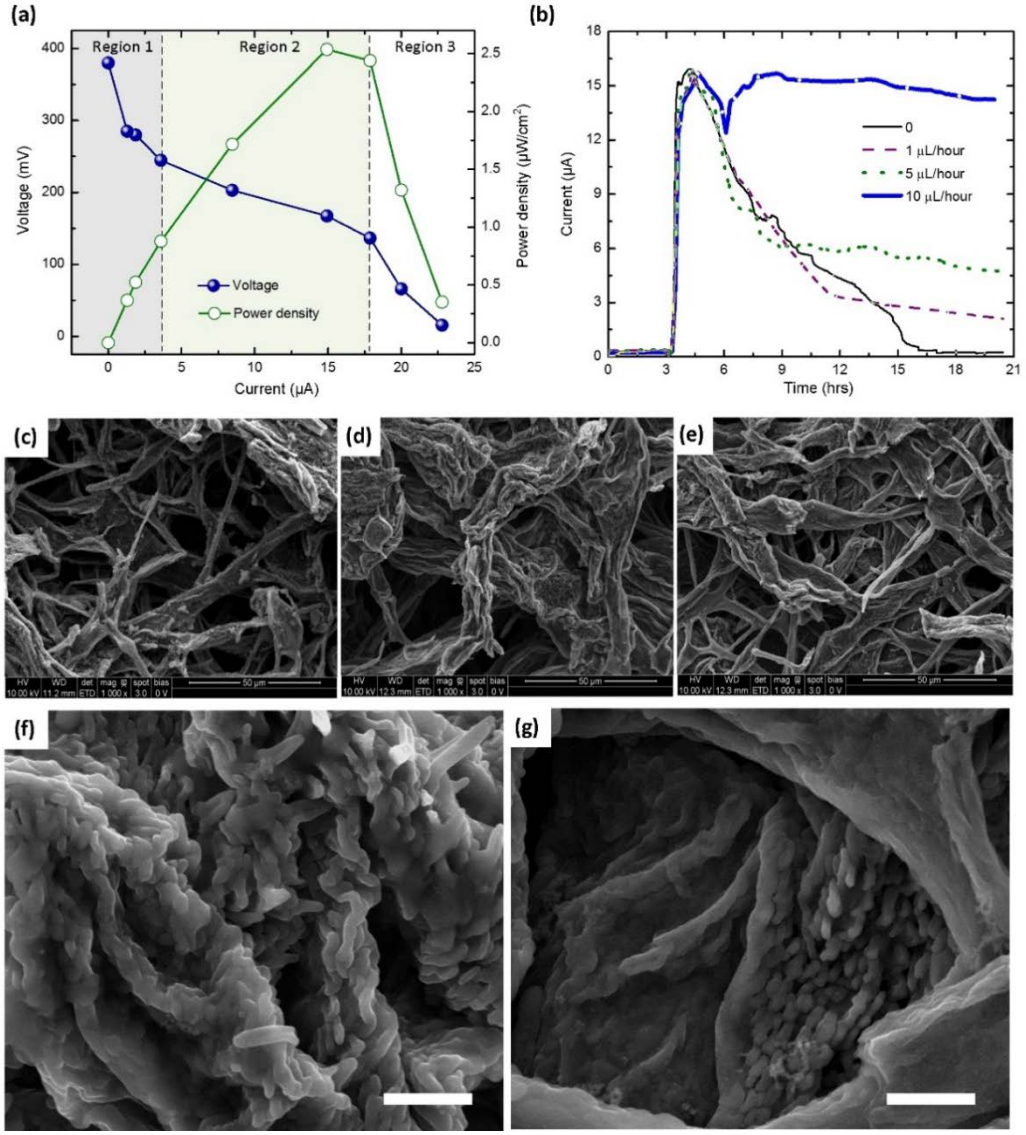

Figure 5.6 *(a) Polarization and power density output of the miniature MFC as a function of current. (b) Output current at different flow rates in the continuous flow mode. (c-e) SEM images of the PEDOT nanofibers covered by S. oneidensis strain MR-1 grown at different TSB culture medium feeding rates: 1 µL/h (c), 5 µL/h (d), and 10 µL/h (e). (f-g) A close up showing bacteria coating the interior surface of the PEDOT nanofibers membrane at a flow rate of 10 µL/h. Scale bars represent 3 µm.*

To investigate the influence of the nutrient medium (TSB) flow rate on current generation we operated the MFC in a continuous-flow mode by continuously injecting the growth medium into the anolyte chamber at different rates. The flow rate of the catholyte was also adjusted to be the same as that of the anolyte. Four identical MFCs were used and inoculated similarly as described in Section 2.5 prior to loading the anolyte chamber with fresh TSB medium for batch

mode operation (starting at 3 hours). During the batch mode operation, the output current signals from the four devices were almost identical. When an obvious current drop was observed (at 5 hours), the continuous flow mode operation was started on three devices by infusing fresh TSB medium into their anolyte chambers at different flow rates (1 µL/hr, 5 µL/hr, and 10 µL/hr). The other device continued operating in the batch mode. The result shows that at a high flow rate (10 µL/h) the output current rose to 16 µA and then transiently dropped to 12 µA (see the blue curve in Figure 5.6b) before returning to near maximal levels. With decreasing flow rate, there was a corresponding increase in length of time before current output stabilized at a particular level (see purple and green lines in Figure 5.6b). In the absence of flow, current output steadily decreased until there was no current generated, presumably because cells were no longer metabolically active due to nutrient deprivation. A possible explanation is that as flow rates decrease it takes longer for biofilms to develop on the anode surfaces and once established they are able to maintain (1 µL/h and 5 µL/h) or increase (10 µL/h) current output. Clearly, the higher the flow rate the greater the output current the device could produce.

To assess the extent of *S. oneidensis* biofilm formation on the PEDOT nanofibers, we examined them by SEM following the continuous-flow mode operation as described above. Figure 4.6c-e shows that the PEDOT nanofibers of the three devices at the medium flow rates of 1 µL/h, 5 µL/h, and 10 µL are all covered by microbes. While it's not easy to determine thickness of the biofilm grown on the cylindrical surface of the nanofibers, we speculate that the higher medium flow rates may lead to forming thicker biofilms on the surface of the nanofibers. To examine whether or not *S. oneidensis* was able to colonize interior regions of the porous nanofiber membrane, we dissected the membrane to expose the interior of the anode. The SEM images (Figure 5.6f-g) show that the surfaces of the interior fibers were accessible to *S. oneidensis*.

In addition, we investigated the influence of the thickness of the PEDOT nanofiber membrane on the output current of the MFC in the continuous-flow mode at the fixed flow rate of 10 µL/h. As shown in Figure 5.7a, output current for nanofiber membranes of varying thickness exhibited similar trends where current rapidly reached a maximum, dropped slightly, and then returned to and maintained the maximal level. What differed was that with increasing thickness there was a corresponding increase in current output (Figure 5.7b). The result is an obvious consequence of increasing the quantity of nanofibers in the thicker membrane, thus increasing the quantity of pores and the total surface area for biofilm formation inside the anode. Unexpectedly, Figure 5.7b shows that current generation was not linearly correlated with nanofiber membrane thickness. This could be because, given the same anode material, the thicker membranes had not only a larger number of pores formed by the randomly distributed nanofibers, but a smaller statistical mean pore size, which in turn, increases the surface area-to-volume ratio of thicker membranes. To test this hypothesis, the mean pore sizes of the nanofiber membranes were measured by using a capillary flow porometer (CFP-1100, PMI, Ithaca, NY). We determined that the mean pore size decreased almost linearly with membrane thickness. Specifically, the mean pore size was 12.1±3.6, 10.2±3.3, 8±2.4, 5.9±2.3, and 3.9±2.3 µm (mean and standard deviation of five independent measurements each) when the membrane thickness was 12.3±3.7 µm, 25.3±5.1 µm, 50±8.7 µm, 75±12.2 µm, and 100.6±13.5 µm, respectively (mean and standard deviation of five independent measurements). However, it is still challenging to determine if the increase in current is mainly due to reduction in pore size or increase in membrane thickness. Nevertheless, because the mean pore size of nanofiber membranes can be controlled easily by varying electrospinning time, this may be important for optimizing the anode structure for improving device performance in the future.

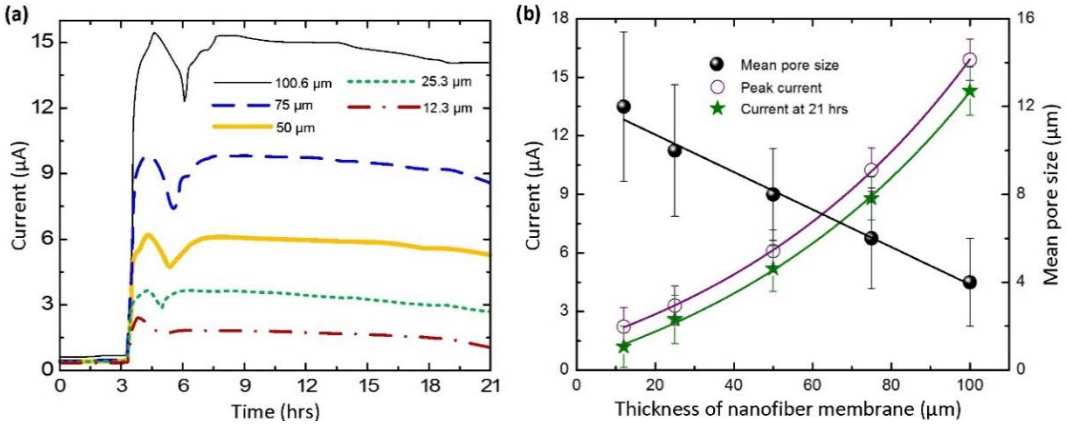

Figure 5.7 *(a) Effect of nanofiber membrane thickness on output current during continuous-flow mode over a 21 h period; (b) The peak current and the current at 21 hours (left y-axis), and the mean pore size of the corresponding nanofiber membrane (right y-axis), as a function membrane thickness. Error bars were obtained by taking the standard deviation of five independent membranes.*

Table 5.1 compares the performance of the present miniature MFC with other previously reported MFCs (both miniature and large-scale types). It should be noted that due to using different device structures and different cultures, it may be difficult to make point-to-point comparisons of power densities normalized to the anode surface area and the volume of the entire anolyte chamber. With the same *S. oneidensis* strain MR-1, our device demonstrated a remarkable volumetric power density of P_{vc} = 423 μW/cm^3, which represents a high value reported for miniature MFCs with *S. oneidensis* MR-1 culture. However, in comparison to the output power density based on the planar anode surface area, the recently reported large-scale MFCs using graphite plates [51] and graphene-based foams [28, 52] as anode materials with the same MR-1 culture are superior to our device. When compared to the MFCs using graphene-PEDOT composite [29] and PEDOT decorated carbon paper/cloth [30] with different cultures, our device provides higher volumetric power density but lower surface area power density. The greater surface area power density of these large devices is presumably because their anolyte chambers are 4-5 orders of magnitude larger than our device, thus providing more nutrients for bacterial metabolic activity. Clearly, the power density of our device is also limited by the electron producing capability of strain MR-1.

Nevertheless, our device still shows higher volumetric power density than many other MFCs in Refs. [16, 19, 23, 25, 26, 29, 30, 53-59, 61] except the miniature devices using *Geobacteraceae*-enrichment culture in Refs. [6, 10-12]. We believe that by using optimally mixed bacterial cultures, the electricity generation capability of our device will be further enhanced. It should be also noted that our device exhibits faster startup than counterpart devices but comparable to the devices reported in Ref. [4] (using MR-1 culture) and Ref. [9] (using *Shewanella* and *Pseudomonas* sp. culture). The faster startup may be attributed to the enhanced bacteria-anode interaction on the interior surface of the nanofiber membrane in the small 12 μL anolyte chamber that may accelerate startup in batch mode.

Table 5.1 *Performance comparisons between the presented miniature MFC and other MFC devices (including both miniature and large-size ones). The upper part of the table includes the MFCs using the same S. oneidensis strain MR-1 as a model biocatalyst. The lower part includes the devices using other biocatalysts.*

Biocatalyst	Anode/area (cm^2)	Cathode/area (cm^2)	Total anolyte chamber volume (µL)	Startup time	Current density ($\mu A/cm^2$)	Power density (P)		Ref.
						Ps ($\mu W/cm^2$)[a]	Pvc ($\mu W/cm^3$)[b]	
***S. oneidensis* MR-1**	PEDOT nanofibers/1	Carbon cloth/1	12	~1 hr	16	2.54	423	This work
	Carbon cloth/0.4	Carbon cloth/0.4	4	6 hrs	10	0.62	62.50	[7]
	Au/0.15	Carbon cloth/0.4	1.50	12 hrs	13	0.15	15.30	[5]
	Au/0.38	Carbon cloth/0.38	154	< 2 hrs	1.64	0.37	0.93	[4]
	Au/0.38	Carbon cloth/0.38	400	< 13 hrs	N/A	2.35	N/A	[8]
	Graphite plate/1.92	Carbon bonded to Pt mesh/828	8×10^5	N/A	N/A	329	0.79	[51]
	Graphite plate/155	Carbon bonded to Pt mesh/828	8×10^5	N/A	N/A	141	27	[51]
	Graphene-PANI foam/1	Carbon cloth/8	1.81×10^5	N/A	N/A	76.8	0.42	[28]
	Graphene-Ni foam/7~10	Carbon cloth/70	2.5×10^4	N/A	71.43	96.43	27	[52]
Escherichia coli	Graphene-PEDOT hybrid/5	Carbon paper/12	1×10^5	N/A	359	87.3	4.36	[29]
S. loihica strain PV-4	PEDOT-carbon paper (carbon cloth)/7.06	Carbon cloth/NA	2.8×10^4	N/A	1.8	14	3.53	[30]
Escherichia coli	PPy-CNTs-carbon paper/7	Carbon paper/7	1×10^5	N/A	N/A	22.8	1.6	[61]
Geobacter sp.	CNT-polymer/0.5	Au/0.5	12.5	5-7 days	259	83	3320	[10]
***Geobacteraceae*-enrichment culture**	Au/2.25	Au/2.25	4.5	2 days	33	4.70	2300	[6]
Geobacter sulfurreducens	Au/0.01	Coiled Au wire/1	350	10 days	140	12	0.34	[53]
***Shewanella* and *Pseudomonas* sp.**	Au/0.06	Au/0.06	1.5	< 2 hrs	1	N/A	N/A	[9]
***Geobacteraceae*-enrichment culture**	Au/3	Au/3	150	20 hrs	26.67	33	667	[12]
***Geobacteraceae*-enrichment culture**	Au/4	Au/4	100	6 days	214	83	3330	[11]
***Domestic wastewater*[c]**	CNT-textile/1	Carbon cloth/10	2×10^5	12 days	720	109.8	1.10	[25]
***Domestic wastewater*[c]**	Graphene-sponge/1	Carbon cloth/10	1.5×10^5	N/A	132	157	1.05	[26]

Table 5.1 continued

Biocatalyst	Anode/area (cm^2)	Cathode/area (cm^2)	Total anolyte chamber volume (μL)	Startup time	Current density ($\mu A/cm^2$)	Power density (P)		Ref.
						Ps ($\mu W/cm^2$)[(a)]	Pvc ($\mu W/cm^3$)[(b)]	
Primiary clarifier overflow	Carbon paper/22.5	Carbon cloth/4.9	3×10^5	N/A	N/A	60	0.98	[23]
Preacclimated bacteria from an active MFC	Carbon Brush/2200	Carbon cloth/7	2.6×10^4	N/A	N/A	240	73	[23]
Preacclimated bacteria from an active MFC	Carbon cloth/7	Carbon cloth/7	1.2×10^4	N/A	N/A	78.6	46	[54]
Preacclimated bacteria from an active MFC	Carbon mesh/7	Carbon cloth/N/A	N/A	N/A	N/A	89.3	45	[55]
D.desulfuricans strain Essex 6(for sulfate removal)	Activated carbon cloth/1.5	Carbon cloth/1.5	1.8×10^4	N/A	N/A	510	42.5	[19]
Preacclimated bacteria from an active MFC	Granular graphite/N/A	Graphite mat/N/A	3.9×10^5	100 hrs	N/A	N/A	90	[56]
Preacclimated bacteria from an active MFC	Graphite felt/N/A	Graphite granules-Graphite rod/N/A	1.56×10^5	12 days	N/A	N/A	386	[57]
Preacclimated bacteria from an active MFC	Carbon felt/N/A	Graphite granules-Graphite rod/N/A	1.56×10^5	12 days	N/A	N/A	356	[57]
Domestic wastewater	Granular activated carbon/6	Carbon cloth/6	4.5×10^5	N/A	N/A	375	5	[58]
Anaerobic sludge from an anaerobic bioreactor treating brewery wastewater	Reticulated vitreous carbon/97	RVC/194	1.9×10^5	3 days	N/A	17	8.67	[59]
Marine sediments	Stainless steel plate/1200	Stainless steel plate/1200	2×10^5	9 days	14	2.3	13.8	[16]
Preacclimated bacteria from an active MFC	Pt-coated Titanium/22	Graphite plate/22	3.3×10^4	N/A	420	N/A	N/A	[60]

[(a)] Calculation based on the planar surface area of the anode electrode.
[(b)] Calculation based on the volume of the entire anolyte chamber.
[(c)] The domestic wastewater contains a diverse microbial community including *Alphaproteobacteria*, *Betaproteobacteria*, *Gammaproteobacteria*, *Deltaproteobacteria*, *Bacteroidetes*, *Flavobacteria*, *Bacilli*, *Clostridia*, *Spirochaetes*, and unclassified.

Table 5.2 compares the conductivity, material form, and fabrication method between the present PEDOT nanofibers with many other conducting materials. As it is difficult to cover the entire literature, a few notable ones on PEDOT-based conducting composites (incorporating graphene, GO, CNT, and etc) and other nanomaterials are listed. Also, as most MFC literature

does not mention exact conductivity values of their anode materials, the table includes the conducting composites research articles that mention conductivity values, but are not necessary with the topic of MFC applications. The conductivity comparison shows that the PEDOT nanofibers are competitive with the PEDOT-based nanocomposites listed in Refs. [31, 34, 36, 37, 39], but not with those incorporating single wall CNTs [32, 35], sulfuric acid treated reduced GO [38], and graphene through in-situ polymerization [33]. When compared to individual graphite fibers of a graphite fiber brush-based anode [23], sprayed CNTs [62], and graphene/reduced GO composite [63], the PEDOT nanofibers show relatively lower conductivity. But, the PEDOT nanofibers are still superior in terms of conductivity to the other nanomaterials [64-68] listed in the second half of the same table. While some composites provide higher conductivity than the PEDOT nanofibers, they are mainly nanocomposite films with small pore size or limited intestinal space supposedly not suitable to increasing bacteria loading capacity. In contrast, the PEDOT nanofibers not only have good conductivity (about 72 S/cm), but also provide extracellular matrix scaffolds with controlled mean pore size (several micrometers or more) suitable to promoting robust bacterial growth and nutrient supply.

Table 5.2 *Comparisons between the present PEDOT nanofibers and other conducting materials. The upper half of the table lists the PEDOT composites with other materials. The lower half of the table lists non-PEDOT based composites.*

Anode	Material form	Conductivity (S/cm)	Fabrication method	Ref.
PEDOT nanofibers	Stacking nanofibers	72±5.2	Electrospinning and VPP	This work
PEDOT/nylon 6	Fabrics	1.89	Polymerization of EDOT monomer on nylon 6	[31]
PEDOT:PSS/polyethylene glycol functionalized single wall CNTs	Fibers (10-12 μm)	400	Wet spinning	[32]
PEDOT:PSS/graphene	Nanocomposite film	637	In situ polymerization	[33]
PEDOT:PSS/graphene	Nanocomposite film	32.13	Spin coating	[34]
PEDOT:PSS/single wall CNTs	Nanocomposite film	400	Coating CNTs with PEDOT:PSS particles	[35]
PEDOT/reduced GO	Nanocomposite film	50.8±5.9	Template-directed in situ polymerization	[36]
PEDOT/graphene in saturated hydrogel.	Nanocomposite film	0.73	In situ polymerization	[37]
PEDOT:PSS/reduced GO treated with H_2SO_4.	Nanocomposite film	180	Solution mixing and oxygen reduction reaction	[38]
Ethylene glycol-PEDOT:PSS/multi wall CNTs	Nanocomposite film	1.67	Coating	[39]
Graphite fiber brush	Brush	645 (single fiber, 7.2 μm diameter)	Cutting of carbon fibers	[23]
CNTs	Sprayed CNTs	150-200	Spraying	[62]
Graphene/reduced GO	Nanocomposite Film (10 nm thick)	550	Dip coating of GO, followed by reduction	[63]
Single-wall CNTs	Incubated CNTs on fabric surface	13.8	Nanotubes incubated	[64]
Multi-wall CNTs/NiSi	Vertically aligned CNTs with NiSi	4.76	Growth with controlled and uniform shapes	[65]
Graphene/1-pyrenebutyrate	Thin sheet	2	Filtration	[66]
Graphene/GO-SiO_2	Nanocomposite film (28 nm thick)	0.45	Spin coating of reduced GO-SiO_2 composite	[67, 68]

While the output power density of conventional MFCs often dramatically decrease with scaling down the device size due to insufficient biofilm formation on the anode, our PEDOT nanofibers-based anode, in conjunction with inexpensive microfabrication methods, has great potential to obtain high-performance microliter-sized MFCs for screening of bacterial species and mutant strains. Future work will be made to develop and integrate an array of the presented miniature MFC devices with a microfluidic control system to realize a high-sensitivity, high-

throughput screening platform, to select suitable bacterial species and strains for use in large-scale MFC-based energy harvesting systems.

5.4 Conclusions

The miniature MFC design resulted in a high volumetric power density of 423 μW/cm^3 based on the volume of the anolyte chamber (12 μL) and a short startup time of one hour, using a pure *S. oneidensis* MR-1 culture as a model biocatalyst without optimization of bacterial culture. The conducting PEDOT nanofibers provided not only a large effective surface area, but a suitable mean pore size to facilitate the transport of bacteria to the interior of the anode and the delivery of the growth medium to the attached bacteria, thus promoting the development of metabolically active biofilms within the 3D anode.

References

1. B. E. Logan, B. Hamelers, R. A. Rozendal, U. Schrorder, J. Keller, S. Freguia, P. Aelterman, W. Verstraete and K. Rabaey, *Environ. Sci. Technol.*, 2006, **40**, 5181-5192.

2. J. Wei, P. Liang and X. Huang, *Bioresour. Technol.*, 2011, **102**, 9335-9344.

3. J. Biffinger, M. Ribbens, B. Ringeisen, J. Pietron, S. Finkel and K. Nealson, *Biotechnol. Bioeng.*, 2009, **102**, 436-444.

4. H. Hou, L. Li, Y. Cho, P. de Figueiredo and A. Han, *Plos One*, 2009, **4**, e6570.

5. F. Qian, M. Baum, Q. Gu and D. E. Morse, *Lab Chip*, 2009, **9**, 3076-3081.

6. S. Choi, H.-S. Lee, Y. Yang, P. Parameswaran, C. I. Torres, B. E. Rittmann and J. Chae, *Lab Chip*, 2011, **11**, 1110-1117.

7. F. Qian, Z. He, M. P. Thelen and Y. Li, *Bioresour. Technol.*, 2011, **102**, 5836-5840.

8. H. Hou, L. Li, C. U. Ceylan, A. Haynes, J. Cope, H. H. Wilkinson, C. Erbay, P. de Figueiredo and A. Han, *Lab Chip*, 2012, **12**, 4151-4159.

9. S. Mukherjee, S. Su, W. Panmanee, R. T. Irvin, D. J. Hassett and S. Choi, *Sensors Actuators A*, 2013, **201**, 532-537.

10. H. Ren, S. Pyo, J.-I. Lee, T.-J. Park, F. S. Gittleson, F. C. C. Leung, J. Kim, A. D. Taylor, H.-S. Lee and J. Chae, *J. Power Sources*, 2015, **273**, 823-830.

11. H. Ren, C. I. Torres, P. Parameswaran, B. E. Rittmann and J. Chae, *Biosens. Bioelectron.*, 2014, **61**, 587-592.

12. S. Choi and J. Chae, *Sensors Actuators A*, 2012, **177**, 10-15.

13. S. Choi, *Biosens. Bioelectron.*, 2015, **69**, 8-25.

14. H.-Y. Wang, A. Bernarda, C.-Y. Huang, D.-J. Lee and J.-S. Chang, *Bioresour. Technol.*, 2011, **102**, 235-243.

15. H. Ren, H.-S. Lee and J. Chae, *Microfluid. Nanofluid.*, 2012, **13**, 353-381.

16. C. Dumas, A. Mollica, D. Feron, R. Basseguy, L. Etcheverry and A. Bergel, *Electrochim. Acta*, 2007, **53**, 468-473.

17. S. Cheng, H. Liu and B. E. Logan, *Environ. Sci.Technol.*, 2006, **40**, 2426-2432.

18. B. Min and B. E. Logan, *Environ. Sci.Technol.*, 2004, **38**, 5809-5814.

19. F. Zhao, N. Rahunen, J. R. Varcoe, A. Chandra, C. Avignone-Rossa, A. E. Thumser and R. C. T. Slade, *Environ. Sci.Technol.*, 2008, **42**, 4971-4976.

20. X. Wang, S. Cheng, Y. Feng, M. D. Merrill, T. Saito and B. E. Logan, *Environ. Sci.Technol.*, 2009, **43**, 6870-6874.

21. S. Cheng and B. E. Logan, *Electrochem. Commun.*, 2007, **9**, 492-496.

22. D. N. Futaba, K. Hata, T. Yamada, T. Hiraoka, Y. Hayamizu, Y. Kakudate, O. Tanaike, H. Hatori, M. Yumura and S. Iijima, *Nat. Mater.*, 2006, **5**, 987-994.

23. B. Logan, S. Cheng, V. Watson and G. Estadt, *Environ. Sci.Technol.*, 2007, **41**, 3341-3346.

24. Y. Qiao, S.-J. Bao, C. M. Li, X.-Q. Cui, Z.-S. Lu and J. Guo, *Acs Nano*, 2008, **2**, 113-119.

25. X. Xie, L. Hu, M. Pasta, G. F. Wells, D. Kong, C. S. Criddle and Y. Cui, *Nano Lett.*, 2011, **11**, 291-296.

26. X. Xie, G. Yu, N. Liu, Z. Bao, C. S. Criddle and Y. Cui, *Energy Environ. Sci.*, 2012, **5**, 6862-6866.

27. T. Sharma, A. L. M. Reddy, T. S. Chandra and S. Ramaprabhu, *Int. J. Hydrogen Energy*, 2008, **33**, 6749-6754.

28. Y.-C. Yong, X.-C. Dong, M. B. Chan-Park, H. Song and P. Chen, *Acs Nano*, 2012, **6**, 2394-2400.

29. Y. Wang, C.-e. Zhao, D. Sun, J.-R. Zhang and J.-J. Zhu, *Chempluschem*, 2013, **78**, 823-829.

30. X. Liu, W. Wu and Z. Gu, *J.Power Sources*, 2015, **277**, 110-115.

31. K. H. Hong, K. W. Oh and T. J. Kang, *J.Appl. Polym.Sci.*, 2005, **97**, 1326-1332.

32. R. Jalili, J. M. Razal and G. G. Wallace, *Sci. Rep.*, 2013, **3**.

33. D. Yoo, J. Kim and J. H. Kim, *Nano Res.*, 2014, **7**, 717-730.

34. G. H. Kim, D. H. Hwang and S. I. Woo, *Phys.Chem. Chem. Phys.*, 2012, **14**, 3530-3536.

35. D. Kim, Y. Kim, K. Choi, J. C. Grunlan and C. Yu, *Acs Nano*, 2010, **4**, 513-523.

36. K. Xu, G. Chen and D. Qiu, *J.Mater. Chem. A*, 2013, **1**, 12395-12399.

37. H. Zhou, W. Yao, G. Li, J. Wang and Y. Lu, *Carbon*, 2013, **59**, 495-502.

38. M. Zhang, W. Yuan, B. Yao, C. Li and G. Shi, *Acs Appl. Mater. Interfaces*, 2014, **6**, 3587-3593.

39. J. Zhou and G. Lubineau, *Acs Appl. Mater. Interfaces*, 2013, **5**, 6189-6200.

40. Y. Xu, Y. Wang, J. Liang, Y. Huang, Y. Ma, X. Wan and Y. Chen, *Nano Res.*, 2009, **2**, 343-348.

41. H. T. Ham, Y. S. Choi, M. G. Chee, M. H. Cha and I. J. Chung, *Polym. Eng. Sci.*, 2008, **48**, 1-10.

42. D. Li and Y. N. Xia, *Adv.Mater.*, 2004, **16**, 1151-1170.

43. D. Chen, Y.-E. Miao and T. Liu, *Acs Appl. Mater. Interfaces*, 2013, **5**, 1206-1212.

44. S. Peng, P. Zhu, Y. Wu, S. G. Mhaisalkar and S. Ramakrishna, *RSC Adv.*, 2012, **2**, 652-657.

45. I. S. Chronakis, S. Grapenson and A. Jakob, *Polymer*, 2006, **47**, 1597-1603.

46. Q. Zhang, Z. Chang, M. Zhu, X. Mo and D. Chen, *Nanotechnology*, 2007, **18**,115611.

47. A. Laforgue and L. Robitaille, *Macromolecules*, 2010, **43**, 4194-4200.

48. S. Chen, H. Hou, F. Harnisch, S. A. Patil, A. A. Carmona-Martinez, S. Agarwal, Y. Zhang, S. Sinha-Ray, A. L. Yarin, A. Greiner and U. Schroeder, *Energy Environ. Sci.*, 2011, **4**, 1417-1421.

49. S. Nair, E. Hsiao and S. H. Kim, *J.Mater.Chem.*, 2008, **18**, 5155-5161.

50. X. Wang, Y. Feng, N. Ren, H. Wang, H. Lee, N. Li and Q. Zhao, *Electrochim. Acta*, 2009, **54**, 1109-1114.

51. A. Dewan, H. Beyenal and Z. Lewandowski, *Environ.Sci.Technol.*, 2008, **42**, 7643-7648.

52. H. Wang, G. Wang, Y. Ling, F. Qian, Y. Song, X. Lu, S. Chen, Y. Tong and Y. Li, *Nanoscale*, 2013, **5**, 10283-10290.

53. E. Parra and L. Lin, *Proceedings of 22th IEEE Micro Electro Mechanical Systems Conference (Sorrento, ITALY)*, 2009, 31-34.

54. X. Zhang, S. Cheng, X. Wang, X. Huang, B. E. Logan, X. Y. Zhang, S. O. Cheng, X. Wang and X. Huang, *Environ.Sci.Technol.*, 2009, **43**, 8456-8461.

55. X. Wang, S. Cheng, Y. Feng, M. D. Merrill, T. Saito and B. E. Logan, *Environ.Sci.Technol.*, 2009, **43**, 6870-6874.

56. K. Rabaey, P. Clauwaert, P. Aelterman and W. Verstraete, *Environ.Sci.Technol.*, 2005, **39**, 8077-8082.

57. P. Aelterman, M. Versichele, M. Marzorati, N. Boon and W. Verstraete, *Bioresour. Technol.*, 2008, **99**, 8895-8902.

58. D. Jiang and B. Li, *Water Sci. Technol.*, 2009, **59**, 557-563.

59. Z. He, S. D. Minteer and L. T. Angenent, *Environ.Sci.Technol.*, 2005, **39**, 5262-5267.

60. A. ter Heijne, H. V. M. Hamelers, M. Saakes and C. J. N. Buisman, *Electrochimica Acta*, 2008, **53**, 5697-5703.

61. Y. Zou, C. Xiang, L. Yang, L.-X. Sun, F. Xu and Z. Cao, *Int. J. Hydrogen Energy*, 2008, **33**, 4856-4862.

62. M. Kaempgen, G. S. Duesberg and S. Roth, *Appl.Surf. Sci.*, 2005, **252**, 425-429.

63. X. Wang, L. Zhi and K. Muellen, *Nano Lett.*, 2008, **8**, 323-327.

64. D. S. Hecht, L. Hu and G. Gruner, *Curr. Appl. Phys.*, 2007, **7**, 60-63.

65. J. E. Mink, J. P. Rojas, B. E. Logan and M. M. Hussain, *Nano Lett.*, 2012, **12**, 791-795.

66. Y. Xu, H. Bai, G. Lu, C. Li and G. Shi, *J. Am.Chem.Soc.*, 2008, **130**, 5856-5857.

67. Y. Zhu, S. Murali, W. Cai, X. Li, J. W. Suk, J. R. Potts and R. S. Ruoff, *Adv. Mater.*, 2010, **22**, 3906-3924.

68. S. Watcharotone, D. A. Dikin, S. Stankovich, R. Piner, I. Jung, G. H. B. Dommett, G. Evmenenko, S.-E. Wu, S.-F. Chen, C.-P. Liu, S. T. Nguyen and R. S. Ruoff, *Nano Lett.*, 2007, **7**, 1888-1892.

CHAPTER 6. MICROFLUIDIC FLOW-THROUGH MICROBIAL FUEL CELL

A paper submitted to *Energy and Environmental Science*

Huawei Jiang, Md Azahar Ali, Zhen Xu, Larry J Halverson, and Liang Dong

Abstract

With continuing efforts in miniaturizing microbial fuel cells (MFCs), liquid volume of bio-convertible substrates present in anolyte chambers decreases dramatically. Therefore, it is desirable to improve electrochemical reactivity between electron-generating bacteria and the substrates to sustain energy production of the device. This paper reports on the development of a high-performance miniaturized MFC or μMFC with an innovative microfluidic flow-through feature: a porous microfluidic anolyte chamber is filled with three-dimensional graphene foam (GF) as an anode, allowing flowing nutritional medium throughout the chamber to intimately interact with the colonized microbes on the scaffolds of GF. This, in turn, can not only minimize consumption of nutritional substrate, but also reduce response time of electricity generation, due to fast mass transport through direct pressure-driven mass flow and rapid diffusion of nutrients within the interstitial pores of GF. We demonstrate that the flow-through μMFC provides a volume power density of 745 $\mu W/cm^3$ based on the total volume of anolyte chamber, and a surface power density of 89.4 $\mu W/cm^2$ based on the planar surface area of GF anode, using *Shewanella oneidensis* MR-1 as a model biocatalyst without any optimization of bacterial culture. The medium consumption is found to reduce by up to 16.4 times and the response time of the device reduces by up to 4.2 times, as the freeway space volume above the GF anode of the counterpart device increases from one to six times the volume of GF anode. This work represents an exploratory effort to introduce a porous GF-based flow-through mechanism into a microfluidic MFC setting. This present approach will translate into a benefit in high-throughput, large-scale screening different

bacterial species and their strains for conversion of carbon-containing substrates to electricity with smaller space, less medium consumption, more parallel experiments, and shorter experimenting time.

6.1 Introduction

Microbial fuel cells (MFC) utilize bacteria as a biocatalyst to convert organic matters in bio-convertible substrates into electrons [1]. Because MFCs are able to remove organic matter from wastewater and simultaneously produce renewable energy, the use of MFCs to treat municipal wastewater is an attractive alternative to traditional treatment processes [2]. Also, MFCs have been suggested as an in-field energy source to power sensors for environmental and process monitoring [3-12]. However, currently, the main applications remain confine to laboratory-scale plants. The limiting factors for the application of MFCs to natural scale plants include a high initial capital cost, especially for electrode construction and membranes, and the limited power density that can be achieved [2, 13-15].

Recently, miniaturized MFCs (μMFCs) have received increasing attention, because this technology can not only deliver significant insights into the potential for green power demand, but also make it possible to realize high-throughput screening of different bacterial species and their strains for high-efficiency conversion of bio-convertible substrates to electricity [2, 13-26]. Qian et al. developed a μMFC device using gold as an anode material with a 1.5 μL anode chamber [5]. Choi et al. reported a μMFC producing a power density of 2300 $\mu W/cm^3$ using an optimal *Geobacter*-enriched mixed bacterial culture [19]. Ren et al. demonstrated another miniaturized device with an increased surface-area-to-volume ratio that led to an improved the power density of 3300 $\mu W/cm^3$ [24]. Siu et al. presented a polydimethylsiloxane (PDMS) based μMFC and obtained about 40-folds enhancement in power density compared to silicon-based counterpart [26].

Qian et al. also devised their PDMS-based device using carbon cloth as an anode and attained a power density of 62.5 W/m^3 using *Shewanella oneidensis* MR-1 strain as a biocatalyst [20]. Other than using gold and carbon as anode materials, several three-dimensional (3D) micro/nanomaterials have been demonstrated as high performance anode materials of µMFCs, due to their larger surface area for bacterial attachment and colonization, and high electrochemical catalytic activity [28-42]. Inoue et al. utilized carbon nanotubes to demonstrate the hypothesis that the electron transport is based on direct attachment of bacteria on the surface of anode [43]. Mink et al. applied multi-walled carbon nanotubes as anode to their µMFC device capable of harvesting stable and high power [44]. Later, they also fabricated a 25 µL µMFC using graphene as anode. This device produced a high current density of 1190 A/m^3, which is more than one order of magnitude higher compared to that using carbon cloth as an anode [45]. Our previous work resulted in another µMFC with electrospun conducting poly(3,4-ethylenedioxythiophene) nanofibers as a 3D porous anode. This device produced a power density of 423 µW /cm^3 using *S. oneidensis* MR-1 as a biocatalyst [46]. Generally, these µMFCs are featured by large surface-area-to-volume ratio, low material consumption, and short start-up time. Despite these considerable efforts, it remains challenging in obtaining high-current and high-power intensity for µMFCs, due to their small processing volume and insufficient biofilm formation.

Graphene foam (GF) is a porous electrically conductive structure formed by vapor deposition of graphene onto a 3D mesh of metal filaments. GF has been utilized in electronic devices [27-29], energy storage and conversion devices [32-42], and neural tissue engineering [47-49]. Recently, GF has been researched for the development of medium-to-large size MFCs as anode materials. Xie et al. developed a high-performance MFC using a GF-based anode and a stainless-steel current collector [27]. A power density of 768 mW/m^2 was obtained using 3D

graphene-polyaniline structure as the anode of MFC [29]. Wang et al. used reduced graphene oxide-nickel foam as an anode in MFC *via* controlled deposition of reduced graphene oxide sheets onto the nickel foam substrate [30]. The aforementioned GF-based MFCs research efforts are all focused on developing large size devices and have demonstrated that the conductive 3D scaffolds are favorable for bacteria colonization and electron mediator. In particular, the pore size of GF on the order of a few hundreds of micrometers enables efficient mass transfer of nutrients and easy access of bacteria to the interstitial space within the 3D anode in order to grow on the surface of scaffolds.

It should be noted almost all existing MFCs, including both large and small size devices, use a similar device structure (with limited variations) where carbon-containing organic substrate solutions flow over the surface of a planar metal anode (e.g. gold and platinum) or 3D micro/nanomaterials based anode (e.g., carbon cloth, CNTs, and GF) laid on the bottom of anolyte chamber or attached to a proton exchange membrane (PEM). During the batch mode operation, mass transport of nutrients to the microbes colonized on the surface of anode is often implemented through a slow diffusion process from the bulk solution outside the anode to the surface or the inside of the anode. In a continuous flow mode, some of the bioconvertable substrates are inevitably wasted as they directly flow out from the anolyte chamber through the freeway space outside the anode, without participating in the reaction with the colonized microbes on the surface of anode.

With continuing efforts in miniaturizing MFCs, the volume of substrate solutions present in the devices decreases dramatically. Therefore, high efficiency use of the nutrients available for the μMFCs is highly desirable towards an increased ability of converting the substrates to electrons in space-limited devices. While numerous efforts have been made to improve electrode materials,

PEM, catholyte medium for obtaining high output power density, it is also believed critical to improve the efficiency of electrochemical reaction between the bio-convertible substrates and the colonized microbes in miniaturized anolyte chambers. The proposed approach is to incorporate a porous 3D GF enabled flow-through (FT) mechanism into a μMFC setting. The proposed FT μMFC device is shown in Figure 6.1. The porous GF anode is embedded in the anolyte chamber and sandwiched by a PEM at the top and a gold electron collector at the bottom of the anolyte chamber. With the built-in interconnected 3D pore network, the GF anode can not only provide 3D scaffolds for cell attachment, inoculation and colonization, but more importantly serve as a natural microfluidic porous channel for flowing nutritional and bacterial media. A bacterial biofilm grows on the surface of scaffolds generating electrons that transfer from bacteria to the scaffolds with high electron transfer efficiency. The catholyte chamber locates on the other side of the PEM, where fabric carbon cloth acts as cathode material. The uniqueness of this μMFC design lies in that the porous GF provides numerous embedded microscale passages for nutritional media to flow through the anode. No nutritional solutions are wasted through flowing over the anode without interacting with the bacteria inside the anode. As a result, efficient use of the nutrients in the culture medium will be obtained. Also, mass transport will be more efficient as it involves direct mass flow driven by pressure and fast diffusion of nutrients directly inside the interstitial pores of the GF toward the biofilm formed on the scaffolds. Over the micrometer length scale, molecular diffusion is fast because the diffusion time scales as the square of the distance. Therefore, this proposed FT design uses intrinsic microporous flows formed within the anode to carry all nutritional media through the anode, thus improving the interaction between the substrate and the inoculated microbes.

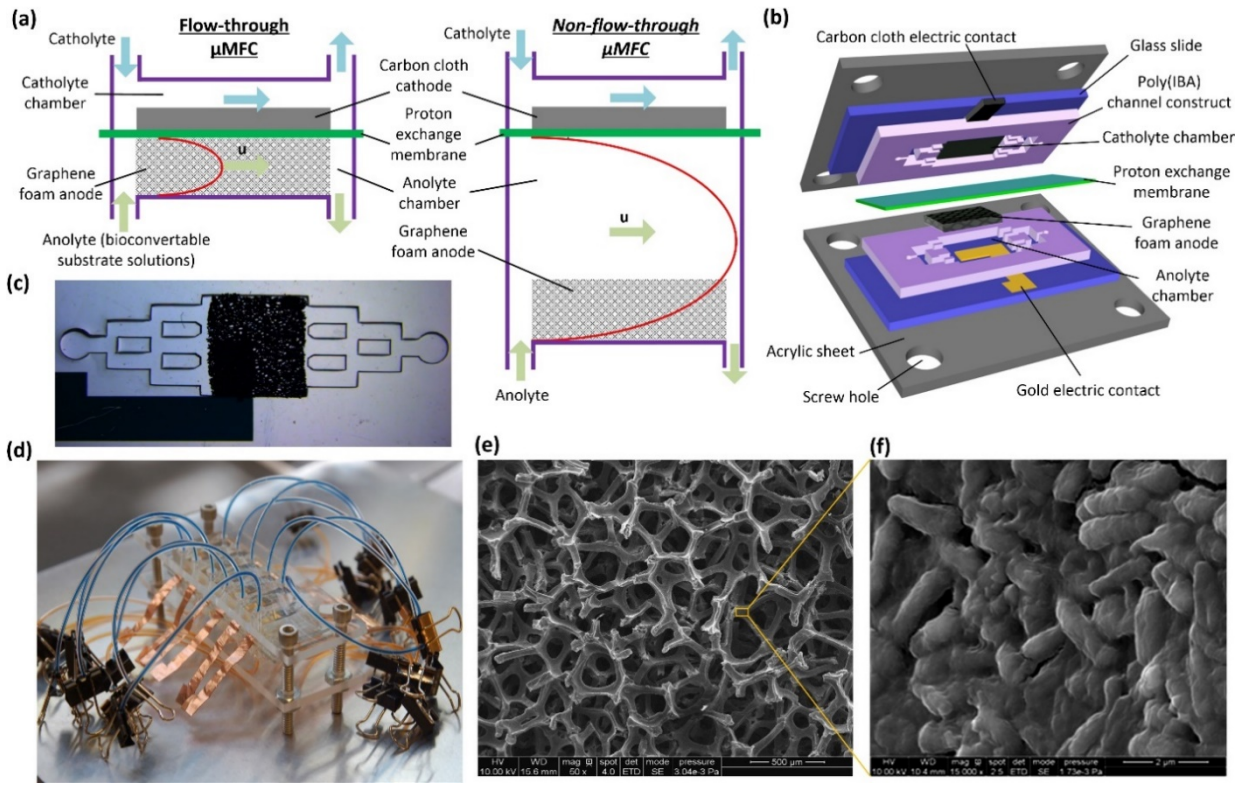

Figure 6.1 *(a) Schematic of the proposed FT (left) and non-FT μMFC devices (right), (b) Schematic showing the device components of the FT μMFC. (c) Optical image of an anolyte chamber with the embedded GF anode. Microfluidic diverging channels are attached to the anolyte chamber to distribute the anolyte solution flow in a relatively uniform manner across the width of the chamber. (d) Photo of an array of six FT μMFCs with the dimensions of about 1×1×3 inch^3. (e, f) Scanning electron microscopy (SEM) images of the porous GF anode with a bacterial biofilm formed on the surface of the scaffolds. A close up in (f) shows the microbial colonization of the scaffolds in (e).*

6.2 Experimental

6.2.1 Chemicals and materials

The following materials were used for fabrication of the proposed μMFCs: GF (multilayer graphene film on nickel foam; thickness: 1.2 mm; pore size: 580 μm; Graphene Supermarket, Calverton, NY), PEM (Nafion 117, Fuel Cells Etc, College Station, TX), carbon cloth (Fuel Cell Store, College Station, TX), acrylic sheets (85 mm×35 mm×3 mm; TAP Plastics, Oakland, CA), glass slides (75 mm × 25 mm × 0.9 mm, Corning, Oneonta, New York), a photopolymerizable precursor solution for making microfluidic channels composed of isobornyl acrylate (IBA, Sigma-Aldrich, St. Louis, MO), tetraethylene glycol dimethacrylate (Sigma-

Aldrich, St. Louis, MO), and 2,2-dimethoxy-2-phenylacet ophenone (Sigma-Aldrich, St. Louis, MO) with a weight ratio of 32 :1.7:1.0, polyethylene sterile tubing (Cole-parmer, Vernon Hills, IL), and mechanical cap screws (M4×0.7; Thorlabs, Newton, NJ). Here, the PEM was pretreated by sequentially boiling in hydrogen peroxide (30% v/v; Fisher Scientific, Fair Lawn, NJ) and de-ionized (DI) water, followed by soaking in 0.5 M sulfuric acid solution (Fisher Scientific, Fair Lawn, NJ) and then DI water, each for hour [18]. The activated PEM was stored in DI water before assembly.

Tryptic soy broth (TSB, Sigma-Aldrich, St. Louis, MO) was used as a culture medium for *S. oneidensis* strain MR-1. Also, a lactate defined minimal medium was prepared to perform electrochemical measurements for the GF anode, consisting of 20 mM sodium lactate per liter of DI water, 28 mM NH_4Cl, 1.34 mM KCl, 5 mM NaH_2PO_4, 0.7 mM Na_2SO_4, 52 mM NaCl, 0.2 mM $CaCl_2$ (the above chemicals purchase from Fisher Scientific, Fair Lawn, NJ), 1 mM $MgSO_4 \cdot 7H_2O$, 10 mg $FeSO_4 \cdot 7H_2O$ (the two chemicals purchase from Alfa Aesar, Ward Hill, MA), 20 mM PIPES [piperazine-*N*,*N*'-bis (2-ethanesulfonic acid)] (Sigma-Aldrich, St. Louis, MO), and 1 mL trace element solution [50]. Potassium ferricyanide (Fisher Scientific, Fair Lawn, NJ) was used as catholyte solutions. For studying electrochemical activity of GF anode electrode, the phosphate buffered saline (PBS) containing 5 mM $[Fe(CN)_6]^{3-/4-}$ (pH = 7.0) was used, where $[Fe(CN)_6]^{3-/4-}$ acted as a redox mediator.

6.2.2 Device fabrication and assembly

The gold electron collector (100-nm-thick Ti/Au) was first formed on the glass slide by e-beam evaporation of gold and conventional photolithography with the help of a film photomask (Fineline Imaging, Colorado Springs, CO) (Figure 6.2a). Subsequently, the anolyte chamber (area: 7×7 mm^2 across; depth: 1.2 mm) was fabricated on the same glass slide using a liquid phase

polymerization process (LP^3) [51]. The diverging channels were designed on the two sides of the porous anolyte chamber to distribute the anolyte solution flow relatively evenly across the width of the anolyte chamber. In the LP^3 step, double sided tapes (3M, St. Paul, MN) were used as spacers to create a 1.2 mm high cavity between the glass slide and another film photomask (Fineline Imaging, Colorado Springs, CO) (Figure 6.2b). The IBA-based photosensitive precursor solution was then injected into the cavity and polymerized under ultraviolet light (8.4 mW/cm^2, 30 s) [51]. After the exposure, the glass slide was washed with ethanol and then baked at 60 ºC for 2 hrs (Figure 6.2c). To fabricate the catholyte chamber, a carbon cloth strip (area: 6 mm×15 mm; thickness: 356 µm) was placed on another glass slide, followed by the LP^3 process to form the catholyte chamber. As shown in Figure 6.2e, three sides of the carbon cloth strip overlapped the photomask by 0.5 mm to fix the carbon cloth on the bottom of the catholyte chamber.

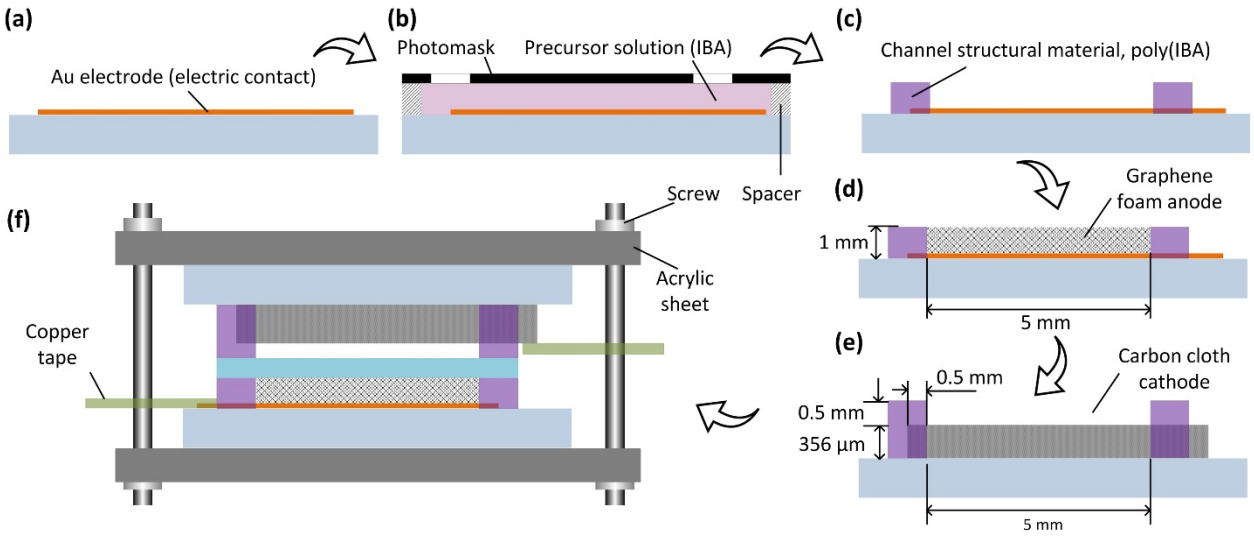

Figure 6.2 *Fabrication processes for the FT µMFC.*

Finally, the MFC device was constructed by assembling all the components shown in Figure 6.1b. These components were clamped between two acrylic plates and held together by four cap screws. To build the electrical connections, copper tapes (Sparkfun, Niwot, CO) were used to

extend the anode and cathode. The anolyte and catholyte chambers were accessed by polyethylene sterile tubing through the inlet and outlet of the device.

6.2.3 Cell inoculation

The µMFCs were sterilized by filling all of compartments with pure ethanol and letting it sit for 20 minutes at room temperature, followed by flushing the devices with DI water for 5 min and then culture medium TSB for another 5 min. To operate the device, *S. oneidensis* strain MR-1 was used as the model exoelectrogenic microbial biocatalyst and TSB was used the nutrient source. TSB medium flowed into the anolyte chamber through the polyethylene tubing using a programmable syringe pump (210P, KD Scientific, Holliston, MA). To minimize possible oxygen contamination in the batch mode operation, the tubing was closed by steel clamps after the injection of bacterial suspension into the anolyte chamber. The catholyte solution of potassium ferricyanide was supplied using a syringe pump.

6.2.4 Electrochemical measurements and calculations

An external resistor (R) was connected between anode and cathode of the µMFC to form a closed circuit. The voltage potential (U) between the two electrodes was measured using a data acquisition device (Model DI-245; DATAQ Instruments, Akron, OH) and recorded once a minute via DATAQ Instruments Hardware Manager software. The current (I) flowing through the resister was calculated *via* $I = U/R$ and the output power was calculated *via* $P = U \times I$. The shunt current was measured to obtain the maximum output current. Electrochemical properties of the GF anode was measured in PBS containing 5 mM $[Fe(CN)_6]^{3-/4-}$ by an electrochemical workstation (SP1, Zive Potentiostat, Seoul, Korea). A platinum (Pt) wire and a silver/silver chloride (Ag/AgCl) wire were used as the counter electrode and reference electrode, respectively. Each electrical

measurement result given in this paper is representative of the typical result obtained over three independent experiments on three identical devices.

6.2.5 Bacterial fixation for SEM

The GF anodes were separated from the disassembled μMFCs, immersed in a glutaraldehyde solution (2%; Sigma-Aldrich, St. Louis, MO) to fix the adherent bacteria on the GF surface, and incubated at 4 ºC for 12 hrs. After rinsing with DI water, the GF anodes were stained with 1% osmium tetroxide solution (Sigma-Aldrich, St. Louis, MO) for 2 hrs, rinsed again, and then, dehydrated by pure ethanol. A field-emission scanning electron microscopy (SEM; Quanta-250; FEI, Hillsboro, OR) was used to investigate the treated GFs.

6.3 Results and discussion

To illustrate how the porous FT structure affected the fluid flow profiles in the anolyte chamber on the small scale, we conducted hydrodynamic simulations using finite element method based commercial software package (COMSOL Multiphysics). As an example, Figure 6.3 shows three different anolyte chamber designs, including the FT design with the GF anode sandwiched by the PEM and the glass slide, and two non-FT counterparts with the freeway space of three and six times the thickness of the GF anode, respectively. Free- and porous-media flow models were used for the simulation. For the porous media, the porosity, permeability, and Forchheimer coefficient were set as 0.9, 1×10^{-7} m^2, and 4.35×10^{3} kg/m^4, respectively [52]. In the settings for fluid properties, the density, dynamic viscosity, and flow rate were set as 1×10^{3} kg/m^3, 1.02×10^{-3} Pa·s, and 4.6×10^{-4} cm/s (calculated by a sample volumetric flow rate of 10 μL/hr used in the experiment), respectively. The width and the side length of the porous media were set to be 1.2 mm and 5 mm, respectively, according to the geometric parameters used in the real device.

Figure 6.3a shows that as the pressure driven laminar flow was pumped through the FT porous anoloyte chamber with no-slip boundary condition, the fluid velocity at the walls was found to be zero and a parabolic velocity profile was produced within the chamber in each case. The parabolic velocity profile has significant implications for the distribution of molecules transporting within the anolyte chamber. Specifically, in the FT case all fluids entered and exited throughout the porous anode, while in the two non-FT cases (shown in Figure 6.3b, c), only a portion of fluids directly interacted with the GF anode and a majority of fluids flowed along the freeway space channel as waste. The wider the freeway space outside the porous anode, the smaller the flow rate inside the anode, thus the less the usage efficiency of the medium. In addition, the FT design will allow for fast nutrient replenishment due to the presence of a higher flow rate inside the GF anode.

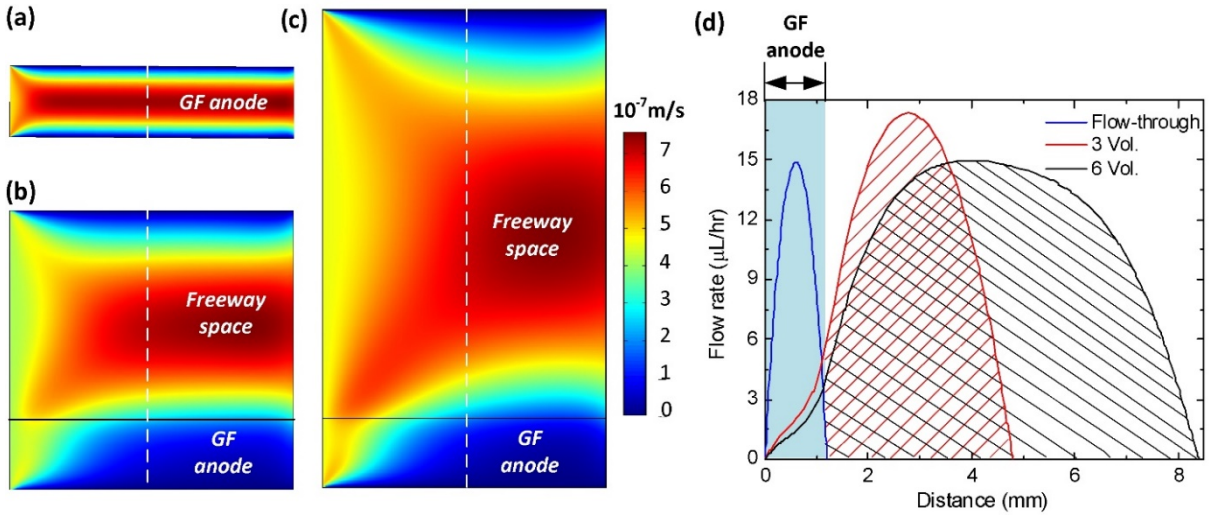

Figure 6.3 *Simulated flow rate distributions within the anolyte chambers of three sample μMFCs: a FT device (a), and two non-FT devices with the freeway space above the GF anode three (b) and six times (c) that of the GF thickness. In (d), simulated flow rates along the vertical dashed white lines across the height of anolyate chambers are given.*

Electric current output of the FT device before and during cell inoculation was monitored using a closed circuit carrying an external resistive load of 11.5 kΩ. First, TSB medium was injected into the anolyte chamber via the inlet tubing. The background current without *S.*

oneidensis bacteria was found as low as 12±10 nA. Subsequently, cell inoculation was conducted by filling the anolyte chamber with TSB medium containing *S. oneidensis* bacteria. Two clips were then used to pinch close the tubing for cell inoculation. The output current was increased to ~43 µA within five hrs and then, decreased gradually. The magnitude of peak current was three orders more than the background current. Considering that the inoculum was not manipulated prior to delivering it to the anolyte, the rapid increases in output current is due to the fast reaction occurring between the bacteria and the nutritional substrate.

Figure 6.4 shows the polarization and power density curves of the FT device plotted by measuring the output voltage and current at different external resistive loads. According to the literature [1], a polarization curve can be divided into three regions reflecting activation loss, ohmic loss, and mass transfer loss. At the activation loss stage, the output current increased from zero (measured at the open circuit voltage of 1240 mV) to 18.1 µA. Due to the need of the activation energy for oxidation reaction, the activation loss occurred at the electrode surface during the electron transfer. The voltage dropped as the external resistance decreased. In the current range from 18.1 to 44.2 µA, the polarization curve presented a near-linear drop in voltage with increasing electric current. As a result, the internal resistance of 7.3 kΩ was obtained through linear fitting of the curve in the ohmic region. In addition, the surface power density reached to a maximum value of 89.8 µW cm^{-2} in the ohmic loss region, while the output voltage decreased in the mass transfer loss region.

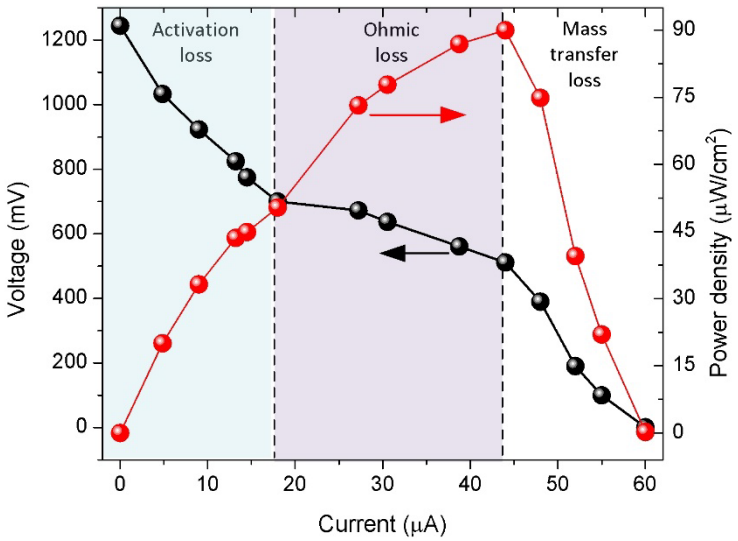

Figure 6.4 *Polarization curve and power density output of the FT μMFC as a function of current.*

To evaluate the influence of the feeding rate of culture medium on the electric current generation of the FT device, TSB culture medium was continuously injected into the FT anode at different flow rates after completing the inoculation process. As shown in Figure 6.5a, at the low flow rates of 2.5 and 5 μL/hr, the output current was at the similar level of ~5 μA. When the flow rate increased to 10 μL/hr, there appeared a dramatic current increase to ~22 μA. It is interesting to observe that the electric currents at the increasing flow rates of more than 20 μL/hr were almost saturated at the level of 45-53 μA, with only a small current increase as the flow rate increased. A possible explanation is that while these high feeding flow rates resulted in providing larger volume culture medium to the GF anode, the nutritional supply to the colonized microbes at the flow rate of 20 μL/hr may be already sufficient enough to support cell growth and respiration. Therefore, further increasing the feeding flow rate beyond 20 μL/hr had only limited influence on the electricity production.

To reveal the advantages of the FT device, we fabricated different non-FT counterpart devices with the freeway space volume (V_{fr}) above the GF anode by varying from one to six times the GF anode volume (V_{gf}). Cell inoculation for the non-FT devices was performed with the same

procedures as those performed for the FT device described above. After the completion of inoculation, we tested electric current generation of the non-FT devices at different medium flow rates in a continuous flow mode. The representative results of three non-FT devices ($V_{fr} = V_{gf}$, $3V_{gf}$, and $6V_{gf}$) are shown in Figure 6.5b-d, where the overall tendencies of electric current output over time at different flow rates are similar to that of the FT device (Figure 6.5a). However, the current response curves indicate that the non-FT devices consumed much more substrates in TSB medium than the FT device to produce the same current level. For the non-FT devices with $V_{fr} = V_{gf}$, $3V_{gf}$, and $6V_{gf}$, the output current reached 35-40 µA (approximate 80% of the maximum output current of each device) with the flow rate of 40 µL/hr at ~6 hrs (Figure 6.5b), 60 µL/hr at ~9 hrs (Figure 6.5c), and 120 µL/hr at ~12 hrs (Figure 6.5d), respectively, while for the FT device, the similar current level was observed at the lower flow rate of 20 µL/hr at shorter time ~5 hrs (Figure 6.5a). The results also explicitly demonstrated that before the output current of each device reached a relatively stable value (~80% of the peak current), the FT design showed a great ability to increase electricity generation compared to the non-FT counterpart designs. This is because the FT device efficiently achieved the nutrients from the input TSB medium to increase the interactions with the colonized microbes. On the contrary, the non-FT devices used only a fraction of the input nutrients to participate in the electrochemical reaction inside the GF anode. Figure 6.6a summaries the output current of the FT and non-FT devices as a function of medium flow rate.

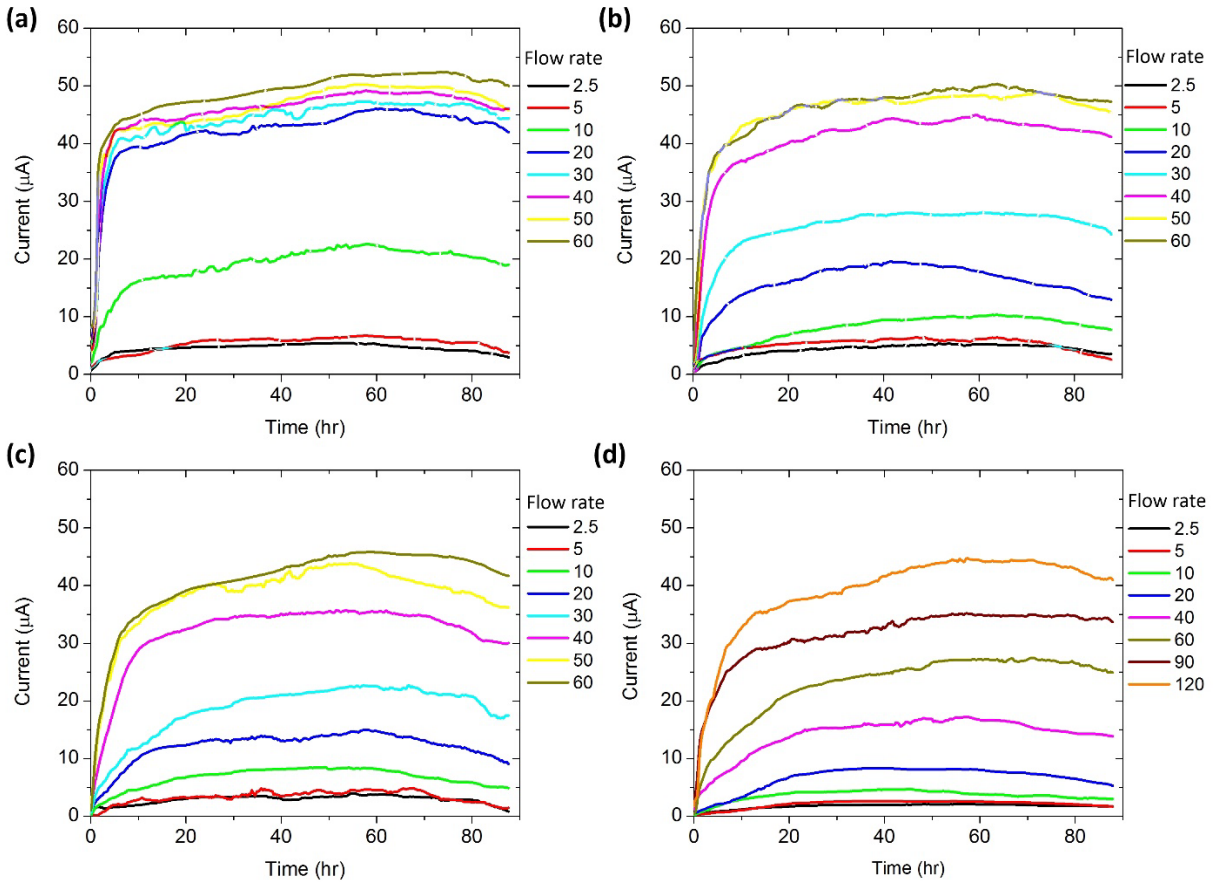

Figure 6.5 *Output current of the FT device (a) and three non-FT devices with the freeway space volume V_{fr} = 1V_{gf} (b), 3V_{gf} (c), and 6V_{gf} (d), in response to feeding TSB medium with different feeding flow rates.*

Figure 6.6b shows the time that the FT device and the six non-FT counterparts took to generate 80% of the peak current (t_I). The result shows that the FT design allowed for significant reduction in t_I. The larger the freeway space volume of the non-FT device, the longer the time t_I of the device. Along the length direction of the GF anode in the FT device, mass transport of nutrients was mainly driven by pressure in the continuous flow mode. As a result, the higher the feeding flow rate was applied, the shorter the time t_I was required. Inside the interstitial pores of the GF anode, the nutrients in the medium diffused to the surface of scaffolds on a small length scale of ~250 μm or half of the mean pore size of the GF, also contributing to the overall short t_I of the FT device. In contrast, the non-FT devices require more time because the nutrients in the freeway space outside the anode diffused over a longer distance to the scaffolds of GF anode. Although the

pressure-driven mass flow also occurred in the non-FT devices, the effective amount of nutrients delivered to the colonized microbes was actually less than that in the FT one, due to the wasted portion of nutrients. As shown in Figure 6b, when the medium flow rate was set at 20, 40, and 60 µL/hr, the response time t_I of the FT device was 4.2, 3.2, and 2.6 times, respectively, shorter than that of the non-FT device with $V_{fr} = 6V_{gf}$.

Figure 6.6c shows the total volume of TSB medium consumed to obtain 80% of the peak output current as a function of freeway space volume of the devices. Here the medium flow rate v and corresponding time t_I were considered to determine the total volume $V_{tot} = v \times t_I$. Specifically, for $V_{fr} = V_{gf}$, $2V_{gf}$, $3V_{gf}$, $4V_{gf}$, $5V_{gf}$ and $6V_{gf}$, the medium consumption was reduced by 2.5, 4.2, 5.6, 9.5, 12.5, and 16.4 times, respectively.

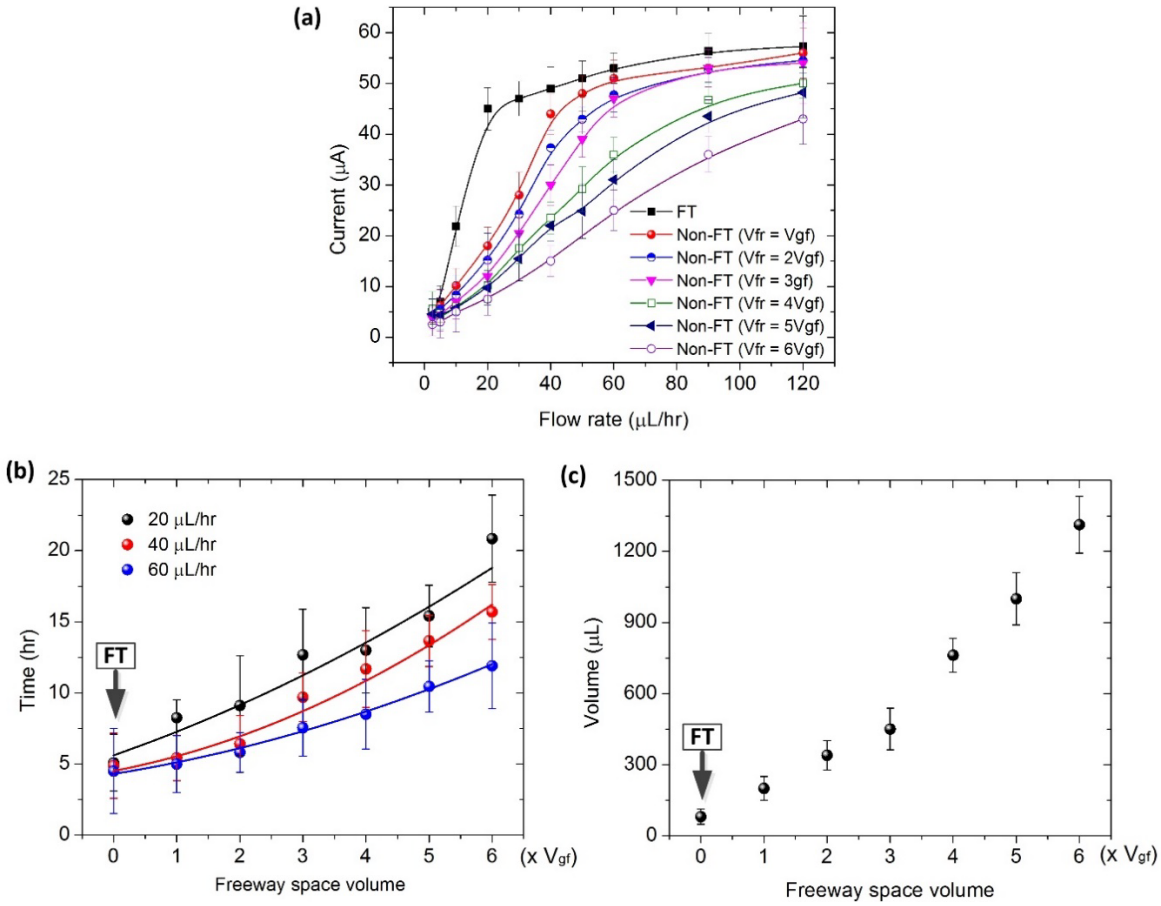

Figure 6.6 *(a) Maximum output current of the FT and non-FT devices at different feeding flow rates of TSB medium. The non-FT devices used here had the freeway space volume V_{fr} varying from V_{gf} to $6V_{gf}$ where V_{gf} represents the volume of the GF anode. (b) Time required for the FT and non-FT devices to obtain 80% of the peak output current as a function of freeway space volume of the devices. (c) Total volume of TSB medium consumed to obtain 80% of the peak output current as a function of freeway space volume of the devices.*

Figure 6.7a, b show the biofilms of *S. oneidensis* strain MR-1 formed on the scaffolds of the GF anode taken out from the FT device and the non-FT counterpart with $V_{fr} = 6V_{gf}$, respectively. The biofilms were examined following the continuous-flow mode operation at the same flow rate of 20 µL/hr. As described in Figure 6.5a, d and Figure 6.6a, at this flow rate the FT device generated electric current exceeding nearly eight times that generated by the non-FT device. The SEM images shows that the surfaces of scaffolds in the FT device was fully covered by the biofilm of *S. oneidensis* strain MR-1, while those in the non-FT device was only partially covered by the biofilm.

Raman spectroscopic study (Figure 6.7c) was performed for the GF anode used in the proposed FT device before and after forming the biofilm shown in Figure 6.7c. The two main bands in the spectra of the untreated GF are known as the G-band at ~1590 cm^{-1} and the 2D band at ~2700 cm^{-1}. The defect related D band at ~1350 cm^{-1} was found to negligibly weak, indicating the highly conductive nature and graphitic-rich quality of the GF anode. For the GF anode with the biofilm, the D-band is slightly appeared and other three spectral bands related to bacteria were also observed at 1170, 1370, and 1540 cm^{-1}, which may be assigned to C-C stretching, CH_2 twisting, and C=C stretching vibration modes, respectively. Therefore, the Raman spectra results were consistent with the result of the SEM study that the biofilm was formed on the surface of scaffolds of GF anode.

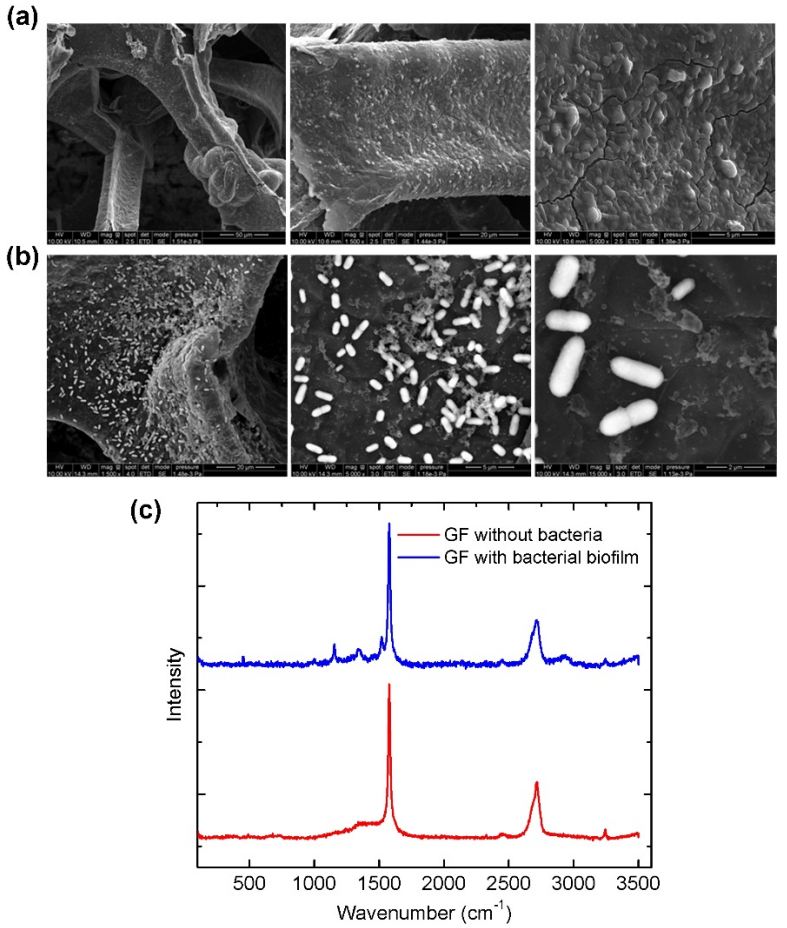

Figure 6.7 *SEM images for the biofilms of S. oneidensis strain MR-1 grown on the scaffolds of the GF anodes of the FT device (a) and non-FT counterpart (b). The biofilms were formed at the TSB medium flow rate of 20 µL/hr. In (c), Raman spectra of the untreated GF anode and the GF with the biofilm shown in (a).*

Next, to better understand the operation of the GF anode in the FT and non-FT µMFC devices, we investigated electrochemical properties of the GF anode by cyclic voltammetry (CV) and electrochemical impedance spectroscopy (EIS) studies. This helped us to develop some intuition on how diffusion coefficients of electroactive species were related to the µMFC design with the GF as an anode. It should be noted that because TSB medium contains complex ingredients of organic carbon sources, the diffusion coefficient obtained through electrochemical measurements would only reflect the overall ability of diffusing molecules in the anolyte chamber, but not any individual molecules. Therefore, in the following discussion, besides illustrating the overall idea of diffusing ability using TSB medium, we also used a lactate defined minimal

medium for *S. onediensis* MR-1 to perform electrochemical measurements for the FT device and non-FT counterpart ($V_{fr} = 6V_{gf}$).

The CV studies were carried out in both TBS and the lactate defined minimal medium at 30 mV/s scan rate within a potential range of 0.7 V to -0.7 V for the GF anode and the carbon cloth cathode of the FT and non-FT devices. For the FT device with TSB medium, a higher oxidation current of -292 µA was obtained at -0.3 V compared to the non-FT one (Figure 6.8a). Essentially, the current was produced due to the anodic reaction resulting from the oxidation of organic carbon in TSB medium in presence of bacteria on the surface of the scaffolds of the GF anode. The obtained higher current indicates faster electron transfer of generated electrons towards the anode from the bulk TSB medium. According to Bard and Faulkner [53], when diffusion process dominates in the electrochemical reactor, the peak current can be given by $i_p = (2.99 \times 10^5)\alpha^{1/2} A C_0 D_0^{1/2} \nu^{1/2}$, where α is the transfer coefficient for the reaction; A is the surface area of the anode (cm^2), ν is the scan rate (mV/s), C_o is the initial concentration of substrate in the medium (mol/cm^3), and D_0 is the diffusion coefficient (cm^2/s). In the case of using TSB medium (Figure 6.8a), the average or overall diffusion coefficients were obtained as 2.38×10^{-10} and 0.2×10^{-10} cm^2/s for the FT and non-FT device, respectively. The overall higher diffusion coefficient of the FT device is believed due to the smaller distance of diffusion path, compared to the non-FT one. When using the lactate defined minimal medium (Figure 6.8b), we also obtained a higher oxidation current of -148 µA in the FT device due to the higher diffusion coefficient of 6.28×10^{-9} cm^2/s, compared to the non-FT one. The higher current with TSB medium than that with the minimal medium may be attributed to more carbon containing ingredients contained in TSB medium than the lactate defined minimal medium.

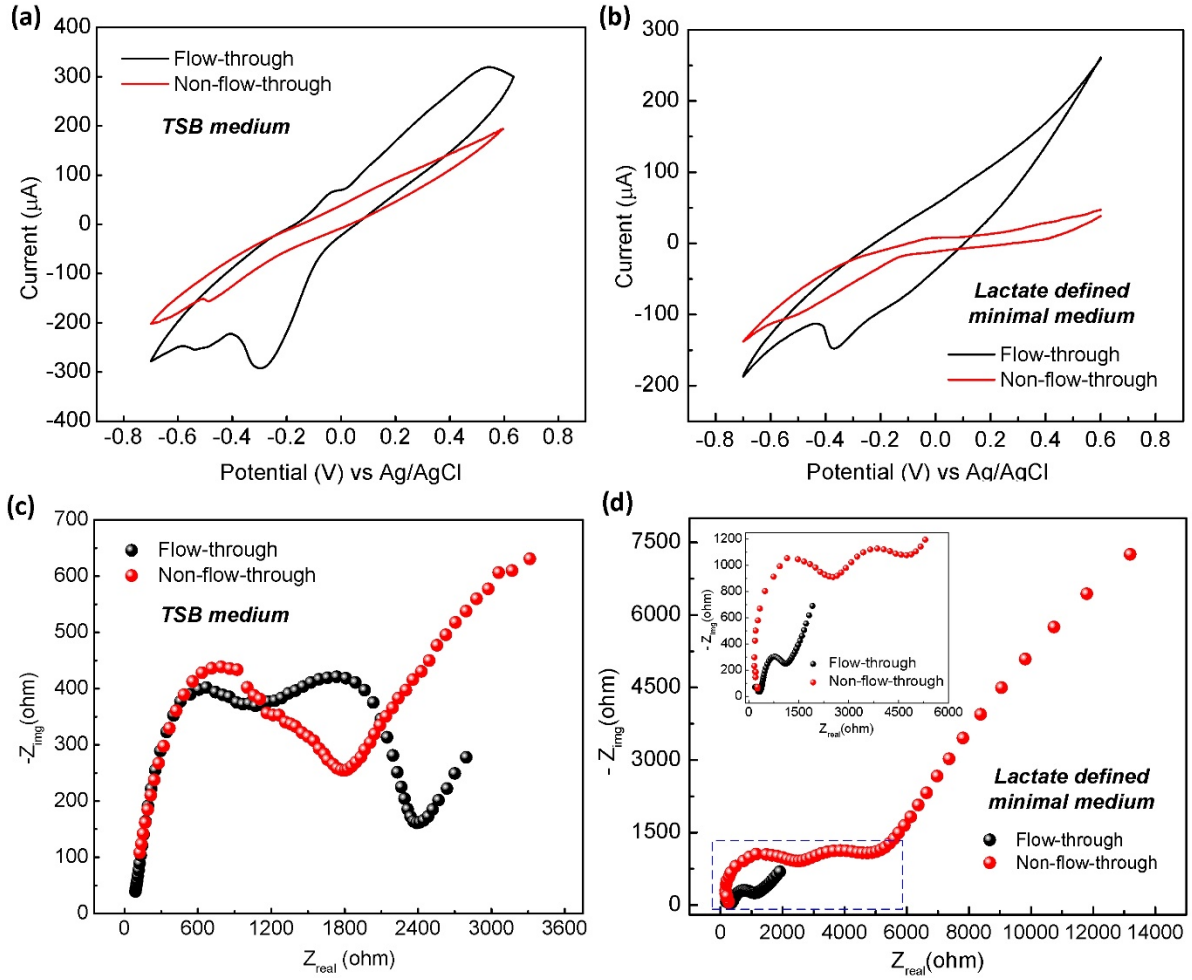

Figure 6.8 *CV characteristics of the GF anodes in the FT and non-FT μMFCs at the scan rate of 30 mV/s with TSB medium (a) and lactate defined minimal medium (b). Nyquist plots of the GF anodes in the FT and non-FT devices with TSB medium (c) and lactate defined minimal medium (d). The inset in (d) shows the enlarged view of the indicated square region in the same figure.*

Furthermore, we compared other kinetic parameters of the FT and non-FT devices, including charge transfer resistance (R_{ct}), and heterogeneous electron transfer rate constant (k_o), based on the results of EIS measurements by applying a small (amplitude: 10 mV) sinusoidal AC signal (frequency range: 0.01 Hz to 100 kHz). In EIS, a Nyquist plot includes a semicircle region with the real axis indicating R_{ct} (plotted with the real part Z_{real} and the imaginary part Z_{img}). The k_0 of the μMFC was calculated using the relation $k_0 = RT/n^2F^2AR_{ct}C$, where T is the temperature, R is the gas constant, n is the electron transfer constant of the substrate (for TSB medium, n = 24;

for the lactate defined minimal medium, n = 4, shown in Table 6.1), F is Faraday constant, A is the anode area, and C is the concentration of the substrate. Figure 6.8c, d show that the EIS spectra for the two µMFC designs using TSB and lactate based culture media, respectively. In the case of the FT device with TSB medium, two semicircles appeared in the Nyquist plot with R_{ct1} = 1.23 kΩ and R_{ct2} = 1.65 kΩ at high and medium frequencies, respectively. At the high frequencies with TSB medium, the non-FT device had a charge transfer resistance R_{ct} = 1.44 kΩ, which is higher than that the FT device provided. Also, the FT device had the higher k_0 values with both TSB and lactate defined minimal media, compared to the non-FT one. Therefore, the FT device exhibited faster electron transfer kinetics than the non-FT device.

Table 6.1 *Comparison of electrochemical parameters for the GF anodes used in the FT and non-FT µMFCs.*

Culture medium	µMFC type	Peak current (i/mA)	Diffusion coefficient ($cm^2\ s^{-1}$)	R_{ct} (kΩ)	k_0 ($cm\ s^{-1}$)
TSB	FT	0.29	2.38×10^{-10}	1.23	3.24×10^{-11}
	Non-FT	0.08	0.20×10^{-10}	1.44	1.94×10^{-12}
Lactate defined minimal medium	FT	0.15	6.28×10^{-9}	0.88	1.13×10^{-10}
	Non-FT	0.07	1.40×10^{-9}	2.96	2.35×10^{-11}

Table 6.2 compares the performance of our devices with many recently reported MFCs with the same model biocatalyst of *S. oneidensis* strain MR-1 [17, 18, 20, 21, 29, 30, 46, 54]. It should be noted that due to using different device structures and different cultures, it may be difficult to make point-to-point comparisons of power densities normalized to the anode surface area and the volume of anolyte chamber. Compared to the recently reported devices using GF [29, 30], carbon cloth [20], Au [17, 18, 21], and PEDOT nanofibers [46] as anode materials with *S. oneidensis* strain MR-1, the present FT µMFC exhibited a higher current density of 91.8 $\mu A/cm^2$, a higher volume power density 745 $\mu W/cm^3$, and a slightly lower but still competitive surface power density of 89.4 $\mu W/cm^2$. Furthermore, compared to the large scale MFCs using graphite as

an anode material [54], our FT μMFC had a lower surface power density. However, because the anolyte chambers of the previous GF- and graphite-based MFC are nearly three orders of magnitude larger than that of our device, larger amounts of nutritional substrates and presumably longer response time are required with lower volume power densities. It should be noted that the electron producing capability of strain MR-1 used in our device has limited the output current and power density of the device. It is believed that by using optimally mixed bacterial cultures, such as *Geobacteraceae*-enrichment cultures [19], the electricity generation capability of the device will be further enhanced.

Table 6.2 *Performance comparison between the proposed devices and other reported μMFCs*

Anode/area (cm^2)	Carbon cloth cathode area (cm^2)	Anolyte chamber volume (μL)	Startup time (hr)	Miniature device (Y/N)	Current density ($\mu A/cm^2$)	Power density (Pmax) P_S[a] ($\mu W/cm^2$)	Power density (Pmax) P_{VC} ($\mu W/cm^3$)	Ref
GF/0.49	0.49	40.8[b]	5[c]	Y	91.8[d]	89.4	745	This work
GF/0.49	0.49	80.2[b]	8.3[c]	Y	89.6[d]	88.5	368.8	
GF/0.49	0.49	120.2[b]	9.1[c]	Y	85.6[d]	86.2	239.4	
GF/0.49	0.49	160.3[b]	11.4[c]	Y	88.2[d]	84.8	176.7	
GF/0.49	0.49	200.4[b]	12.8[c]	Y	94.9[d]	82.2	137	
GF/0.49	0.49	240.5[b]	15.4[c]	Y	79.8[d]	85.7	119	
GF/0.49	0.49	280.6[b]	20.8[c]	Y	81.6[d]	77.8	96.8	
GF-PANI/1	8	1.81×10^5	N/A	N	N/A	76.8	0.42	[29]
GF/7~10	70	2.5×10^4	N/A	N	71.43	96.43	27	[30]
Carbon cloth/0.4	0.4	4	6	Y	10	0.62	62.50	[20]
Au/0.15	0.4	1.50	12	Y	13	0.15	15.30	[18]
Au/0.38	0.38	154	N/A	Y	1.64	0.37	0.93	[17]
Au/0.38	0.38	400	< 13	N	N/A	2.35	N/A	[21]
Graphite plate/1.92	828[e]	8×10^5	N/A	N	N/A	329	0.79	[54]
Graphite plate/155	828[e]	8×10^5	N/A	N	N/A	141	27	[54]
PEDOT nanofibers/ 1	1	12	~ 1	Y	16	2.54	423	[46]

[a] Calculation based on the planar surface area of the anode electrode.
[b] The diverging microfluidic channels on the two sides of the porous anolyte chamber are excluded in the volume calculation.
[c] Data are obtained from the black curve (at 20 μL/hr) in Fig. 6.6b.
[d] The current values refer to 80% of the maximum current shown in Fig. 6.6a.
[e] Carbon bonded to platinum mesh.

6.4 Conclusions

In summary, we have demonstrated the 3D GF-enabled FT μMFC that allows flowing nutrition medium throughout the porous anolyte chamber to enhance its interaction with the colonized microbes on the scaffolds of GF. Using *S. oneidensis* MR-1 as a model biocatalyst, the device provided 745 $\mu W/cm^3$ volume power density based on the total volume of anolyte chamber,

and 89.4 μW/cm^2 surface power density and surface current density of 91.8 μA/cm^2 based on the planar surface area of GF anode. The medium consumption and the current generation response time were reduced by up to 16.4 and 4.2 times, as the freeway space volume of the counterpart device is six times the volume of GF anode. Further work include using the present FT mechanism to develop a high-throughput, large-scale assay device for screening optimal bacterial species and their strains for MFC applications.

References

1. B. E. Logan, B. Hamelers, R. A. Rozendal, U. Schrorder, J. Keller, S. Freguia, P. Aelterman, W. Verstraete and K. Rabaey, *Environ. Sci. Technol.*, 2006, **40**, 5181-5192.

2. J. Wei, P. Liang and X. Huang, *Bioresour. Technol.*, 2011, **102**, 9335-9344.

3. A. E. Franks and K. P. Nevin, *Energies*, 2010, **3**, 899-919.

4. S. K. Chaudhuri and D. R. Lovley, *Nat. Biotechnol.*, 2003, **21**, 1229-1232.

5. I. S. Chang, J. K. Jang, G. C. Gil, M. Kim, H. J. Kim, B. W. Cho and B. H. Kim, *Biosens. Bioelectron.*, 2004, **19**, 607-613.

6. G.-X. Yang, Y.-M. Sun, X.-Y. Kong, F. Zhen, Y. Li, L.-H. Li, T.-Z. Lei, Z.-H. Yuan and G.-Y. Chen, *Water Sci. Technol.*, 2013, **68**, 1914-1919.

7. K. Rabaey, G. Lissens, S. D. Siciliano and W. Verstraete, *Biotechnol. Lett.*, 2003, **25**, 1531-1535.

8. P. Aelterman, K. Rabaey, H. T. Pham, N. Boon and W. Verstraete, *Environ. Sci. Technol.*, 2006, **40**, 3388-3394.

9. B. Lin, M. Braster, B. M. van Breukelen, H. W. van Verseveld, H. V. Westerhoff and W. F. M. Roling, *Appl. Environ. Microb.*, 2005, **71**, 5983-5991.

10. J. N. Rooney-Varga, R. T. Anderson, J. L. Fraga, D. Ringelberg and D. R. Lovley, *Appl. Environ. Microb.*, 1999, **65**, 3056-3063.

11. D. R. Lovley, M. J. Baedecker, D. J. Lonergan, I. M. Cozzarelli, E. J. P. Phillips and D. I. Siegel, *Nature*, 1989, **339**, 297-300.

12. R. T. Anderson, J. N. Rooney-Varga, C. V. Gaw and D. R. Lovley, *Environ. Sci. Technol.*, 1998, **32**, 1222-1229.

13. S. Choi, *Biosens. Bioelectron.*, 2015, **69**, 8-25.

14. H.-Y. Wang, A. Bernarda, C.-Y. Huang, D.-J. Lee and J.-S. Chang, *Bioresour. Technol.*, 2011, **102**, 235-243.

15. H. Ren, H.-S. Lee and J. Chae, *Microfluid. Nanofluid.*, 2012, **13**, 353-381.

16. J. Biffinger, M. Ribbens, B. Ringeisen, J. Pietron, S. Finkel and K. Nealson, *Biotechnol. Bioeng.*, 2009, **102**, 436-444.

17. H. Hou, L. Li, Y. Cho, P. de Figueiredo and A. Han, *Plos One*, 2009, **4**, e6570.

18. F. Qian, M. Baum, Q. Gu and D. E. Morse, *Lab Chip*, 2009, **9**, 3076-3081.

19. S. Choi, H.-S. Lee, Y. Yang, P. Parameswaran, C. I. Torres, B. E. Rittmann and J. Chae, *Lab Chip*, 2011, **11**, 1110-1117.

20. F. Qian, Z. He, M. P. Thelen and Y. Li, *Bioresour. Technol.*, 2011, **102**, 5836-5840.

21. H. Hou, L. Li, C. U. Ceylan, A. Haynes, J. Cope, H. H. Wilkinson, C. Erbay, P. de Figueiredo and A. Han, *Lab Chip*, 2012, **12**, 4151-4159.

22. S. Mukherjee, S. Su, W. Panmanee, R. T. Irvin, D. J. Hassett and S. Choi, *Sens. Actuators A*, 2013, **201**, 532-537.

23. H. Ren, S. Pyo, J.-I. Lee, T.-J. Park, F. S. Gittleson, F. C. C. Leung, J. Kim, A. D. Taylor, H.-S. Lee and J. Chae, *J. Power Sources*, 2015, **273**, 823-830.

24. H. Ren, C. I. Torres, P. Parameswaran, B. E. Rittmann and J. Chae, *Biosens. Bioelectron.*, 2014, **61**, 587-592.

25. S. Choi and J. Chae, *Sens. Actuators A*, 2012, **177**, 10-15.

26. C.-P.-B. Siu and M. Chiao, *J. Microelectromech. S.*, 2008, **17**, 1329-1341.

27. X. Xie, G. Yu, N. Liu, Z. Bao, C. S. Criddle and Y. Cui, *Energy Environ. Sci.*, 2012, **5**, 6862-6866.

28. T. Sharma, A. L. M. Reddy, T. S. Chandra and S. Ramaprabhu, *Int. J. Hydrogen Energy*, 2008, **33**, 6749-6754.

29. Y.-C. Yong, X.-C. Dong, M. B. Chan-Park, H. Song and P. Chen, *Acs Nano*, 2012, **6**, 2394-2400.

30. Y. Wang, G. Wang, Y. Ling, F. Qian, Y. Song, X. Lu, S. Chen, Y. Tong, and Y. Li, *Nanoscale*, 2013, **5**, 10283-10290.

31. X. Liu, W. Wu and Z. Gu, *J.Power Sources*, 2015, **277**, 110-115.

32. K. H. Hong, K. W. Oh and T. J. Kang, *J. Appl. Polym. Sci.*, 2005, **97**, 1326-1332.

33. R. Jalili, J. M. Razal and G. G. Wallace, *Sci. Rep.*, 2013, **3**, 3438.

34. D. Yoo, J. Kim and J. H. Kim, *Nano Res.*, 2014, **7**, 717-730.

35. G. H. Kim, D. H. Hwang and S. I. Woo, *Phys.Chem. Chem. Phys.*, 2012, **14**, 3530-3536.

36. D. Kim, Y. Kim, K. Choi, J. C. Grunlan and C. Yu, *Acs Nano*, 2010, **4**, 513-523.

37. K. Xu, G. Chen and D. Qiu, *J. Mater. Chem. A*, 2013, **1**, 12395-12399.

38. H. Zhou, W. Yao, G. Li, J. Wang and Y. Lu, *Carbon*, 2013, **59**, 495-502.

39. M. Zhang, W. Yuan, B. Yao, C. Li and G. Shi, *Acs Appl. Mater. Interfaces*, 2014, **6**, 3587-3593.

40. J. Zhou and G. Lubineau, *Acs Appl. Mater. Interfaces*, 2013, **5**, 6189-6200.

41. Y. Xu, Y. Wang, J. Liang, Y. Huang, Y. Ma, X. Wan and Y. Chen, *Nano Res.*, 2009, **2**, 343-348.

42. H. T. Ham, Y. S. Choi, M. G. Chee, M. H. Cha and I. J. Chung, *Polym. Eng. Sci.*, 2008, **48**, 1-10.

43. Y. Inoue, Y. Suzuki, Y. Minami, J. Muramatsu, Y. Shimamura, K. Suzuki, A. Ghemes, M. Okada, S. Sakakibara, F. Mimura and K. Naito, *Carbon*, 2011, **49**, 2437-2443.

44. J. E. Mink, J. P. Rojas, B. E. Logan and M. M. Hussain, *Nano Lett.*, 2012, **12**, 791-795.

45. J. E. Mink, R. M. Qaisi, B. E. Logan and M. M. Hussain, *Npg Asia Materials*, 2014, **6**, e89.

46. H. Jiang, L. J. Halverson and L. Dong, *J. Micromech. Microeng.*, 2015, **25**, 125017.

47. S. Ryu and B.-S. Kim, *Tissue Eng. Regen. Med.*, 2013, **10**, 39-46.

48. N. Li, Q. Zhang, S. Gao, Q. Song, R. Huang, L. Wang, L. Liu, J. Dai, M. Tang and G. Cheng, *Sci. Rep.*, 2013, **3**, 1604.

49. S. K. Lee, H. Kim and B. S. Shim, *Carbon Lett.*, 2013, **14**, 63-75.

50. Y. J. Tang, A. L. Meadows, J. Kirby and J. D. Keasling, *J. Bacteriol.*, 2007, **189**, 894-901.

51. L. Dong, A. K. Agarwal, D. J. Beebe and H. Jiang, *Nature*, 2006, **442**, 551-554.

52. J. BEAR, *Dynamics of Fluids in Porous Media*, Dover, New York, 1972.

53. A. J. Bard, L. R. Faulkner, *Electrochemical Methods-Fundamentals and Applications*; 2nd ed.; John Wiley & Sons: 2001.

54. A. Dewan, H. Beyenal and Z. Lewandowski, *Environ.Sci.Technol.*, 2008, **42**, 7643-7648.

CHAPTER 7. MINIATURE PLANT MICROBIAL FUEL CELLS

7.1 Introduction

Bioenergy harvesting from living organisms is relatively new research field that has recently attracted considerable attention. Plant microbial fuel cells (PMFCs) are considered to be a clean and renewable energy due to no environment-hazardous emission during the whole process [1, 2]. In the PMFCs, rhizodeposition of organic mass are first fixed around plant roots through photosynthesis, and then converted into carbon dioxide via the electrochemically active bacteria. Cast-off electrons are transferred to cathode by the external circuit to form output electricity [2-6]. Two necessary components, i.e., plant growth chamber and MFC chamber, of the PMFC are thus needed. As a result, several important questions in two aspects need to be answered. First, whether or not and how the exudates and secretions from the plant roots can transport to the MFC chamber to sustain the life of the colonized microbes on the surface of anode? Second, whether or not the electron-generating bacteria and culture medium used in the MFC will diffuse into the plant chamber to negatively affect plant growth during operating the PMFC? Third, which bacteria, plants, and their strains, and which possible combination of bacteria and plants will be optimal to generate maximum electricity? Lastly, since direct testing of these bacteria and plants in field is inconvenient, expensive and labor intensive, how can we design a low-cost and user-friendly system to screen different plant and bacterial organisms in a PMFC setting?

The main objective of this chapter is to develop a miniature PMFC or μPMFC device to explore the possibility of screening different plants, bacteria and their strains for generating electricity using living plants. The system integrates a MFC and a plant growth chamber. The design is featured by using a semi-permeable filtering membrane with nanopores to block any possible bacteria in the MFC entering the plant chamber, while the carbon-containing substances

exudated from the plants still can diffuse into the plant chamber. The plant roots directly grow on the surface of the semi-permeable membrane. We would note that that mass transport of organic carbohydrates exudates from the plant chamber into the anolyte chamber of the MFC will be faster, because it is based on molecular diffusion over a small length scale (~millimeter) and diffusion time scales as the square of the distance. On the contrary, all existing PMFCs worked on a larger length scale on the order of centimeters and more. As a result, in the proposed µPMFC device, the effect of the root exudates on electricity generation of the device will be seen much faster. After the device is built, we will investigate which carbohydrates are exudated from plant roots to sustain the life of bacteria in the MFC using gas chromatography-mass spectroscopy (GC-MS). Furthermore, we will conduct pilot experiments to demonstrate the workability of the device to screen different bacteria, plants, and/or their strains for generating electricity.

7.2 Experimental details

7.2.1 Device fabrication and assembly

The design of the proposed µPMFC is shown in Figure 7.1. For the MFC unit, fabric carbon cloth (Fuel Cell Store, College Station, TX) is used as both anode and cathode materials. The carbon cloth anode is on top of the anolyte chamber. The carbon cloth cathode is placed at the bottom of the catholyte chamber. The anolyte and catholyte chambers are separated by a proton exchange membrane (PEM, Nafion 117, Fuel Cells Etc, College Station, TX). The volume of the anolyte and cathode chamber is 5.77 mL and 3.84 mL, respectively. The plant growth chamber is placed above the MFC unit. As mentioned earlier, a semi-permeable membrane (thickness: 0.4 µm; Polyester (PETE) membrane filter, Sterlitech Corporation, Kent, WA) is used to stop bacteria entering the plant growth chamber. All chambers are made of poly(methyl methacrylate) or PMMA (TAP Plastics, Oakland, CA), a biocompatible material. All components are assembled

together with mechanical cap screws (M4×0.7; Thorlabs, Newton, NJ). To build electrical connections, metal wires are used to extend the anode and cathode. The anolyte and catholyte chambers are accessed by polyethylene sterile tubing through the inlet and outlet of the device with proper fluid fittings.

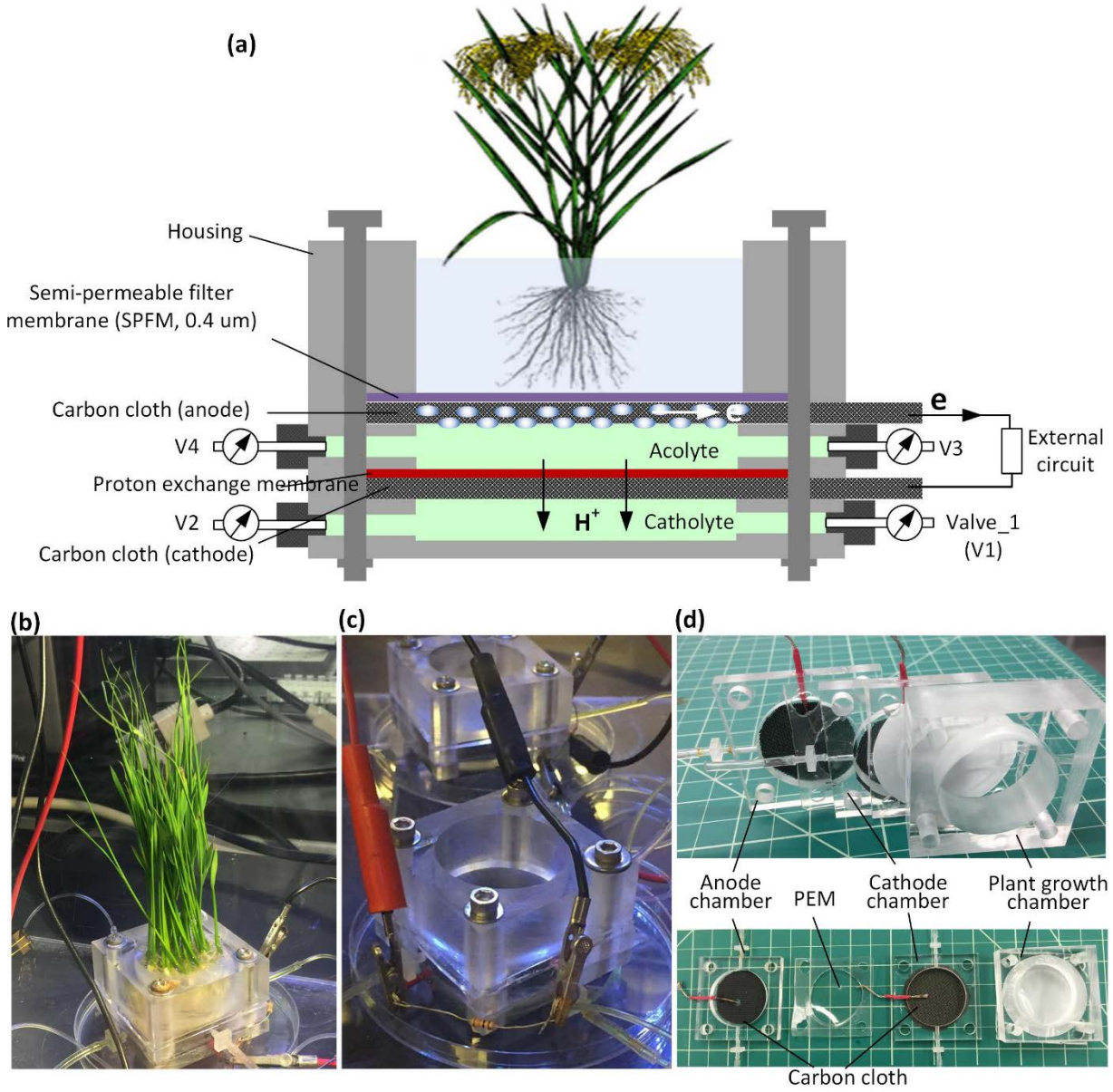

Figure 7.1 *(a) Schematic of the proposed µPMFC device, and (b) Photo of the fabricated µPMFC with rice plants. (c) Photo of the µPMFC with microfluidic tubing and electrical connections. The dimensions of the device is about 50×50×30 mm^3 (excluding the rice plants). (d) Photos of the device components of the µPMFC. The side length of the grid on the cutting mat surface represents 1 inch.*

7.2.2 Preparation for bacteria, plants, and chemicals

The µPMFCs were sterilized by filling all of compartments with pure ethanol and letting it sit for 20 minutes at room temperature, followed by flushing the devices with DI water for 5 min and then culture medium for another 5 min. To operate the device, *Shewanella. oneidensis* strain MR-1 and *Pseudomonas. aeruginosa* strain PA14 (provided by Dr. Larry J. Halverson's lab at Iowa State University) were used as the model exoelectrogenic microbial biocatalyst and a lactate defined minimal medium (consisting of 20 mM sodium lactate per liter of deionized (DI) water, 28 mM NH_4Cl, 1.34 mM KCl, 5 mM NaH_2PO_4, 0.7 mM Na_2SO_4, 52 mM NaCl, 0.2 mM $CaCl_2$ (the above chemicals purchase from Fisher Scientific, Fair Lawn, NJ), 1 mM $MgSO_4 \cdot 7H_2O$, 10 mg $FeSO_4 \cdot 7H_2O$ (the two chemicals purchase from Alfa Aesar, Ward Hill, MA), 20 mM PIPES [piperazine-*N*,*N*'-bis (2-ethanesulfonic acid)] (Sigma-Aldrich, St. Louis, MO), and 1 mL trace element solution [7]) was used the nutrient source for inoculation of bacteria, and a lactate-free culture is used for growing plants. The lactate defined minimal medium flowed into the anolyte chamber through the polyethylene tubing using a programmable syringe pump (210P, KD Scientific, Holliston, MA). To minimize possible oxygen contamination in the batch mode operation, the tubing was closed by steel clamps after the bacterial suspension was flowed into the analyte chamber. The catholyte solution of potassium ferricyanide (Fisher Scientific, Fair Lawn, NJ) was supplied using another syringe pump. Two varieties of rice plant cultivar, *Kitaake* and *IR24*, were used as model plant (provided by Dr. Bin Yang's lab at Iowa State University).

7.2.3 Electrochemical measurements and calculations

An external resistor (R) was connected between anode and cathode of the µPMFC to form a closed circuit. The voltage potential (U) between the two electrodes was measured using a data acquisition device (Model DI-245; DATAQ Instruments, Akron, OH) and recorded every 2 min

via DATAQ Instruments Hardware Manager software. The current (I) flowing through the resister was calculated via I = U/R and the output power was calculated via P = U×I. The shunt current was measured to obtain the maximum output current. Each electrical measurement result given in this paper is representative of the typical result obtained over three independent experiments on three identical devices.

7.2.4 Bacterial fixation for SEM

The carbon cloth anodes were taken out from the disassembled μPMFCs, immersed in a glutaraldehyde solution (2%; Sigma-Aldrich, St. Louis, MO) to fix the adherent bacteria on the carbon cloth surface, and incubated at 4 ºC for 12 hr. After rinsing with DI water, the carbon cloth anodes were stained with 1% osmium tetroxide solution (Sigma-Aldrich, St. Louis, MO) for 2 hr, rinsed again, and then, dehydrated by pure ethanol. A field-emission SEM (Quanta-250; FEI, Hillsboro, OR) was used to examine the treated carbon cloth.

7.2.5 Gas chromatography-mass spectrometry (GC-MS)

Gas chromatography-mass spectrometry (GC-MS) is an analytical method for analysis and quantitation of organic compounds which combines the features of gas chromatography and mass spectrometry. The GC-MS consists of two major building parts: the gas chromatograph and the mass spectrometer. The gas chromatograph separates mixtures into individual molecule using a temperature-controlled capillary column. The separated molecules are retained eluted from the column at different retention time. And then, the mass spectrometer breaks each molecule into ionized fragments and detects these fragments indicated by their mass-to-charge ratio [8, 9].

The Agilent 6890N GC with Agilent 5963N MS detector was used to analyse the components in the exudates, gas chromatograph-quadrupole mass selective detector (EI) operated at 70 eV. The column used for all analyses was an Agilent 19091S-433 HP-5MS, 30 m, 250 µm i.d., 0.25 µm film thickness. The MS was operated in scan mode.

GC-MS parameters: The oven temperature was initially held at 50 ºC. And then the temperature was raised with a gradient of 5 ºC/min until 180 ºC. Thereafter, the temperature was increased to 320 ºC with a gradient of 20 ºC/min and held for 2 min. The helium carrier gas flow through the column was held constant at 1.0 mL/min. Injection volume, 1 µL. split ratio, 2:1. Temperature of the inlet, 280 ºC. Interface temperature, 280 ºC. Quadrupole temperature 150 ºC. Source temperature 230 ºC.

7.3 Results and discussion

To investigate whether the culture medium for the microbes in the anode chamber enter the plant growth chamber, and whether the exudates from the plant roots transport to the anode chamber to sustain the life of the colonized microbes on the surface of anode. We performed analysis of the root exudates and medium solution using Agilent GC-MS.

Figure 7.2 shows four different testing objects, including:

1) Sample device A: The device is a complete µPMFC with both rice plants and a MFC. A lactate defined minimal medium is in the anode chamber of the MFC. A lactate free medium for plant growth is in the plant chamber (shown in Figure 7.2a).
2) Control device B: The device has an MFC unit with lactate defined minimal medium, but does not have any plants in the plant chamber. A lactate-free culture medium in the plant chamber (shown in Figure 7.2b).

3) Control device C: The device has a plant chamber with the rice plants, but does not have a MFC or semi-permeable membrane. A lactate-free culture medium is in the plant chamber (shown in Figure 7.2c).

4) Sample device D: The device is a complete µPMFC with both rice plants and a MFC. Cell inoculation is first conducted in the anode chamber using a lactate defined minimal culture medium. After the completion of the cell inoculation, the solution in the anode chamber is replaced with a lactate-free medium. The plant uses a lactate-free medium in the plant chamber (shown in Figure 7.2d).

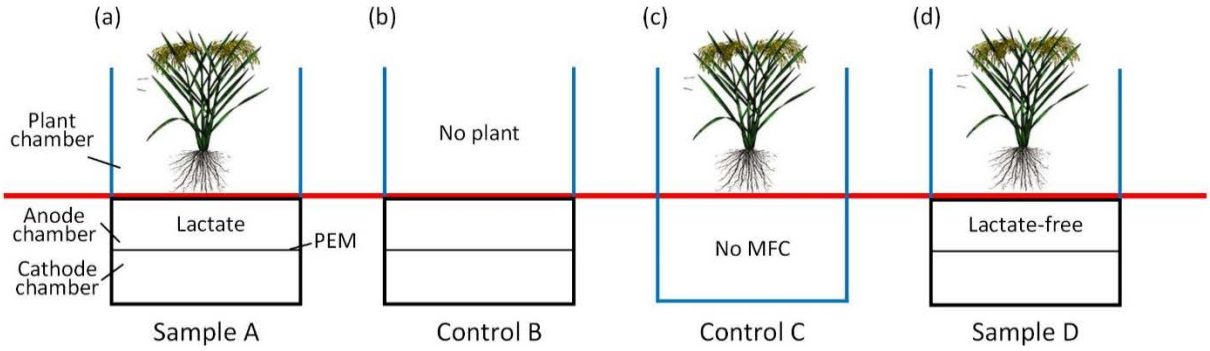

Figure 7.2 *Schematic of four different testing samples, (a) complete µPMFC with both rice plants and a MFC cultured with lactate medium in anode chamber, (b) µMFC without having plant, (c) rice plants grown at plant chamber without having µMFC, (d) complete µPMFC with both rice plants and a MFC replaced with lactate-free medium in anode chamber after inoculation.*

We sampled liquid solutions (1 µL) from the plant chamber once a day for three consecutive days after the rice plants were planted in the plant chamber, and then from the anode chamber on the third (last) day.

In order to realize whether the carbohydrates are released from rice roots. We compares the carbohydrates (alpha.-D-lactose and beta.-D-lactose) of the plant root exudates in the control device C (Figure 7.3a) on day 1 and day 3. The result of GC-MS (Figure 7.3b) shows that the peaks at 32.6 min and 33 min on day 1 (black color) have much higher intensity than those on day 3 (blue color), indicating that the carbohydrates released from the root decreases as time goes on.

This information lays the foundation for the entire operation of the proposed device where the microbes break down the organic compounds to generate electricity through electrochemical reactions.

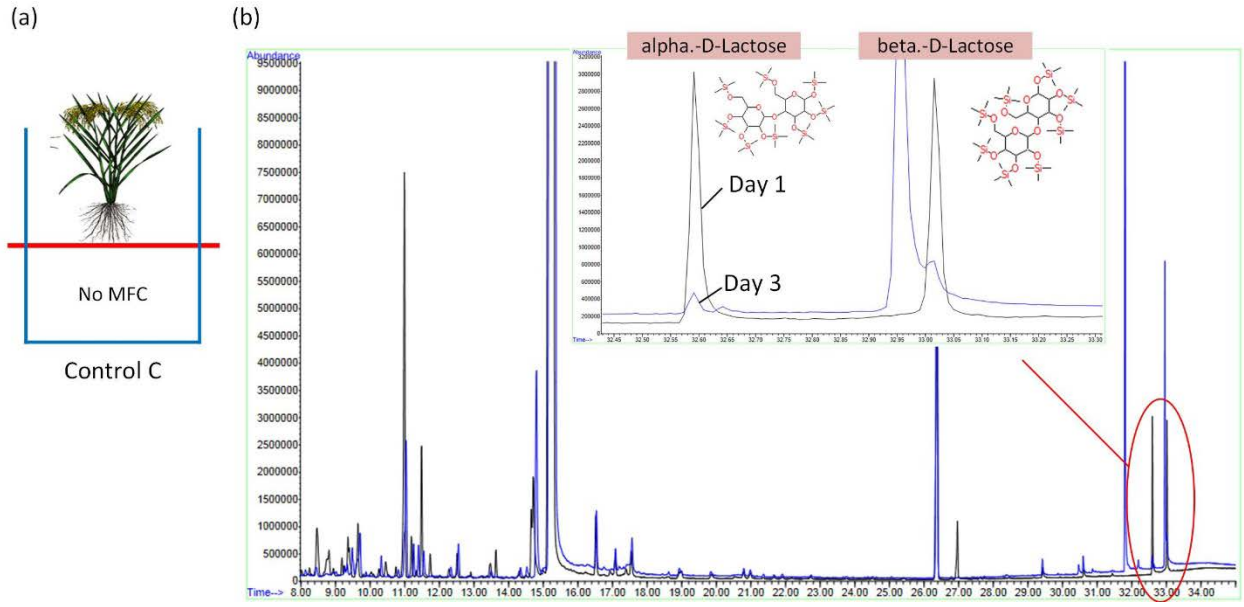

Figure 7.3 *(a) schematic of rice plants grown at plant chamber without having µMFC, (b) GC-MS curves of the plant root exudates in the control device C on day 1 (black color) and day 3(blue color).*

To detect whether the sample D that replaced with lactate-free culture in anode chamber contain lactate content. Figure 7.4b compares the lactic acid content between the lactate defined minimal source medium and the liquid solution extracted from the anode chamber of the sample device D after the aforementioned medium replacement on day 1. The higher peak intensity of the blue-color curve declares that the solution replacement method works perfectly to minimize the lactate content in the anode chamber. This method allows us to eliminate the distraction from other organic matt for the analysis, but only consider the lactate content diffused from the plant chamber.

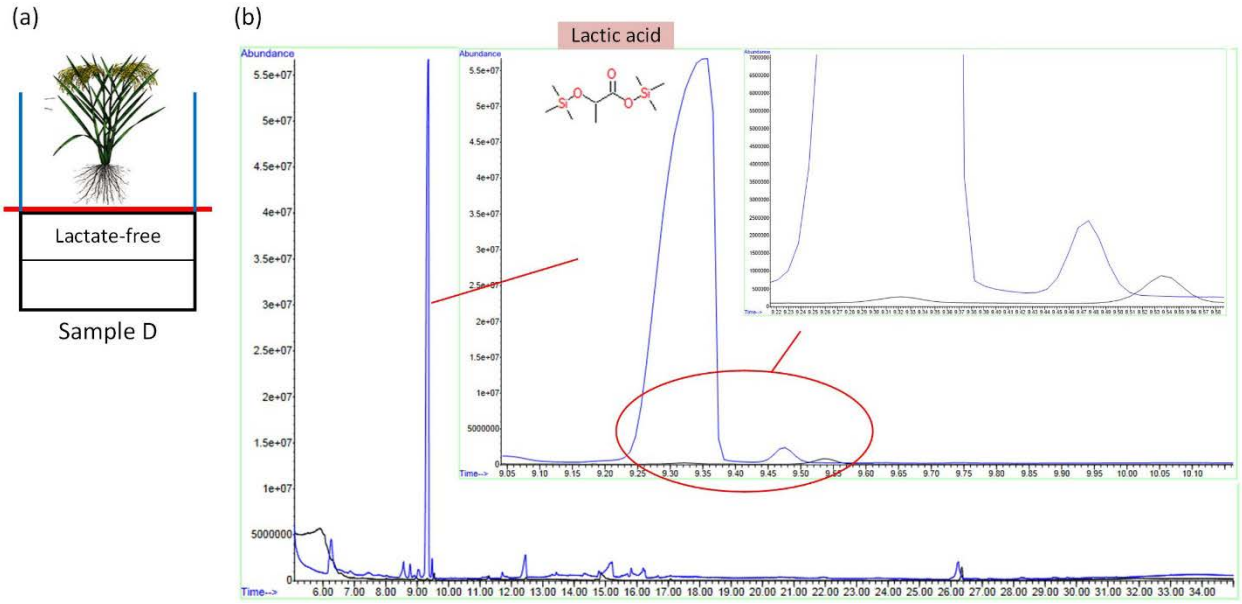

Figure 7.4 *(a) schematic of complete µPMFC with both rice plants and a MFC replaced with lactate-free medium in anode chamber after inoculation, (b) GC-MS curves of the lactate defined minimal source medium (blue color) and the liquid solution extracted from the anode chamber of the sample device D after the lactate-free culture medium replacement on day 1(black color).*

To confirm the carbohydrates released from rice roots diffuse from plant chamber to anode chamber of µMFC. Figure 7.5b displays the GC-MS result of the carbohydrate exudates from the plant roots. There is no characteristic peak of any carbohydrates in the extractives from either the control device C or from the anode chamber of the sample device D on day 3. Note that the two high-intensity peaks on the black curve are not the peaks associated with any carbohydrates. A possible explanation is that the carbohydrates released on day 3 always are less than that released on day 1 and day 2, as evident by Figure 7.3. However, even small amounts of carbohydrates released from the plant roots can transport to the anode chamber of the MFC unit to feed microbes for generating electrons.

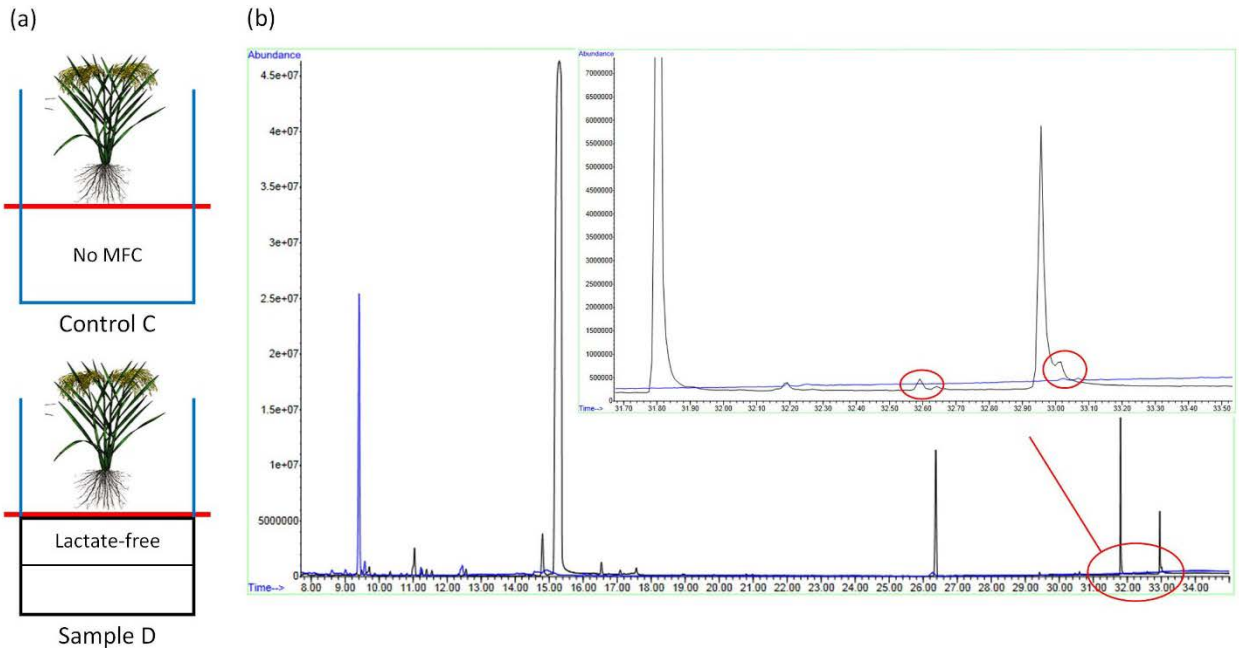

Figure 7.5 *(a) schematic of rice plants grown at plant chamber without having µMFC, and complete µPMFC with both rice plants and a MFC replaced with lactate-free medium in anode chamber after inoculation, (b) GC-MS curves of the extractives from the control device C (black color) and from the anode chamber of the sample device D on day 3 (blue color).*

To verify whether the lactate medium diffuse from anode chamber to plant chamber. Figure 7.6 shows that the culture medium extracted from the plant chamber in the control device B on day 3 contains only a little amount of lactate, compared to the lactate defined culture medium (blue color). This result demonstrates that the plant growth chamber hardly has lactate diffused from the bacteria containing anode chamber. Therefore, the lactate in the culture medium of the microbes in the MFC will not affect the growth of the plants.

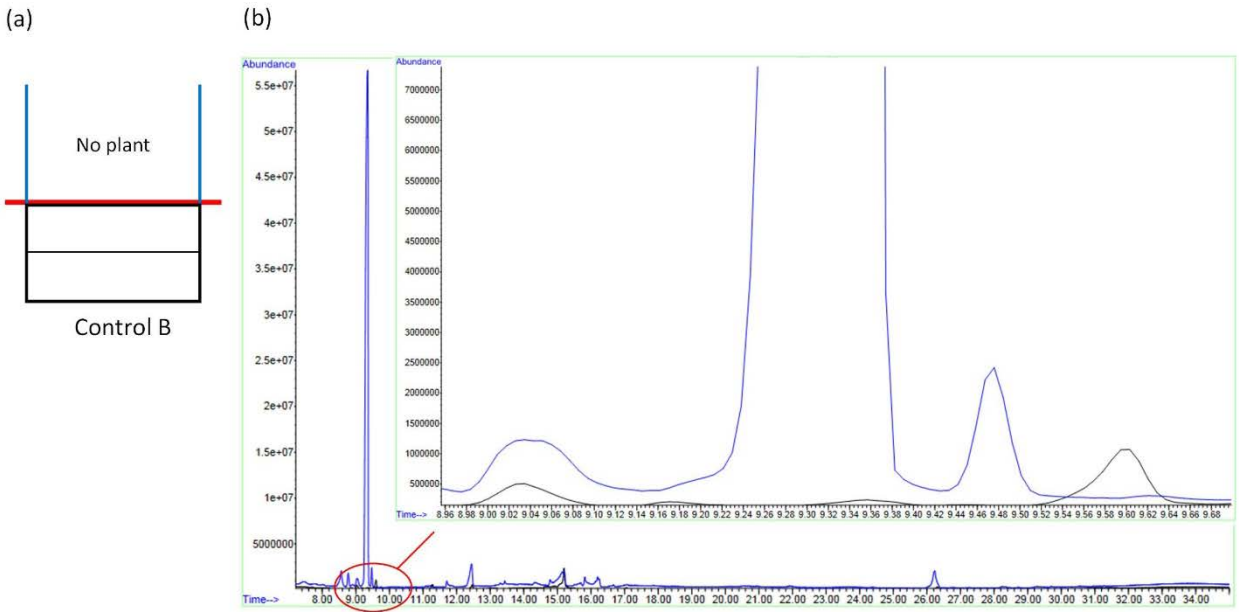

Figure 7.6 *(a) schematic of µMFC without having plant, (b) GC-MS curves of the culture medium extracted from the plant chamber in the control device B on day 3 (black color) and the lactate defined culture medium (blue color).*

In Figure 7.4, we have come to the conclusion that the sample D that replaced with lactate-free culture in anode chamber contain tiny lactate content. Thereafter, we compare the electricity generation performance of the sample devices A and D. Recall that these two devices have the same device components and are treated by the same materials and processes, except that after the cell inoculation the lactate defined minimal medium used in the anode chamber of the sample device D is replaced by the lactate free medium. On the contrary, the lactate defined medium used for the cell inoculation still remains in the anode chamber of the sample device A. We test electric current output of the two sample devices in a batch mode operation for a 5-day period, including the 2-day cell inoculation time without having rice plants, and the following 3-day rice plant growth time. The results are shown in Figure 7.7b. The overall tendencies of the current output response of the two devices are roughly the same, indicating that after the cell inoculation the remaining solution in the sample device A does not contribute to the current generation of the device. The results also show that for both of the devices, the output currents keep decreasing until

the rice plants are planted in their corresponding growth chambers at 48 hrs, and then, they tend to sustain a stable current output after a current rise occurred between 48 and 62 hours.

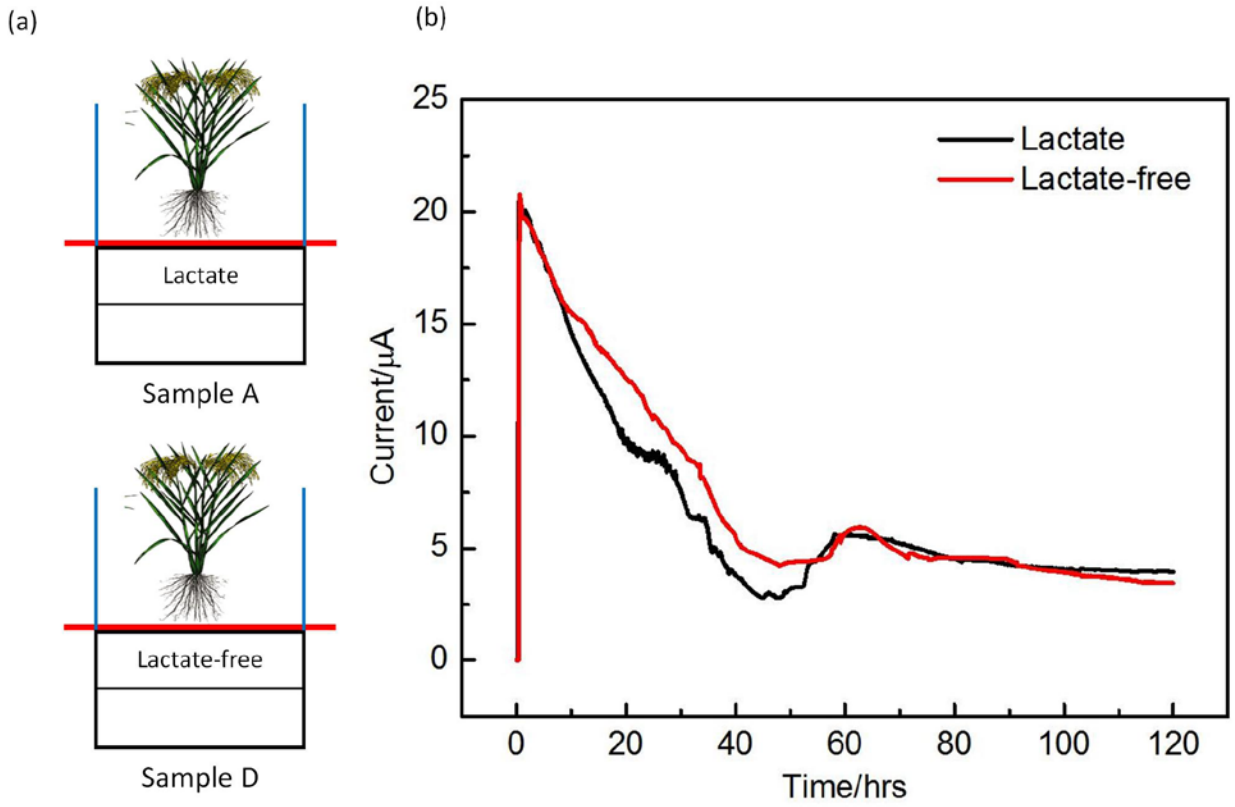

Figure 7.7 *(a) schematic of two types μPMFC, sample A: complete μPMFC with both rice plants and a MFC cultured with lactate medium in anode chamber, and sample D: complete μPMFC replaced with lactate-free medium in anode chamber after inoculation, (b) output current of two types μPMFC.*

To demonstrate the workability of the μPMFC device in screening suitable plant species and strains, we plant two different rice varieties, i.e., *Kitaake* and *IR24* (7 days old), in the plant chambers of two μPMFC devices and monitor their output currents. The two devices use the same *S. oneidensis* MR-1 strain as a biocatalysts in the anode chambers. A control device is also used with the same bacteria, but there are no any plants growing in the plant chamber. The three devices are treated with the same cell inoculation process for two days during which the similar current responses are found (Figure 7.8a). Specifically, the output currents rapidly increase to ~20 μA, and then gradually drop to ~3 μA in two days. After the plants are placed in the growth chambers,

the output currents are found to increase a little bit and then gradually decrease. However, later each current stays at a level higher than it was at the beginning of placing corresponding rice plants into the chamber. Both of the plant-containing devices generate higher currents than the control device without any plants. More importantly, it should be pointed out that the wild type rice cultivar *Kitaake* allows the device to generate more electricity than *IR24*. At the end of day 5, the control device has only ~0.1 μA current output, while the devices with *Kitaake* and *IR24* generate ~4 and ~2.5 μA, respectively. We also check the size of *Kitaake* and *IR24* before and after the device operation (shown in Figure 7.8b). Both of them grow taller. But, the tips of leaves become a little brown, probably due to lacking necessary nutrients in the lactate free medium used in the plant growth chamber.

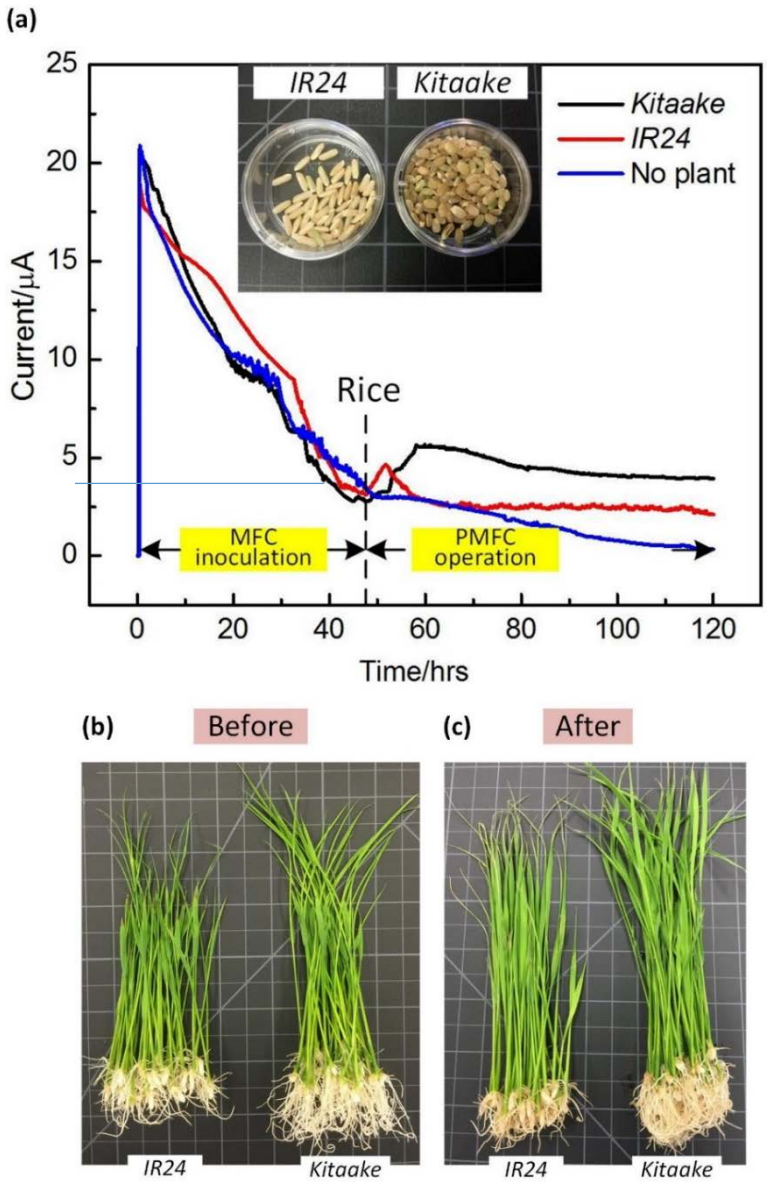

Figure 7.8 *(a) Output current of two species of rice plants using in PMFC, (b) before, and (c) after physiognomy of two types of plant species.*

Furthermore, we demonstrate using the μPMFC devices to select suitable bacteria species to work with rice plants for electricity generation (shown in Figure 7.9). To do this, we inoculate two different bacteria species, i.e., *S. oneidensis* MR-1 strain and *P. aeruginosa* 14, separately in the anolyte chambers of two identical devices using the same method as previously described. At the end of day 2, wild type rice cultivar *Kitaake* is placed in the plant chambers of these two sample devices. Another device is used as a control where *P. aeruginosa* 14 is inoculated but no any plants

are grown. During the inoculation period, the output current signal from the device with *P. aeruginosa* 14 drops slightly faster than that using *S. oneidensis* MR-1. The plants are placed on day 3. An obvious current rise is found in both sample devices, while the output current of the control device continues dropping. It is noteworthy that at the end of day 5, the output current generation from the device with *S. oneidensis*. MR-1 almost stays at ~4 µA, about 33% higher than that generated from the other device with *P. aeruginosa* 14 (~3 µA). On the contrary, the control device has almost zero current at the end of day 5.

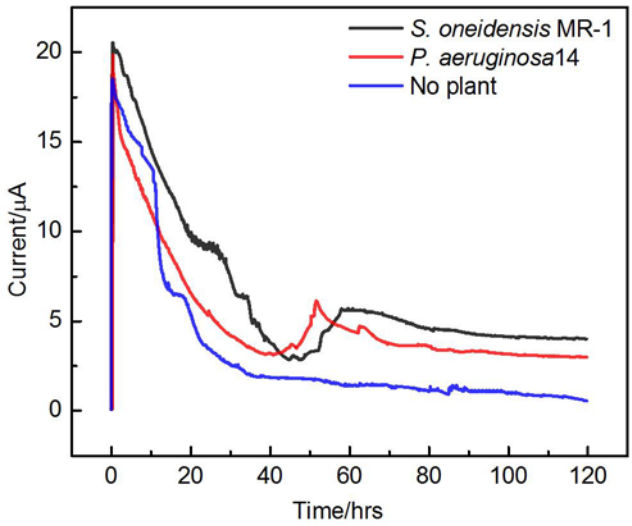

Figure 7.9 *Output current of two species of microbes using in PMFC.*

To assess the extent of *S. oneidensis* biofilm formation on the carbon cloth anode, we examined the surface morphology of the anode using SEM. The carbon cloth anode was obtained from the disassembled µPMFC grown with *Kitaate* after the entire operation period (5 days). Figure 7.10 the surface of the carbon fibers with *S. oneidensis*. However, it is difficult to see whether or not *S. oneidensis* biofilm is formed in the interior regions of the carbon cloth.

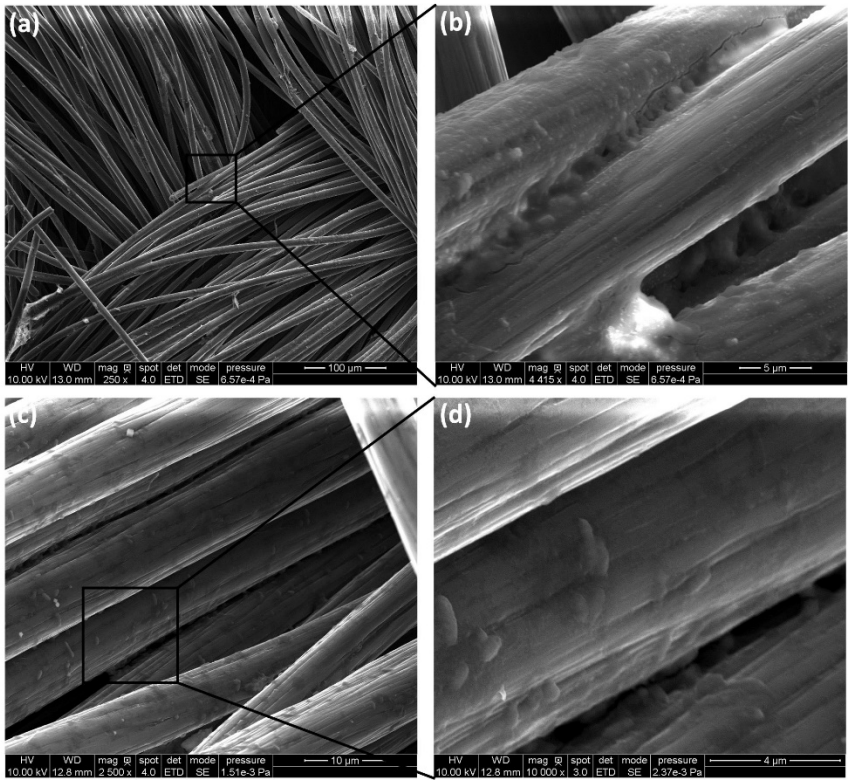

Figure 7.10 *SEM images for the biofilms of S. oneidensis strain MR-1 grown on the carbon cloth in PMFC device with magnification (a) (c), and a close up showing bacteria coating the surface of carbon cloth (b) (d).*

7.3 Conclusions

In summary, we develop the µPMFC device by integrating a MFC, a semi-permeable filtering membrane, and a plant growth chamber. GC-MS study demonstrates that the carbohydrates exudates from the roots of rice cultivar *Kitaake* can diffuse through the semi-permeable membrane into the MFC unit. The semi-permeable membrane successfully blocks bacteria from entering the plant chamber. We also demonstrate the workability of the proposed µPMFC in screening different varieties of rice plant and different bacteria species, using the rice cultivar *Kitaake* and *IR24* as model plants and *S. oneidensis* MR-1 strain and *P. aeruginosa* 14 as model bacteria. The electrical measurement result shows that *Kitaake* provides more carbohydrates excudates than *IR24* for the MR-1 strain to produce more electricity, while *S. oneidensis* MR-1 strain can generate more electricity than *P. aeruginosa* 14 when working with *Kitaake*. To our

knowledge, this is the first effort of realizing a miniature plant-MFC device for the purposing of screening suitable plants and bacteria for producing electricity.

References

1. https://www.wageningenur.nl/en/show/Plants-create-energy.htm

2. http://www.gizmag.com/plant-microbial-fuel-cell/25163/

3. D. P. B. T. B. Strik, H. V. M. Hamelers, J. F. H. Snel and C. J. N. Buisman, *Int. J. Energ. Res.*, 2008, **32**, 870-876.

4. S. K. Chirag and B. N. Yagnik, *Res. J. Biotechnol.*, 2013, **8**, 84-90.

5. http://spectrum.ieee.org/energy/environment/plugging-in-to-plant-roots

6. http://plant-e.com/technology.html

7. Y. J. Tang, A. L. Meadows, J. Kirby and J. D. Keasling, *J. Bacteriol.*, 2007, **189**, 894-901.

8. http://www.eag.com/mc/gas-chromatography-mass-spectrometry.html

9. https://en.wikipedia.org/wiki/Gas_chromatography%E2%80%93mass_spectrometry

CHAPTER 8. CONCLUSIONS

We have developed a microfluidic toolkit with multiple miniature devices, including plant chip, seed chip, miniature greenhouse, MFC, and plant-MFC, to tackle important problems in the fields of plant phenotyping and bioenergy harvesting. The development of these device will benefit in high-throughput plant phenotyping for understanding the gene-environment interactions, and in harvesting bio/chemical energy from microbes, plants, soil, and organic pollutants in wastewater.

First, we developed a vertical and transparent microfluidic chip for high-throughput phenotyping of *Arabidopsis* thaliana plants. Multiple *Arabidopsis* seeds can be germinated and grown hydroponically over more than two weeks in the chip, thus enabling large-scale and quantitative monitoring of plant phenotypes. The novel vertical arrangement of this microfluidic device not only allows for normal gravitropic growth of the plants, but also, more importantly, makes it convenient to continuously monitor phenotypic changes in plants at the whole organismal level, including seed germination and root and shoot growth (hypocotyls, cotyledons, and leaves), as well as at the cellular level. We also developed a hydrodynamic trapping method to automatically place single seeds into seed holding sites of the device, and to avoid potential damage to seeds that might occur during manual loading. We demonstrated general utility of this microfluidic device by showing clear visible phenotypes of the *immutans* mutant of *Arabidopsis*, and also with changes occurring during plant-pathogen interactions at different developmental stages. *Arabidopsis* plants grown in the device maintained normal morphological and physiological behaviour, and distinct phenotypic variations consistent with apriori data were observed via high-resolution images taken in real-time. Moreover, the timeline for different developmental stages for plants grown in this device was highly comparable to growth on conventional agar plate method. This prototype plant-chip technology is expected to lead to the

establishment of a powerful experimental and cost-effective framework for high-throughput and precise plant phenotyping.

Second, we demonstrated that by changing the spinning time of electrospinning deposition, it is possible to control statistically the pore size distributions of ENMs. The mean pore diameter is decreased exponentially from several micrometers to a couple of hundred nanometers, with increasing spinning time. The decrease of the mean pore size may possibly cause to attenuate the amount of heat energy from a remote heat source. This pore-size regulation approach enables us to create various temperature conditions on the microfluidic chips for phonemic analysis of seed growth.

Third, we developed a set of miniature greenhouses that can flexibly change the environment condition to observe the phenotyping of Arabidopsis thaliana plants. Also, the usage of liquid crystal shutter enables easily accessing the inside of greenhouse without breaking growth condition. Through designed electronic circuits, it not only controls the plant growth environment for studying plant phenotypes on a multi-scale level with sufficient throughput, but commands multiple digital cameras to take images from outside of the device when needed.

Fourth, we developed a novel miniature MFC with an improved output power density and short startup time, utilizing electrospun conducting poly(3,4-ethylenedioxythiophene) (PEDOT) nanofibers as a 3D porous anode within a 12 µL anolyte chamber. This device results in 423 $\mu W/cm^3$ power density based on the volume of the anolyte chamber, using *Shewanella oneidensis* MR-1 as a model biocatalyst without any optimization of bacterial culture. The device also excels in startup time of only 1hr. The high conductivity of the electrospun nanofibers makes them suitable for efficient electron transfer. The mean pore size of the conducting nanofibers is only several micrometers, which is favorable for bacterial penetration and colonization of surfaces of

the nanofibers. We demonstrate that *S. oneidensis* can fully colonize the interior region of this nanofibers-based porous anode. This work represents a new attempt to explore the use of electrospun PEDOT nanofibers as a 3D anode material for MFCs. The presented miniature MFC potentially will provide a high-sensitivity, high-throughput tool to screen suitable bacterial species and mutant strains for use in large-size MFCs.

Fifth, we developed a high-performance miniature MFC or μMFC with innovative microfluidic flow-through feature: the anolyte chamber is filled with 3-dimensional graphene foam based anode (GF) to form a porous microfluidic chamber. This feature design allows flowing nutrition medium throughout the chamber to intimately interact with the colonized microbes on the scaffolds of GF. This, in turn, can not only minimize consumption of nutritional substrate, but also reduce response time of output current, due to fast mass transport through direct pressure-driven mass flow and rapid diffusion of nutrients within the interstitial pores of GF to the surface of scaffolds. We demonstrate that the flow-through μMFC provides 745 $\mu W/cm^3$ volume power density based on the total volume of anolyte chamber, and 89.4 $\mu W/cm^2$ surface power density based on the planar surface area of GF anode, using *Shewanella oneidensis* MR-1 as a model biocatalyst without any optimization of bacterial culture. The medium consumption is reduced by up to 16.4 times and the response time of the device is reduced by up to 4.2 times, as the freeway space volume above its GF anode of the counterpart device increased from one to six times the volume of the GF anode. This work represents an exploratory effort to introduce a porous GF-based flow-through mechanism into a microfluidic MFC setting. This approach will have a benefit in high-throughput, large-scale screening different bacterial species and their strains for conversion of carbon-containing substrates to electricity with less space and medium consumption, more parallel experiments, and shorter experimenting time.

Lastly, we developed a µPMFC device by integrating a MFC, a semi-permeable filtering membrane, and a plant growth chamber. GC-MS study demonstrates that the carbohydrates exudates from the roots of rice cultivar *Kitaake* can diffuse through the semi-permeable membrane into the MFC unit. The semi-permeable membrane successfully blocks bacteria from entering the plant chamber. We also demonstrate the workability of the proposed µPMFC in screening different varieties of rice plant and different bacteria species, using the rice cultivar *Kitaake* and *IR24* as model plants and *S. oneidensis* MR-1 strain and *P. aeruginosa* 14 as model bacteria. The electrical measurement result shows that *Kitaake* provides more carbohydrates excudates than *IR24* for the MR-1 strain to produce more electricity, while *S. oneidensis* MR-1 strain can generate more electricity than *P. aeruginosa* 14 when working with *Kitaake*. To our knowledge, this is the first effort of realizing a miniature plant-MFC device for the purposing of screening suitable plants and bacteria for producing electricity.

APPENDIX A CYCLIC VOLTAMMETRY (CV)

Cyclic Voltammetry or CV is an electrochemical technique which is the most widely used to acquire qualitative information about electrochemical reactions. CV provides a rapid location of redox potentials of the electroactive species, which is executed by cycling the potential of a working electrode, and measuring the resulting current [1-4].

The potential of the working electrode is measured with a reference electrode and a constant potential. Figure 1 shows a typical reduction (a to d) and an oxidation (d to g). During the initial forward scan (from a to d), an increasing number of reducing potential is carried out. After going through the point of switching potential where is adequate enough to result in an oxidation or reduction of an analyte, the reverse scan occurs from d to g. In CV, the scan rate (V/s) is represented by the rate of voltage change over time during each of these phases and can be varied, and also the cycle can be repeated, Hence, the information about redox potentials and electrochemical reaction rates can be obtained from CV curve [1, 3].

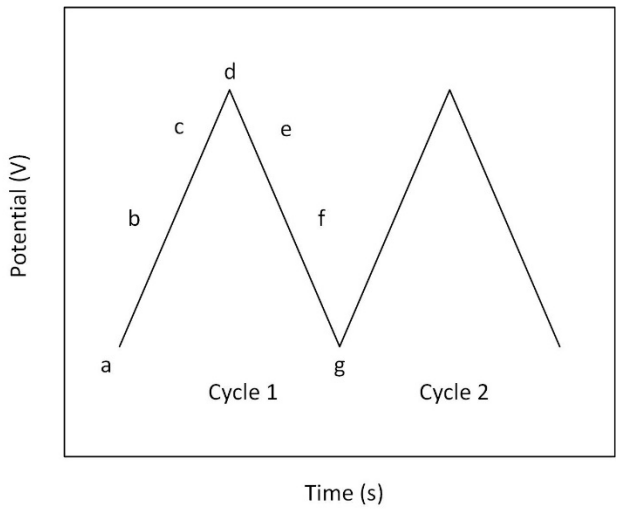

Figure 1 *Cyclic voltammetry waveform.*

The potential is applied between the working electrode and the reference electrode, and the current is measured between the working electrode and the counter electrode. All of the data are plotted as current (i) versus potential (E), and the important parameters for a cyclic voltammogram are the peak potentials E_p and peak currents i_p (shown in Figure 2) [1-3].

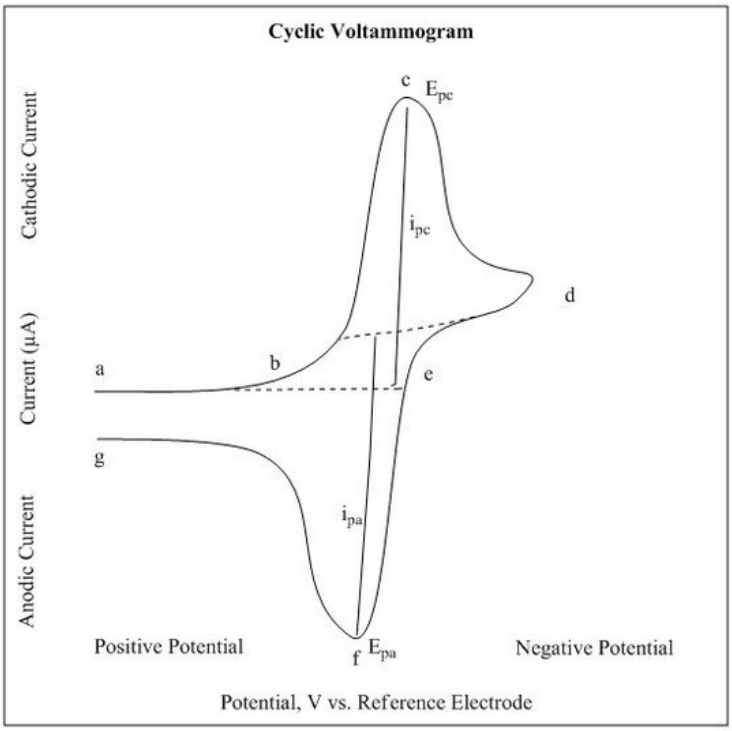

Figure 2 *Typical cyclic voltammogram where i_{pc} and i_{pa} show the peak of cathodic and anodic current respectively for a reversible reaction.*

References

1. http://chemwiki.ucdavis.edu/Analytical_Chemistry/Instrumental_Analysis/Cyclic_Voltammetry

2. https://www.basinc.com/mans/EC_epsilon/Techniques/CycVolt/cv_analysis.html

3. https://en.wikipedia.org/wiki/Cyclic_voltammetry

4. G. A. Mabbott, *J. Chem. Educ.*, 1983, **60**, 697-702.

APPENDIX B IMPEDANCE SPECTROSCOPY (EIS)

Electrochemical Impedance Spectroscopy (EIS) is a powerful measurement that initially is used to the determination of the double-layer capacitance [1-4] and in ac polarography [5-7], recently is applied to the characterization of electrode processes and complex interfaces.

Three fundamental sources of voltage loss have involved in microbial fuel cell: charge transfer activation or "kinetic" losses, electron transport or "ohmic" losses, and concentration or "mass transfer" losses [8]. Here, we use EIS to characterize the performance of microbial fuel cells, as well as separate and quantify these sources of polarization. The electrochemical processes existing in the fuel cell are modeled as equivalent circuit with a network of passive electrical circuit element (i.e., capacitors, inductors and resistors). And then, the qualitative and quantitative data in regard to the sources of impedance can be obtained. The EIS response of an equivalent circuit can be calculated and compared to the actual EIS response of the electrochemical cell [8].

The EIS data is most often displayed in Nyquist and Bode plots (shown in Figure 1). The Nyquist plot present the imaginary impedance as the function of the real impedance of the cell, which results from the electrical circuit consisted of resistor, capacitor and inductor. In Figure 1a, the semicircle is a characteristic of a single "time constant". Often one or several semicircles exist in Nyquist plot. In bode plot (shown in Figure 1b), the impedance is indicated with logarithmic-scale frequency on the horizontal axis and both the absolute values of the impedance and the phase-shift on the vertical axis. The advantages of Nyquist plot are that the individual charge transfer processes are resolvable and the small impedances can be swamped by large impedances. But it also has the disadvantages of implicit frequency-dependence data. Therefore, the general method is Nyquist and Bode plots are applied together [8, 9].

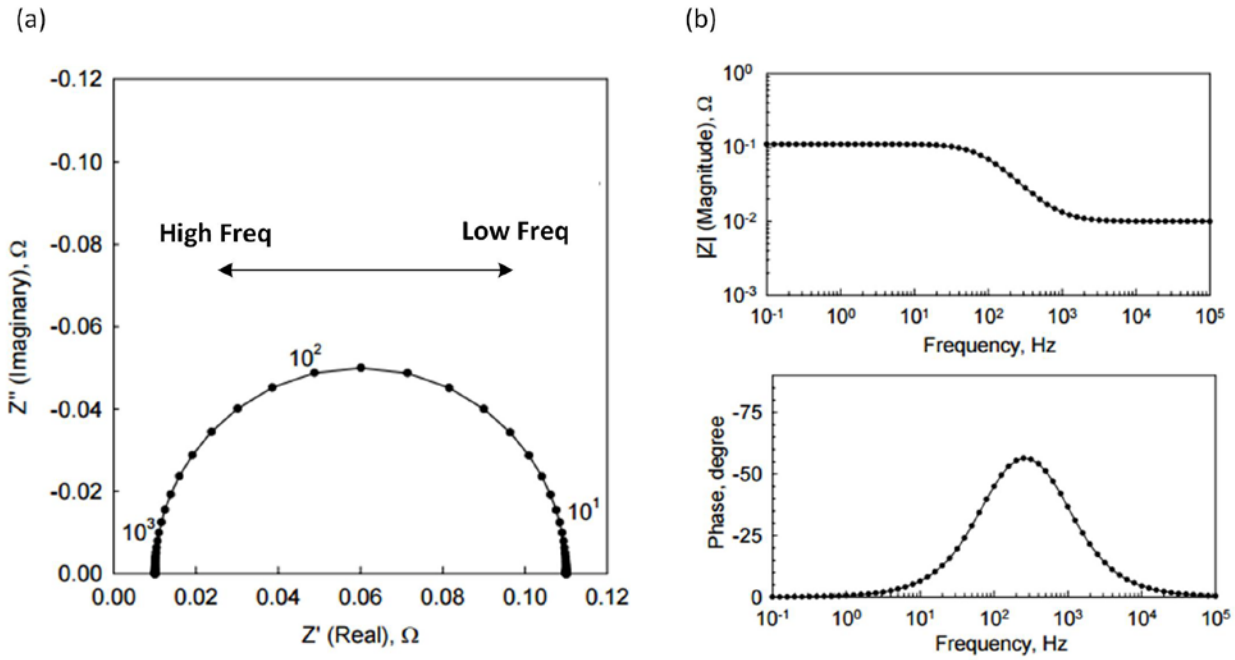

Figure 1 *(a) The complex plane (Nyquist) plot, and (b) bode plot.*

References

1. D.C. Graham, *Chem. Rev.*, 1947, **41**, 441.

2. R. Parsons, *Mod. Aspect. Electroc.*, 1954, **1**, 103.

3. P. Delahay, *Double Layer and Electrode Kinetics*, Wiley-Interscience, New York, 1965.

4. D.M. Mohilner, *Electroanalytical Chemistry*, A.J. Bard, Ed., Dekker, New York, 1966, 241.

5. B. Breyer and H.H. Bauer, *Alternating Current Polarography and Tensammetry*, *Chemical Analysis Series*, P.J. Elving and I.M. Kolthoff, Eds., Wiley-Interscience, New York, 1963.

6. D.E. Smith *Electroanalytical Chemistry*, A.J. Bard, Ed., Dekker, New York, 1966, **1**, 1.

7. A.M. Bond, *Modern Polarographic Techniques in Analytical Chemistry*, Dekker, New York, 1980.

8. http://www.scribner.com/files/tech-papers/Scribner%20Associates%20-%20Electrochemical%20Impedance%20Spectroscopy%20for%20Fuel%20Cell%20Research.pdf

9. https://www.gamry.com/application-notes/EIS/basics-of-electrochemical-impedance-spectroscopy/